Phénomènes quantiques cohérents dans les monocouches désordonnées de dichalcogénures de métaux de transition

Stefan Ilic

Stefan Ilic. Phénomènes quantiques cohérents dans les monocouches désordonnées de dichalcogénures de métaux de transition. Superconductivity [cond-mat.supr-con]. Université Grenoble Alpes, 2019. English. NNT : 2019GREAY038 . tel-02491411

HAL Id: tel-02491411
https://theses.hal.science/tel-02491411v1

Submitted on 26 Feb 2020

Communauté
UNIVERSITÉ Grenoble Alpes

THÈSE

Pour obtenir le grade de

DOCTEUR DE LA COMMUNAUTE UNIVERSITE GRENOBLE ALPES

Spécialité : **Physique théorique**

Arrêté ministériel : 25 mai 2016

Présentée par

Stefan Ilić

Thèse dirigée par **Julia S. Meyer, Professeur – Université Grenoble Alpes**,
et codirigée par **Manuel Houzet, Chercheur – CEA Grenoble**

préparée au sein du **IRIG/PHELIQS/GT**
dans **l'École Doctorale de Physique**

Quantum Coherent Phenomena in Disordered Transition Metal Dichalcogenide Monolayers

Thèse soutenue publiquement le **4 octobre 2019**,
devant le jury composé de :

M. Pascal Simon
Professeur – Université Paris Sud, Rapporteur
Mme Adeline Crépieux
Maître de conférences – Université Aix-Marseille, Rapporteur
M. Denis Basko
Directeur de Recherche – CNRS, Président
M. Nicolas Bergeal
Maître de conférences – ESPCI Paris, Examinateur

Abstract

Transition metal dichalcogenide monolayers (TMDs) are recently discovered two-dimensional materials. They host a strong intrinsic spin-orbit coupling (SOC), that acts as an effective Zeeman field with opposite, out-of-plane orientations in the +K and –K corners of the Brillouin zone (valleys). This SOC, and its interplay with disorder, strongly influences the behavior of quantum coherent phenomena in TMDs. In this thesis, we investigate two such phenomena: superconductivity and interference corrections to the conductance, which include weak (anti-) localization and universal conductance fluctuations.

Several superconducting TMDs have been experimentally found in both *n*-doped (MoS_2, WS_2) and *p*-doped ($NbSe_2$, TaS_2) regimes. Here, the intrinsic SOC causes unusual "Ising pairing" of the Cooper pairs, formed of electrons from opposite valleys with strongly pinned out-of-plane spins. In-plane magnetic fields are thus not efficient in breaking the Cooper pairs by the paramagnetic effect, which results in a large enhancement of the in-plane upper critical field – the main signature of Ising superconductivity. In the first part of this work, we calculate the upper critical field as well as the density of states of disordered superconducting TMDs. We show that intravalley scattering does not affect these properties, but that they strongly depend on intervalley scattering, which provides a depairing mechanism. In *p*-doped Ising superconductors, where multiple bands cross the Fermi level, we identify interband scattering as another important mechanism. We show that weak intervalley and interband scattering can explain experimental observations in *n*- and *p*-doped TMD superconductors, respectively.

In the second part of this work, we calculate the interference corrections to the conductance in the normal state of TMDs, which can serve as an independent probe of SOC and disorder. Because of the interplay between valley structure and SOC, these materials exhibit a rich behavior of weak (anti-) localization and universal conductance fluctuations, which is qualitatively different from other two-dimensional systems such as conventional metals or graphene. Our results can also be used to describe graphene/TMD heterostructures, where SOC is induced in the graphene sheet. We discuss parameter regimes that can be used to interpret recent experiments and assess the strength of SOC and disorder. Furthermore, we show that an in-plane Zeeman field can be used to distinguish contributions of different kinds of SOC to the weak (anti-) localization.

Résumé

Les monocouches de dichalcogénures de métaux de transition (TMD) sont des matériaux bidimensionnels découverts récemment. Ils possèdent un fort couplage spin-orbite (SOC) intrinsèque qui agit comme un champ Zeeman effectif perpendiculaire, mais avec des orientations opposées dans chaque vallée située autour des points +K et -K de la zone Brillouin. En présence de désordre, ce SOC influence fortement les phénomènes quantiques cohérents dans les TMD. Dans cette thèse, nous étudions deux de ces phénomènes : la supraconductivité et les corrections à la conductance dues aux interférences quantiques, telles que la localisation ou l'anti-localisation faible, ainsi que les fluctuations universelles de la conductance.

Une supraconductivité a été identifiée expérimentalement dans plusieurs TMD, aussi

bien dans les régimes dopés n (MoS_2, WS_2) que p ($NbSe_2$, TaS_2). Dans ces matériaux, le SOC intrinsèque provoque un “appariement d’Ising” inhabituel des paires de Cooper. En effet, celles-ci sont formées avec des électrons provenant de vallées opposées, donc leurs spins sont figés perpendiculairement à la couche. Un champ magnétique appliqué parallèlement à la couche n’est donc pas efficace pour briser les paires de Cooper par l’effet paramagnétique, ce qui entraîne une augmentation considérable du champ critique dans le plan. C’est la signature principale de la supraconductivité d’Ising. Dans la première partie de ce travail, nous calculons le champ critique et la densité des états dans les TMD supraconducteurs désordonnés. Nous montrons que la diffusion intra-vallée n’affecte pas ces propriétés. En revanche, elles dépendent fortement de la diffusion inter-vallée qui produit un mécanisme de brisure des paires de Cooper. Dans les supraconducteurs Ising dopés p, dans lesquels plusieurs bandes croisent le niveau de Fermi, nous identifions la diffusion inter-bande comme un autre mécanisme important de brisure des paires. Nous montrons qu’une faible diffusion inter-vallée ou inter-bande peut expliquer les observations expérimentales dans les supraconducteurs TMD dopés n ou p, respectivement.

Dans la deuxième partie de ce travail, nous calculons les corrections à la conductance dues aux interférences quantiques dans les TMD métalliques. Leur mesure peut servir de sonde indépendante pour identifier la nature du SOC et du désordre. En raison de l’interaction entre la structure de la vallée et le SOC, ces matériaux présentent un riche comportement de localisation (ou anti-localisation) faible et des fluctuations universelles de la conductance, qui sont qualitativement différents des autres systèmes bidimensionnels, comme les métaux conventionnels ou le graphène. Nos résultats peuvent également être utilisés pour décrire les hétéro-structures graphène/TMD, dans lesquelles le SOC est induit dans la couche de graphène. Nous discutons différents régimes de paramètres qui permettent d’interpréter des expériences récentes et d’évaluer l’intensité du SOC et du désordre. En outre, nous montrons qu’un champ Zeeman dans le plan peut être utilisé pour distinguer les contributions de différents types de SOC à la localisation ou l’anti-localisation faible.

Contents

Chapter 1

Introduction

Since the discovery of graphene [1], atomically thin two-dimensional (2D) materials have become a focus of scientific interest, due to their exceptional electrical, optical, and mechanical properties not found in the bulk. Graphene, for instance, is characterized by significant mechanical strengh and flexibility, and has high electron mobility [2]. A new addition to the family of 2D materials are monolayers of transition metal dichalcogenides (TMDs). TMDs, in their most common $2H$ variant (see Sec. 2.1), have a hexagonal lattice structure, with two inequivalent lattice sites. Like graphene, they have minima/maxima of the conduction/valence band at the $\pm K$ corners of the Brillouin zone, called valleys. Unlike graphene, however, they are not inversion-symmetric. This allows for a large band gap in their spectrum [3, 4], making them a promising candidate for a new generation of transistors [4, 5].

One of the most intriguing properties of TMDs is their intrinsic spin-orbit coupling (SOC), which is due both to their heavy constituent atoms and the absence of inversion symmetry. It is often dubbed "Ising" SOC, as it acts as an effective Zeeman field with opposite, out-of-plane orientations in the two valleys [7–9]. The coupling of spin and valley degrees of freedom leads to a variety of novel phenomena in spintronics [4] and optics, as electrons from different valleys can be excited selectively with circularly polarized light [10, 11].

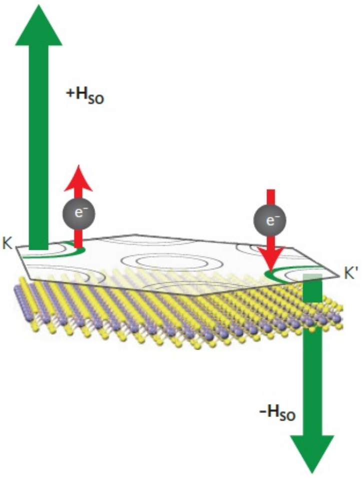

Figure 1.1: Schematic representation of Ising SOC. Taken from [6].

The Ising spin-orbit coupling also plays an important role in the intrinsic superconductivity that has been observed in several TMDs [12–15]. Namely, it causes unusual "Ising pairing" of the Cooper pairs and a great enhancement of the in-plane upper critical field. Furthermore, Ising SOC can be induced in graphene sheets by coupling them to TMDs in heterostructures. This hybrid system can exhibit interesting phenomena such as edge states [16, 17] and the spin Hall effect [18–20] (see Sec. 2.4).

Understanding the role of disorder in TMDs is of particular importance for assessing the possibility of their applications, and has recently become a subject of intensive theoretical study [21–26]. Disorder is unavoidable in TMDs, and can be caused by the gating techniques used to prepare the samples, the substrate, as well as the defects in the crystal lattice. We can distinguish intravalley disorder, associated with small momentum transfer (within a single valley), and intervalley disorder, associated with large momentum transfer (between two valleys). The latter is of particular significance, as it acts as an effective spin-flip mechanism. Namely, electrons scattered from one valley to another "feel" the opposite orientations of Ising SOC field.

In this thesis, we theoretically investigate two quantum coherent phenomena in disordered TMDs: superconductivity and the quantum interference corrections to conductance. Both are very well understood in "conventional" thin materials (such as 2D electron gasses [27, 28]), whereas in TMDs the unique interplay of SOC, disorder, and valley structure leads to qualitatively novel behavior. Our work contributes to understanding the role of disorder in TMDs, both in the normal and superconducting state, and provides a framework for interpreting numerous recent experiments.

TMDs belong to a large family of superconductors without inversion symmetry, which are, in general, platforms for unconventional superconductivity [29,30]. In Sec. 1.1, after a brief introduction to non-centrosymmetric superconductors, we introduce exotic "Ising" superconductivity in TMDs, which is the subject of the first part of this thesis. In Sec. 1.2 we discuss quantum interference effects in TMDs, including weak localization and universal conductance fluctuations, which are the subject of the second part of this thesis. These phenomena are especially useful as a probe of disorder and SOC. Section 1.3 provides a detailed outline of this work.

1.1 TMDs as non-centrosymmetric superconductors

Superconductivity is the phenomenon of zero electrical resistance below a certain (critical) temperature [31], accompanied by an expulsion of magnetic fields from the superconducting body (Meissner effect) [32]. Historically, it is one of the first studied macroscopic quantum phenomena. Bardeen, Cooper, and Schrieffer (BCS) [33] gave its microscopic description, proposing that electrons pair into bosonic Cooper pairs due to an attractive electron-phonon interaction. Cooper pairs in the so-called conventional superconductors are spin-singlets with zero total momentum, meaning that they are formed from electrons with opposite spins and momenta. Furthermore, conventional superconductors exhibit a gap in their quasiparticle spectrum, with sharp peaks in the density of states at the gap edge.

Within the Landau theory of phase transitions, superconductors are characterized by a complex order parameter $\Psi = |\Psi|e^{i\theta}$ with a given phase θ. It is not invariant under global phase shifts, meaning that the $U(1)$ gauge symmetry[1] is broken in the superconducting state (see Refs. [34, 35] for more details). The fact that every superconductor has a phase leads to important consequences which are measurable in experiment, such as the Josephson effect [36].

Superconductors can be classified with respect to the symmetries that are broken upon transitioning from the normal state. If only the $U(1)$ gauge symmetry is broken, the superconductor is *conventional.* On the other hand, if some other symmetry of the

---

[1] $U(1)$ is the group of complex numbers with unity modulus, which can be represented as $e^{i\theta}$ (θ is real).

normal state is broken as well (such as lattice symmetries or time-reversal symmetry), the superconductor is *unconventional*. Unconventional superconductivity was studied since the 80's in the context of high-critical-temperature [37] and heavy fermion superconductors [38]. It remains a very active research field today, linked with many applications such as superconducting spintronics [39] and topological superconductivity [40].

If inversion symmetry is absent in a superconductor, it can host strong SOC, which can be of Dresselhaus [41] or Rashba [42] kind. This SOC splits the Fermi surface and lifts the spin degeneracy. This has little effect on singlet pairing, but it can promote unconventional triplet pairing, where the Cooper pairs form from electrons with the same spin. As parity is not a good quantum number in these systems, singlet-triplet mixing can take place [43]. Numerous non-centrosymmetric superconductors have been discovered in recent years, including heavy fermion systems, rare earth compounds, various 2D materials (oxide interfaces, Pb monolayers, TMD monolayers), and many more [29,30].

In thin superconducting films, upon applying an in-plane Zeeman field $\mathbf{H}$, the Fermi surface becomes spin-split and momenta of spin-up and -down electrons become shifted by $\pm\mathbf{q} = \pm\frac{1}{2}g\mu_B\mathbf{H}/v_F$, where μ_B is the Bohr magneton, g is the g-factor, and v_F is the Fermi velocity. Then, at low temperatures, it becomes energetically favorable to pair a spin-up electron, with the momentum $\mathbf{k}+\mathbf{q}$, and a spin-down electron, with the momentum $-\mathbf{k}+\mathbf{q}$. Thus, a Cooper pair with a finite momentum $2\mathbf{q}$ is formed, and the order parameter is spatially modulated $\Delta(\mathbf{x}) = \Delta_0 e^{2i\mathbf{qx}}$. This is the Fulde-Ferrell-Larkin-Ovchinnikov (FFLO) phase [44,45]. In non-centrosymmetric superconductors, the combined effect of magnetic field and Rashba SOC can stabilize a different modulated phase – the so-called helical phase [46], whose modulation is fixed to the direction transverse to the field and depends on the strength of SOC. Ising SOC, by contrast, is not expected to stabilize a spatially non-uniform phase [24]. Namely, only some SOC, which satisfies the so-called gyrotropic point group symmetry, can lead to the appearance of helical phases [47].

Helical phases are linked with a novel coupling of magnetic fields and supercurrents. This leads to various magnetoelectric effects, such as the possibility of static magnetization inducing supercurrents (in 2D) and vice-versa [29,30]. As TMD superconductors do not support helical phases, they are not expected to exhibit magnetoelectric effects (except if uniaxial strain is applied to the monolayers, as shown in Ref. [47]).

In addition, non-centrosymmetric superconductors could present a way to realize topological superconductors. This exotic state of matter exhibits a quasiparticle gap in the bulk, but hosts gapless edge states, called Majorana modes, at its boundaries [48]. Majorana modes can be combined to form extended fermionic states, making them robust against local perturbations. Furthermore, they satisfy non-Abelian statistics. These properties offer a promising platform to realize topologically protected quantum computing [29,49].

Most proposals to realize topological superconductivity rely on combining several conventional materials. A prime example is a hybrid structure of a conventional superconductor and a semiconducting nanowire with Rashba SOC [50]. Non-centrosymmetric superconductors provide an alternative to these approaches, as they could host topological superconductivity intrinsically, provided that strong enough spin-triplet pairing gap is present in the system [40]. Note that these superconductors can be either nodal or "fully gapped". In the former case, the superconducting gap vanishes at some points on the Fermi surface, while in the latter case the gap is non-zero on the whole Fermi surface.

TMDs where only one spin-split band is occupied, have been identified as intrinsic topological superconductors [51]. Such a regime can be achieved in p-doped TMDs, because of the large spin-splitting due to Ising SOC in the valence band (see Sec. 2.2). Furthermore, a nodal topological phase has been proposed in $NbSe_2$ subject to high in-plane fields [52]. Finally, hybrid structures of a TMD superconductor and a half-metal have been proposed to host Majorana modes [53].

An important aspect to address when studying unconventional superconductivity is the effect of impurities. In conventional superconductors, robustness against non-magnetic disorder is guaranteed by the Anderson theorem [54], provided that disorder in not strong enough to cause localization of single-particle states. Namely, although momentum is not a good quantum number in the presence of disorder, such that there are no states of opposite momentum that can pair, the Anderson theorem states that Cooper pairs can still form from time-reversed states and that disorder, therefore, has no effect. The situation is different for unconventional superconductivity, which is generally destroyed by disorder [35].

1.1.1 Ising superconductivity

Superconductivity has been found in several TMDs: MoS_2 [12, 13] and WS_2 [55] in the n-doped regime, and $NbSe_2$ and TaS_2 [14, 15] in the p-doped regime. Notably, measurements of the in-plane upper critical field (H_{c2})[2], in these materials reach up to 60 T, greatly surpassing the so-called Pauli limit $H_p = \sqrt{2}\Delta_0/(g\mu_B)$, which corresponds to the magnetic field at which the paramagnetic energy is equal to the condensation energy of a Cooper pair. Here $\Delta_0 = 1.76 k_B T_c$, and T_c is the critical temperature of the superconductor. This enhancement of H_{c2} can be understood as a consequence of Ising SOC and the 2D nature of TMDs. Namely, the Cooper pairs are formed from electrons from opposite valleys, with strongly pinned out-of-plane spins due to the Ising SOC. This is the so-called "Ising" pairing. Magnetic fields can suppress superconductivity by two different mechanisms: by coupling to the momentum of electrons (orbital effect) or by coupling to their spins (paramagnetic effect). In 2D, in-plane fields do not couple to the electron momentum, so the orbital effect can be neglected [27]. On the other hand, due to the Ising SOC, the in-plane field is also not efficient in breaking the Cooper pairs by the paramagnetic effect. Thus, the in-plane upper critical field is greatly enhanced.

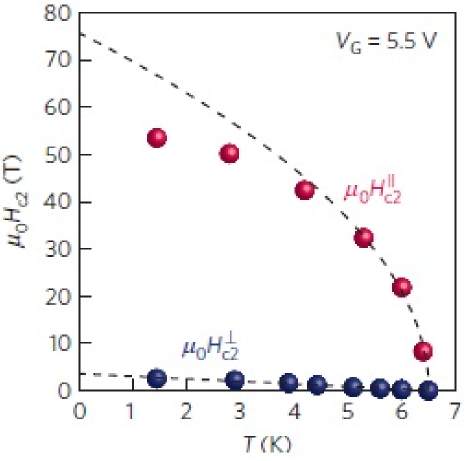

Figure 1.2: In-plane upper critical field in MoS_2. Taken from [12]

Ising superconductivity is not unconventional in a sense of the classification provided

---

[2] The upper critical field H_{c2} is defined the magnetic field at which the transition to the normal state happens in type II superconductors. In experiment, the transition point is usually defined as the point where the resistance of the sample reaches 50% of the normal state resistance [14, 27].

earlier in this section, as it does not break any additional symmetries of the normal state. Nevertheless, it is significantly different from the ordinary singlet pairing phase, and exhibits several unusual properties, as will be discussed in the following. If an in-plane field H is applied along the x-direction, the effective magnetic field in the two valleys is given by $\vec{h}_\eta^{\text{eff}} = h\mathbf{e}_x + \eta\Delta_{so}\mathbf{e}_z$, where $\mathbf{e}_i$ is a unit vector in the i-direction, $h = \frac{1}{2}g\mu_B H$ is the energy associated with an in-plane Zeeman field, Δ_{so} is Ising SOC, and $\eta = \pm 1$ is the valley index [see Fig. 1.3 (a)]. For finite in-plane fields, we can think of two separate singlet-pairing channels: one for degenerate and one for non-degenerate electrons (at opposite momenta). The non-degenerate channel corresponds to pairing where one electron is aligned whereas the other electron is anti-aligned with their respective "local" field. These electrons have an energy difference of $\sqrt{h^2 + \Delta_{so}^2}$ when their momenta are opposite and, thus, their contribution to pairing is suppressed by the field. The amplitude of the non-degenerate channel is $h^2/(h^2 + \Delta_{so}^2)$, determined by the overlap of electron spin directions. The degenerate channel corresponds to pairing of electrons that are both aligned or anti-aligned with their respective "local" field, and have the same energy when their momenta are opposite. Thus, their contribution to pairing is not affected by the field. Here the channel amplitude is given as $\Delta_{so}^2/(h^2 + \Delta_{so}^2)$.

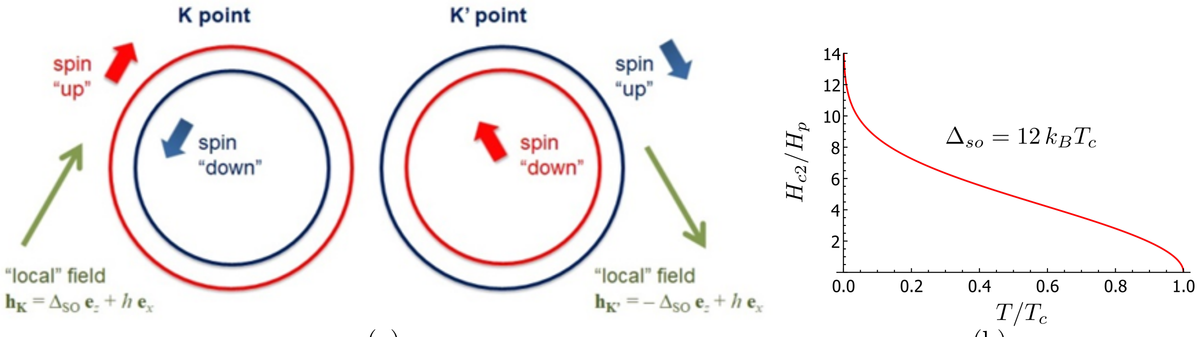

(a) (b)

Figure 1.3: (a) Fermi surface of TMDs at finite in-plane magnetic fields. (b) Upper critical field calculated from Eq. (1.1).

The degenerate channel does not exist in the conventional singlet-pairing phase. In Ising superconductors, by contrast, it plays a very important role and leads to a divergence of the in-plane upper critical field, as degenerate pairing can persist up to arbitrary fields at zero temperature. This divergence is a unique property of Ising superconductors. The expression for the upper-critical field $h_{c2} = \frac{1}{2}g\mu_B H_{c2}$ takes the form [24, 56]

$$\ln\frac{T_c}{T} = \frac{h_{c2}^2}{h_{c2}^2 + \Delta_{so}^2}\Re\left[\psi\left(\frac{1}{2} + \frac{i\sqrt{h_{c2}^2 + \Delta_{so}^2}}{2\pi T}\right) - \psi\left(\frac{1}{2}\right)\right], \tag{1.1}$$

where T and T_c are the critical temperatures at finite and zero field, respectively, ψ is the digamma function, and we choose the units where $k_B = \hbar = 1$. Here, the amplitude of the pairing channel enters as a prefactor, while the energy difference of paired electrons enters in the ψ functions. Figure 1.3 (b) shows the temperature dependence of H_{c2} obtained from Eq. (1.1) for a realistic value of SOC in MoS$_2$ (Δ_{so} is obtained from first-principle calculations [12]) .

Experimental measurements of H_{c2}, which go to temperatures as low as $T \sim 0.1T_c$, show no upturn at low temperatures and no indications of the divergence, and it is clear that the simple theory presented above fails to quantitatively describe superconductivity in TMDs. This can be remedied by adding additional ingredients to the theory, that would limit h_{c2} and cut-off the divergence. Rashba SOC caused by gating was considered in Refs. [12, 13]. While it indeed acts as a competing effect to Ising SOC by driving the electron spins to an in-plane orientation, an unrealistically large value is needed in order to explain the measurements [12].

In Chapter 5, we show that disorder provides a realistic mechanism that limits h_{c2}. We calculate the in-plane upper critical field and the density of states in the superconducting state. We show that intravalley scattering does not affect the superconducting properties, similarly to the Anderson theorem for conventional superconductors. Intervalley scattering, on the other hand, provides an effective spin-flip mechanism and breaks Cooper pairs. It suppresses the degenerate pairing channel and cuts-off the divergence. We show that weak intervalley scattering can explain the H_{c2} measurements in n-doped TMD superconductors (MoS_2 and WS_2).

1.1.2 Multiband superconductivity

The band structure of p-doped TMDs is more complicated compared to their n-doped counterparts. Here, aside from the band associated with the $\pm K$ points, another band centered around the Γ point is also present at the Fermi level [see Fig. 1.4 (b)]. Note that the Γ band also exhibits intrinsic SOC, but significantly weaker in comparison to the K band [14, 15]. If both these bands contribute to superconductivity in p-doped TMD superconductors ($NbSe_2$ and TaS_2), the theory presented in Chapter 5 no longer applies. Indeed, tunneling measurements of the density of states in trilayer $NbSe_2$ show a two-gap structure, suggesting contributions from two bands [see Fig. 1.4 (a)].

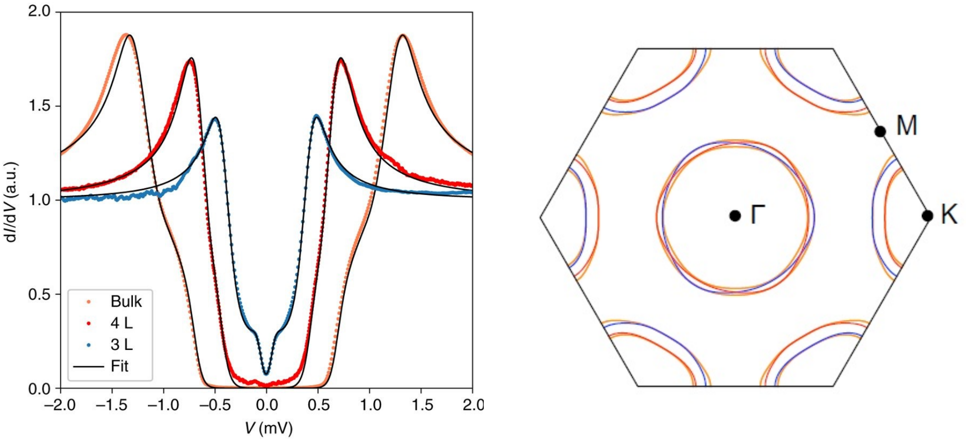

(a) (b)

Figure 1.4: (a) Quasiparticle spectra of bulk and few-layer $NbSe_2$. Taken from [57]. (b) Band structure of p-doped $NbSe_2$ at the Fermi level. Taken from [58].

Quasiparticle spectra at zero in-plane magnetic field in Ref. [57] are well described within the McMillan model [59, 60]. This model assumes that the coupling of the two bands comes from scattering of quasiparticles from one band to the other. By fitting the experimental data with this model, it is found that superconductivity develops predominantly in the K-band (with a large superconducting gap) and is induced by proximity effect in the Γ-band (giving rise to a smaller gap). Similar arguments have been invoked to interpret the quasiparticle spectra of the well-known multiband superconductors MgB_2 [61] and bulk NbSe_2 [62].

An additional argument in favor of this explanation comes from the dependence of the quasiparticle spectra on in-plane fields measured in Ref. [57]. The smaller gap in the spectrum is completely suppressed by the field of 1.2 T, while the larger gap remains barely affected up to the maximal field used in this experiment – 6.4 T. This is compatible with a larger gap coming from the K-band and being “protected” from the in-plane fields by the Ising SOC. On the other hand, the smaller gap comes from the Γ-band, where SOC is weak and does not provide such “protection” from the field.

In Chapter 6 we develop a model for two band Ising superconductors. We assume that the superconductivity originates from the K-band and that it is induced in the Γ band. We consider disorder within the K band (intra- and intervalley), within the Γ band, as well as interband disorder. We calculate the in-plane upper critical field and the density of states in the superconducting state, generalizing the results of Chapter 5 to a multiband scenario. We show that interband scattering presents an additonal mechanism that limits H_{c2}. Due to the inverse proximity effect in the K-band, the Cooper pairs “leak” into the Γ-band, where there is no Ising protection and the supperconductivity is more easily suppressed by the field.

Small interband scattering, of the order of the superconducting gap, allows us to account both for the shape of the density of states [57] and for the magnitude of H_{c2} [14,15] in p-doped TMD superconductors.

1.2 Quantum interference corrections in TMDs

In disordered materials, scattering from impurities causes the electron trajectories to behave as a random walk. The conductance of this system is then related to the probability of electrons to propagate between two points $\mathbf{x_1}$ and $\mathbf{x}_2$,

$$\mathcal{P}(\mathbf{x}_1 \to \mathbf{x}_2) = \left| \sum_i A_i \right|^2, \tag{1.2}$$

where A_i represents the amplitudes of all possible paths between the two points. As disorder is random, different paths will have different phases. Then, we may assume that all interference terms $A_i A_j$ $(i \neq j)$ will have a disorder-dependent phase and vanish upon disorder averaging, yielding

$$\langle \mathcal{P}(\mathbf{x}_1 \to \mathbf{x}_2) \rangle = \sum_i |A_i|^2, \tag{1.3}$$

which amounts to the well-known classical, or Drude, conductance. In the full quantum mechanical treatment of this problem, however, certain interference terms can, in fact, “survive” the averaging. For example, if two electrons move along time reversed paths in loops, their phases will cancel out, and this process will contribute to the probability

$\langle \mathcal{P} \rangle$. This introduces correction to the Drude conductance in forms of weak localization (WL) corrections and universal conductance fluctuations (UCF)[3].

These phenomena are especially relevant in one- and two-dimensional systems, where electron interference is more pronounced than in 3D systems. WL and UCF have been extensively studied in the 80's and 90's [28], as they can be used as a probe of electron coherence times, as well as momentum and spin relaxation rates. They remain invaluable today in the study of the properties of novel materials. In TDMCs, WL and UCF are governed by the interplay of SOC and disorder, similarly to Ising superconductivity, as we will discuss in the further text.

An important quantity which limits the quantum interference phenomena is the so-called inelastic dephasing rate τ_ϕ^{-1}. It increases as a function of temperature T, and can be due to electron-electron interaction ($\tau_\phi^{-1} \propto T$), electron-phonon interaction ($\tau_\phi^{-1} \propto T^4$), or other mechanisms that introduce dephasing [64]. Coherent quantum transport in the entire sample is possible only if the length of the sample L does not exceed the coherence length $L_\phi = \sqrt{D\tau_\phi}$, where D is the diffusion constant.

1.2.1 Weak (anti-) localization

In conventional metals, constructive electron interference along time-reversed trajectories increases the probability of electrons moving in closed loops (see Fig. 1.5). As a consenquence, the conductance will be smaller compared to the classical Drude case. This phenomenon is known as WL [66]. In the presence of strong SOC, on the other hand, the spin precession of electrons can lead to a phase shift, which results in destructive interference and a positive correction to the Drude conductance, known as weak anti-localization (WAL) [67]. Observation of WAL in a material is often taken as a proof of strong SOC. W(A)L in two-dimensional, single-band systems with SOC is theoretically well understood withing the Hikami-Larkin-Nagaoka (HLN) theory [67], which describes the corrections to the Drude conductivity due to W(A)L.

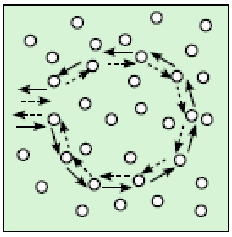

Figure 1.5: Quantum interference along time-reversed paths. Taken from [65].

In Dirac materials, such as TMDs, graphene, or surface states of topological insulators, the physical picture becomes more complex. The band structure of these materials is characterized by a non-trivial Berry phase, which introduces a phase shift of $\phi_B = \pi(1 - E_g/\mu)$ to electron interference. Here, $2E_g$ is the band-gap or so-called "Dirac mass", and μ is the chemical potential. In the massless limit (e.g. in graphene), this phase shift is $\phi_B = \pi$ (leading to WAL [68]), while no phase shift is introduced in the large mass limit (leading to WL [69]). Furthermore, in materials with multiple valleys, processes that break valley degeneracy, such as intervalley scattering, also influence the WL corrections [70, 71]. A theory which takes all these effects into account for the case of graphene was

---

[3] Note that we assume sufficiently dilute disorder, such that the correction to the conductance due to quantum interference is small compared to the Drude conductance. At high disorder concentrations, single-particle states localize and electron transport comes to a complete halt. This is the so-called strong (or Anderson) localization [63].

developed by McCann and Fal'ko (MF) [72]. It gives a full description of WL and WAL with any disorder that satisfies time-reversal symmetry. In the presence of spin-orbit impurities and in the regime of strong intervalley scattering, such that the valley physics is suppressed, it reduces to the HLN formula.

W(A)L can be probed experimentally by applying a perpendicular magnetic field, which break the time-reversal symmetry and, thus, suppresses the electron interference [67]. By measuring the resulting magnetoconductance as a function of the field and fitting it to the theoretical models, one can extract parameters such as momentum or spin relaxation rates, and gain insight into the amplitude and mechanism of SOC[4].

Recently, a significant number of WL magnetoconductance measurements were performed in TMDs [76–78] and graphene/TMD heterostructures [17,79–83], and were interpreted using the HLN and MF theories, respectively. However, the applicability of HLN and MF theories to these materials is limited, since they were both developed to describe spin-degenerate systems and do not capture the spin splitting caused by the presence of Ising SOC. A theory for TMDs that takes it into account was given by Ochoa *et al.* [23] in the regime close to the bottom/top of the conduction/valence band, $|\mu| \approx E_g$. This parameter regime, however, does not fully describe graphene/TMD heterostructures and highly doped TMDs, where $|\mu| \gg E_g$[5].

In Chapter 7, we develop a general theory of W(A)L for a diffusive Dirac material with Ising SOC, that can be applied to TMDs and graphene/TMD heterostructures. Namely, we generalize Ref. [23] for any chemical potential. As discussed above, a number of mechanisms influence the interference correction in these materials, including SOC, Berry phase induced by the Dirac-like band structure, and the valley structure. This results in a rich and complex behavior of WL and WAL, which we analyze in several regimes of interest for the interpretation of recent experiments. Similarly to Ising superconductivity, we find that one of the most important mechanisms for describing W(A)L is the interplay between Ising SOC and intervalley scattering. Since both TMDs and graphene/TMD heterostructures are expected to have substantial Ising SOC [8, 16, 17], our newfound regimes are experimentally relevant and can be used to extract parameters from the interference-induced magnetoconductance in both systems.

One of the main difficulties when interpreting the experiments comes from the fact that there may be multiple parameter combinations that can fit the same data equally well. For example, both Ising SOC and spin-dependent scattering can lead to pronounced WAL signals. For this reason, we include an in-plane Zeeman fields in our theory, which can help overcome these ambiguities, as different kinds of disorder and SOC yield a different interplay with the field.

---

[4] An interesting application of W(A)L magnetoconductance measurements is found in the study of the surface states of topological insulators such as Bi_2Se_3 [73–75]. Namely, at zero or positive top gate bias, only the electrons from the *n*-doped bulk contribute to the quantum transport, while at negative bias, the Dirac point of the gapless surface states contributes as well. Both the surface and bulk states produce WAL signals of equal amplitude, originating from the Berry phase and strong spin-orbit coupling, respectively. By tuning the top-gate bias from zero to negative, several experiments [74, 75] observed doubling of the amplitude of the WAL. This is a strong indication of the presence of the conducting channel on the surface of Bi_2Se_3 due to the topological surface states.

[5] Note that the parameter regime $|\mu| \gg E_g$ is not relevant in superconducting TMDs, where $\mu \gtrsim E_g$ holds [12, 14].

1.2.2 Universal conductance fluctuations

Let us imagine a d-dimensional, macroscopic, diffusive conductor of the size L. Assuming that $L_c = \max(L_\phi, L_T)$ is the size of the smallest piece of the conductor that remains statistically independent, such that $L \gg L_c$, the fluctuations of conductance are of the order $\delta G^2/G^2 \propto (L_c/L)^d$ [28], where G is the Drude conductance. Here, $L_T = D/T$ is the characteristic thermal length. We see that, for a macroscopic conductor, conductance fluctuations are small and diminish with sample size.

However, in mesoscopic samples whose size is smaller than the electron coherence length, $L_\phi > L$, much larger conductance fluctuations of the order $\delta G \propto e^2/h$ are found. These fluctuations are said to be *universal*, as they do not depend on disorder, but only on the shape and size of the sample. This phenomenon is a consequence of electron interference, and was predicted independently by Altshuler [84] and Lee *et al.* [85].

A simple qualitative explanation of the UCF can be given in terms of energy level statistics for disordered systems [86]. Namely, the average conductance in units e^2/h can be expressed as a number of electron energy levels in an energy window with a width of the order of the Thouless energy $E_T = 2\pi D/L^2$, centered around the Fermi level. As the fluctuation of the number of energy levels in any interval are predicted to be of order 1 [86], this automatically yields conductance fluctuations of the order e^2/h.

Similarly to WL, UCF is sensitive to SOC due to the dephasing introduced by spin precessions [87, 88]. In the presence of strong spin-orbit scattering, for instance, the amplitude of UCF reduces four times compared to the case without SOC with the same sample geometry. In graphene, as well as other multivalley materials, the amplitude of UCF is four times larger compared to conventional metals, due to valley degeneracy. Breaking this degeneracy by intervalley scattering reduces this amplitude [89,90]. We see that the amplitude of UCF can be a rich source of information on SOC, valley structure, and electron decoherence.

Experimentally, UCF is usually not investigated on a large ensemble of samples. Rather, it is done by varying a physical parameter such as the chemical potential or magnetic field in a single sample. Conductance as a function of this parameter fluctuates, and is called a “fingerprint” of the specific sample. It is reproducible and thus readily distinguished from external noise, and allows for the determination of the amplitude of UCF. As UCF can be measured in the same experimental setup as W(A)L, these two phenomena are often studied jointly.

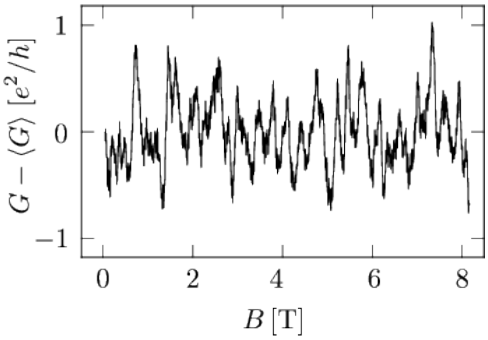

Figure 1.6: “Magnetofingerprint” of a gold nanowire. Taken from [91].

In Chapter 8, we calculate the UCF for TMDs and their heterostructures with graphene. We calculate the amplitude of UCF, which aside from sample geometry, again, mainly depends on the ratio of Ising SOC and intervalley scattering. In contrast to W(A)L, UCF in these materials was not extensively studied in experiments. Our results could motivate more experimental efforts, and serve as an additional probe of SOC and disorder, complementary to WL and WAL.

1.3 Outline of the thesis

The first few Chapters of this thesis, 2, 3 and 4, serve to set the stage and introduce imporant concepts, before discussing our main results in the subsequent Chapters (Part I and Part II).

Chapter 2 introduces TMDs, their structure, physical, and chemical properties, and Ising SOC. This is followed by an overview of experiments in superconducting TMDs, including the measurements of the upper critical field, whose great enhancement suggests exotic Ising superconducitivity in these materials. Finally, we introduce graphene/TMD heterostructures, where Ising SOC is induced in graphene sheets in contact with TMDs.

Next, in Chapter 3, we present a low-energy model for the normal state of TMDs and their heterostructures with graphene, in the form of the Dirac Hamiltonian. By assuming that the chemical potential is the dominant energy scale in the system, this model can be significantly simplified by projecting to the conduction or valence band. We account for disorder in these systems phenomenologically, by introducing symmetry-allowed scattering potentials and expressing them in the projected basis.

In Chapter 4 we provide the basics of the theoretical formalisms used to obtain our main results in Part I and Part II. We introduce standard diagrammatic techniques for disordered systems, followed by the quasiclassical (Eilenberger) formalism for disordered superconductors.

In Part I, we study the behavior of disordered Ising superconductors subjected to in-plane magnetic fields. In Chapter 5, we focus on n-doped TMD superconductors, such as $\mathrm{MoS_2}$ and $\mathrm{WS_2}$, where only the $\pm K$ pockets of the Fermi surface participate in superconductivity. We discuss the important role of interevalley scattering, which provides an effective spin-flip and pair-breaking mechanism. In Chapter 6, we study p-doped TMD superconductors, such as $\mathrm{NbSe_2}$ and $\mathrm{TaS_2}$. Here, in addition to $\pm K$ pockets, the Γ pocket of the Fermi surface also contributes to superconductivity. We show that even a small amount of interband scattering (from K to Γ pocket, and vice-versa) has a profound effect on the superconducting properties.

In Part II, we study interference corrections to the conductance in TMDs and their heterostructures with graphene, which can be used as an effective probe of SOC and disorder in these systems. In Chapters 7 and 8, we calculate weak (anti-) localization correction and universal conductance fluctuations, respectrivelly. We show that both quantities depend on a complex interplay between SOC, disorder, and valley structure, and discuss parameter regimes of interest for the interpretation of recent experiments.

In Chapter 9, we summarize the main results of this thesis and discuss possible directions for further research.

Appendices provide technical details related to the results presented in the main text.

Chapter 2

Introduction to TMDs

In this Chapter, we provide a brief introduction to TMDs, including their physical properties (Sec. 2.1), Ising SOC (Sec. 2.2), and superconducting properties (Sec. 2.3). Finally, in Sec. 2.4, we introduce graphene/TMD heterostructures, and discuss their properties and applications.

2.1 Structure and properties

Transition metal dichalcogenide monolayers are two-dimensional, atomically thin materials of the form MX_2, where M is a transition metal (from groups IV, V and VI of the periodic table, with partially filled d sub-shells) and X is a chalcogen (group XVI of the periodic table). These compounds can crystalize in many structures, including $2H$-, $1T$-, $1T'$- and T_d-type lattices. In this thesis, we study only TMDs of the most common $2H$ type[1] (M=Mo, W, Nb, Ta and X=S, Se), whose lattice has hexagonal structure when looked at from above, similar to graphene, but with two different atoms in the unit cell. Each monolayer consists of three layers of atoms: layer of M atoms is sandwiched between two layers of X atoms [see Fig. 2.1 (a)].

Bulk TMDs are formed of monolayers which are weakly interacting via Van-der-Waals forces. This allows for production of monolayers by exfoliation techniques (top-down methods). They can also be synthesized by chemical vapor deposition on metal supstrates, as well as epitaxially on SiC substrates (bottom-up methods) [4]. Note that the properties of the quasi two-dimensional bulk crystals which consist of many stacked monolayers ($N > 10$), such as well-studied bulk $NbSe_2$, are not determined by the monolayer.

Mo- and W-based TMDs are intrinsically semiconducting, with a band gap of the order 1 eV. On the other hand, Nb and Ta have one less d-electron in the outermost shell compared to Mo and W. As a result, the chemical potential of Nb and Ta- based TMDs intrinsically lies in the valence bands, and these materials exhibit p-type metallic behavior.

Monolayer TMDs show a variety of properties which are not present in the bulk. For instance, in semiconducting TMDs, there is a transition from the indirect band gap in the bulk to a direct one in the monolayer. This is of particular importance for application

---

[1] TMDs with structures other than $2H$ have also been identified as platforms for novel quantum transport [92–94] and superconducting [95–97] phenomena. Most notably, recent experiments in $1T'$ WTe_2, which has a monoclinic crystal lattice, have confirmed a quantum spin Hall insulator state [98,99].

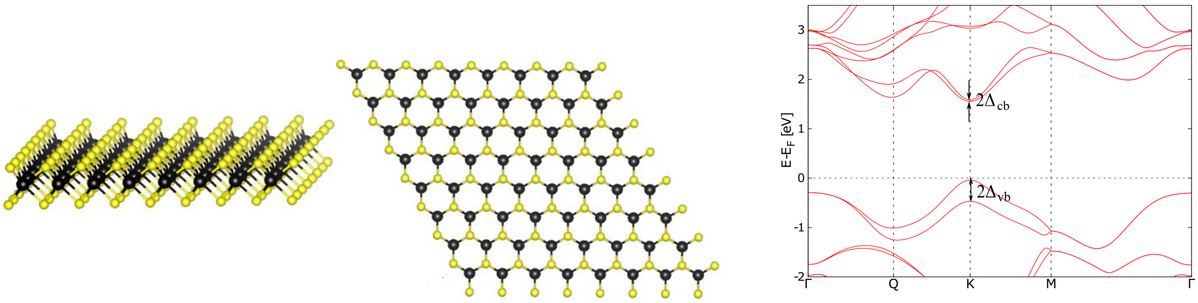

(a) (b)

Figure 2.1: (a) Structure of TMDs, as seen from the side and from above. Black sites correspond to M atoms, while yellow sites correspond to X atoms. Taken from [100]. (b) Band structure of TMDs, obtained by density functional theory (DFT) calculations. $2\Delta_{cb}$ and $2\Delta_{vb}$ denote spin-splitting in the conduction and valence band, respectively. Taken and adapted from Ref. [8].

of these materials in electronics [3, 5]. More importantly, absence of inversion symmetry in the monolayers allows for a large intrinsic SOC (see Sec. 2.2), whereas in the bulk the effective spin-orbit fields originating from adjacent mirror-symmetric planes cancel out.

The low-energy band structure of TMDs is dominated by d-orbitals originating from transition metals. As seen in Fig. 2.1 (b), minimum of the conduction band is at the $\pm K$ corners of the Brillouin zone, called valleys. In the valence band, aside from the $\pm K$ points, the Γ point contributes to the low-energy physics as well. Note that the orbital character of carriers changes depending on the momentum and the chemical potential. Namely, at the $\pm K$ points in the conduction band and at the Γ point in the valence band, the carriers are predominantly from the d_{z^2} orbitals. At the $\pm K$ points in the valence band, the carriers are predominantly from the $d_{x^2-y^2} \pm i d_{xy}$ orbitals.

2.2 Ising spin-orbit coupling

The d orbitals of heavy transition metal atoms are responsible for sizeable spin-orbit interaction in TMD monolayers. Near the $\pm K$ points in the Brillouin zone, this SOC takes a form of an effective out-of-plane Zeeman field, with opposite orientations in the two valleys. As a consequence, a large valley-dependent spin-splitting occurs in the valence band as well as in the conduction band, though with a much smaller magnitude [see Fig. 2.2 and Fig. 2.1 (b)]. This difference in magnitude of SOC comes from the different orbital character of carriers in the conduction and valence band at the K-point, as discussed in Sec. 2.1. Table 2.1 shows the magnitude of spin-splitting in some of the most studied TMD monolayers.

In the Γ pocket of p-doped TMDs, intrinsic SOC that drives the electron spins to out-of-plane orientation exists as well. It is significantly weaker (by more than an order of magnitude [15, 58]) compared to the SOC in the K pockets, which is due to different orbital character of the K and Γ pockets in the valence band. Furthermore, it is anisotropic, with a form $\Delta^{\Gamma}_{so}(\theta) \sim \Delta^{\Gamma}_{so}\cos(3\theta)$, where θ is the angle associated with momentum direction [see Fig. 1.4 (b)].

In few-layer TMDs, the adjacent layers have opposite orientations of Ising SOC due to the inversion of crystal field between layers. Then, total SOC of a few-layer sample is

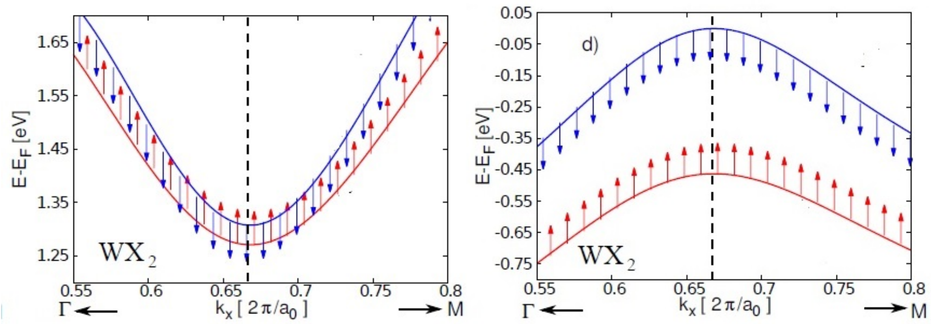

Figure 2.2: Results of a DFT band structure calculation showing spin-splitting in the conduction and valence band of TMDs in the vicinity of the K point. Taken from [8].

	MoS_2	$MoSe_2$	WS_2	WSe_2	$NbSe_2$	TaS_2
$2\Delta_{so}^{cb}$[meV]	3	22	-32	-37	/	/
$2\Delta_{so}^{vb}$[meV]	148	186	429	466	150	330

Table 2.1: Spin-splitting in the conduction and valence band at the $\pm K$ points for various TMD monolayers. Data for Mo- and W-based TMDs was obtained from numerical band structure calculations from Ref. [8]. This reference also provides values of the SOC in the valence band estimated from various optical experiments, which agree well with the reported theoretical values. Data for $NbSe_2$ and TaS_2 is obtained from numerical band structure calculations from Refs. [14, 15, 52] and [15], respectively.

weaker compared to monolayer ones, due to partial cancellation of SOC between layers. However, the coupling of adjacent layers is much weaker compared to Ising SOC, according to first principle calculations [15, 58], meaning that strong spin-valley locking due to Ising SOC is expected in few-layer TMDs as well. In the bulk, the cumulative effect of interlayer coupling between many layers completely cancels out the Ising SOC.

It is important to distinguish intrinsic Ising SOC from the better known extrinsic Rashba SOC [42]. The latter appears due to interaction with a substrate or external electric fields, and breaks the mirror symmetry of the system. Rashba SOC acts as a competing effect to Ising SOC, as it drives the electron spins to an in-plane orientation. Its effect in TMDs is expected to be weak – for example, in Ref. [12], it is estimated by numerical band structure calculations that in ionic liquid-gated (see Sec. 2.3) n-doped MoS_2 Rashba SOC amounts for ~1% of total spin-polarization. Moreover, Rashba SOC is anisotropic and creates a spin texture on the Fermi surface, in contrast to Ising SOC which only polarizes the spins.

2.3 Superconducting TMDs

Bulk $NbSe_2$ is a well studied superconductor, whose properties are well described by the two-band McMillan model [60] (see Ref. [62] and its references). It was even studied in ultrathin samples obtained by exfoliation [101] in 1971, where superconductivity was found in 4-layer samples. However, superconductivity in few-layer TMDs has attracted significant scientific attention only recently, when they were identified as a platform for exotic “Ising” superconductivity.

In addition to p-doped $NbSe_2$ [14] monolayers, intrinsic superconductivity was confirmed in n-doped MoS_2 [12, 13] and WS_2 [55], as well as in p-doped TaS_2 [15] monolayers. MoS_2 and WS_2, which are intrinsically semiconducting, need to be heavily doped to achieve sufficient carrier density for superconductivity, which is usually done by the ionic liquid gating technique [102]. On the other hand, no gating is necessary in $NbSe_2$ and TaS_2, where the chemical potential intrinsically lies in the valence band.

Highest critical temperature of $T_c \sim 7K$ [12, 13] was reported in MoS_2 flakes with a thickness of ∼1nm, where high carrier density and superconductivity was induced in the topmost layer only by liquid gating. In true monolayers, $T_c \sim 1.5K$ for MoS_2 [78] and WS_2 [55], and $T_c \sim 3K$ for $NbSe_2$ [14] and TaS_2 [15]. These experiments also confirm superconductivity in few-layer counterparts of these materials, where the critical temperature generally rises as a function of the number of layers. The reasons for “weaker” superconductivity in monolayer compared to few-layer samples may include the effect of quantum fluctuations or Coulomb interaction between electrons, both of which are more pronounced in thinner samples and negatively affect superconductivity (see Ref. [78] for a detailed discussion of these phenomena). An exception to this trend is TaS_2 where, surprisingly, T_c decreases as the number of layers increases, which is still not well understood [15].

The main distinguishing feature of superconductivity in TMD monolayers is its exceptional robustness to in-plane magnetic fields. This is understood as a consequence of the 2D nature of these materials, which excludes orbital depairing by the field, combined with strong Ising SOC, which suppresses paramagnetic depairing (as discussed in Sec. 1.1.1). Fig. 2.3 shows the $H_{c2}(T)$ measurements for TMD superconductors, and comparison with other superconductors with strongly enhanced H_{c2}. In few-layer TMDs, H_{c2} is also significantly enhanced, but smaller compared to monolayers, as interlayer coupling competes with Ising SOC and decreases its effective magnitude. This is illustrated using the example of TaS_2 in the right panel of Fig. 2.3.

Spectroscopy of few-layer $NbSe_2$ superconductors was performed in several experiments [57, 58, 107]. In Refs. [57, 107], the two-gap structure can be resolved in the density of states in the superconducting phase [see Fig. 1.4 (a)], and the ratio $\Delta/T_c \approx 2$ was found (different from the standard BCS result $\Delta/T_c \approx 1.76$). Both of these results are compatible with multiband superconductivity[2]. Refs. [57, 58] studied the evolution of quasiparticle spectra as a function of in-plane fields, and showed that the spectral gap is very robust to applied fields, in-line with “Ising” protection of the Cooper pairs in the K-band.

2.4 Graphene/TMD heterostructures

The low-energy band structure of graphene is described by the Dirac cones, situated at the $\pm K$ corners of the Brillouin zone. Their unusual linear dispersion, $\xi_{\mathbf{q}} = v_F|\mathbf{q}|$, where

---

[2] The shape of the quasiparticle spectra could, alternatively, be explained by considering a single anisotropic gap [62]. Moreover, the high ratio of Δ and T_c can be accounted for by strong-coupling corrections [27]. The multiband scenario, however, is corroborated by band structure calculations, and thus more likely.

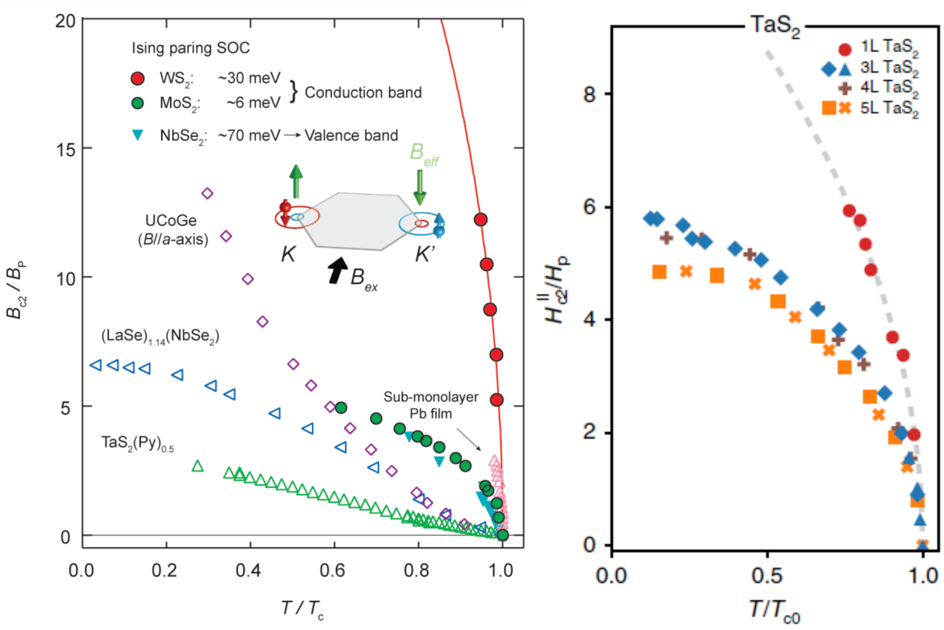

Figure 2.3: Left: $H_{c2}(T)$ curve of various superconducting TMDs: MoS_2, WS_2 and $NbSe_2$, and comparison with other superconductors with strongly enhanced H_{c2}. The latter include a ferromagnetic superconductor UCoGe (where triplet pairing is predicted [103]), layered superconductors $(LaSe)_{1.14}(NbSe_2)$ [104] and $TaS_2(Py)_{0.5}$ [105], and thin Pb films (where strong Rashba SOC is expected [106]). Taken from [55]. Right: $H_{c2}(T)$ curve of superconducting TaS_2 for various material thicknesses, from monolayer (1L) to five-layer (5L). Taken from [15]. B_p and H_p denote the Pauli limit, introduced in Sec. 1.1.1.

v_F is the Fermi velocity and $\mathbf{q}$ is the momentum measured from $\pm K$, yields a non-trivial Berry phase $\phi_B = \pi$. This has remarkable repercussions in quantum transport, most notably, weak-antilocalization (as discussed in Sec. 1.2.1) [108] and an unusual quantum Hall effect [109], where the quantization of conductance is observed in experiment even at room temperatures. Furthermore, in their seminal work, Kane and Mele showed that the so-called Kane-Mele SOC, which satisfies the lattice and mirror symmetry of the graphene sheet, can lead to the appearance of the quantum spin Hall insulator state [110]. This state is topologically protected, and is characterized by helical edge states, where the two spin-species move in opposite directions along the sample edge. However, Kane-Mele SOC in graphene is found to be too weak for observation of this phenomenon in experiment. For this reason, a lot of experimental effort is devoted to inducing SOC in graphene. One of the most promising approaches to do so are heterostructures of graphene and semiconducting TMDs. A number of magnetoconductance measurements [17, 79–83] in these systems, reveal weak antilocalization signals, consistent with strong induced SOC. At the same time, there are no adverse effects to transport quality in the graphene sheets.

Numerical band structure calculations of graphene/TMD heterostructures show that the Dirac cones of graphene are well preserved inside the band-gap of TMDs, as shown in Fig. 2.4 (a). Upon zooming in to the vicinity of $\pm K$ points [Fig. 2.4 (b)], we see out-of-plane spin-polarization due to induced Ising SOC. Physically, induced SOC originates from hybridization of π orbitals of graphene with d orbitals of transition metal [17].

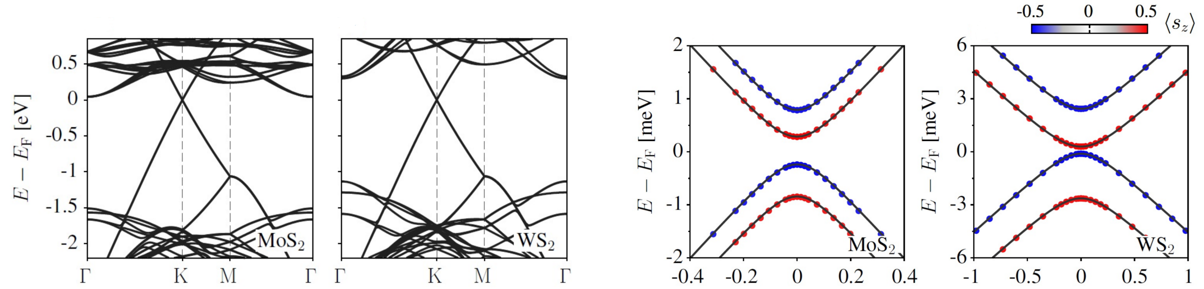

(*a*) (*b*)

Figure 2.4: Results of the electronic band structure calculations for graphene/TMD heterostructures. Taken and adapted from [16]. (a) Band structure along high-symmetry lines. Dirac cones of grapene are well preserved within the TMD band-gap. (b) Band structure in the vicinity of $\pm K$. Two spin-split subbands are visible, due to induced Ising SOC.

Aside from the Kane-Mele SOC [110] mentioned previously, TMDs also induce the so-called valley-Zeeman SOC in the graphene sheet, which breaks its inversion symmetry and causes spin splitting in the band structure [see Eq. (3.1)]. First principle calculations [16, 17] suggest that the valley-Zeeman component dominates over the Kane-Mele one. Although valley-Zeeman SOC is not compatible with the quantum spin Hall effect, it can lead to other novel phenomena in graphene, such as the spin Hall effect [18–20]. Furthermore, a combined effect of the valley-Zeeman and Rashba SOC can lead to the appearance of a new kind of edge states which are not of topological origin [16, 17].

Chapter 3

Modeling disordered TMDs and their heterostructures with graphene

In this Chapter, we introduce a model for disordered TMDs and their heterostructures with graphene, which will be used in the remainder of this thesis. In Sec. 3.1, we start by formulating a low-energy model for the K-band. This includes the Dirac-like Hamiltonian describing the band structure, and a phenomenological disorder potential. Assuming that the chemical potential is the dominant energy scale, we proceed by projecting this model to the conduction/valence band. As discussed in Sec. 3.2, the simpler effective model obtained this way is appropriate for the description of n-doped TMDs, and n- or p-doped graphene/TMD heterostructures. On the other hand, for p-doped TMDs, it needs to be supplemented with additional ingredients to account for the Γ-band and related disorder.

3.1 Model in the vicinity of $\pm K$ points

The low-energy Hamiltonian describing TMD monolayers in the vicinity of the $\pm\mathbf{K}$ points, and in the presence of a parallel magnetic field is given by [8] $H_{\mathbf{q}} = H_0 + H_{SOC} + H_W + H_{||}$, where

$$\begin{aligned}
H_0 &= v(q_x\sigma_x\eta_z + q_y\sigma_y) + E_g\sigma_z, \\
H_{SOC} &= \Delta_{KM}\sigma_z s_z\eta_z + \Delta_{VZ} s_z\eta_z + \lambda(\sigma_x s_y\eta_z - \sigma_y s_x) + \zeta(q_x\sigma_x s_z + q_y\sigma_y s_z\eta_z), \\
H_W &= \kappa(q_x^2 - q_y^2)\sigma_x - 2\kappa q_x q_y\sigma_y\eta_z, \\
H_{||} &= h s_x.
\end{aligned} \tag{3.1}$$

Here, we use units where $\hbar = k_B = 1$. The two Dirac cones are described by H_0, where $\mathbf{q} = (q_x, q_y) = q(\cos\theta, \sin\theta)$ is a small momentum measured from $\pm\mathbf{K}$, v is the velocity associated with the linearized kinetic dispersion, and E_g is the difference in on-site energy responsible for opening the band gap. Spin-orbit coupling is described by H_{SOC}, where Δ_{KM} and Δ_{VZ} characterize Kane-Mele and valley-Zeeman SOC [1], respectively. Rashba SOC, which is related to a mirror symmetry breaking due to the substrate or external

---

[1] The fact that Ising SOC in TMDs is strong in the valence and weak in the conduction band [8], taking into account that the σ-matrices roughly span the space of these two bands, means that Δ_{KM} and Δ_{VZ} are of similar amplitudes but with opposite signs in these materials. Note that this is not necessarily the case in graphene/TMD heterostructures.

fields, is described by λ. The spin-dependence of the velocity is accounted for by ζ. H_W describes the so-called trigonal warping, which accounts for the slight anisotropy of the Fermi surface [8]. Finally, $H_{||}$ is the in-plane Zeeman field, where the Zeeman energy $h = \frac{1}{2} g\mu_B B_{||}$ is determined by the amplitude of the in-plane magnetic field and the g-factor, which is expected to take the standard value $g \approx 2$ in these materials for in-plane fields. We introduce Pauli matrices $\sigma_{x,y,z}$, $s_{x,y,z}$ and $\eta_{x,y,z}$, defined as

$$\sigma_x = s_x = \eta_x = \begin{pmatrix} 0 & 1 \\ 1 & 0 \end{pmatrix}, \qquad \sigma_y = s_y = \eta_y = \begin{pmatrix} 0 & -i \\ i & 0 \end{pmatrix}, \qquad \sigma_z = s_z = \eta_z = \begin{pmatrix} 1 & 0 \\ 0 & -1 \end{pmatrix}. \tag{3.2}$$

The matrices $\sigma_{x,y,z}$ span the basis of d-orbitals of the transition metal, $|d_{z^2}\rangle$ and $1/\sqrt{2}$ $(|d_{x^2-y^2}\rangle + i\eta\, |d_{xy}\rangle)$, which dominate the states in the conduction and valence band of TMDs, respectively. Here, the index $\eta = \pm 1$ describes the two valleys. The matrices $s_{x,y,z}$ and $\eta_{x,y,z}$ act in spin and valley space, respectively. The Hamiltonian (3.1) contains all terms up to the first order in $\mathbf{q}$ allowed by the symmetries of the system, as well as H_W and $H_{||}$, which break rotational and time-reversal symmetry[2], respectively.

Furthermore, the low-energy sector of graphene/TMD heterostructures is also well described by the Hamiltonian (3.1). The matrices $\sigma_{x,y,z}$ in this case act in the space of two sublattices of graphene. As discussed in Sec. 2.4, the Dirac cones of graphene in these heterostructures are preserved and are within the TMD band gap. The coupling to the TMD modifies the graphene spectrum by introducing the staggered sublattice potential, $E_g\sigma_z$, and SOC, H_{SOC}.

3.1.1 Projection to the conduction/valence band

To proceed, we assume that the Dirac Hamiltonian H_0 gives the dominant contribution to the energy of the system. H_0 is diagonalized by a unitary transformation

$$U_{\mathbf{q}} = e^{-i\eta_z\alpha_{\mathbf{q}}}\, e^{i\beta_{\mathbf{q}}\sigma_y\eta_z}\, e^{i\alpha_{\mathbf{q}}\sigma_z\eta_z}, \qquad \tan 2\alpha_{\mathbf{q}} = \frac{q_y}{q_x}, \qquad \tan 2\beta_{\mathbf{q}} = \frac{vq}{E_g}. \tag{3.3}$$

It has a simple spectrum, $E_{\mathbf{q}} = \pm\sqrt{q^2v^2 + E_g^2}$. After projecting $U_{\mathbf{q}} H_{\mathbf{q}} U_{\mathbf{q}}^\dagger$ onto the conduction or valence band, we obtain the effective Hamiltonian

$$\mathcal{H}_{\mathbf{q}} = \pm\xi_{\mathbf{q}} + \Delta_{so} s_z\eta_z \pm \lambda\frac{vq_F}{\mu}(s_y\cos\theta - s_x\sin\theta) + \kappa\frac{vq_F^3}{\mu}\cos(3\theta)\,\eta_z + hs_x. \tag{3.4}$$

Here, the upper and lower sign, correspond to projection onto the conduction and valence band, respectively. The energy is measured from the chemical potential, $\xi_{\mathbf{q}} = E_{\mathbf{q}} - \mu$. Furthermore, we have introduced the Fermi momentum $q_F = \sqrt{\mu^2 - E_g^2}/v$ and spin-orbit splitting

$$\Delta_{so} = \pm\Delta_{KM}\frac{E_g}{\mu} + \Delta_{VZ} \pm \zeta\frac{vq_F^2}{\mu}. \tag{3.5}$$

Note that at $E_g = 0$ (as in the case of graphene, e.g.), Kane-Mele SOC does not contribute to the spin-orbit splitting. The chemical potential μ is assumed to be sufficiently above the band gap E_g, so that it is the dominant energy scale, $|\mu| - E_g \gg \Delta_{so}, \lambda, h, \kappa q_F^2$. Note

---

[2] Note that the time-reversal operator in this basis is $\mathcal{T} = is_y\eta_x\mathcal{K}$, where $\mathcal{K}$ is complex conjugation.

that the effective Hamiltonian (3.4) holds only if the both spin-split bands are occupied. For instance, in p-doped TMDs, due to the very large spin-splitting (see Sec. 2.2), it is possible to achieve doping such that only one spin-split band is occupied. This doping regime is not addressed in our work, but the related quantum coherent phenomena were previously studied in Ref. [23] (weak localization) and Ref. [26] (superconductivity).

The spectrum of the Hamiltonian (3.4) in the conduction band is represented schematically in Fig. 3.1.

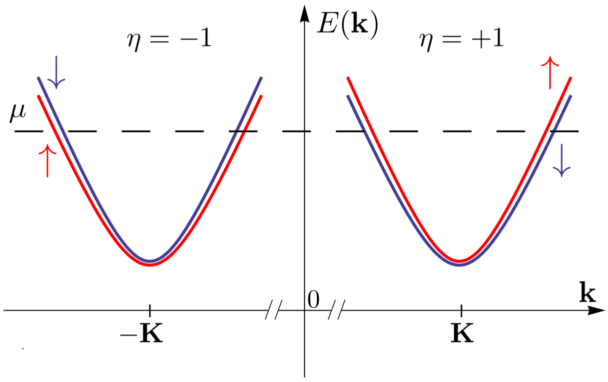

Figure 3.1: Schematic representation of the conduction band of TMD monolayers in the vicinity of the $\pm K$ corners of the Brillouin zone. The spin splitting in the two valleys is opposite due to the Ising SOC.

3.1.2 Model for disorder

The effect of potential impurities can be modeled by introducing a random disorder,

$$H^{D0}_{\mathbf{qq}'} = U^0_{\mathbf{q}-\mathbf{q}'} + \sum_{i=\pm,x} \sum_{j=x,y} V^{ij}_{\mathbf{q}-\mathbf{q}'} \sigma_i \eta_j, \tag{3.6}$$

where $\sigma_\pm = 1 \pm \sigma_z$, which describe two individual sites (" $+$ " and " $-$ ") in the space of σ matrices. The first term in Eq. (3.6) is the intravalley contribution, which is diagonal in spin space and in the space of σ matrices. The second term represents all spin-independent intervalley contributions allowed by time-reversal and hexagonal symmetry, and includes on-site ($i = \pm$), and hopping ($i = x$) contributions. Intervalley disorder requires large momentum transfer, and is caused by short-range impurities, such as atomic defects. Upon rotating $U_\mathbf{q} H^{D0}_{\mathbf{qq}'} U^\dagger_{\mathbf{q}'}$ and projecting to the conduction band, a variety of other scattering processes will be generated as combinations of the band structure and potential scattering parameters.

For simplicity, we will account for these processes, as well as all other possible scattering processes, phenomenologically, by independent scattering potentials. To do so, we supplement $H^{D0}_{\mathbf{qq}'}$ with all the other disorder terms allowed by the time-reversal symmetry. The disorder Hamiltonian is then given as $H^D_{\mathbf{qq}'} = H^{D0}_{\mathbf{qq}'} + \delta H^D_{\mathbf{qq}'}$, where

$$\delta H^D_{\mathbf{qq}'} = \sum_{i=x,y,z} U^i_{\mathbf{q}-\mathbf{q}'} \Sigma_i + \sum_{i=0,x,y,z} \sum_{j=x,y,z} A^{ij}_{\mathbf{q}-\mathbf{q}'} \Sigma_i s_j \eta_z + \sum_{j=x,y} \sum_{i=x,y,z} M^{ij}_{\mathbf{q}-\mathbf{q}'} \sigma_y s_i \eta_j. \tag{3.7}$$

Here $\Sigma_{0,z,x} = \sigma_{0,x,z}$ and $\Sigma_y = \sigma_y \eta_z$. The first and second term account for spin-dependent and spin-independent intravalley contributions, respectively. The third term describes spin-dependent intervalley disorder. We characterize the random disorder potentials by Gaussian correlators and assume that different kinds of disorder are uncorrelated:

$$\langle U^i_{\mathbf{q}} U^j_{\mathbf{q}'} \rangle = U_i^2 \delta_{ij} \delta_{\mathbf{q}\bar{\mathbf{q}}'}, \qquad \langle X^{ij}_{\mathbf{q}} X^{kl}_{\mathbf{q}'} \rangle = X_{ij}^2 \delta_{ik} \delta_{jl} \delta_{\mathbf{q}\bar{\mathbf{q}}'}. \tag{3.8}$$

Here, the brackets $\langle ... \rangle$ represent disorder averaging and $X = A, V, M$. Furthermore, we use the abbreviation $\bar{\mathbf{q}} = -\mathbf{q}$.

We proceed by writing the rotated phenomenological disorder Hamiltonian, $U_{\mathbf{q}} H^D_{\mathbf{q}\mathbf{q}'} U^\dagger_{\mathbf{q}'}$, in the projected basis as sum of the potential component $\mathcal{H}^{D0}_{\mathbf{q}\mathbf{q}'}$, and the non-potential component $\delta\mathcal{H}^D_{\mathbf{q}\mathbf{q}'}$, namely, as $\mathcal{H}^D_{\mathbf{q}\mathbf{q}'} = \mathcal{H}^{D0}_{\mathbf{q}\mathbf{q}'} + \delta\mathcal{H}^D_{\mathbf{q}\mathbf{q}'}$, where

$$\begin{aligned}
\mathcal{H}^{D0}_{\mathbf{q}\mathbf{q}'} &= U^0_{\mathbf{q}-\mathbf{q}'} + \sum_{j=x,y} \sum_{i=\pm,x} V^{ij}_{\mathbf{q}-\mathbf{q}'} g^i_{\theta,\theta'} \eta_j, \\
\delta\mathcal{H}^D_{\mathbf{q}\mathbf{q}'} &= \sum_{i=x,y,z} U^i_{\mathbf{q}-\mathbf{q}'} f^i_{\theta,\theta'} + \sum_{i=0,x,y,z} \sum_{j=x,y,z} A^{ij}_{\mathbf{q}-\mathbf{q}'} f^i_{\theta,\theta'} s_j \eta_z + \sum_{j=x,y} \sum_{i=x,y,z} M^{ij}_{\mathbf{q}-\mathbf{q}'} g^y_{\theta,\theta'} s_i \eta_j.
\end{aligned} \tag{3.9}$$

Here, the functions $f^i_{\theta,\theta'}$ and $g^i_{\theta\theta'}$ capture the anisotropy of the projected disorder potential, which is due to the momentum dependence of the unitary transformation $U_{\mathbf{q}}$ introduced in Eq. (3.3). In particular,

$$\begin{aligned}
2f^0_{\theta,\theta'} &= 1 + e^{-i\eta_z(\theta-\theta')} \pm \frac{E_g}{\mu}\left(1 - e^{-i\eta_z(\theta-\theta')}\right), \; 2f^x_{\theta,\theta'} = \pm\frac{vq_F}{\mu}\left(e^{-i\eta_z\theta} + e^{i\eta_z\theta'}\right)\eta_z, \\
g^+_{\theta,\theta'} &= \left(1 \pm \frac{E_g}{\mu}\right), \; g^-_{\theta,\theta'} = \left(\frac{E_g}{\mu} \mp 1\right) e^{i\eta_z(\theta+\theta')}.
\end{aligned} \tag{3.10}$$

Furthermore, $f^y_{\theta,\theta'} = i f^x_{\theta,\bar{\theta}'} \eta_z$, $f^z_{\theta,\theta'} = f^0_{\bar{\theta},\theta'}$, $g^x_{\theta,\theta'} = f^0_{-\bar{\theta},\theta'}$, and $g^y_{\theta,\theta'} = i\eta_z f^x_{-\theta,\theta'}$. Here, we used the notation $\bar{\theta} = \theta + \pi$. As in Eq. (3.4), the upper and lower sign correspond to the projection onto the conduction and valence band, respectively. Anisotropy of the disorder potential will play an important role in describing the quantum interference phenomena in Part II of this thesis. Namely, in simple metals, anisotropic disorder usually only leads to the renormalization of the diffusion constant and the transport time. It has more profound physical consequences in our system, as it captures the Berry curvature due to the Dirac-like band structure.

The total scattering rate due to disorder, calculated in the self-consistent Born approximation (see Chapter 4) is

$$\tau^{-1} = \tau_0^{-1} + \tau_z^{-1} + \tau_{iv}^{-1} + \sum_{i=z,zv,iv} \sum_{j=e,o} \tau_{i,j}^{-1}. \tag{3.11}$$

The individual contributions to Eq. (3.11) are defined in the left column of Table 3.1[3], where we introduced the Fermi velocity, $v_F = v^2 q_F/\mu$, and the density of states per valley and per spin at the Fermi level at the K-points, $\nu_{0K} = \mu/(2\pi v_F^2)$.

---

[3] The fact that there are 11 distinct scattering rates, excluding the diagonal τ_0^{-1}, can be understood as follows. As discussed in the caption of Table 7.1 in Chapter 7, there are 11 distinct Cooperon/diffuson gaps. Therefore, there should be 11 independent scattering rates to accommodate the same number of independent Cooperon/diffuson channels.

Assuming that only potential disorder is present in the system, we can estimate the phenomenological scattering rates, related with the parameters in Eq. (3.8), as shown in the right column of Table 3.1. We do so by comparing the disorder terms generated by $H^D_{\mathbf{qq}'}$ after rotation and projection onto the conduction band with the terms generated by $H^{D0}_{\mathbf{qq}'}$ only, but taking into account corrections up to order $1/\mu$. In this way, we can relate the phenomenological disorder parameters with the main Hamiltonian (3.1) and the magnitude of the potential disorder.

3.2 Effective model in the conduction and valence band

As the low-energy behavior in n-doped TMDs, and n- or p-doped graphene/TMDs heterostructures is dominated by the K band, these materials are well described by the effective Hamiltonian $\mathcal{H}_{\mathbf{q}}$ and the disorder potential $\mathcal{H}^D_{\mathbf{qq}'}$. This model is used in the study of single-band Ising superconductivity in Chapter 5, and to study quantum corrections to the conductance in Part II of this thesis.

In p-doped TMDs, the Γ band is also relevant. In this case, the Hamiltonian becomes

$$\mathcal{H}^{K\Gamma}_{\mathbf{q}} = \begin{pmatrix} \mathcal{H}_{\mathbf{q}} & 0 \\ 0 & \mathcal{H}^{\Gamma}_{\mathbf{q}} \end{pmatrix}_{K\Gamma}, \tag{3.12}$$

where $K\Gamma$ denotes the matrix structure in the $K-\Gamma$ band space. Note that the blocks in the matrix in Eq. (3.12) have different sizes, namely, $\mathcal{H}_{\mathbf{q}}$ is a 4×4 matrix in spin and valley space, while $\mathcal{H}^{\Gamma}_{\mathbf{q}}$ is a 2×2 matrix in spin space. The Hamiltonian $\mathcal{H}^{\Gamma}_{\mathbf{q}}$ describes the Γ band and is given as

$$\mathcal{H}^{\Gamma}_{\mathbf{q}} = \frac{p_\Gamma^2}{2m^*} + \Delta^{\Gamma}_{so}\cos(3\theta_\Gamma)s_z + hs_x. \tag{3.13}$$

Here, p_Γ is the momentum and θ_Γ is the angle associated with its direction, m^* is the effective mass of holes, while Δ^{Γ}_{so} is the strength of the anisotropic SOC.

Disorder potential which accounts for the presence of the Γ band has the form

$$\mathcal{H}^{D,K\Gamma}_{\mathbf{qq}'} = \begin{pmatrix} \mathcal{H}^D_{\mathbf{qq}'} & \beta_{\mathbf{q}-\mathbf{q}'} \\ \beta_{\mathbf{q}-\mathbf{q}'} & \alpha_{\mathbf{q}-\mathbf{q}'} \end{pmatrix}_{K\Gamma}. \tag{3.14}$$

Here, we have introduced two new scattering processes, with the random potentials $\alpha_{\mathbf{q}-\mathbf{q}'}$ and $\beta_{\mathbf{q}-\mathbf{q}'}$, which describe scattering within the Γ band and between two bands, respectively. We characterize them by the Gaussian correlators

$$\langle \alpha_{\mathbf{q}}\alpha_{\mathbf{q}'}\rangle = \alpha^2\delta_{\mathbf{q}\bar{\mathbf{q}}'}, \qquad \langle \beta_{\mathbf{q}}\beta_{\mathbf{q}'}\rangle = \beta^2\delta_{\mathbf{q}\bar{\mathbf{q}}'}. \tag{3.15}$$

We define scattering rates associated with the new processes (in the self-consistent Born approximation) as

$$\frac{1}{2\tau_\Gamma} = \pi\nu_{0\Gamma}\alpha^2, \qquad \Gamma_{\Gamma K} = \pi\nu_{0\Gamma}\beta^2, \qquad \Gamma_{K\Gamma} = \pi\nu_{0K}\beta^2. \tag{3.16}$$

Intravalley scattering rates			Estimates
$\tau_0^{-1} = \pi\nu_{0K} U_0^2 (1 + \frac{E_g^2}{\mu^2})$			/
$\tau_{z1}^{-1} = \pi\nu_{0K}(U_x^2 + U_y^2)\frac{v^2 q_F^2}{\mu^2}$	$\tau_{z2}^{-1} = \pi\nu_{0K} U_z^2 (1 + \frac{E_g^2}{\mu^2})$	$\tau_z^{-1} = \tau_{z1}^{-1} + \tau_{z2}^{-1}$	$\tau_{z1}^{-1}, \tau_{z2}^{-1} \propto \tau_0^{-1}(\frac{\kappa v q_F^3}{\mu^2})^2$
$\tau_{z,e1}^{-1} = \pi\nu_{0K}(A_{xz}^2 + A_{yz}^2)\frac{v^2 q_F^2}{\mu^2}$	$\tau_{z,e2}^{-1} = \pi\nu_{0K} A_{zz}^2 (1 + \frac{E_g^2}{\mu^2})$	$\tau_{z,e}^{-1} = \tau_{z,e1}^{-1} + \tau_{z,e2}^{-1}$	$\tau_{z,e1}^{-1}, \tau_{z,e2}^{-1} \propto \tau_0^{-1}(\frac{\Delta_{KM} v^2 q_F^2}{\mu^3})^2$
$\tau_{z,o1}^{-1} = \pi\nu_{0K}\sum_{i,j=x,y}(A_{ij}^2)\frac{v^2 q_F^2}{\mu^2}$	$\tau_{z,o2}^{-1} = \pi\nu_{0K}(A_{zx}^2 + A_{zy}^2)(1 + \frac{E_g^2}{\mu^2})$	$\tau_{z,o}^{-1} = \tau_{z,o1}^{-1} + \tau_{z,o2}^{-1}$	$\tau_{z,o1}^{-1}, \tau_{z,o2}^{-1} \propto \tau_0^{-1}(\frac{\lambda v q_F}{\mu^2})^2$
$\tau_{zv,e}^{-1} = \pi\nu_{0K} A_{0z}^2 (1 + \frac{E_g^2}{\mu^2})$			$\tau_{zv,e}^{-1} \propto \tau_0^{-1}(\frac{\kappa v \Delta_{KM} q_F^3}{\mu^3})^2$
$\tau_{zv,o}^{-1} = \pi\nu_{0K}(A_{0x}^2 + A_{0y}^2)(1 + \frac{E_g^2}{\mu^2})$			$\tau_{zv,o}^{-1} \propto \tau_0^{-1}(\frac{\lambda E_g v q_F}{\mu^3})^2$
Intervalley scattering rates			**Estimates**
$\tau_{iv}^{-1} = \pi\nu_{0K}\sum_{i=x,y}[2\sum_{j=\pm} V_{ji}(1 + j\frac{E_g}{\mu})^2 + (V_{xi}^2)\frac{v^2 q_F^2}{\mu^2}]$			/
$\tau_{iv,e}^{-1} = \pi\nu_{0K}(M_{zx}^2 + M_{zy}^2)\frac{v^2 q_F^2}{\mu^2}$			$\tau_{iv,e}^{-1} \propto \tau_{iv}^{-1}(\frac{\Delta_{KM} v q_F}{\mu^2})^2$
$\tau_{iv,o}^{-1} = \pi\nu_{0K}\sum_{i,j=x,y}(M_{ij}^2)\frac{v^2 q_F^2}{\mu^2}$			$\tau_{iv,o}^{-1} \propto \tau_{iv}^{-1}(\frac{\lambda v q_F}{\mu^2})^2$

Table 3.1: Left: Diagonal scattering rate, τ_0^{-1}, and the 11 other independent scattering rates originating from the disorder Hamiltonian (3.9). The notation for the scattering rates was taken and adapted from Ref. [72]. The index z indicates that the related disorder has a structure in the space of σ matrices. zv and iv indicate coupling to the valley matrices η_z and $\eta_{x,y}$, respectively. Indices e and o indicate coupling to the spin matrices s_z and $s_{x,y}$, respectively. Spin-independent disorder is represented by the rates τ_0^{-1}, τ_z^{-1}, and τ_{iv}^{-1}, which describe diagonal, intervalley, and σ matrix-dependent intravalley disorder, respectively. Spin-dependent disorder is represented by the rates $\tau_{i,j}^{-1}$ ($i = z, zv, iv; j = e, o$), which describe intra- ($i = z, zv$) or intervalley ($i = iv$), and spin-preserving ($j = e$) or spin-flipping ($j = o$) disorder. Right: Estimates of the phenomenological scattering rates, obtained by the combination of band structure parameters and potential disorder only, assuming that all intervalley components of the potential disorder are of similar strength.

Here, $\nu_{0\Gamma} = m^*/(2\pi)$ is the density of states per spin in the Γ-band. Note that we have defined two interband rates, corresponding to scattering from K to Γ band ($\Gamma_{K\Gamma}$) and vice-versa ($\Gamma_{\Gamma K}$). They are different due to different densities of states in the two bands.

Note that we model the Γ-band and related disorder using only the simplest terms, in contrast to our description of the K-band in Eqs. (3.4) and (3.9), where we account for all possible processes allowed by the time-reversal symmetry. The minimal model given in Eqs. (3.12) and (3.14) will be sufficient for our discussion of multiband Ising superconductivity in Chapter 6.

Chapter 4

Theoretical tools

In this Chapter, we will present basics of the theory for disordered systems, which will be used to obtain most of the results in this work. The main objective of this theory is to obtain the Green's function G of a disordered system, which captures its microscopic details, and can be used to calculate measurable quantities of interest. Important concepts in this theory are *disorder-averaging* and the *ergodic hypothesis*. Namely, we assume that the statistical average of some property of a disordered system is equal to its ensemble average over all possible disorder realizations. Therefore, instead of calculating the Green's function for a given system (which is in general very complicated), we calculate the disorder-averaged Green's function $\langle G \rangle$, which is more accessible and suitable for further manipulations and analytical calculations.

There are a number of different approaches to calculate $\langle G \rangle$ and higher-order correlations (e.g. $\langle GG \rangle$). The most general, non-perturbative method is provided by functional field integration and the non-linear sigma model [111]. For our work, simpler perturbative methods, such as diagrammatic [112,113] and quasiclassical methods [114], are sufficient, as we will study only weak disorder on the scale of the Fermi energy.

In the normal state, we use the diagrammatic method, which provides an intuitive framework for studying quantum coherent phenomena. We use it to calculate WL and UCF corrections in Part II of this work. In the superconducting state, diagrammatic calculations are still possible, but become more cumbersome due to a more complex structure of the Green's functions. The quasiclassical method provides a simpler, but equivalent, alternative. We use it in the calculation of superconducting properties of TMDs in Part I of this work.

After defining Green's functions in Sec. 4.1, we proceed by introducing basic principles of the diagrammatic method in Sec. 4.2. In Sec. 4.3, we provide an introduction to the BCS theory of superconductivity, after which we define Gor'kov Green's functions and the quasiclassical method for superconductivity. For clarity, we will illustrate these methods on an example of the simplest, 2D electron gas (2DEG) Hamiltonian. In TMDs these methods are readily generalized, and Green's functions acquire a matrix structure in the spin and valley space.

4.1 Green's functions

Let us consider the Hamiltonian of the form

$$H = \sum_{\mathbf{p}} c^\dagger_{\mathbf{p}} \xi_{\mathbf{p}} c_{\mathbf{p}}, \tag{4.1}$$

where $\xi_{\mathbf{p}}$ describes energy dispersion of the system, and $c^{(\dagger)}_{\mathbf{p}}$ is an annihilation (creation) operator. In the imaginary time formalism, at finite temperature, we may define Green's function as

$$\mathcal{G}_{\mathbf{p}}(\tau) = -\langle T_\tau c_{\mathbf{p}}(\tau) c^\dagger_{\mathbf{p}'}(0)\rangle_T, \tag{4.2}$$

where τ is the imaginary time, and T_τ is the time-ordering operator given as

$$T_\tau[A(\tau_1)B(\tau_2)] = \Theta(\tau_1 - \tau_2)A(\tau_1)B(\tau_2) - \Theta(\tau_2 - \tau_1)B(\tau_2)A(\tau_1). \tag{4.3}$$

Here, $\langle ...\rangle_T$ denotes the thermodynamic average, and Θ is the Heaviside step function. Evolution of the operators is given by the following law in the Heisenberg representation

$$\frac{dc^{(\dagger)}_{\mathbf{p}}(\tau)}{d\tau} = [H, c^{(\dagger)}_{\mathbf{p}}]. \tag{4.4}$$

Next, we introduce the Fourier transform

$$\mathcal{G}_{\mathbf{p}\omega_n} = \int_0^{1/T} d\tau e^{i\omega_n \tau} \mathcal{G}_{\mathbf{p}}(\tau), \tag{4.5}$$

where $\omega_n = 2\pi T(n + \frac{1}{2})$ is the fermionic Matsubara frequency, T is the temperature, and $\mathcal{G}_{\mathbf{p}\omega_n}$ is the Matsubara Green's function. Combining the above equations, we find that it satisfies

$$\mathcal{G}_{\mathbf{p}} = (i\omega_n - \xi_{\mathbf{p}})^{-1}. \tag{4.6}$$

It is often of interest to calculate zero-temperature retarded (R) and advanced (A) Green's functions $G^{R,A}_{\mathbf{p}\epsilon}$, which are related to many measurable physical quantities. They are obtained from Matsubara Green's functions by the analytical continuation

$$G^{R,A}_{\mathbf{p}}(\epsilon) = \mathcal{G}_{\mathbf{p}}(i\omega_n \to \epsilon \pm i0^+) = (\epsilon - \xi_{\mathbf{q}} \pm i0)^{-1}. \tag{4.7}$$

4.2 Diagrammatic methods for disordered systems

Let us supplement the Hamiltonian (4.1) with a disorder term

$$H_D = \sum_{\mathbf{p}\mathbf{p}'} c^\dagger_{\mathbf{p}} V_{\mathbf{p}-\mathbf{p}'} c_{\mathbf{p}'}. \tag{4.8}$$

Here, $V_{\mathbf{p}-\mathbf{p}'}$ is a random potential. For simplicity, we assume Gaussian white-noise distribution. Namely

$$\langle V_{\mathbf{p}}\rangle = 0, \qquad \langle V_{\mathbf{p}} V_{\mathbf{p}'}\rangle = V^2 \delta_{\mathbf{p}\bar{\mathbf{p}}'}. \tag{4.9}$$

Here, $\langle ...\rangle$ represents disorder averaging. To start, we define Feynman rules of a diagrammatic theory for disordered systems, as shown in Fig. 4.1. Thin lines represent "bare" Green's function of a clean system, whereas the thick lines correspond to disorder-averaged Green's function. Here, we consider zero-temperature Green's functions for simplicity, but similar considerations hold at finite temperature [112]. Dashed lines represents the impurity potential. Note that, although disorder breaks translational invariance, it is restored in $\langle G\rangle$ by disorder averaging, i.e. $\langle G_{\mathbf{qq}'}\rangle = \langle G_{\mathbf{q}}\rangle\delta_{\mathbf{qq}'}$.

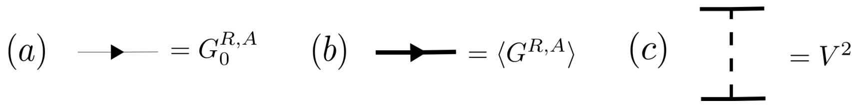

Figure 4.1: Feynman rules for disordered systems. (a) "Bare" Green's function. (b) "Dressed", disorder-averaged Green's function. (c) Impurity line.

Next, we expand the disorder averaged Green's function perturbatively in V, as shown in Fig. 4.2. Note that all impurity lines need to be paired, as diagrams with unpaired impurity lines vanish upon disorder averaging, as dictated by the condition $\langle V_{\mathbf{p}}\rangle = 0$.

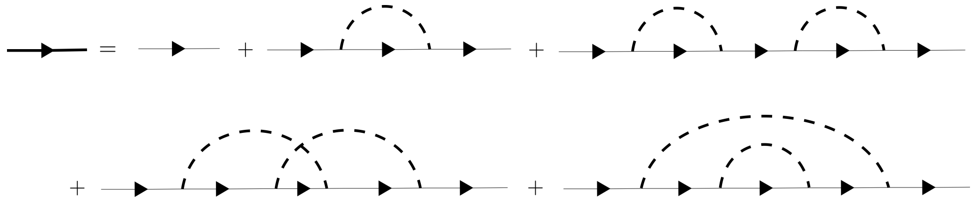

Figure 4.2: First few terms in the diagrammatic expansion of the disorder-averaged Green's function. For the definition of diagram elements, see Fig. 4.1.

We can now express $\langle G\rangle$ using the Dyson equation, represented diagramatically in Fig. 4.3 (a)

$$\langle G\rangle = G_0 + G_0\Sigma\langle G\rangle, \qquad \text{or} \qquad \langle G\rangle = (G_0^{-1} - \Sigma)^{-1}. \tag{4.10}$$

Here Σ is the self-energy, which is a sum of all irreducible diagrams, that is, all diagrams that cannot be split into simpler ones by cutting G_0 lines. Contribution of the reducible diagrams is negligible if disorder is weak on the scale of the Fermi energy.

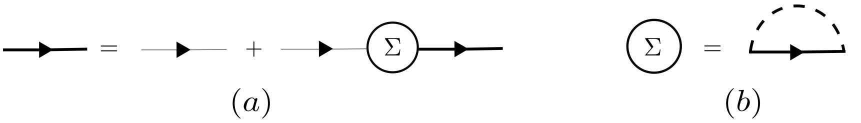

Figure 4.3: (a) Diagrammatic representation of the Dyson equation. (b) Diagrammatic representation of the self-energy in the self-consistent Born approximation.

The dominant, lowest order, contribution to Σ is given by the second term in the diagrammatic expansion in Fig. 4.2. Neglecting all other terms in the self-energy constitutes the so-called *first Born approximation.* Then, we have

$$\Sigma_{\mathbf{p}}^{R,A} = \int \frac{d^2\mathbf{q}}{(2\pi)^2}\langle V_{\mathbf{q}} G_{\mathbf{p}-\mathbf{q}0}^{R,A} V_{\bar{\mathbf{q}}}\rangle = V^2 \int \frac{d^2\mathbf{p}}{(2\pi)^2} G_{\mathbf{p}0}^{R,A} = \frac{1}{2\tau}\int d\xi_{\mathbf{p}} G_{\mathbf{p}0}^{R,A}. \tag{4.11}$$

Here, we have introduced the scattering rate associated with the disorder potential, $1/(2\tau) = \pi\nu_0 V^2$, where $\nu_0 = m/(2\pi)$ is the density of states at the Fermi level and

m is the effective mass of electrons. Using the expression for the Green's function (4.7) and assuming the dispersion of the 2DEG, $\xi_{\mathbf{p}} = |\mathbf{p}|^2/2m - \mu$, where the chemical potential μ is the dominant energy scale, $\mu \gg 1/(2\tau)$, we solve the last integral in Eq. (4.11). It yields $\Sigma^{R,A}_{\mathbf{p}} = \Re\Sigma \pm i/(2\tau)$, the real part of which can be absorbed into the chemical potential, and thus neglected. The disorder-averaged Green's function is then

$$\langle G^{R,A}_{\mathbf{p}} \rangle = \left(\epsilon - \xi_{\mathbf{p}} \pm \frac{i}{2\tau} \right)^{-1}. \tag{4.12}$$

Finally, using $\langle G^{R,A}_{\mathbf{p}} \rangle$ obtained this way to calculate the self-energy in Eq. (4.11), as shown diagramatically in Fig. 4.3 (b), constitutes the *self-consistent Born approximation*. In the model we are considering, it yields the same result as the first Born approximation.

4.2.1 Two-particle correlation functions: diffusons and Cooperons

Having established the method to calculate single-particle disorder averages, we now turn to two-particle correlation functions of the form $\langle G^R G^A \rangle$. Such quantities are related with many response functions [112]. Most importantly for our study in Part II of this thesis, they are used in the calculation of the conductances within the linear response theory. We may write

$$\begin{aligned} \langle G^R_{\mathbf{p_1 p_1'}\epsilon} G^A_{\mathbf{p_2 p_2'}\epsilon+\omega} \rangle &= \langle G^R_{\mathbf{p_1}\epsilon} \rangle \langle G^A_{\mathbf{p_2}\epsilon+\omega} \rangle \delta_{\mathbf{p_1 p_1'}} \delta_{\mathbf{p_2 p_2'}} \\ &+ \langle G^R_{\mathbf{p_1}\epsilon} \rangle \langle G^A_{\mathbf{p_2}\epsilon+\omega} \rangle \Gamma_{\mathbf{p_1 p_2}, \mathbf{p_1' p_2'}\omega} \langle G^R_{\mathbf{p_1'}\epsilon} \rangle \langle G^A_{\mathbf{p_2'}\epsilon+\omega} \rangle \delta_{\mathbf{p_1 - p_2 - p_1' + p_2'}}, \end{aligned} \tag{4.13}$$

where the first line is the disconnected part, and the function Γ is the so-called vertex function. Momentum conservation at the diagram vertices is accounted for by the δ-functions.

We proceed by calculating the vertex function Γ. Within the approximation $\mu \gg 1/\tau$, the dominant contributions to it are non-crossing (ladder) diagrams and maximally crossed diagrams, as ilustrated in Fig. 4.4 (a) and (b), respectively. Note that, as in the case of single-particle disorder averaging, all impurity lines need to be paired.

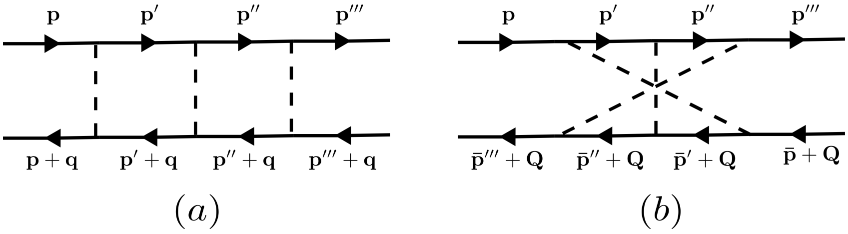

Figure 4.4: (a) Example of a ladder diagram. (b) Example of a maximally crossed diagram. The arrows represent disorder-averaged single-particle Green's functions.

The sum of all ladder diagrams can be found using a two-particle analogue to the Dyson equation – the Bethe-Salpeter equation, represented diagrammatically in Fig. 4.5. As illustrated in Fig. 4.4 (a), the vertex function only depends on the difference $\mathbf{q} =$

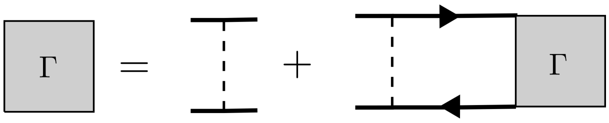

Figure 4.5: Diagrammatic representation of the Bethe-Salpeter equation.

$\mathbf{p_1} - \mathbf{p_2} = \mathbf{p_1'} - \mathbf{p_2'}$, so we have

$$\Gamma_{\mathbf{q}\omega} = V^2 + 2\pi V^2 \Pi_{\mathbf{q}\omega}\Gamma_{\mathbf{q}\omega}, \tag{4.14}$$

where $\Pi_{\mathbf{q}\omega}$ is the polarization operator, defined as

$$\Pi_{\mathbf{q}\omega} = \nu_0 \int d\xi_{\mathbf{p}} \langle G^R_{\mathbf{p}\epsilon}\rangle \langle G^A_{\mathbf{p}+\mathbf{q}\epsilon+\omega}\rangle \approx \nu_0\tau(1 + i\omega\tau - D|\mathbf{q}|^2). \tag{4.15}$$

Here, we have introduced the diffusion constant $D = \frac{1}{2}v_F^2\tau$, and assumed that disorder is sufficiently strong, such that $\tau\omega, \tau D|\mathbf{q}|^2 \ll 1$. Finally, the vertex function is

$$\Gamma_{\mathbf{q}\omega} = \frac{1}{2\pi\nu_0\tau^2}\frac{1}{D|\mathbf{q}|^2 - i\omega} = D(\mathbf{q}). \tag{4.16}$$

This is the so-called *diffuson* or diffusion pole, which is related to the classical diffusion probability of electrons and determines the Drude conductance.

We proceed by calculating the sum of all maximally crossed diagrams, which can be related to ladder diagrams by inverting the lower branch of the diagram, as illustrated in Fig. 4.6. Therefore, we can again employ the Bethe-Salpeter equation to find the vertex function Γ. In this case, it depends only on the momentum $\mathbf{p_1} + \mathbf{p_2'} = \mathbf{p_2} + \mathbf{p_1'} = \mathbf{Q}$, and we have

$$\Gamma_{\mathbf{Q}\omega} = \frac{1}{2\pi\nu_0\tau^2}\frac{1}{D|\mathbf{Q}|^2 - i\omega} = C(\mathbf{Q}). \tag{4.17}$$

This is the so-called *Cooperon*. It describes an additional contribution to the diffusion probability of electrons due to quantum interference, which leads to weak localization and antilocalization.

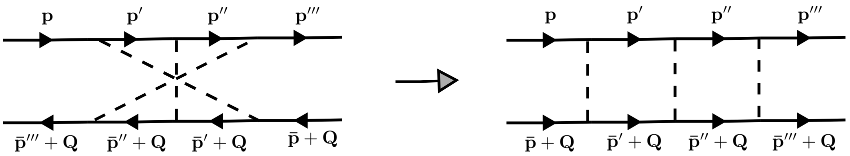

Figure 4.6: Relation between the maximally-crossed and ladder diagrams

Cooperons and diffusons are central objects in the study of mesoscopic transport phenomena, which will be employed extensively in Part II of this thesis. An important difference between these two quantities stems from their response to perpendicular magnetic fields, in whose presence the momenta are modified as $\mathbf{p} \to \mathbf{p} - e\mathbf{A}$, where $\mathbf{A}$ is a vector potential. In diffusons, the momentum $\mathbf{q}$ remains unchanged by the field, while in Cooperons $\mathbf{Q} \to \mathbf{Q} - 2e\mathbf{A}$. As a consequence, diffusons are unaffected by such fields, whereas the Cooperons become quickly suppressed (as the Cooperon pole (4.17) decays).

4.3 Quasiclassical methods for superconductivity

4.3.1 Basics of BCS theory

The microscopic theory of superconductivity proposed by Bardeen, Cooper and Schrieffer, has been exceptionally successful in the description of conventional superconductivity [33]. Its extensions are also widely used in the study of unconventional superconducting phases [35].

The basic idea of BCS is that electrons in a solid form the Cooper pairs, mediated by an attractive interaction between electrons. Such attraction is most commonly due to electron-phonon interaction in conventional superconductors. The corresponding Hamiltonian is

$$H_{BCS} = \sum_{\mathbf{p}} c^\dagger_{\mathbf{p}} \xi_{\mathbf{p}} c_{\mathbf{p}} + \sum_{\mathbf{p}\mathbf{p}'} \lambda_{\mathbf{p}\mathbf{p}'} c^\dagger_{\mathbf{p}\uparrow} c^\dagger_{\bar{\mathbf{p}}\downarrow} c_{\bar{\mathbf{p}}'\downarrow} c_{\mathbf{p}'\uparrow}, \tag{4.18}$$

where $\lambda_{\mathbf{p}\mathbf{p}'}$ describes the attractive interaction. We approximate it by

$$\lambda_{\mathbf{p}\mathbf{p}'} = \begin{cases} -\lambda, & \text{for } |\xi_{\mathbf{p}}| < \Omega_D, \\ 0, & \text{for } |\xi_{\mathbf{p}}| > \Omega_D, \end{cases} \tag{4.19}$$

where λ is the so-called BCS coupling constant, and Ω_D is the Debye frequency. We use the shorthand notation $\bar{\mathbf{p}} = -\mathbf{p}$. Then, we treat the interaction term in Eq. (4.18) in the mean field approximation, by defining the superconducting order parameter Δ as

$$\Delta = -\lambda \sum_{\mathbf{p}} \langle c_{\bar{\mathbf{p}}\downarrow} c_{\mathbf{p}\uparrow} \rangle_T. \tag{4.20}$$

The above equation is often called the self-consistent gap equation. The BCS Hamiltonian is now

$$H_{BCS} = \sum_{\mathbf{p}} c^\dagger_{\mathbf{p}} \xi_{\mathbf{p}} c_{\mathbf{p}} + \Delta \sum_{\mathbf{p}} c^\dagger_{\mathbf{p}\uparrow} c^\dagger_{\bar{\mathbf{p}}\downarrow} + h.c. \tag{4.21}$$

Next, we introduce the Nambu spinor $\Psi_{\mathbf{p}} = (c_{\mathbf{p}s}\ s c^\dagger_{\bar{\mathbf{p}}\bar{s}})^T$, where $s = \pm 1$ is the spin index. The Hamiltonian becomes, up to a constant shift in the chemical potential,

$$H_{BCS} = \sum_{\mathbf{p}} \Psi^\dagger_{\mathbf{p}} H^{BdG}_{\mathbf{p}} \Psi_{\mathbf{p}}, \qquad H^{BdG}_{\mathbf{p}} = \xi_{\mathbf{p}} \tau_z + \Delta \tau_x, \tag{4.22}$$

where $\tau_{x,y,z}$ are Pauli matrices in particle-hole space. $H^{BdG}_{\mathbf{p}}$ is the Bogoliubov-de Gennes Hamiltionan. It is readily diagonalized, with eigenvalues $E_{\mathbf{p}} = \pm\sqrt{\xi^2_{\mathbf{p}} + \Delta^2}$. From here, we can find the density of states in the superconducting state

$$\nu(\epsilon) = \nu_0 \frac{|\epsilon|}{\sqrt{\epsilon^2 - \Delta^2}} \Theta(|\epsilon| - \Delta), \tag{4.23}$$

where ν_0 is the density of states in the normal state. A finite superconducting order parameter opens a gap of size 2Δ in the quasiparticle spectrum, with sharp coherence peaks at the gap edge, as shown in Fig. 4.7.

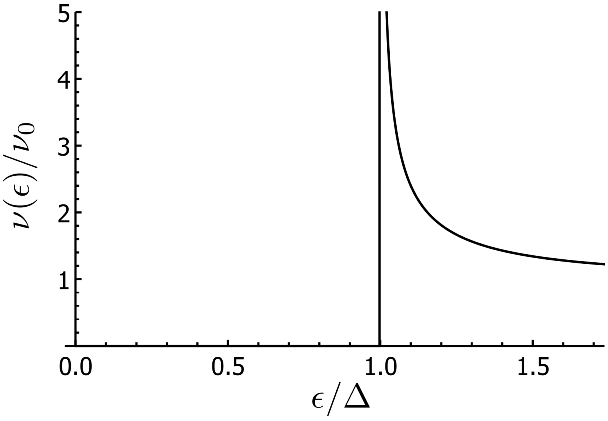

Figure 4.7: Density of states of a conventional superconductor.

The superconducting gap Δ depends on temperature T through the self-consistency condition (4.20), and decays as T is increased until it vanishes at the critical temperature T_c. At zero temperature, the superconducting gap can be related with T_c as

$$\Delta(T=0) = \Delta_0 = 1.76T_c. \tag{4.24}$$

Assuming the vanishing gap, $\Delta \to 0$, the self-consistency condition yields another important result

$$T_c \approx 1.13\Omega_D e^{-1/(\lambda\nu_0)}. \tag{4.25}$$

This allows one to replace two parameters of the theory which are not accessible in experiments, Ω_D and λ, with a measurable quantity T_c. Furthermore, Eq. (4.25) showcases the so-called BCS instability, as an arbitrarily small attraction λ is sufficient for the onset of superconductivity, due to the exponential dependence.

4.3.2 Green's functions for superconductivity

Analogously to Sec. 4.1, we can introduce Green's functions for the superconducting state as

$$\hat{\mathcal{G}}_{\mathbf{p}\omega_n 0} = -\int_0^{1/T} d\tau e^{i\omega_n\tau}\langle T_\tau \Psi_{\mathbf{p}}(\tau) \otimes \Psi^\dagger_{\mathbf{p}}(0)\rangle_T. \tag{4.26}$$

Here, the symbol "$\otimes$" denotes the tensor product.

Using the equation of motion, $d\Psi^{(\dagger)}_{\mathbf{p}}(\tau)/d\tau = [H_{BCS}, \Psi^{(\dagger)}_{\mathbf{p}}]$, we find that it satisfies

$$\hat{\mathcal{G}}_{\mathbf{p}\omega_n 0} = (i\omega_n - H^{BdG}_{\mathbf{p}})^{-1} = \begin{pmatrix} \mathcal{G} & \mathcal{F} \\ \mathcal{F}^\dagger & \mathcal{G}^\dagger \end{pmatrix}. \tag{4.27}$$

$\hat{\mathcal{G}}$ is called Gor'kov Green's function, and it has a matrix structure in the particle-hole space. The component $\mathcal{G} \sim \langle c^\dagger c\rangle$ is related to normal-state correlations, while $\mathcal{F} \sim \langle cc\rangle$ is related to superconducting correlations and vanishes in the normal state.

The disorder Hamiltonian (4.8) in the Nambu basis is given as $H_D = \sum_{\mathbf{q}\mathbf{q}'} \Psi^\dagger_{\mathbf{q}} V_{\mathbf{q}-\mathbf{q}'}\tau_z \Psi_{\mathbf{q}'}$. Within the Born approximation, we obtain for the disorder-averaged Gor'kov Green's function

$$\langle\hat{\mathcal{G}}_{\mathbf{p}\omega_\mathbf{n}}\rangle(i\omega_n - H^{BdG}_\mathbf{p} - \hat{\Sigma}_\mathbf{p}) = 1, \qquad \text{or} \qquad (i\omega_n - H^{BdG}_\mathbf{p} - \hat{\Sigma}_\mathbf{p})\langle\hat{\mathcal{G}}_{\mathbf{p}\omega_\mathbf{n}}\rangle = 1,$$
$$\text{where} \qquad \hat{\Sigma}_\mathbf{p} = \frac{1}{2\tau}\int d\xi_\mathbf{p}\tau_z\hat{\mathcal{G}}_{\mathbf{p}\omega_n 0}\tau_z. \tag{4.28}$$

4.3.3 Quasiclassical approximation

The equations for the Gor'kov Green's functions simplify significantly within the quasiclassical approximation, which assumes a separation of the energy scales related to the normal-state and superconducting properties: $\mu \gg \Delta, 1/\tau$. We define the quasiclassical Green's function as

$$g = \frac{i}{\pi}\int d\xi_\mathbf{p}\tau_z\langle\hat{\mathcal{G}}_{\mathbf{p}\omega_n}\rangle. \tag{4.29}$$

Then, we multiply the two equations from the first line of Eq. (4.28) by τ_z, from left and right, respectively, and subtract them. The source term, $\xi_\mathbf{q}$, cancels out as a result. After integrating the resulting expression over energies, we find that the quasiclassical Green's function satisfies the following commutator equation

$$[\omega_n\tau_z + \Delta\tau_y + \frac{1}{2\tau}g, g] = 0, \tag{4.30}$$

known as the Eilenberger equation. Similar derivation for the more general case of non-homogeneous superconductivity can be found in Ref. [114].

The statement of the Anderson theorem for the uniform superconducting phase immediately follows from Eq. (4.30), as the self-energy due to disorder potential commutes with g. Thus, simple scalar disorder does not modify the superconducting properties (this is not the case, however, for e.g. magnetic disorder).

The solution of Eq. (4.30) is not unique, and it needs to be supplemented by the normalization condition,

$$g^2 = 1. \tag{4.31}$$

Right-hand side of Eq. (4.31) is the unity matrix acting in the particle-hole and spin space. For a detailed derivation of this condition, see e.g. Ref. [114]. In short, it can be shown that $g^2 = const$. Then, since in the normal state $g = \tau_z$, we have $g^2 = \tau_z^2 = 1$.

Finally, let us relate the Green's function g with some physical quantities. The self-consistency condition (4.20) can be rewritten as

$$\Delta = \frac{1}{2}\lambda T\pi\nu_0\sum_{\omega_n}\mathrm{Tr}[\tau_x g(\omega_n)], \tag{4.32}$$

whereas the density of states in the superconducting phase is given as

$$\nu(\epsilon) = \nu_0\mathrm{Tr}[\tau_z g(i\omega_n \to \epsilon + i0^+)]. \tag{4.33}$$

Part I

Ising superconductivity in in-plane magnetic fields

Chapter 5

Single-band Ising superconductors

In this Chapter, we study n-doped TMD superconductors (MoS_2, WS_2), where only the K-band is present at the Fermi level. We focus on superconducting properties in the presence of in-plane magnetic fields. As the orbital effect is negligible for such fields, superconductivity is only affected by the paramagnetic effect which competes with strong pinning of the electron spins to out-of-plane orientation by the Ising SOC. Studying the evolution of superconducting properties as a function of an in-plane fields provides insight into exotic Ising superconductivity.

We formulate the quasiclassical equations for disordered Ising superconductors in Sec. 5.1 and use it to calculate the in-plane upper critical field and the density of states. In Sec. 5.2 we discuss our results in the absence of intervalley scattering, where, notably, h_{c2} diverges at zero temperatures. Sec. 5.3 is devoted to the role of intervalley scattering, which provides an effective spin-flip mechanism and leads to the saturation of h_{c2}, consistent with experiments. In Sec. 5.4, we examine the conditions for realizing a non-uniform FFLO phase and/or first-order phase transition in Ising superconductors. The part of these results related to h_{c2} was published in Ref. [24], where we used a more complicated diagrammatic method instead of quasiclassics (as discussed in Sec. 5.1.2).

5.1 Model for Ising superconductors

The Hamiltonian for disordered TMD superconductors is given as

$$H_{BCS} = \sum_{\mathbf{q}\mathbf{q}'} \Psi^\dagger_{\mathbf{q}} H^{BdG}_{\mathbf{q}\mathbf{q}'} \Psi_{\mathbf{q}'}, \qquad H^{BdG}_{\mathbf{q}\mathbf{q}'} = \begin{pmatrix} H_{\mathbf{q}}\delta_{\mathbf{q}\mathbf{q}'} + H^D_{\mathbf{q}\mathbf{q}'} & \Delta\delta_{\mathbf{q}\mathbf{q}'} \\ \Delta\delta_{\mathbf{q}\mathbf{q}'} & -s_y\eta_x[H_{\bar{\mathbf{q}}}\delta_{\mathbf{q}\mathbf{q}'} + H^D_{\bar{\mathbf{q}}'\bar{\mathbf{q}}}]^T s_y\eta_x \end{pmatrix}, \tag{5.1}$$

where $\Psi_{\mathbf{q}} = (c_{\mathbf{q}\sigma s\eta}\, s c^\dagger_{\bar{\mathbf{q}}\sigma\bar{s}\bar{\eta}})^T$ is the Nambu spinor. The normal state Hamiltonian $H_{\mathbf{q}}$ and the phenomenological disorder potential $H^D_{\mathbf{q}\mathbf{q}'}$ were introduced in Chapter 3. We model superconductivity with the simplest singlet-pairing potential, where Cooper pairs necessarily form from electrons in two different valleys, as their momenta need to be opposite.

To proceed, we simplify the model by neglecting Rashba SOC and trigonal warping, as well as all disorder terms except potential disorder $H^{D0}_{\mathbf{q}\mathbf{q}'}$. BdG Hamiltonian then becomes

$$H^{BdG}_{\mathbf{q}\mathbf{q}'} = [H_0 + \Delta_{KM}\sigma_z s_z \eta_z + \Delta_{VZ} s_z \eta_z]\delta_{\mathbf{q}\mathbf{q}'}\tau_z + H^{D0}_{\mathbf{q}\mathbf{q}'}\tau_z + \Delta\delta_{\mathbf{q}\mathbf{q}'}\tau_x + h\delta_{\mathbf{q}\mathbf{q}'} s_x. \tag{5.2}$$

We proceed by rotating it, $[1_{ph} \otimes U_{\mathbf{q}}]H^{BdG}_{\mathbf{qq}'}[1_{ph} \otimes U^{\dagger}_{\mathbf{q}'}]$, where 1_{ph} is the unity matrix in the particle-hole space, and projecting to the conduction band. The unitary transformation $U_{\mathbf{q}}$ was introduced in Chapter 3. We assume that the chemical potential μ is sufficiently far above E_g on the relevant energy scales determining the superconducting properties $(\Delta, T \ll |\mu - E_g|)$. The BdG Hamiltonian in the conduction band is then given as

$$\mathcal{H}^{BdG}_{\mathbf{qq}'} = [\xi_{\mathbf{q}}\delta_{\mathbf{qq}'} + \Delta_{so}\delta_{\mathbf{qq}'}s_z\eta_z + \mathcal{H}^{D0}_{\mathbf{qq}'}]\tau_z + \Delta\delta_{\mathbf{qq}'}\tau_x + h\delta_{\mathbf{qq}'}s_x, \tag{5.3}$$

where $\mathcal{H}^{D0}_{\mathbf{qq}'}$ is the potential disorder in the projected basis.

5.1.1 Quasiclassical equations

Starting from the projected Hamiltonian Eq. (5.3), the derivation of the quasiclassical Eilenberger equation is standard (see Chapter 4.3 and Appendix B.1). We obtain

$$[(\omega_n + ihs_x)\tau_z + i\eta\Delta_{so}s_z + \Delta\tau_y + \frac{1}{2\tau_0}g_\eta + \frac{1}{2\tau_{iv}}g_{\bar{\eta}}, g_\eta] = 0. \tag{5.4}$$

Here g_η is the quasiclassical Green's function for valley η, which must satisfy the normalization condition $g_\eta^2 = 1$. Note that the above equation holds for arbitrary values of intra- and intervalley scattering (i.e., the diffusive limit was not assumed [1]). We see that intravalley scattering drops out immediately from the Eilenberger equation, as the relevant contribution to the self-energy commutes with g_η. Therefore, intravalley disorder does not affect the superconducting properties of Ising superconductors, similarly to the Anderson theorem for conventional superconductors where scalar disorder has no effect, as discussed in Sec. 4.3.

The quasiclassical Green's function that solves (5.4) has the following structure

$$g_\eta = c_0\tau_y + c_x\tau_y s_x + d_0\tau_z + d_x\tau_z s_x + \eta b_y s_y\tau_x + \eta a_z s_z, \tag{5.5}$$

which is readily checked by substituting this form into Eq. (5.4) and verifying that no additional terms are generated. The components d_0 and c_0 are the only ones that exist at zero magnetic field, and in that case they correspond to the normal and anomalous part of the Green's function, respectively. The components d_x and c_x describe the influence of an in-plane Zeeman field, while the components a_z and b_y capture the effect of Ising SOC and its interplay with the field.

The self-consistency condition can be written as

$$\Delta = \lambda T\pi\nu_{0K}\sum_{\omega_n} c_0(\omega_n), \tag{5.6}$$

while the density of states is obtained from the component d_0 after the analytical continuation

$$\nu(\epsilon) = \nu_{0K}\Re[d_0(i\omega_n \to \epsilon + i0^+)]. \tag{5.7}$$

---

[1] The quasiclassical Eilenberger equation paired with the diffusive approximation is known as the Usadel equation [114]. In our theory, these equations are equivalent, as intravalley scattering has no effect.

Combining the normalization condition $g_\eta^2 = 1$ and Eq. (5.5), we obtain

$$a_z = \frac{b_y d_x}{c_0}, \qquad c_x = -\frac{d_x d_0}{c_0}, \tag{5.8}$$

and the normalization condition becomes

$$(c_0^2 + d_0^2 + b_y^2)\left(1 + \frac{d_x^2}{c_0^2}\right) = 1. \tag{5.9}$$

Then, substituting Eq. (5.5) into the Eilenberger equation, we obtain the following set of equations for the components of g_η

$$\begin{aligned} \omega_n b_y - i\eta\Delta_{so}\frac{d_x d_0}{c_0} + \frac{1}{\tau_{iv}} b_y d_0 \left(1 + \frac{d_x^2}{c_0^2}\right) &= 0, \\ \omega_n \frac{d_x d_0}{c_0} - ihc_0 - i\eta\Delta_{so} b_y + \Delta d_x &= 0, \\ -\omega_n c_0 + ih\frac{d_x d_0}{c_0} + \Delta d_0 &= 0, \\ -ih\frac{b_y d_x}{c_0} + i\eta\Delta_{so} d_x - \Delta b_y - \frac{1}{\tau_{iv}} b_y c_0 \left(1 + \frac{d_x^2}{c_0^2}\right) &= 0. \end{aligned} \tag{5.10}$$

We use this system of equations, together with the normalization condition (5.9) as a starting point to calculate the in-plane upper critical field and the density of states in the superconducting phase.

The calculation of the upper critical field can be done by assuming a vanishing superconducting gap ($\Delta \to 0$), and linearizing the system by keeping only the first order terms in Δ, as presented in Sec. 5.1.2.

Obtaining the density of states is more challenging, as the system needs to be solved for any Δ, which, in general, needs to be done numerically. However, analytical solutions are possible in the absence of intervalley scattering (see Appendix B.1, where we provide the full g_η for this case), as well as in various regimes of the intervalley scattering strenght, as we will discuss in Sec. 5.3.

5.1.2 Solution near the phase transition

Close to the phase transition, where $\Delta \to 0$, the quasiclassical Green's function can be written as $g_\eta \approx \tau_z + \delta g_\eta$. Here, τ_z is the normal state contribution, and $\delta g_\eta \sim \Delta$ is a small correction due to superconductivity. Assuming $\delta g_\eta^2 \ll 1$, the normalization condition yields $0 = \{\tau_z, \delta g_\eta\}$, which implies $\delta g_\eta = c_0 \tau_y + c_x s_x \tau_y + \eta b_y s_y \tau_x$, and $d_0 \approx 1$, $a_z, d_x \approx 0$. Now, the system of equations (5.10) can be readily solved to obtain $c_0(\omega_n)$. Combining this with the self-consistency condition (5.6) and using the standard BCS result $T_c \approx 1.13\,\Omega_D e^{-1/(\lambda\nu_{0K})}$, we finally have

$$\ln\frac{T}{T_c} = 2\pi T \sum_{\omega_n} \left[\frac{\Delta_{so}^2 + \omega_n(\omega_n + \tau_{iv}^{-1})}{h_{c2}^2(\omega_n + \tau_{iv}^{-1}) + \omega_n[\Delta_{so}^2 + \omega_n(\omega_n + \tau_{iv}^{-1})]} - \frac{1}{\omega_n} \right], \tag{5.11}$$

where h_{c2} is the upper critical field. The above equation can be used to obtain the $h_{c2}(T)$ curve.

This result can alternatively be obtained using diagrammatic methods, as presented in Appendix B.4. This approach has been used in our publication, Ref. [24]. As can be seen by comparing the calculations in this section and in Appendix B.4, the calculation within the quasiclassics is much simpler, illustrating the superiority of this method for studying Ising superconductivity.

5.2 Superconducting properties in the absence of intervalley scattering

In the absence of intervalley scattering, $1/\tau_{iv} = 0$, the critical line given by Eq. (5.11) does not depend on disorder. In that case, Eq. (5.11) can be alternatively expressed as

$$\ln\frac{T_c}{T} = \frac{h_{c2}^2}{\rho^2}\Re\left[\psi\left(\frac{1}{2}+\frac{i\rho}{2\pi T}\right)-\psi\left(\frac{1}{2}\right)\right], \tag{5.12}$$

where $\psi(z)$ is the digamma function, and $\rho = \sqrt{\Delta_{so}^2 + h^2}$. In this form, it ressembles – and generalizes to arbitrary intravalley disorder – an expression derived by Frigeri *et al.* [115] in the clean case. It also reproduces the $h_{c2}(T)$ calculation from Ref. [12], where the linearized gap equation was solved numerically in the disorder-free case, using a complex tight-binding model for the conduction band of MoS_2.

As seen in Fig. 5.1, h_{c2} is enhanced in the presence of spin-orbit coupling, especially at low temperatures. In fact, it diverges in the zero-temperature limit for finite Δ_{so}. Physically, this can be understood as a consequence of the inability of the Zeeman field to completely align the electron spins in the in-plane orientation, due to the anti-parallel out-of-plane field provided by the Ising SOC. As discussed in Sec. 1.1, Ising superconductors have a degenerate pairing channel with the weight Δ_{so}^2/ρ^2, that is not suppressed by the magnetic fields, thus leading to the divergence.

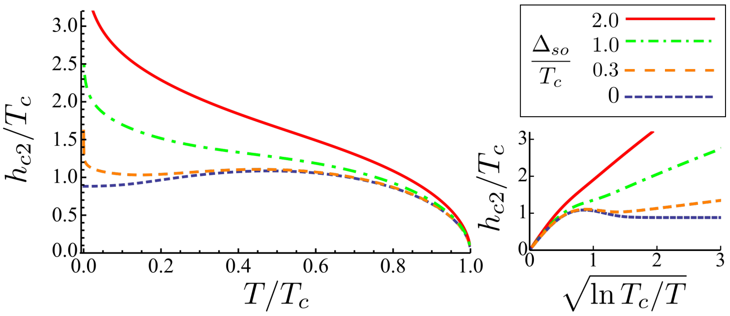

Figure 5.1: Upper critical field as a function of temperature in the absence of intervalley scattering for different values of Ising SOC, as described by Eq. (5.12). The plot on the right shows the same result but with a different scale for the x-axis to illustrate the logarithmic divergence at low temperature when $\Delta_{so} \neq 0$.

At low temperatures, using the asymptotic behavior of the digamma function $\psi(z) \approx \ln|z|$ for $|z| \gg 1$, Eq. (5.12) yields $\ln[T_c/T] = (h_{c2}^2/\rho^2)\ln[4e^{\gamma}\rho/(2\pi T)]$, where $\gamma \approx 0.577$.

As in the limit $T \to 0$ h_{c2} diverges, we can approximate our results assuming $h_{c2} \gg \Delta_{so}, \Delta_0$. Then, we have

$$\ln \frac{2h_{c2}}{\Delta_0} \approx \frac{\Delta_{so}^2}{h_{c2}^2} \ln \frac{T_c}{T}. \tag{5.13}$$

For weak Ising SOC ($\Delta_{so} \ll \Delta_0$), the critical curve $h_{c2}(T)$ only deviates from the conventional one at very low temperatures, where Eq. (5.13) yields

$$h_{c2} \propto \Delta_{so} \sqrt{\ln \frac{T_c}{T}} \qquad \text{for} \qquad \frac{T}{T_c} \ll \exp\left(- c \frac{\Delta_0^2}{\Delta_{so}^2} \right). \tag{5.14}$$

Here, c is a dimensionless constant of order 1. In the more interesting case of large Ising SOC, $\Delta_{so} \gg \Delta_0$, Eq. (5.13) yields a logarithmic divergence starting at higher temperatures,

$$h_{c2} \approx \Delta_{so} \sqrt{\ln \frac{T_c}{T} / \ln \frac{2\Delta_{so}}{\Delta_0}} \qquad \text{for} \qquad \frac{T}{T_c} \ll \frac{\Delta_0}{\Delta_{so}}. \tag{5.15}$$

Close to T_c, the critical field h_{c2} is small, and the assumptions $\Delta_{so} \gg h_{c2}$ and $\ln \frac{T_c}{T} \approx \frac{T_c - T}{T_c}$ hold. In the limit $\Delta_0 \gg \Delta_{so}$, one obtains the standard result $h_{c2} \approx 2.16 T_c \sqrt{1 - T/T_c}$. For strong SOC, $\Delta_{so} \gg \Delta_0$, we obtain a square-root dependence on temperature as well, but with an enhanced prefactor,

$$h_{c2} \approx \Delta_{so} \frac{1}{\sqrt{\ln \frac{2\Delta_{so}}{\Delta_0}}} \sqrt{1 - \frac{T}{T_c}}. \tag{5.16}$$

The density of states in the absence of intervalley scattering can be obtained from the full quasiclassical Green's function, specified in Appendix B.2. In the regime $\Delta_{so} \gg \Delta_0, \epsilon$, the DoS acquires a particularly simple form

$$\nu(\epsilon) = \nu_{0K} \Re \frac{|\epsilon|}{\sqrt{\epsilon^2 - \tilde{\Delta}^2}}, \qquad \text{with} \qquad \tilde{\Delta} = \frac{\Delta_{so}}{\rho} \Delta. \tag{5.17}$$

This result resembles the one for conventional superconductors at $h = 0$, but with a renormalized superconducting gap $\tilde{\Delta}$ which is reduced by h. Fig. 5.6 (a) shows the plot of the DoS in this regime. Ising protection of Cooper pairs is apparent from the form of $\tilde{\Delta}$, where we see that the superconductivity remains barely affected until the magnetic field reaches $h \sim \Delta_{so}$. In contrast to conventional superconductors, which exhibit spin-splitting of the coherence peak once the Zeeman field is applied, Ising superconductors will have a single coherence peak even at high magnetic fields due to Ising protection. Spin-splitting occurs, however, if Ising SOC is weak, $\Delta_{so} \lesssim \Delta_0$. Close to zero temperature, the gap in the quasiparticle spectrum does not close for arbitrary magnetic field, which is in line with the divergence of h_{c2}.

5.3 Role of intervalley scattering

At finite magnetic fields, intervalley scattering provides an effective spin-flip mechanism, since electrons scattered between different valleys "feel" opposite values of the Ising SOC field. This pair-breaking effect leads to a saturation of h_{c2} (as illustrated in Fig. 5.2), as well as rounding of the coherence peaks in the quasiparticle spectra. We will focus on the realistic case of strong Ising SOC $\Delta_{so} \gg \Delta_0$, and discuss h_{c2} and the DoS in the regimes $\tau_{iv}^{-1} \ll \Delta_{so}^2/\Delta_0$ and $\tau_{iv}^{-1} \gg \Delta_0$, as well as in the overlap regime, $\Delta_0 \ll \tau_{iv}^{-1} \ll \Delta_{so}^2/\Delta_0$, where the results acquire the simplest form. In Appendix B.3, we show a numerical calculation of h_{c2} in the limits $T \to 0$ and $T \to T_c$ in a broad range of intervalley disorder strength, and compare these results with the analytical estimates made in this section.

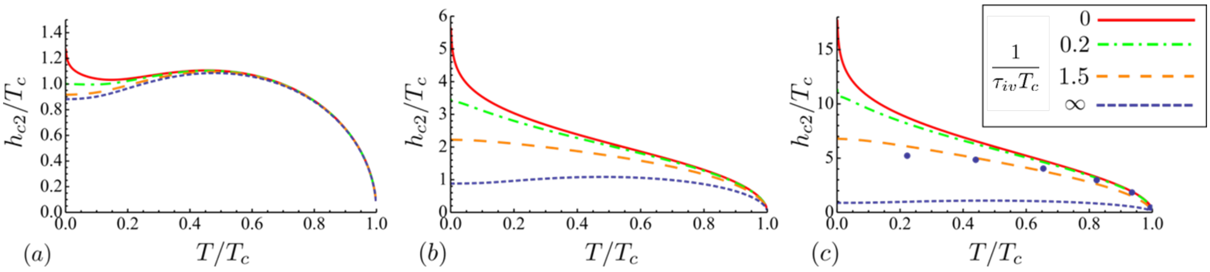

Figure 5.2: Upper critical field as a function of the temperature for various strengths of Ising SOC and intervalley scattering: (a) $\Delta_{so}/T_c = 0.3$, (b) $\Delta_{so}/T_c = 3$, and (c) $\Delta_{so}/T_c = 12$. The choice of parameters $\Delta_{so}/T_c = 12$ and $1/(\tau_{iv}T_c)$=1.5 [dashed line in (c)] gives a good fit of the experimental data from Ref. [12] [blue dots in (c)] taking the g-factor to be $g = 2$.

5.3.1 Regime $\tau_{iv}^{-1} \ll \Delta_{so}^2/\Delta_0$

In this regime, poles in the ω_n-dependent terms in the expression for the critical line Eq. (5.11) can be evaluated perturbatively to yield:

$$\ln\frac{T_c}{T} = \frac{\Delta_{so}^2}{\rho^2}\Re\left[\psi\left(\frac{1}{2}+\frac{h_{c2}^2}{2\pi\tau_{iv}\rho^2 T}\right)-\psi\left(\frac{1}{2}\right)\right]+\frac{h_{c2}^2}{\rho^2}\Re\left[\psi\left(\frac{1}{2}+\frac{i\rho}{2\pi T}\right)-\psi\left(\frac{1}{2}\right)\right]. \tag{5.18}$$

The above result holds even if SOC is weak ($\lesssim \Delta_0$), as long as $\Delta_{so}\tau_{iv} \gg 1$. The first and second term here correspond to the degenerate and non-degenerate pairing channels (introduced in Sec. 1.1.1), respectively. By comparing with Eq. (5.12), we see that the main effect of weak intervalley scattering is to provide an effective pair-breaking rate for the degenerate pairing channel, which yields an additional mechanism for the suppression of h_{c2}. As a consequence, h_{c2} now saturates at $T \to 0$.

Assuming $1/\tau_{iv} \ll \Delta_0$, such that $h_{c2} \gg \Delta_{so}$ still holds, we estimate from Eq. (5.18) that $\ln[2h_{c2}/\Delta_0] \approx \Delta_{so}^2/h_{c2}^2 \ln[\tau_2 h_{c2}]$, which evaluates to

$$h_{c2}(T=0) \approx \Delta_{so}\sqrt{\ln(\Delta_0\tau_{iv})/\ln\frac{2\Delta_{so}}{\Delta_0}} \tag{5.19}$$

in logarithmic accuracy, at zero temperature. In the vicinity of T_c, the critical line is still described by Eq. (5.16) in that parameter regime. If intervalley scattering is stronger $\tau_{iv}^{-1} \gg \Delta_0$, the upper critical field satisfies $h_{c2} \ll \Delta_{so}$, so the expression (5.18) reduces to Eq. (5.23).

Weak intervalley scattering of the order of Δ_0 is compatible with h_{c2} measurements in both MoS_2 [12,13] and WS_2 [55]. The curve corresponding to $1/(\tau_{iv}T_c) = 1.5$ shown in

Fig. 5.2 (c) gives a good fit of the experimental data for MoS_2 from Ref. [12] using their estimate for Δ_{so}/T_c. The experimental data for WS_2 from Ref. [55] is only available in a small temperature window close to T_c (see Fig. 2.3). It can be well explained even without intervalley scattering, taking $\Delta_{so} = 19.5$ meV$=150T_c$ [55], which sets the lower bound for Ising SOC. The value of SOC obtained from first-principle calculations is slightly larger, $\Delta_{so} = 30$ meV$=230T_c$. In this case, intervalley scattering of $1/(\tau_{iv}T_c) = 6$ is required to explain the data.

The density of states in the superconducting phase is given by

$$\nu(\epsilon) = \nu_{0K}\Re\frac{|\epsilon|}{\sqrt{\epsilon^2 - \Delta^2(\epsilon)}}, \tag{5.20}$$

where we have defined an effective energy-dependent gap $\Delta(\epsilon)$, determined from the equation

$$\Delta(\epsilon) = \frac{\tilde{\Delta}}{1 + \frac{\tilde{\alpha}}{\sqrt{\Delta(\epsilon)^2 - \epsilon^2}}}, \qquad \text{where} \qquad \tilde{\Delta} = \frac{\Delta_{so}}{\rho}\Delta,\ \tilde{\alpha} = \frac{1}{\tau_{iv}}\frac{h^2}{\rho^2}. \tag{5.21}$$

The derivation of Eq. (5.21) is given in Appendix B.2. This result resembles the well known Abrikosov-Gor'kov formula (AG), where $\tilde{\alpha}$ corresponds to a depairing parameter. AG theory was originally derived to describe superconductors with magnetic impurities [116], but its validity was since extended to many other situations where time-reversal symmetry is broken and a dissipation mechanism that mixes time-reversed states is present [117]. In our case, time-reversal symmetry is broken by the magnetic field, while intervalley scattering provides the dissipation mechanism.

In most AG superconductors, depairing parameter is quadratic or linear in the time-reversal symmetry breaking field[2]. In the case of Ising superconductors, this dependence is more complex, and the renormalized gap $\tilde{\Delta}$ also depends on the field. At large intervalley scattering $\tau_{iv}^{-1} \gg \Delta_0$, where $\Delta_{so} \gg h_{c2}$, we recover the standard quadratic dependence as $\tilde{\alpha} \approx h^2/(\tau_{iv}\Delta_{so}^2)$ and $\tilde{\Delta} \approx \Delta$.

Energy at the gap edge can be expressed using the standard expression [116]

$$\epsilon_g^{2/3} = \tilde{\Delta}^{2/3} - \tilde{\alpha}^{2/3}. \tag{5.22}$$

One of the most notable features of the AG theory is the appearance of the gapless superconducting phase, which occurs when the gap edge disappears at $\tilde{\Delta} = \tilde{\alpha}$. Furthermore, the shape of the quasiparticle spectra depends only on a single parameter $\tilde{\alpha}/\tilde{\Delta}$, as shown in Fig. 5.3.

5.3.2 Overlap regime $\Delta_0 \ll \tau_{iv}^{-1} \ll \Delta_{so}^2/\Delta_0$

In this disorder range, the regimes presented in Secs. 5.3.1 and 5.3.3 overlap. Both h_{c2} and the DoS can be captured using a Abrikosov-Gor'kov depairing parameter $\alpha = h^2/(\Delta_{so}^2\tau_{iv})$.

---

[2] If a magnetic field is applied, examples of quadratic-in-field depairing include superconductors with strong spin-orbit scattering and the orbital effect in thin films, while superconducting surface sheaths exhibit linear-in-field depairing [117].

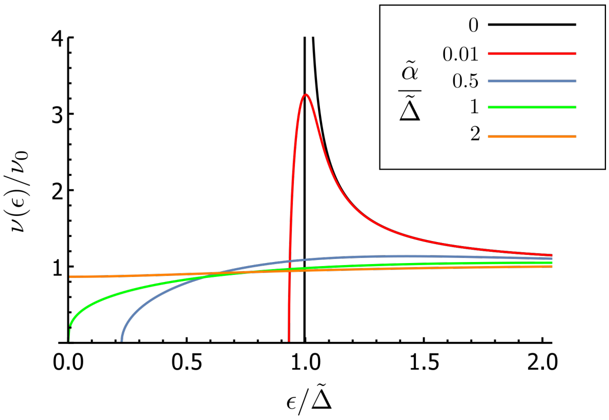

Figure 5.3: Quasiparticle spectra for superconductors described by the AG theory, for various values of the parameter $\tilde{\alpha}/\tilde{\Delta}$. Note that $\tilde{\Delta}$ depends on $\tilde{\alpha}$ through the self-consistent gap equation.

Namely, the critical line $h_{c2}(T)$ is given by

$$\ln\frac{T_c}{T}=\Re\left[\psi\left(\frac{1}{2}+\frac{\alpha}{2\pi T}\right)-\psi\left(\frac{1}{2}\right)\right], \tag{5.23}$$

which is known as the standard depairing equation. The DoS satisfies Eq. (5.21), with $\tilde{\alpha}\to\alpha$ and $\tilde{\Delta}\to\Delta$.

At $T\to 0$, we calculate

$$h_{c2}(T=0)\approx\sqrt{\frac{\Delta_{so}^2\tau_{iv}\Delta_0}{2}}, \tag{5.24}$$

while close to T_c we have

$$h_{c2}=\sqrt{\frac{4}{\pi}\Delta_{so}^2\tau_{iv}(T-T_c)}. \tag{5.25}$$

5.3.3 Regime $\tau_{iv}^{-1}\gg\Delta_0$

For strong intervalley scattering, electrons are so frequently scattered between the two valleys that the valley structure becomes suppressed. The effect of Ising SOC can then be captured by an effective spin-orbit scattering rate $\Delta_{so}^2\tau_{iv}$, and the system behaves as a conventional superonductor with spin-orbit impurities. A theory for such systems was developed by Maki *et al.* [118]. The upper critical line is given by

$$\ln\frac{T_c}{T}=2\pi T\sum_{\omega_n}\left[\frac{\omega_n+\Delta_{so}^2\tau_{iv}}{h_{c2}^2+\omega_n(\omega_n+\Delta_{so}^2\tau_{iv})}-\frac{1}{\omega_n}\right], \tag{5.26}$$

and the density of states is

$$\nu(\epsilon)=\nu_{0K}\frac{1}{2}\sum_{\pm}\Re\frac{|\epsilon|}{\sqrt{\epsilon^2-\Delta_{\pm}^2(\epsilon)}},\qquad\text{where}\qquad\Delta_{\pm}(\epsilon)=\frac{\Delta}{1\mp\frac{h}{\epsilon}+\frac{1}{2}\frac{\Delta_{so}^2\tau_{iv}}{\sqrt{\Delta_{\mp}^2(\epsilon)-\epsilon^2}}}. \tag{5.27}$$

The derivation of the last equation is given in Appendix B.2. Here, $\Delta_\pm(\epsilon) = [c_0(\epsilon) \pm c_x(\epsilon)]/[d_0(\epsilon) \pm d_x(\epsilon)]$ is related to spin-up (+) and spin-down electrons (-). The two spin species therefore contribute differently to the DoS, which leads to spin-splitting in the quasiparticle spectra, as illustrated in Fig. 5.6 (d). However, if the effective spin-orbit rate is strong, $\Delta_{so}^2\tau_{iv} \gg \Delta_0$, the two spin species mix, there is no spin-splitting, and we recover the Abrikosov-Gor'kov regime presented in Sec. 5.3.1.

Intervalley scattering of the order $\tau_{iv}^{-1} \gg \Delta_{so}^2/\Delta_0$ completely suppresses the effect of Ising SOC. In this regime, we find the standard paramagnetically limited formula for the upper critical field

$$\ln\frac{T_c}{T} = \Re\left[\psi\left(\frac{1}{2} + \frac{ih_{c2}}{2\pi T}\right) - \psi\left(\frac{1}{2}\right)\right]. \tag{5.28}$$

At zero temperature, Eq. (5.28) gives $h_{c2}(T=0) \approx \Delta_0/2$, while close to T_c we have $h_{c2} \approx 2.16T_c\sqrt{1-T/T_c}$. The density of states is

$$\nu(\epsilon) = \nu_{0K}\frac{1}{2}\sum_\pm \Re\frac{\epsilon \pm h}{\sqrt{(\epsilon \pm h)^2 - \Delta^2}}, \tag{5.29}$$

where the effect of the Zeeman field is to simply shift the energies of spin-up and spin-down electrons by $\pm h$.

The presented results cover the full range of intervalley disorder strength. Summary of all analyzed regimes is given in Fig. 5.4. In Fig. 5.5, we show the results of a self-consistent calculation of the superconducting gap as a function of magnetic field, done by numerically solving the system of equations (5.10) paired with the self-consistency condition (5.6). Finally, in Fig. 5.6, we show the evolution of the quasiparticle spectra in magnetic fields, for various values of intervalley disorder.

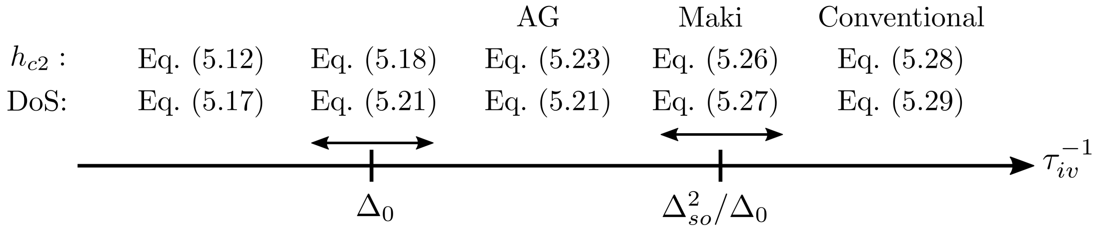

Figure 5.4: Summary of all regimes of intervalley scattering, assuming large Ising SOC $\Delta_{so} \gg \Delta_0$.

5.4 Nature of the phase transition

In Secs. 5.1-5.3, we assumed that the normal-superconductor phase transition of the second order and into a uniform superconducting state. However, at lower temperatures, this is not necessarily true. Firstly, in conventional paramagnetically limited superconductors, singlet-paired Cooper pairs yield nearly zero spin susceptibility at low temperatures, which leads to an abrupt, first-order phase transition at H_{c2} [27]. Secondly, as discussed in Sec. 1.1, a transition to the non-uniform FFLO phase can occur [44, 45]. In order to study the nature of the phase transition, we consider quadratic corrections in a finite

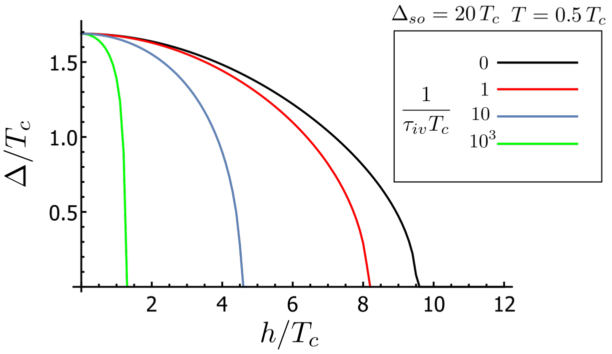

Figure 5.5: Superconducting gap Δ as a function of the in-plane magnetic field, for various values of intervalley disorder. Ising SOC is set to $\Delta_{so} = 20T_c$, and the temperature is $T = 0.5T_c$. All quantities are normalized with respect to T_c – the critical temperature at $h = 0$.

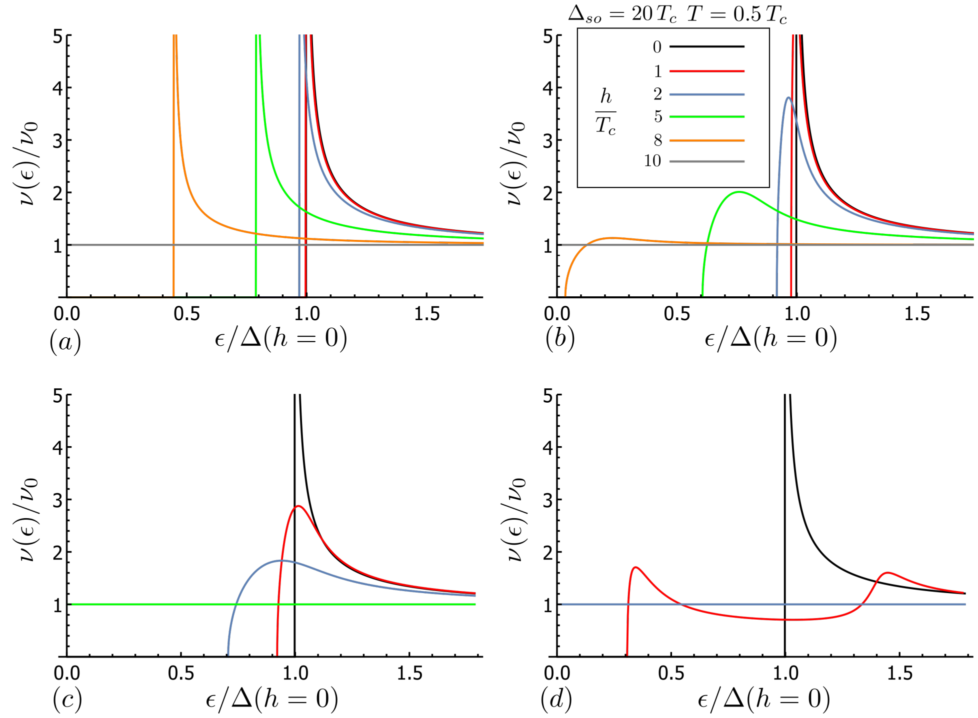

Figure 5.6: Quasiparticle spectra of Ising superconductors subjected to in-plane fields, for various values of intervalley scattering: (a) $\tau_{iv}^{-1} = 0$ ($h_{c2} \approx 9.5T_c$), (b) $\tau_{iv}^{-1} = T_c$ ($h_{c2} \approx 8.2T_c$), (c) $\tau_{iv}^{-1} = 10T_c$ ($h_{c2} \approx 4.5T_c$), (d) $\tau_{iv}^{-1} = 10^3 T_c$ ($h_{c2} \approx 1.2T_c$). Ising SOC is set to $\Delta_{so} = 20T_c$. Values of the superconducting gap Δ were obtained self-consistently for every parameter combination at the temperature $T = 0.5T_c$ (See Fig. 5.5). The relatively high temperature was chosen for numerical convenience, as the self-consistent calculation of Δ converges quicker, while the qualitative behavior remains the same compared to lower temperatures.

modulation wave vector and cubic corrections in the gap amplitude Δ in the vicinity of the transition. We find that both do not affect the transition when $\Delta_{so} \gtrsim \Delta_0$, and that moderate disorder does not change these conclusions.

5.4.1 FFLO phase

In the FFLO phase, the superconductor is spatially modulated. At the second-order transition into that state, we account for an exponentially modulated order parameter $\Delta(\mathbf{x}) = \Delta_{\mathbf{p}} e^{i\mathbf{p}.\mathbf{x}}$, where $\mathbf{p}$ is the modulation wavevector, by modifying the pairing term in the BCS Hamiltonian,

$$H_{FFLO} = \sum_{\eta\mathbf{q}} c^{\dagger}_{\eta\mathbf{q}} \mathcal{H}_{\eta\mathbf{q}} c_{\eta\mathbf{q}} + \Delta_{\mathbf{p}} \sum_{\eta\mathbf{q}} c^{\dagger}_{\eta\mathbf{q}+\mathbf{p}/2\uparrow} c^{\dagger}_{\bar{\eta}\bar{\mathbf{q}}+\mathbf{p}/2\downarrow} + \text{h.c.}. \tag{5.30}$$

Then, the Eilenberger equation in the clean case has a form

$$[(\omega_n + ihs_x + i\hat{\Delta}(\mathbf{x}))\tau_z + i\eta\Delta_{so}s_z, g_\eta(\mathbf{x})] = \frac{1}{2}\hat{\mathbf{q}} v_F \nabla_{\mathbf{x}} g_\eta(\mathbf{x}), \tag{5.31}$$

where the gradient source term accounts for the spatial dependence of the Green's function [114]. Here, $\hat{\Delta}(x) = \Delta(\tau_+ e^{i\mathbf{p}\mathbf{x}} + \tau_- e^{-i\mathbf{p}\mathbf{x}})$, with $\tau_\pm = (\tau_x \pm i\tau_y)/2$. In the vicinity of the phase transition, we have $g_\eta(\mathbf{x}) = \tau_z + f_\eta(\tau_+ e^{i\mathbf{p}\mathbf{x}} + \tau_- e^{-i\mathbf{p}\mathbf{x}})$, where $f_\eta = f_0 + f_x s_x + \eta f_y s_y$. After solving Eq. (5.31) to obtain f_0, we have

$$\Delta_{\mathbf{p}} = \lambda T \pi \nu_{0K} \sum_{\omega_n} \int \frac{d\theta}{2\pi} f_0(\omega_n) = \lambda T \pi \nu_{0K} \sum_{\omega_n} \int \frac{d\theta}{2\pi} \frac{\tilde{\omega}_n^2 + \Delta_{so}^2}{\tilde{\omega}_n(\tilde{\omega}_n^2 + \rho^2)}, \tag{5.32}$$

where $\tilde{\omega}_n = \omega_n - iv_F \mathbf{p}.\hat{\mathbf{q}}/2$. In order to consider the instability toward an FFLO state along the upper critical line $h_{c2}(T)$, we further assume that the modulation wavevector is small, $v_F|\mathbf{p}| \ll \Delta_0$. After summing over Matsubara frequencies, we obtain

$$\ln\frac{T}{T_c} = \int \frac{d\theta}{2\pi} \Re\left\{ \frac{\Delta_{so}^2}{\rho^2}\left[\psi\left(\frac{1}{2}\right) - \psi\left(\frac{1}{2} - \frac{iv_F\mathbf{p}.\hat{\mathbf{q}}}{4\pi T}\right)\right] + \frac{h_{c2}^2}{\rho^2}\left[\psi\left(\frac{1}{2}\right) - \psi\left(\frac{1}{2} + \frac{2i\rho - iv_F\mathbf{p}.\hat{\mathbf{q}}}{4\pi T}\right)\right]\right\}. \tag{5.33}$$

Expanding the above expression in small $\mathbf{p}$ and integrating over angles yields

$$\ln\frac{T}{T_c} = -\frac{h_{c2}^2}{\rho^2}\Re\left[\psi\left(\frac{1}{2} + \frac{i\rho}{2\pi T}\right) - \psi\left(\frac{1}{2}\right)\right] + \frac{v_F^2|\mathbf{p}|^2 T_c^2}{16\pi^2 h_{c2}^2 T^2} F_1(T, \Delta_{so}), \tag{5.34}$$

where

$$F_1(T, \Delta_{so}) = -\left(\frac{h_{c2}}{T_c}\right)^2 \left\{\psi^{(2)}\left(\frac{1}{2}\right) + \frac{h_{c2}^2}{\rho^2}\Re\left[\psi^{(2)}\left(\frac{1}{2} + \frac{i\rho}{2\pi T}\right) - \psi^{(2)}\left(\frac{1}{2}\right)\right]\right\}. \tag{5.35}$$

Here, $\psi^{(2)}(z)$ is the second derivative of the digamma function.

The last term in Eq. (5.34) is the correction to the result in the uniform case, Eq. (5.12), due to the modulation. The instability toward the FFLO state is determined by the sign of F_1 along the line $h_{c2}(T)$ for the uniform state. Namely, if $F_1 > 0$ (resp. $F_1 < 0$), h_{c2} decreases (resp. increases) when the order parameter is modulated.

We evaluate F_1 along the upper critical line derived for the uniform state in Fig. 5.7 (a). At $\Delta_{so} = 0$, F_1 changes sign at $T^* = 0.56T_c$, signaling a transition into the FFLO state below that temperature. At small Δ_{so}, we find that F_1 changes sign at two temperatures T_1^* and T_2^*, with $T_1^* < T < T_2^*$. The range of temperatures $T_1^* < T < T_2^*$, where the FFLO state can be expected shrinks as Δ_{so} increases, and it eventually disappears at $\Delta_{so} \gtrsim 0.30\Delta_0$, thus excluding the possibility of an FFLO phase at larger Δ_{so}.

In general, the FFLO phase is quickly destroyed by weak disorder [119], which is what we expect as well for Ising superconductors, even in the presence of intravalley scattering only.

5.4.2 First-order phase transition

In order to study the possibility of a first-order phase transition, the linearized self-consistency equation is not sufficient and we need to include higher order terms in Δ. Starting from the full expression for $c_0(\omega_n)$ (see Appendix B.2), expanding up to third order in Δ, and summing over Matsubara frequencies, the self-consistency condition becomes

$$\ln\frac{T}{T_c} = -\frac{h_{c2}^2}{\rho^2}\Re\left[\psi\left(\frac{1}{2}+\frac{i\rho}{2\pi T}\right)-\psi\left(\frac{1}{2}\right)\right]+\frac{\Delta^2 T_c^4}{16\pi h_{cs}^4 T^2}F_2(T,\Delta_{so}), \tag{5.36}$$

where

$$F_2(T,\Delta_{so}) = \frac{4h_{c2}^4}{\pi T_c^4}(2\pi T)^3\sum_{\omega_n>0}\frac{(\Delta_{so}^2+\omega_n^2)[h_{c2}^2(\Delta_{so}^2-3\omega_n^2)+(\Delta_{so}^2+\omega_n^2)^2]}{\omega_n^3(h_{c2}^2+\Delta_{so}^2+\omega_n^2)^3}. \tag{5.37}$$

The last term in Eq. (5.36) is the correction to the linearized gap equation (5.12) due to a finite amplitude of the order parameter in the vicinity of the transition. The order of the transition is determined by the sign of F_2 along the second-order transition line $h_{c2}(T)$. Namely, if $F_2 > 0$ (resp. $F_2 < 0$), the transition remains second-order (resp. a change of the order of the transition occurs).

At $\Delta_{so} = 0$, we find that $F_2 = (h_{c2}/T_c)^2 F_1$. Thus, the sign change occurs at the same temperature and, as a consequence, for $T < T^* = 0.56T_c$ the transition into the FFLO state is in competition with a first-order transition. At finite Δ_{so}, we evaluate F_2 along the upper critical line derived for the uniform state in Fig. 5.7 (b). We find that its temperature dependence is qualitatively similar to, though quantitatively different from F_1. Thus, a change of the transition order may occur in a finite temperature range, if Ising SOC is weak. On the other hand, F_2 remains positive at all temperatures if $\Delta_{so} \gtrsim 0.52\Delta_0$, and therefore the transition remains a second-order transition at larger Ising SOC.

As large intervalley disorder $\tau_{iv}^{-1} \sim \Delta_{so}^2/\Delta_0$ negates the effect of Ising SOC, the possibility of a first-order transition is restored in this regime.

5.5 Summary

In conclusion, in this Chapter we have formulated a quasiclassical theory of Ising superconductivity and used it to study the effect of disorder on n-doped TMD monolayer superconductors. We have calculated in-plane upper critical field and density of states in the superconducting phase. We have predicted that these quantities are robust to intravalley scattering, while intervalley scattering suppresses h_{c2} and introduces smearing of the density of states. Furthermore, we have identified intervalley scattering as a likely mechanism for the more moderate enhancement of h_{c2} observed in experiment, as weak disorder of this kind can explain the experimetal data.

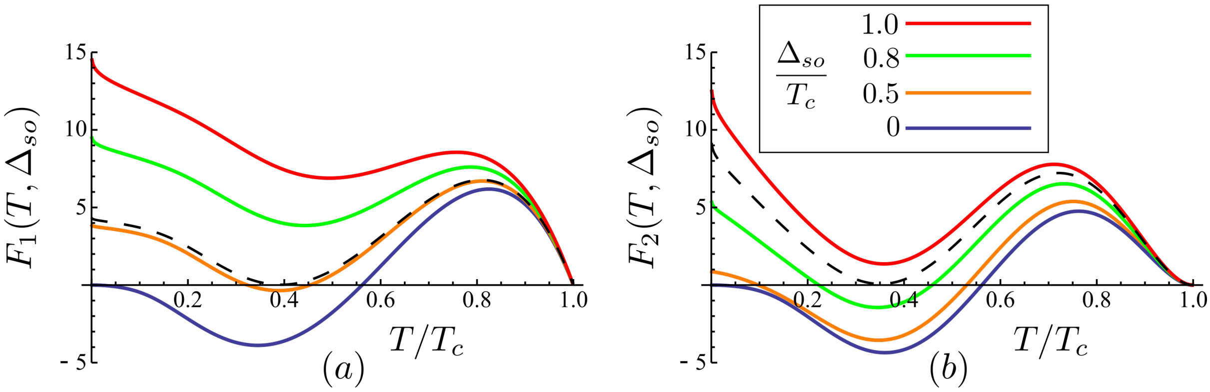

Figure 5.7: Temperature-dependence of $F_{1/2}(T, \Delta_{so})$ for various values of the Ising SOC. (a) FFLO: $F_1(T, \Delta_{so})$ defined in Eq. (5.35), evaluated along the upper critical line in the uniform state. The dashed black line corresponds to the critical value of the Ising SOC, $\Delta_{so}^{FFLO} = 0.53T_c \simeq 0.30\Delta_0$, above which the function F_1 remains positive for all temperatures. (b) First order phase transition: $F_2(T, \Delta_{so})$ defined in Eq. (5.37), evaluated along the upper critical line in the uniform state. The dashed black line corresponds to the critical value of Ising SOC $\Delta_{so}^{1\to 2} = 0.92T_c \simeq 0.52\Delta_0$, above which the function F_2 remains positive for all temperatures.

Chapter 6

Multiband Ising superconductors

In Chapter 5, we showed that the properties of n-doped TMD superconductors (MoS_2 and WS_2) are well explained with a model incorporating Ising SOC and intervalley scattering. However, this model is not sufficient in p-doped TMDs ($NbSe_2$ and TaS_2), as their multiband nature plays an important role in the superconducting properties (as discussed in Secs. 1.1.2 and 2.3). In this Chapter, we present a quasiclassical theory of Ising superconductivity which accounts for the multiband effects.

We assume that superconductivity originates from the K-band and is induced in the Γ-band by proximity effect in the momentum space. The mechanism coupling the two bands is provided by interband scattering. At zero magnetic field, a theoretical description of this system is given by the McMillan model [60]. It is in excellent agreement with measured quasiparticle spectra of trilayer $NbSe_2$ from Ref. [57], and can account for the observed two-gap structure. Note that our model neglects intrinsic superconductivity in the Γ-band, which is mainly motivated by convenience in calculations. Allowing for intrinsically superconducting Γ-band would not introduce any qualitative changes to our results. In fact, it would introduce small quantitative changes, which would quickly become negligible at higher fields where this band transitions to the normal state (while the K-band remains superconducting).

Furthermore, the single-band theory from Chapter 5 cannot explain the h_{c2} measurements in p-doped TMDs. SOC at the $\pm K$ points is larger by an order of magnitude in the valence band compared to conduction band (see Chapter 2.2). Yet, H_{c2} in p-doped TMDs is only slightly larger than in MoS_2 (see Fig. 2.3). The magnitude of intervalley scattering required to compete with such a large SOC, and to explain the experiments, is unphysically large ($\tau_{iv}^{-1} \sim \Delta_{so} \gg T_c$) [15]. In Sec. 6.3, we show that interband scattering provides an additional mechanism that limits H_{c2}, and that weak disorder of this kind ($\sim T_c$) can explain the experimental data.

The structure of this Chapter is as follows. We start by formulating the quasiclassical Eilenberger equations in Sec. 6.1, using the model of the K- and Γ-band presented in Chapter 3. In Sec. 6.2, we discuss the superconducting properties in the absence of a magnetic field, reproducing the results of the McMillan model. Next, we calculate the in-plane upper critical field in Sec. 6.3 and compare it to experimental mesurements. In Sec. 6.4, we calculate the density of states in the superconducting state as a function of magnetic field. Finally, in Sec. 6.5, we discuss the regime of strong SOC in both bands, where our results significantly simplify. Our analysis in this Chapter is mostly focused on the regime of strong SOC in the K-band, $\Delta_{so} \gg T_c, \tau_{iv}^{-1}, (\Delta_{so}^{\Gamma})^2\tau_\Gamma, \Gamma_{K\Gamma}, \Gamma_{\Gamma K}$ (in-line with first principle calculations, see Sec. 2.2), and weak interband disorder $\Gamma_{K\Gamma}, \Gamma_{\Gamma K} \sim T_c$ (in-line with experiment [57]).

6.1 Quasiclassical equations

Starting from the model for disordered p-doped TMDs from Chapter 3, we derive quasiclassical Eilenberger equations for the K-band

$$[(\omega_n + ihs_x)\tau_z + i\eta\Delta_{so}s_z + \Delta\tau_y + \Gamma_{K\Gamma}g^\Gamma + \frac{1}{2\tau_{iv}}g^K_{\bar\eta}, g^K_\eta] = 0, \tag{6.1}$$

and for the Γ-band

$$[(\omega_n + ihs_x)\tau_z + \frac{1}{2\tau_{\Gamma,so}}s_z g^\Gamma s_z + \frac{\Gamma_{\Gamma K}}{2}(g^K_\eta + g^K_{\bar\eta}), g^\Gamma] = 0. \tag{6.2}$$

Here, we introduced two quasiclassical Green's functions, g^K_η and g^Γ, which describe the K-band and the Γ-band, respectively. As in Chapter 5, we neglect Rashba SOC and trigonal warping, as well as non-potential disorder in the K-band. Intervalley scattering (τ_{iv}^{-1}) couples the two valleys in the K-band, while interband scattering ($\Gamma_{K\Gamma}$ and $\Gamma_{\Gamma K}$) couples the two bands, as illustrated in Fig. 6.1. We account for the effect of spin-orbit coupling in the Γ-band by an effective rate $\tau_{\Gamma,so}^{-1} = (\Delta_{so}^\Gamma)^2\tau_\Gamma$. Namely, if we assume sufficiently strong disorder, $\tau_\Gamma^{-1} \gg \Delta_{so}^\Gamma$, which randomizes the direction of momenta, the anisotropic SOC in the Γ-band will contribute as an effective spin-orbit scattering rate $\tau_{\Gamma,so}^{-1}$. This statement is derived in Appendix C.1. Both Eilenberger equations need to be supplemented with the normalization condition

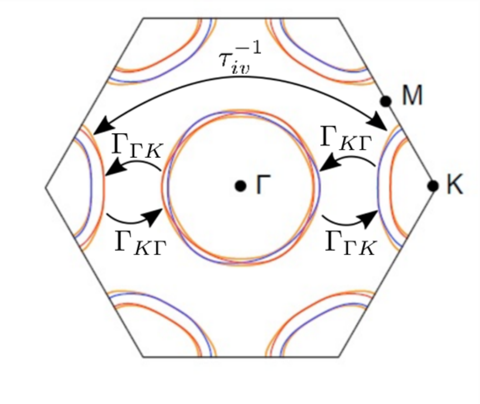

Figure 6.1: Schematic representation of the intervalley and interband scattering.

$$[g^K_\eta]^2 = 1, \qquad [g^\Gamma]^2 = 1. \tag{6.3}$$

The form of the quasiclassical Green's function for the K-band, which solves Eq. (6.1), is the same as the one used in Chapter 5, namely

$$g^K_\eta = c^K_0\tau_y + c^K_x\tau_y s_x + d^K_0\tau_z + d^K_x\tau_z s_x + \eta b^K_y s_y\tau_x + \eta a^K_z s_z. \tag{6.4}$$

The Green's function for the Γ-band, which solves Eq. (6.2), is given as

$$g^\Gamma = c_0^\Gamma \tau_y + c_x^\Gamma \tau_y s_x + d_0^\Gamma \tau_z + d_x^\Gamma \tau_z s_x. \tag{6.5}$$

Substituting the expressions (6.4) and (6.5) into the Eilenberger equations (6.1) and (6.2), and taking into account the normalization condition (6.3), leads to a system of coupled equations for the components of g_η^K and g_Γ, as written in Appendix C.2.

The superconducting order parameter Δ is determined self-consistently by

$$\Delta = \lambda T \pi \nu_{0K} \sum_{\omega_n} c_0^K(\omega_n). \tag{6.6}$$

Note that only g^K contributes to Eq. (6.6), as our model assumes that superconductivity originates from the K-band only. The density of states can be written as

$$\nu(\epsilon) = N_K \nu_{0K} \Re[d_0^K(\epsilon)] + N_\Gamma \nu_{0\Gamma} \Re[d_0^\Gamma(\epsilon)], \tag{6.7}$$

after the analytical continuation $i\omega_n \to \epsilon + i0^+$. Here, we introduced phenomenological parameters N_K and N_Γ, called the tunneling selectivity towards the K- and-Γ band, respectively, where $N_K + N_\Gamma = 1$. These quantities account for possible preferential tunneling to certain bands in experiment, due to the details of the band structure of the material and/or the experimental setup [62].

6.2 Multiband superconductivity in the absence of a magnetic field

In the absence of an in-plane Zeeman field, the form of the quasiclassical Eilenberger equations and quasiclassical Green's functions significantly simplifies. We have

$$[\omega_n \tau_z + \Delta \tau_x + \Gamma_{K\Gamma} g^\Gamma, g_\eta^K] = 0, \qquad [\omega_n \tau_z + \frac{\Gamma_{\Gamma K}}{2}(g_\eta^K + g_{\bar\eta}^K), g^\Gamma] = 0, \tag{6.8}$$

where

$$\begin{aligned} g_\eta^K &= c_0^K \tau_y + d_0^K \tau_z, \qquad (c_0^K)^2 + (d_0^K)^2 = 1, \\ g^\Gamma &= c_0^\Gamma \tau_y + d_0^\Gamma \tau_z, \qquad (c_0^\Gamma)^2 + (d_0^\Gamma)^2 = 1. \end{aligned} \tag{6.9}$$

After substituting Eq. (6.9) into Eq. (6.8), performing the analytical continuation $i\omega_n \to \epsilon + i0^+$, and defining effective energy-dependent order parameters $\Delta_X(\epsilon) = -i\epsilon c_0^X(\epsilon)/d_0^X(\epsilon)$, where $X = K, \Gamma$, we obtain

$$\Delta_K(\epsilon) = \frac{\Delta + \Gamma_{K\Gamma} \frac{\Delta_\Gamma(\epsilon)}{\sqrt{\Delta_\Gamma^2(\epsilon) - \epsilon^2}}}{1 + \frac{\Gamma_{K\Gamma}}{\sqrt{\Delta_\Gamma^2(\epsilon) - \epsilon^2}}}, \qquad \Delta_\Gamma(\epsilon) = \frac{\Gamma_{\Gamma K} \frac{\Delta_K(\epsilon)}{\sqrt{\Delta_K^2(\epsilon) - \epsilon^2}}}{1 + \frac{\Gamma_{\Gamma K}}{\sqrt{\Delta_K^2(\epsilon) - \epsilon^2}}}. \tag{6.10}$$

The density of states is then given as

$$\nu(\epsilon) = N_K \nu_{0K} \Re \frac{|\epsilon|}{\sqrt{\epsilon^2 - \Delta_K^2(\epsilon)}} + N_\Gamma \nu_{0\Gamma} \Re \frac{|\epsilon|}{\sqrt{\epsilon^2 - \Delta_\Gamma^2(\epsilon)}}. \tag{6.11}$$

This result is equivalent to the so-called McMillan formula for multiband superconductivity [60]. It was first derived for junctions of normal metals and superconductors [60], and later found to be valid for multiband superconductors where bands are coupled by disorder [59]. As a superconductor (or a superconducting band) is coupled to a normal metal (or a normal band), the Cooper pairs can transfer to the normal metal (normal band) and induce superconductivity in it. This is the so-called superconducting proximity effect.

In Fig. 6.2, we plot Eq. (6.11) for various values of interband scattering. The quasiparticle spectra in the K- and Γ-band have the same gap edge. The spectrum in the Γ-band exhibits one coherence peak at the energy corresponding to the induced superconducting gap. In the K-band, at sufficiently weak disorder (black and read curves in Fig. 6.2) two features are visible in the spectrum, corresponding to the intrinsic superconducting gap (at higher energies) and to an induced gap (at lower energies). These features cannot be resolved at stronger disorder (green curve in Fig. 6.2), due to a higher degree of band mixing.

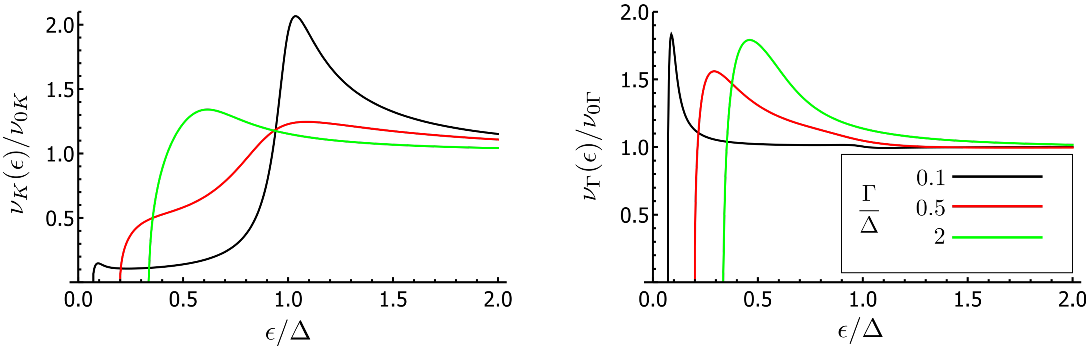

Figure 6.2: Density of states in the superconducting state for a multiband superconductor in the absence of magnetic field, for various strengths of interband disorder. For simplicity, we assume $\nu_{0K} = \nu_{0\Gamma}$, such that $\Gamma_{K\Gamma} = \Gamma_{\Gamma K} = \Gamma$. Left and right panel describe the K and Γ band, respectively. Note that the superconducting gap depends on interband disorder through the self-consistency condition (6.6).

Interband scattering modifies the superconducting critical temperature, due to the inverse proximity effect. Solving the self-consistent gap-equation (6.6) in the vicinity of the phase transition to the normal state, we obtain

$$\ln\frac{T_c^*}{T_c} = \frac{\Gamma_{K\Gamma}}{\Gamma_{K\Gamma}+\Gamma_{\Gamma K}}\Re\left[\psi\left(\frac{1}{2}+\frac{\Gamma_{K\Gamma}+\Gamma_{\Gamma K}}{2\pi T_c}\right)-\psi\left(\frac{1}{2}\right)\right]. \tag{6.12}$$

Here, T_c is the real critical temperature, while T_c^* is the "bare" critical temperature, corresponding to the case without interband disorder, and defined using the standard BCS relation $T_c^* = 1.13\Omega_D \exp[-1/(\lambda\nu_{0K})]$. Equation (6.12) therefore describes the degree to which the bare critical temperature is suppressed by interband disorder.

The standard BCS relation at zero temperature, $\Delta_0 \approx 1.76T_c$, no longer holds in multiband superconductors. This is illustrated in Fig. 6.3, where we see that in the presence of interband disorder, the ratio Δ/T_c is enhanced compared to the standard BCS result.

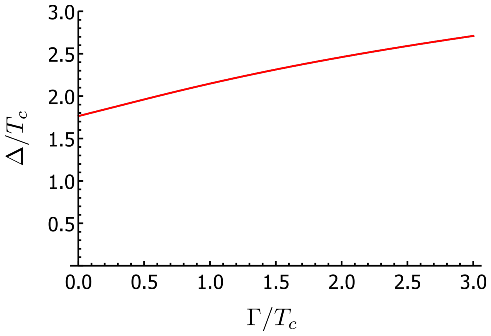

Figure 6.3: Superconducting gap at zero temperature as a function of interband disorder strength, obtained self-consistently from Eq. (6.6). For simplicity, we assume $\nu_{0K} = \nu_{0\Gamma}$, such that $\Gamma_{K\Gamma} = \Gamma_{\Gamma K}= \Gamma$.

Let us discuss these results in comparison with experiments in few-layer superconducting NbSe$_2$, which measured its quasiparticle spectra [57,58,107]. Refs. [57,107] measured an unusual shape of the density of states compatible with multiband superconductivity. As mentioned previously in Sec. 1.1.2, Ref. [57] found a very good agreement with the McMillan model, taking interband disorder to be $\Gamma_{K\Gamma}, \Gamma_{\Gamma K} \sim T_c$. Furthermore, all experiments found the ratio $\Delta/T_c > 1.76$, which is also a feature of multiband superconductivity.

6.3 Upper critical field

In this section, we calculate the effect of interband scattering on the upper critical field in Ising superconductors, by solving the self-consistent gap equation (6.6) in the vicinity of the phase transition, where $\Delta \to 0$. Here, the quasiclassical Green's functions can be written as $g^K_\eta = \tau_z + \delta g^K_\eta$ and $g^\Gamma_\eta = \tau_z + \delta g^\Gamma$, where τ_z is the normal state contribution and δg^K_η, $\delta g^\Gamma \sim \Delta$. Close to the second-order phase transition, we have $(\delta g^K_\eta)^2, (\delta g^\Gamma)^2 \ll 1$. Then, the normalization condition (6.3) yields $\{\tau_z, \delta g^K_\eta\} = 0$ and $\{\tau_z, \delta g^\Gamma\} = 0$, which leads to $\delta g^K_\eta = c^K_0 \tau_y + c^K_x s_x \tau_y + \eta b^K_y s_y \tau_x$, $\delta g^\Gamma = c^\Gamma_0 \tau_y + c^\Gamma_x s_x \tau_y$, and $d^K_0, d^\Gamma_0 \approx 1$; $a^K_z, d^K_x, d^\Gamma_x \approx 0$. Now, we can use the system of equations specified in Appendix C.2 to obtain c^K_0. Combining this with the self-consistency condition (6.6) and the relation (6.12) yields

$$\ln \frac{T}{T^*_c} = 2\pi T \sum_{\omega_n} \left[\frac{\Delta^2_{so} + \tilde{\omega}_n(\tilde{\omega}_n + \tilde{\tau}^{-1}_{iv})}{\tilde{h}^2_{c2}(\tilde{\omega}_n + \tilde{\tau}^{-1}_{iv}) + (\tilde{\omega}_n - \tilde{\tau}^{-1}_{\Gamma,so})[\Delta^2_{so} + \tilde{\omega}_n(\tilde{\omega}_n + \tilde{\tau}^{-1}_{iv})]} - \frac{1}{\omega_n} \right]. \tag{6.13}$$

Here, we have introduced

$$\begin{aligned} &\tilde{\omega}_n = \omega_n + \Gamma_{K\Gamma} - A\Gamma_{K\Gamma}\Gamma_{\Gamma K}(\omega_n + \Gamma_{\Gamma K}), && \tilde{h}_{c2} = h_{c2} + A\Gamma_{K\Gamma}\Gamma_{\Gamma K} h_{c2}, \\ &\tilde{\tau}^{-1}_{iv} = \tau^{-1}_{iv} + A\Gamma_{K\Gamma}\Gamma_{\Gamma K}(\omega_n + \Gamma_{\Gamma K}), && \tilde{\tau}^{-1}_{\Gamma,so} = A\Gamma_{K\Gamma}\Gamma_{\Gamma K}\tau^{-1}_{\Gamma,so}, \\ &A = [(\omega_n + \Gamma_{\Gamma K})(\omega_n + \Gamma_{\Gamma K} + \tau^{-1}_{\Gamma,so}) + h^2_{c2}]^{-1}. \end{aligned} \tag{6.14}$$

Equation (6.13) can be used to numerically calculate the $h_{c2}(T)$ diagram. We chose the notation so that Eq. (6.13) resembles the results from the single-band scenario, Eq. (5.11). Namely, in the absence of interband scattering, we have $\tilde{\omega}_n \to \omega_n$, $\tilde{\tau}^{-1}_{iv} \to \tau^{-1}_{iv}$, $T^*_c \to T_c$ and $\tilde{\tau}^{-1}_{\Gamma,so} \to 0$, and Eq. (6.13) reduces to Eq. (5.11).

In Fig. 6.4 (a) we plot the $h_{c2}(T)$ curve for various strengths of interband disorder, taking strong SOC of $\Delta_{so} = 100T_c$. For simplicity, we take $\Gamma_{K\Gamma} = \Gamma_{\Gamma K}$. For comparison, in Fig. 6.4 (b), we plot the $h_{c2}(T)$ diagram for a single-band system with intervalley scattering of the same strength. Similarly to intervalley scattering (see Chapter 5), interband scattering also suppresses the H_{c2} divergence at zero temperature. The mechanism of suppression is the inverse proximity effect in the K-band. Namely, proximity-induced superconductivity in the Γ band is not protected by strong Ising SOC from the in-plane magnetic fields. Due to interband scattering, the Cooper pairs from the K-band can "leak" into the Γ band, where they are easily broken by the magnetic field. As seen from Fig. 6.4, this process is very efficient is suppressing superconductivity, much more so than intervalley scattering.

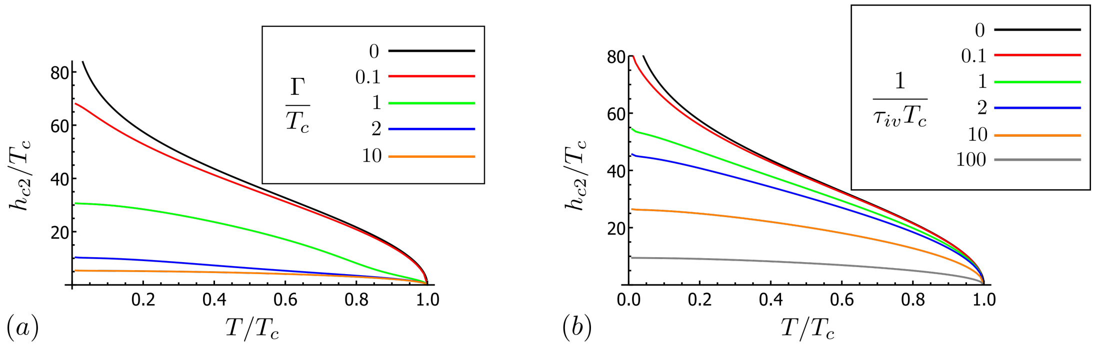

Figure 6.4: Upper critical field as a function of temperature at $\Delta_{so} = 100T_c$: (a) for various strengths of interband disorder, taking $\tau_{iv}^{-1} = \tau_{\Gamma,so}^{-1} = 0$; (b) for various strengths of intervalley disorder. For simplicity, we assume $\nu_{0K} = \nu_{0\Gamma}$, such that $\Gamma_{K\Gamma} = \Gamma_{\Gamma K} = \Gamma$.

The green curve in Fig. 6.4 showcases an important feature of multiband superconductivity, as the $h_{c2}(T)$ curve in this case has qualitatively different behaviors at high and low fields. Namely, at low fields, superconductivity exists in both bands. However, after some threshold field, superconductivity in the Γ-band gets suppressed, and this band transitions to the normal state. As the field is further increased, only the K-band contributes to superconductivity, resulting in a qualitatively different behavior compared to low fields. For stronger interband disorder (blue and orange curves in Fig. 6.4) this feature is absent due to the higher degree of band-mixing.

In Fig. 6.5 (a), we examine how SOC in the Γ-band affects the upper critical field. It "protects" the superconductivity in the Γ-band, making it more robust to applied magnetic fields. First, let us consider the case $\tau_{\Gamma,so}^{-1} \ll \Delta_{so}$, where the Γ-band will become normal at some threshold field while the K-band remains superconducting above it. In this case, $\tau_{\Gamma,so}^{-1}$ only modifies the low-field part of the $h_{c2}(T)$ diagram. SOC in the Γ-band has a more significant impact on the upper critical field only if it is comparable to the SOC in the K-band ($\tau_{so,\Gamma}^{-1} \sim \Delta_{so}$), which is not expected in realistic TMDs.

In Fig. 6.5 (b), we examine how intervalley scattering affects h_{c2} in the multiband Ising superconductor. Unsurprisingly, its main effect is an additional suppression of h_{c2}.

Experimental measurements of the upper critical field in monolayer and few-layer samples of NbSe$_2$ [14,15,58] and TaS$_2$ [15] can be explained by taking high Ising SOC as expected for these systems (of the order magnitude $\Delta_{so}^K \sim 100T_c$), and weak interband disorder ($\Gamma_{K\Gamma}, \Gamma_{\Gamma K} \sim T_c$). This situation corresponds to the blue curve in Fig. 6.4

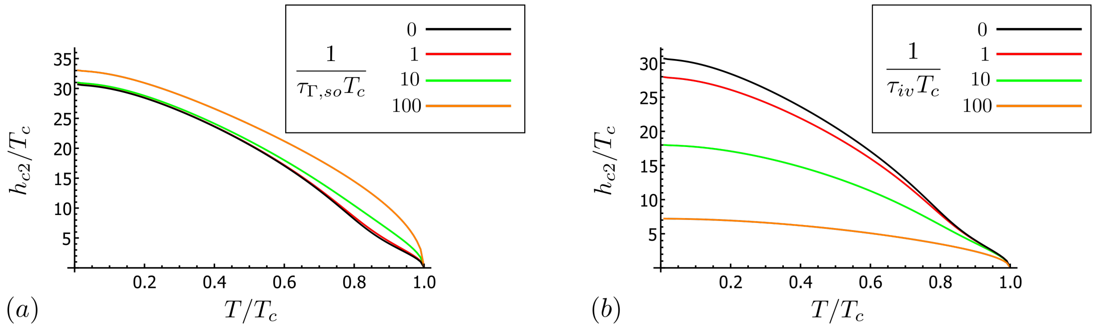

Figure 6.5: Upper critical field as a function of temperature at $\Delta_{so} = 100T_c$, $\Gamma_{K\Gamma} = \Gamma_{\Gamma K} = T_c$: (a) for various values of SOC in the Γ-band, taking $\tau_{iv}^{-1} = 0$; (b) for various values of intervalley scattering, taking $\tau_{\Gamma,so}^{-1} = 0$.

(a). In order to obtain similar h_{c2} within the single-band model, an unrealistically large intervalley scattering would be needed ($\tau_{iv}^{-1} \sim \Delta_{so}$), as illustrated by the gray curve in Fig. 6.4 (b). In Fig. 6.6, we show that our multiband model is in a good agreement with the h_{c2} measurements from Ref. [14].

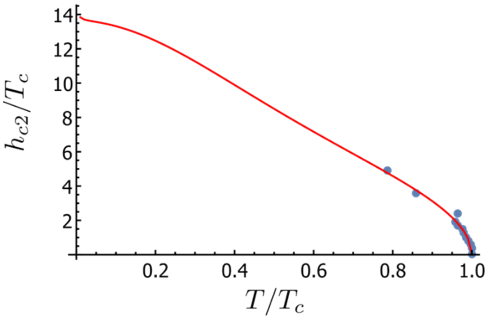

Figure 6.6: Comparison of experimental data from Ref. [14] (blue dots) and our multiband model for the parameter combination: $\Delta_{so} = 150T_c$ (compatible with values extracted from first-principles, see Table 2.1), $\Gamma_{K\Gamma} = \Gamma_{\Gamma K} = \tau_{iv}^{-1} = 2T_c$, $\tau_{\Gamma,so}^{-1} = 3.5T_c$.

Note that these measurements of $h_{c2}(T)$ did not find a qualitatively different behavior at high and low fields [like in the green curve in Fig. 6.4 (a)]. Within our model, the absence of this feature suggests either strong-enough interband scattering [as illustrated in Fig. 6.4 (a)] or strong-enough SOC in the Γ-band [as illustrated in Fig. 6.5 (a)].

6.4 Density of states

In this section, we will examine the evolution of the density of states in the superconducting state with applied in-plane field. As in the previous text, we will make two realistic assumptions: strong SOC in the K-band, $\Delta_{so} \gg T_c, \tau_{iv}^{-1}, \tau_{\Gamma,so}^{-1}, \Gamma_{K\Gamma}, \Gamma_{\Gamma K}$, and weak interband disorder $\Gamma_{K\Gamma}, \Gamma_{\Gamma K} \sim T_c$. Under these assumptions, the Eilenberger equations (6.1) and (6.2) become

$$\begin{aligned}\Delta_K(\epsilon) &= \frac{\Delta_{so}}{\rho}\frac{\Delta + \frac{\Gamma_{K\Gamma}}{2}\sum_{\pm}\frac{\Delta_\Gamma^\pm(\epsilon)}{\sqrt{[\Delta_\Gamma^\pm(\epsilon)]^2-\epsilon^2}}}{1+\sum_{\pm}\frac{\Gamma_{K\Gamma}}{2\sqrt{[\Delta_\Gamma^\pm(\epsilon)]^2-\epsilon^2}} + \frac{h^2}{\rho^2\tau_{iv}}\frac{1}{\sqrt{\Delta_K^2(\epsilon)-\epsilon^2}}}, \\ \Delta_\Gamma^\pm(\epsilon) &= \frac{\frac{\Delta_{so}}{\rho}\frac{\Gamma_{\Gamma K}\Delta_K(\epsilon)}{\sqrt{\Delta_K^2(\epsilon)-\epsilon^2}} + \frac{1}{2\tau_{\Gamma,so}}\frac{\Delta_\Gamma^\mp(\epsilon)}{\sqrt{[\Delta_\Gamma^\mp(\epsilon)]^2-\epsilon^2}}}{1 \mp \frac{h}{\epsilon} + \frac{\Gamma_{\Gamma K}}{\sqrt{\Delta_K^2(\epsilon)-\epsilon^2}} + \frac{1}{2\tau_{\Gamma,so}}\frac{1}{\sqrt{[\Delta_\Gamma^\mp(\epsilon)]^2-\epsilon^2}}}.\end{aligned} \tag{6.15}$$

where $\rho = \sqrt{\Delta_{so}^2 + h^2}$. Here $\Delta_K(\epsilon)$ and $\Delta_\Gamma^\pm(\epsilon)$ are effective energy dependent order parameters in the K- and Γ-band, respectively. The two signs in $\Delta_\Gamma^\pm(\epsilon)$ denote spin-up (+) and spin-down (-) electrons of the Γ-band. The derivation of Eq. (6.15) is given in Appendix C.2. The density of states is given as

$$\nu(\epsilon) = N_K\nu_{0K}\Re\frac{|\epsilon|}{\sqrt{\epsilon^2-\Delta_K^2(\epsilon)}} + \frac{1}{2}N_\Gamma\nu_{0\Gamma}\sum_{\pm}\Re\frac{|\epsilon|}{\sqrt{\epsilon^2-[\Delta_\Gamma^\pm(\epsilon)]^2}}. \tag{6.16}$$

Here, the factor 1/2 is required to account for the contribution of the single spin species of the Γ-band to the DoS. Equation (6.16) reduces to Eq. (6.6) when there is no spin-splitting in the Γ-band ($\Delta_\Gamma^+ = \Delta_\Gamma^-$).

In Fig. 6.7 we plot the DoS using Eqs. (6.15) and (6.16), taking strong SOC $\Delta_{so} = 100T_c$ and weak interband scattering $\Gamma_{K\Gamma} = \Gamma_{\Gamma K} = T_c$. In Fig. 6.7 (a) we consider the case $\tau_{iv}^{-1} = \tau_{\Gamma,so}^{-1} = 0$. In Figs. 6.7 (b) and 6.7 (c), we examine how SOC in the Γ-band and intervalley scattering modify this case, respectively.

In Fig. 6.7 (a), upon increasing the Zeeman field, the quasiparticle peak in the Γ-band first becomes spin-split (red curve), followed by complete suppression of superconductivity (green curve). In the K-band, this manifests itself in a suppression of the smaller (induced) gap in the quasiparticle spectrum. Further increasing the magnetic field results in a suppression of the larger (intrinsic) gap.

In Fig. 6.7 (b), due to the SOC of the Γ-band, applying an in-plane Zeeman field does not cause spin-splitting of the DoS, and the Γ-band remains superconducting up to higher fields compared to the previous case. The high field behavior in the K-band remains essentially unchanged compared to Fig. 6.7 (a).

The behavior of the DoS in 6.7 (c) is qualitatively very similar to Fig. 6.7 (a), the main difference being that total suppression of superconductivity in the K-band occurs at lower fields due to the effect of intervalley scattering.

6.5 Regime of strong SOC in both bands

The expression for the linearized gap equation, Eq. (6.13), and for the density of states, Eqs. (6.15) and (6.16), significantly simplify if SOC is sufficiently strong in both the K- and the Γ-band, if we assume $\Delta_{so}^2\tau_{iv}, \tau_{\Gamma,so}^{-1} \gg T_c, \Gamma_{K\Gamma}, \Gamma_{\Gamma K}$, and either $h/\Delta_{so} \ll 1$ or $\tau_{iv}^{-1} \gg T_c, \Gamma_{K\Gamma}, \Gamma_{\Gamma K}$. Under these assumptions, the effect of magnetic field is captured by the Abrikosov-Gor'kov depairing parameters

$$\alpha^K(h) = \frac{h^2}{\Delta_{so}^2\tau_{iv}}, \qquad \alpha^\Gamma(h) = h^2\tau_{\Gamma,so}. \tag{6.17}$$

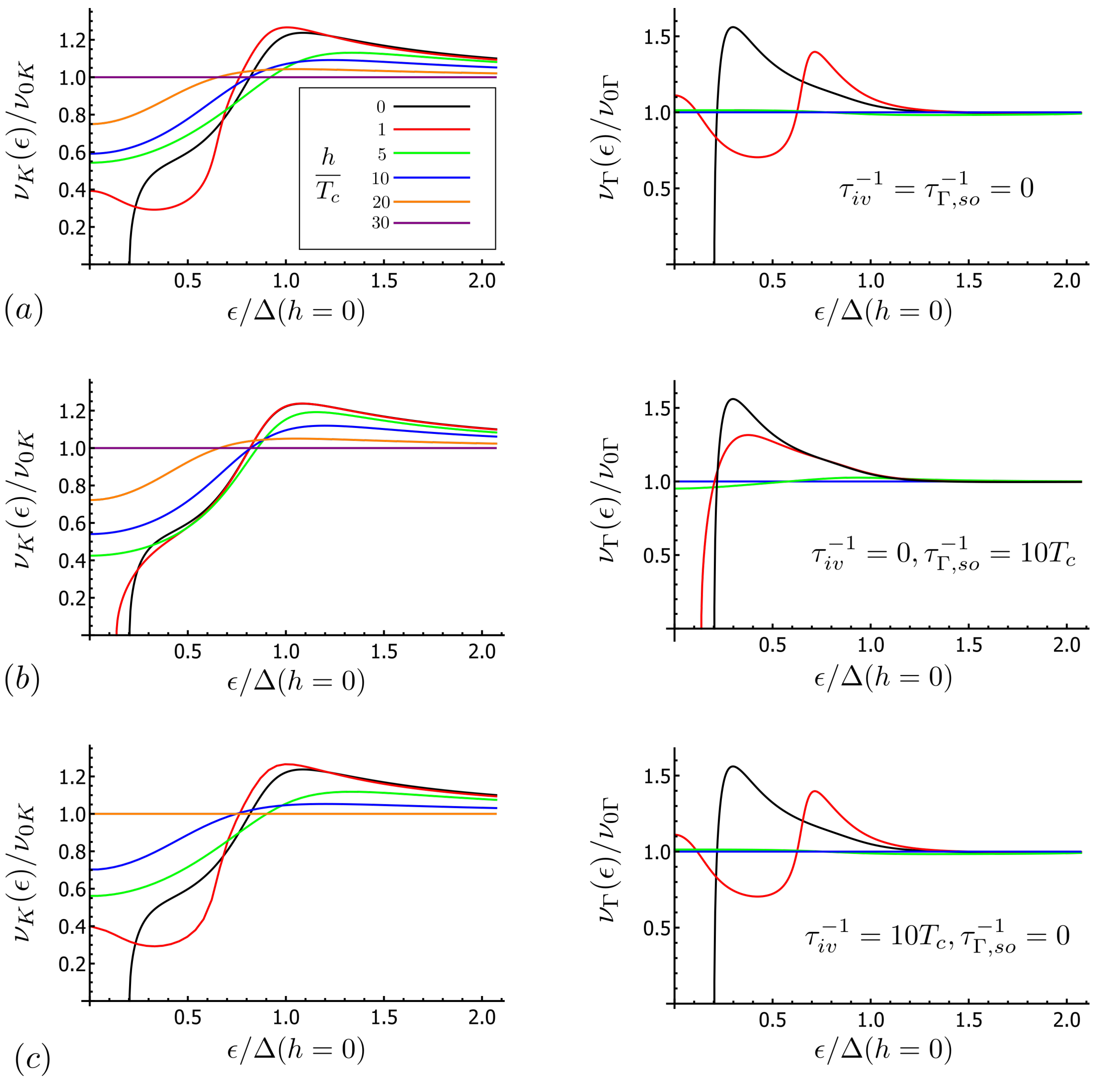

Figure 6.7: Density of states in the superconducting state for multiband Ising superconductors at $\Delta_{so} = 100T_c$, $\Gamma_{K\Gamma} = \Gamma_{\Gamma K} = T_c$, for various in-plane magnetic fields. Panels on the left-hand (right-hand) side correspond to the K-band (Γ-band). Parameters used are: (a) $\tau_{iv}^{-1} = \tau_{\Gamma,so}^{-1} = 0$ ($h_{c2} \approx 27T_c$); (b) $\tau_{iv}^{-1} = 0, \tau_{\Gamma,so}^{-1} = 10T_c$ ($h_{c2} \approx 27T_c$); (c) $\tau_{iv}^{-1} = 10T_c, \tau_{\Gamma,so}^{-1} = 0$ ($h_{c2} \approx 16T_c$). The graphs were plotted using Eqs. (6.15) and (6.16), where the gap Δ was calculated self-consistently for the given parameter combination at $T = 0.3T_c$. The relatively high temperature was chosen for numerical convenience, as the self-consistent calculation of Δ converges quicker, while the qualitative behavior remains the same compared to lower temperatures.

The linearized gap equation can now be written as

$$\ln\frac{T}{T_c^*} = 2\pi T \sum_{\omega_n} \left[\frac{1}{\omega_n + \alpha^K(h_{c2}) + \Gamma_{K\Gamma} - \Gamma_{K\Gamma}\Gamma_{\Gamma K}[\omega_n + \alpha^\Gamma(h_{c2}) + \Gamma_{\Gamma K}]^{-1}} - \frac{1}{\omega_n} \right]. \quad (6.18)$$

Eq. (6.18) can be alternatively expressed in terms of digamma functions ψ, as shown in Appendix C.3. This form allows us to make analytical estimates of h_{c2} in the limits $T \to T_c$ and $T \to 0$ (see Appendix C.3 for detailed derivations).

For temperatures in the vicinity of T_c, taking $\Delta_{so}^2 \tau_{iv} \gg \tau_{\Gamma,so}^{-1}$, which is likely the case in TMDs, and $\Gamma_{K\Gamma}, \Gamma_{\Gamma K} \sim T_c$, we obtain

$$h_{c2} = C\sqrt{\frac{T_c - T}{T_c}}\sqrt{\tau_{\Gamma,so}^{-1} T_c}. \tag{6.19}$$

Here, C is a dimensionless quantity of the order 1, which depends on interband disorder, and is defined in Appendix C.3. On the other hand, close to $T = 0$, assuming that $\Delta_{so}^2 \tau_{iv} \gg \tau_{\Gamma,so}^{-1}$, such that $h_{c2}^2 \tau_{\Gamma,so} \gg T_c$, we have

$$h_{c2}(T = 0) = \sqrt{\left(\frac{\Delta_0^*}{2} - \Gamma_{K\Gamma}\right)\Delta_{so}^2 \tau_{iv}}, \tag{6.20}$$

where $\Delta_0^* = 1.76 T_c^*$. The expressions (6.19) and (6.20) showcase the qualitatively different behavior of h_{c2} in multiband superconductors for temperatures $T \to T_c$ and $T \to 0$, at low and high fields, respectively, as discussed previously in Sec. 6.3. The low-field behavior given in Eq. (6.19) is determined by the Γ-band, as the induced superconductivity diminishes and ultimately disappears as the field is increased, while the K-band remains largely unaffected. By contrast, the high field behavior given in Eq. (6.20) (where the Γ-band is normal) is dominated by the K-band.

Next, we consider the DoS in the regime of strong SOC in both bands, where the effective order parameters from Eq. (6.15) simplify to

$$\Delta_K(\epsilon) = \frac{\Delta + \frac{\Gamma_{K\Gamma}\Delta_\Gamma(\epsilon)}{\sqrt{\Delta_\Gamma^2(\epsilon) - \epsilon^2}}}{1 + \frac{\Gamma_{K\Gamma}}{\sqrt{\Delta_\Gamma^2(\epsilon) - \epsilon^2}} + \frac{\alpha^K(h)}{\sqrt{\Delta_K^2(\epsilon) - \epsilon^2}}}, \qquad \Delta_\Gamma(\epsilon) = \frac{\frac{\Gamma_{\Gamma K}\Delta_K(\epsilon)}{\sqrt{\Delta_K^2(\epsilon) - \epsilon^2}}}{1 + \frac{\Gamma_{\Gamma K}}{\sqrt{\Delta_K^2(\epsilon) - \epsilon^2}} + \frac{\alpha^\Gamma(h)}{\sqrt{\Delta_\Gamma^2(\epsilon) - \epsilon^2}}}. \tag{6.21}$$

The DoS can now be expressed using Eq. (6.16). In this regime, we don't need to distinguish between the two spin species in the Γ-band, in contrast to Eq. (6.15), due to the large SOC that mixes them. Eq. (6.20) has the same form as the so-called Keiser-Zuckermann model [120]. It is a refinement of the McMillan model, developed to describe superconductors in contact with normal metals, where Abrikosov-Gor'kov depairing comes from magnetic impurities.

Eq. (6.21) has been found to be in good agreement with measured quasiparticle spectra of trilayer NbSe$_2$ subjected to low fields ($H < 3.5T$) in Ref. [57], see Fig. 6.8. This study found that the secondary gap in the quasiparticle spectrum gets suppressed by low fields, while the primary gap remained unchanged up to $H = 6.4T$. This corresponds to the parameter regime $\alpha^\Gamma \gg \alpha^K$, consistent with strong SOC in the K-band and weak SOC in the Γ-band.

6.6 Summary

In this Chapter, we have formulated a quasiclassical theory for multiband superconductivity in p-doped TMD monolayers, and studied their behavior in in-plane magnetic fields. We show that weak interband disorder, of the order $\sim T_c$, can account for both the amplitude of h_{c2} and the shape of the density of states measured in these materials.

We are currently collaborating with the experimental group of Marco Aprili and Charis Quay (Laboratoire de Physique des Solides, Paris), and applying the theory developed in this Chapter to explain their measurements of quasiparticle spectra of trilayer NbSe$_2$ subjected to high in-plane fields.

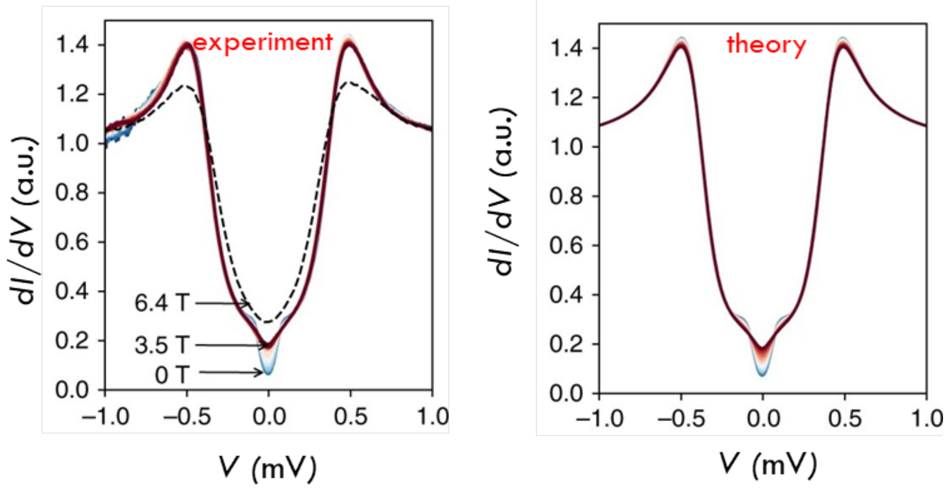

Figure 6.8: Comparison between experimental measurements of the density of states in trilayer $NbSe_2$ (left) and the fit provided by the Keiser-Zuckermann equation (6.21) (right) from Ref. [57]. Parameters of the fit presented in the right panel are: $\Delta_0 = 0.42$ meV, $\Gamma_{K\Gamma} = \Gamma_{\Gamma K} = 0.09$ meV, $\tau^{-1}_{\Gamma,so}$ =0.5 meV and $\Delta^2_{so}\tau_{iv}$ >6.7 meV.

Part II

Interference correction to the conductance in TMDs and graphene/TMD heterostructures

Chapter 7

Weak localization

In Part I, we found that the interplay of Ising SOC and disorder, particularly intervalley and interband scattering, plays a crucial role in explaining the properties of superconducting TMDs. In order to learn more about the role of disorder in these materials, we turn to their normal state. Namely, in Part II of this thesis, we study quantum interference corrections to the conductance, W(A)L in this Chapter and UCF in the next. These phenomena are sensitive to, and provide an independent source of information on SOC, disorder, and Berry phase due to the Dirac-like band structure. Our results also extend to graphene/TMD heterostructures, whose properties are described by the same model as TMDs (see Chapter 3).

In Part II, we will focus only on the physics of $\pm K$ points, meaning that the presented results hold in n-doped TMDs and n-and p-doped graphene/TMD heterostructures, but not in p-doped TMDs, where the Γ-band appears in the spectrum.

Note that the model presented in Chapter 3 is used under different assumptions in Parts I and II. Firstly, and most importantly, in order to carry out analytical calculations in Part II, we need to assume that the diagonal disorder rate τ_0^{-1} is the dominant one, i.e., $\tau^{-1} \approx \tau_0^{-1}$, and to use the diffusive approximation $|\mu| - E_g \gg \tau_0^{-1} \gg \Delta_{so}, h, \lambda, \kappa q_F^2$. This is not the case in Part I, where the presented results hold for any disorder strength and any ratio of intra- and intervalley scattering. Secondly, in Part II, we are able to account for the effect of Rashba SOC, trigonal warping, and non-potential disorder (See Eqs. (3.4) and (3.7)), which was not possible (analytically) in Part I , where the diffusive approximation was not assumed.

In this Chapter, we develop a theory of W(A)L for both TMDs and graphene/TMD heterostructures. These phenomena were recently very actively explored in experiments, as they can reveal information about SOC and disorder, which is of interest for numerous applications of these materials (see Chapters 1 and 2 for more details). In Sec. 7.1, to set the stage, we calculate the classical, Drude conductivity for TMDs and their heterostructures with graphene. In Sec. 7.2, we calculate the Cooperons, which are the main ingreadients for formulating the theory of W(A)L. In Sec. 7.3, we write the general expression for the W(A)L magnetoconductance and the main result of this Chapter, which we then analyze in several regimes of interest for interpreting recent experiments. Finally, we consider the effect of an in-plane Zeeman field in Sec. 7.4, which can be used to distinguish the contributions of different kinds of SOC to the WL magnetoconductance. In Sec. 7.4, we compare our results with recent experiments. The results presented in this Chapter are published in Ref. [25].

7.1 Drude conductivity

In order to describe quantum transport in our system, we will employ the standard diagrammatic technique for disordered systems. In particular, we introduce disorder-averaged, zero-temperature retarded (R) and advanced (A) Green's functions as

$$G^{R,A}_{\mathbf{q}\omega} = \left(\omega - \mathcal{H}_{\mathbf{q}} \pm \frac{i}{2\tau}\right)^{-1}. \tag{7.1}$$

Here, $\mathcal{H}_{\mathbf{q}}$ describes TMDs in the n-doped regime, or graphene/TMD heterostructures in the n- and p-doped regimes, and is given in Eq. (3.4). The self-energy $\pm i/(2\tau)$ is calculated from the self-consistent Born approximation, ω is the frequency, and the inverse scattering time τ^{-1} is given in Eq. (3.11).

In the following, we will assume that the diagonal disorder rate τ_0^{-1} is the dominant one, i.e., $\tau^{-1} \approx \tau_0^{-1}$, and we will use the diffusive approximation $|\mu| - E_g \gg \tau_0^{-1} \gg \Delta_{so}, h, \lambda, \kappa q_F^2$.

The current operator along the x-direction for Dirac materials is given by $J_{\mathbf{q}} = \partial H_{\mathbf{q}}/\partial q_x = v\sigma_x\eta_z$ [121]. Upon projecting to the conduction/valence band, it becomes $\mathcal{J}_{x\mathbf{q}} = v_F \cos\theta$. As the disorder potential in the projected basis becomes anisotropic, the current vertex is renormalized, as illustrated in diagrammatic form in Fig. 7.1 (a). Namely, the bare vertex is dressed by a series of ladder diagrams, known as diffusons. The renormalized vertex is then given as

$$\tilde{\mathcal{J}}_{x\mathbf{q}} = \frac{\tau_{tr}}{\tau_0}\mathcal{J}_{x\mathbf{q}} \quad \text{with} \quad \tau_{tr} = \left(1 + \frac{v^2 q_F^2}{4E_g^2 + v^2 q_F^2}\right)\tau_0. \tag{7.2}$$

Here, we have introduced the transport time τ_{tr}, which takes the value τ_0 at the bottom of the conduction band $\mu \approx E_g$, where the spectrum is parabolic (similarly to conventional metals), and $2\tau_0$ deep in the conduction band $\mu \gg E_g$, where the spectrum is linear (as in graphene) [70]. Within the linear response theory, the Drude conductivity is then given as

$$\sigma = \frac{e^2}{2\pi}\int \frac{d^2\mathbf{p}}{(2\pi)^2}\mathrm{Tr}\left[\tilde{\mathcal{J}}_{x\mathbf{q}} G^R_{\mathbf{q}\omega} \mathcal{J}_{x\mathbf{q}} G^A_{\mathbf{q}\omega}\right] = 4e^2\nu_{0K}D, \tag{7.3}$$

where $D = \frac{1}{2}v_F^2\tau_{tr}$ is the diffusion constant, and the factor 4 originates from spin and valley degeneracy. The corresponding diagram is shown in Fig. 7.1 (b). Derivation of Eqs. (7.2) and (7.3) is presented in Appendix D.1.

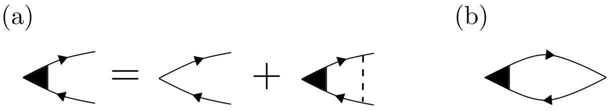

Figure 7.1: (a) Vertex renormalization. (b) Drude conductivity diagram. Solid arrows represent Green's functions, while the dashed lines represent disorder. The upper (lower) branch of the diagrams corresponds to retarded (advanced) Green's functions.

7.2 Cooperons

The interference correction to the Drude conductivity (7.3) can be expressed in terms of Cooperons, $C^{ab,a'b'}_{\alpha\beta,\alpha'\beta'}$, which represent disorder averages of two Green's functions and correspond to maximally crossed diagrams [28]. The Greek indices in the subscript (Latin indices in the superscript) correspond to the spin (valley) degree of freedom and take values ±1. The Cooperons are determined from a system of coupled Bethe-Salpeter equations, as shown in diagrammatic form in Fig. 7.2 (a). Namely,

$$\begin{aligned}C^{ab,a'b'}_{\alpha\beta,\alpha'\beta'}(\theta,\theta';\mathbf{Q}) &= W^{ab,a'b'}_{\alpha\beta,\alpha'\beta'}(\theta,\theta') \\ &+ \int_0^{2\pi}\frac{d\theta''}{2\pi}W^{aa_1,bb_1}_{\alpha\alpha_1,\beta\beta_1}(\theta,\theta'')\Pi^{a_1b_1}_{\alpha_1\beta_1,\alpha_2\beta_2}(\theta'';\mathbf{Q})C^{a_1b_1,a'b'}_{\alpha_2\beta_2,\alpha'\beta'}(\theta'',\theta';\mathbf{Q}). \quad (7.4)\end{aligned}$$

Here, summation over repeated indices is assumed, and we have introduced the disorder correlator W and the polarization operator Π as

$$\begin{aligned}W^{ab,a'b'}_{\alpha\beta,\alpha'\beta'}(\theta,\theta') &= \langle[\mathcal{H}^D_{\mathbf{q}\mathbf{q}'}]^{aa'}_{\alpha\alpha'}[\mathcal{H}^D_{\bar{\mathbf{q}}\bar{\mathbf{q}}'}]^{bb'}_{\beta\beta'}\rangle \qquad \text{and} \\ \Pi^{ab}_{\alpha\beta,\alpha'\beta'}(\theta;\mathbf{Q}) &= \nu_{0K}\int d\xi_{\mathbf{q}}[G^R_{\mathbf{q}\epsilon+\omega}]^a_{\alpha\alpha'}[G^A_{\bar{\mathbf{q}}+\mathbf{Q}\omega}]^b_{\beta\beta'}, \quad (7.5)\end{aligned}$$

respectively. Note that the Green's functions are diagonal in valley space, so the polarization operator only depends on two valley indices. The weak localization correction $\delta\sigma$ can now be expressed in terms of Cooperons as

$$\begin{aligned}\delta\sigma = \frac{e^2}{2\pi}\int\frac{d^2\mathbf{Q}}{(2\pi)^2}&\int_0^{2\pi}\frac{d\,\theta}{2\pi}\frac{d\,\theta'}{2\pi}4\pi\nu_{0K}\tau_0^3 \\ &\times\left[2\pi\delta(\theta-\theta')-2\pi\nu_{0K}\tau_0W^{ab,ab}_{\alpha\beta,\alpha\beta}(\theta,\theta')\right]\tilde{\mathcal{J}}_{x\mathbf{q}}\tilde{\mathcal{J}}_{x\bar{\mathbf{q}}'}C^{ab,ba}_{\alpha\beta,\beta\alpha}(\theta,\bar{\theta}';\mathbf{Q}). \quad (7.6)\end{aligned}$$

Here, the first contribution in the square bracket comes from the bare Hikami box [28] [shown in Fig. 7.2 (b)], while the second one comes from two Hikami boxes dressed by an intravalley impurity line [shown in Fig. 7.2 (c)].

We proceed by solving Eq. (7.4) in the presence of the dominant diagonal scattering only in Sec. 7.2.1, in order to resolve the angular structure of the Cooperons. Next, we include all other types of disorder in Sec. 7.2.2.

7.2.1 Cooperons in the presence of diagonal disorder only

In order to resolve the angular structure of the Cooperons, we will first consider the case where only the diagonal disorder with rate τ_0^{-1} is present. The other types of scattering will not affect this structure, but only introduce additional Cooperon gaps. Furthermore, the angular structure is independent of the spin structure. Therefore, we also neglect the spin structure here, setting Δ_{so} and h to zero. To simplify the notation, spin indices are omitted in this subsection.

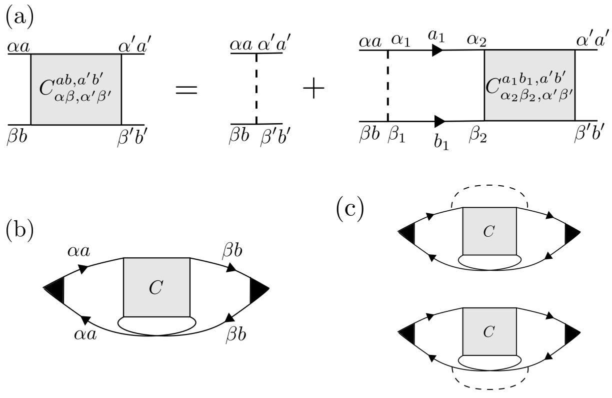

Figure 7.2: (a) Bethe-Salpeter equation for the Cooperons. (b) Bare Hikami box. The Hikami boxes with external lines that are diagonal in spin-space give a dominant contribution to the quantum correction in the diffusive limit. (c) Dressed Hikami boxes. For the definition of diagram elements, see Fig. 7.1. Greek indices in the subscript describe spin, while Latin indices in the superscript describe the valley degree of freedom.

We proceed with this calculation in the same spirit as in Ref. [122]. First, we expand the Cooperons and the disorder correlator in harmonics,

$$\begin{aligned} C^{ab,a'b'}(\theta,\theta';\mathbf{Q}) &= \sum_{n,m=-\infty}^{\infty} C^{ab,a'b'}_{nm}(\mathbf{Q}) e^{-i(n\theta-m\theta')}, \\ W^{ab,a'b'}(\theta,\theta') &= \sum_{n=-\infty}^{\infty} W^{ab,a'b'}_{n} e^{-in(\theta-\theta')}. \end{aligned} \tag{7.7}$$

Furthermore, $a=a'$ and $b=b'$ in the absence of intervalley scattering. The only Cooperon that enters the interference correction (7.6) is the intravalley one, $C^{aa,aa}(\theta,\theta')$. From Eqs. (7.4) and (7.7), we get a system of coupled equations for its harmonics, whose solution yields

$$\begin{aligned} & C^{aa,aa}(\theta,\theta';\mathbf{Q}) = C^{aa,aa}_{00}(\mathbf{Q}) + C^{aa,aa}_{aa}(\mathbf{Q}) e^{-ia(\theta-\theta')} \\ & \text{with} \quad C^{aa,aa}_{ii}(\mathbf{Q}) = \frac{1}{2\pi\nu_{0K}\tau_0^2} \frac{1}{D_i|\mathbf{Q}|^2 - i\omega + \tau_\phi^{-1} + \Gamma_i}. \end{aligned} \tag{7.8}$$

Here, $a=\pm 1$, $\Gamma_0 = \frac{1}{\tau_0}\frac{(\mu-E_g)^2}{(\mu+E_g)^2}$ and $\Gamma_a = \frac{1}{\tau_0}\frac{2E_g^2}{\mu^2-E_g^2}$ are the relevant Cooperon gaps, and $D_0 = \frac{1}{8}v_F^2\tau_0(3+\frac{E_g^2}{\mu^2})$ and $D_a = v_F^2\tau_0\frac{(E_g^2+\mu^2)^2}{(\mu^2-E_g^2)^2}$ are diffusion constants. Furthermore, we introduced the inelastic dephasing rate, τ_ϕ^{-1}. Detailed derivation of Eq. (7.8) is given in Appendix D.2.1.

We see that, in general, both C_{00} and C_{aa} will have a large gap of the order τ_0^{-1} and, thus, will be suppressed in the diffusive limit, except in two special cases. Firstly, Γ_0 vanishes at $\mu = E_g$. Close to the band bottom, for $\mu/E_g - 1 \lesssim 2\sqrt{\tau_0/\tau_\phi}$, one finds $\Gamma_0 \lesssim \tau_\phi^{-1}$. Thus, in this regime, the Cooperon C_{00} is not suppressed. Secondly, Γ_a vanishes for $\mu \to \infty$. Thus, deep in the band, at $\mu/E_g \gtrsim \sqrt{2\tau_\phi/\tau_0}$, one finds $\Gamma_a \lesssim \tau_\phi^{-1}$, and the Cooperon C_{aa} is not suppressed either. Higher-order harmonics, although non-zero, will always have a non-vanishing gap of the order τ_0^{-1} and will be neglected. We can therefore write

$$C^{aa,aa}(\theta,\bar{\theta};\mathbf{Q}) = \frac{\Xi}{2\pi\nu_{0K}\tau_0^2}\frac{1}{D|\mathbf{Q}|^2 - i\omega + \tau_\phi^{-1} + \Gamma_\Xi},$$
$$\text{where } \Xi = \begin{cases} 1, & \frac{\mu}{E_g} - 1 \lesssim 2\sqrt{\frac{\tau_0}{\tau_\phi}}, \\ 0, & 2\sqrt{\frac{\tau_0}{\tau_\phi}} \ll \frac{\mu}{E_g} - 1 \ll \sqrt{\frac{2\tau_\phi}{\tau_0}}, \\ -1, & \frac{\mu}{E_g} \gtrsim \sqrt{\frac{2\tau_\phi}{\tau_0}}, \end{cases} \tag{7.9}$$

and $\Gamma_1 = \tau_0^{-1}[vq_F/(2\mu)]^4$, $\Gamma_{-1} = 2\tau_0^{-1}(E_g/\mu)^2$. Note that the diffusion constants D_0 and D_a reduce to D, introduced in Eq. (7.3), in the relevant limits.

Upon inserting Eq. (7.9) into Eq. (7.6), we obtain the quantum correction for massive Dirac fermion systems in the presence of smooth disorder, consistent with Ref. [122]. Its behavior is governed by the doping-dependent coefficient Ξ: for a large Dirac mass E_g ($\Xi = 1$), we get WL, whereas in the massless system ($\Xi = -1$), we get WAL. The quantum correction vanishes in the intermediate mass regime. This can be reinterpreted [122] in terms of the Berry phase of a massive Dirac material given as $\varphi_B = \pi(1 - E_g/\mu)$, which introduces no phase shift to the electron interference in the large mass limit (leading to WL), and a shift of π for massless systems (leading to WAL).

Next, we will find the intervalley Cooperon $C^{a\bar{a},a\bar{a}}(\theta,\theta')$. Note that it does not enter the quantum correction (7.6), but it is useful to resolve its angular structure for later use. We find that the only harmonic that is not gapped is C_{00}, and we can write

$$C^{a\bar{a},a\bar{a}}(\theta,\theta';\mathbf{Q}) = C_{00}^{a\bar{a},a\bar{a}}(\mathbf{Q}) = \frac{1}{2\pi\nu_{0K}\tau_0^2}\frac{1}{D|\mathbf{Q}|^2 - i\omega + \tau_\phi^{-1}}. \tag{7.10}$$

Detailed derivation of Eq. (7.10) is presented in Appendix D.2.2.

7.2.2 Cooperons in the presence of all disorder terms

We proceed to solve the Cooperon equation (7.4) in the presence of all disorder terms. Additional intervalley Cooperons of the form $C^{a\bar{a},\bar{a}a}$ can now exist. Since they are coupled to $C^{a\bar{a},a\bar{a}}$ via intervalley scattering, which does not introduce additional angular dependence, they will also be angularly-independent. Using Eqs. (7.9) and (7.10), we can write for all Cooperons

$$\begin{aligned} C^{ab,a'b'}(\Xi;\mathbf{Q}) &= [C_{00}^{aa,aa}(\mathbf{Q})\delta_{\Xi,1} + C_{aa}^{aa,aa}(\mathbf{Q})\delta_{\Xi,-1}]\delta_{aa'}\delta_{bb'}\delta_{ab} + C_{00}^{a\bar{a},b\bar{b}}(\mathbf{Q})\delta_{a\bar{b}}\delta_{a'\bar{b}'}, \\ W^{ab,a'b'}(\Xi) &= [W_0^{aa,aa}\delta_{\Xi,1} + W_a^{aa,aa}\delta_{\Xi,-1}]\delta_{aa'}\delta_{bb'}\delta_{ab} + W_0^{a\bar{a},b\bar{b}}\delta_{a\bar{b}}\delta_{a'\bar{b}'}. \end{aligned} \tag{7.11}$$

We explicitly write the components of the disorder correlator W from Eq. (7.11) in Appendix D.2.3. Eq. (7.4) can now be written in a simpler, angularly-independent form,

$$C_{\alpha\beta,\alpha'\beta'}^{ab,a'b'}(\Xi;\mathbf{Q}) = W_{\alpha\beta,\alpha'\beta'}^{ab,a'b'}(\Xi) + W_{\alpha\alpha_1,\beta\beta_1}^{aa_1,bb_1}(\Xi)\Pi_{\alpha_1\beta_1,\alpha_2\beta_2}^{a_1b_1}(\mathbf{Q})C_{\alpha_2\beta_2,\alpha'\beta'}^{a_1b_1,a'b'}(\Xi;\mathbf{Q}). \tag{7.12}$$

Using Eq. (7.11), the expression for the inteference correction $\delta\sigma$ (7.6), after solving the integrals over angles, can be written in a simpler manner as

$$\delta\sigma = -\frac{e^2D}{\pi}(2\pi\nu_{0K}\tau_0^2)\int\frac{d^2\mathbf{Q}}{(2\pi)^2}C_{\alpha\beta,\beta\alpha}^{ab,ba}(\Xi,\mathbf{Q})[\Xi\delta_{ab} + \delta_{a\bar{b}}], \tag{7.13}$$

where summation over repeated indices is assumed.

Next, we employ a transformation to the singlet-triplet basis [72] in spin and valley space,

$$M_{ss'}^{ll'} = \frac{1}{4}[s_y s_s]_{\alpha\beta}[\eta_x\eta_l]^{ab} M_{\alpha\beta,\alpha'\beta'}^{ab,a'b'}[s_{s'}s_y]_{\beta'\alpha'}[\eta_{l'}\eta_x]^{b'a'}, \tag{7.14}$$

where indices $s, s' = 0$ and $l, l' = 0$ correspond to spin- and valley-singlet Cooperon modes, respectively, while $s, s' = x, y, z$ and $l, l' = x, y, z$ correspond to spin- and valley-triplet modes. Here, the operator M can stand for a Cooperon (C), disorder correlator (W), or a polarization operator (Π). The disorder correlator is diagonal in the singlet-triplet space, $W_{ss'}^{ll'}(\Xi) = W_s^l(\Xi)\delta_{ss'}\delta_{ll'}$, and the Cooperon equation (7.12) after the transformation becomes

$$C_{ss'}^{ll'}(\Xi;\mathbf{Q}) = W_s^l(\Xi)\delta_{ss'}\delta_{ll'} + W_s^l(\Xi)\Pi_{ss_1}^{ll_1}(\mathbf{Q})C_{s_1s'}^{l_1l'}(\Xi;\mathbf{Q}). \tag{7.15}$$

The quantum correction involves only the diagonal Cooperons $C_{ss}^{ll} \equiv C_s^l$. Note that triplets modes C_s^x and C_s^y are related to the intravalley Cooperons, while the valley-singlet C_s^0 and triplet C_s^z are related to intervalley ones. Finally, the interference correction, Eq. (7.13), in the new basis has the form

$$\delta\sigma = -\frac{e^2D}{\pi}(2\pi\nu_{0K}\tau_0^2)\int\frac{d^2\mathbf{Q}}{(2\pi)^2}\sum_s c_s\left[\sum_{l=0,z}c^lC_s^l(\Xi;\mathbf{Q}) + \Xi\sum_{l=x,y}c^lC_s^l(\Xi;\mathbf{Q})\right], \tag{7.16}$$

where $c_s = -1, 1, 1, 1$ and $c^l = 1, 1, 1, -1$ for $s, l = 0, x, y, z$. Eq. (7.16) generalizes similar expressions from Refs. [72] and [23], which are valid at $\Xi = -1$ and $\Xi = 1$, respectively. In Appendix D.3, we present derivation of Eqs. (7.15) and (7.16), as well as explicit forms of the polarization operator Π and the disorder correlator W in the singlet-triplet basis.

The diagonal Cooperon modes C_s^l, necessary to compute $\delta\sigma$, are determined by solving Eq. (7.15). Due to the spin-splitting described by Δ_{so} and h, the polarization operator $\Pi_{ss'}^{ll'}(\mathbf{Q})$ is not diagonal in the singlet-triplet space. As a consequence, some Cooperon modes are coupled. As will be discussed in the further text, the coupling of different Cooperon modes by the spin-splitting fields suppresses them. In a physical sense, Cooperons coupled by the fields describe interference of electrons coming from two spin-split bands, which is suppressed by the energy difference of the electrons. On the other hand, interference of electrons in degenerate bands is described by the non-coupled Cooperons. Note that momentum-dependent parts of the Hamiltonian (3.4), such as Rashba SOC and trigonal warping, do not cause coupling of different Cooperon modes in the diffusive limit, but only enter their gaps.

a. Non-coupled Cooperon modes. First, we solve the Cooperons that are not coupled by the Ising SOC or the in-plane field, with the indices $(s, l) = (y, x), (y, y), (z, 0), (z, z)$. They are given by

$$C_s^l = \frac{1}{2\pi\nu_{0K}\tau_0^2}\frac{1}{\mathcal{P}_s^l}, \tag{7.17}$$

(see Appendix D.4 for derivation). Here, we introduced $\mathcal{P}_s^l = D|\mathbf{Q}|^2 - i\omega + \tau_\phi^{-1} + \Gamma_s^l$, where the Cooperon gaps Γ_s^l are specified in Table 7.1. Because the intravalley Cooperons have different angular dependence in the two extreme limits of Eq. (7.9), their gaps Γ_s^x and Γ_s^y will also depend on the relevant limit (right-hand side of Table 7.1). Intervalley

Cooperons, on the other hand, do not depend on angles and chemical potential and have the same gaps for any μ (left-hand side of Table 7.1).

The Cooperon gaps contain the scattering rates originating from the phenomenological disorder potential (3.9). Their estimates, listed in Table 3.1, are inversely proportional to the scattering times τ_0 and τ_{iv}. These rates are therefore induced and reinforced by disorder, and behave similarly to the Elliott-Yafet spin relaxation mechanism [123, 124]. This includes the well-known scattering rate due to the Kane-Mele SOC [72], captured by $\tau_{z,e}^{-1} \propto \tau_0^{-1}(\frac{\Delta_{KM} v^2 q_F^2}{\mu^3})^2$ (see Table 3.1). Additionally, scattering rates that are proportional to the potential scattering time τ_0 also enter the gaps:

$$\tau_{BR}^{-1} = 2\left(\frac{\lambda v q_F}{\mu}\right)^2 \tau_{tr}, \quad \tau_W^{-1} = 2\left(\frac{\kappa v q_F^3}{\mu}\right)^2 \tau_0. \tag{7.18}$$

They are related with Rashba SOC and trigonal warping, respectively. These rates appear since electrons, due to the details of the band structure, acquire an additional phase upon propagation in-between two scattering events. This effect is suppressed by disorder. The first rate in Eq. (7.18) is associated with the Dyakonov-Perel [125] spin relaxation mechanism. The second rate describes the suppression of intravalley Cooperons due to the breaking of rotational symmetry by trigonal warping, as discussed in Ref. [70].

b. Coupled Cooperon modes. Next, we address the coupled Cooperon modes. The effect of the in-plane Zeeman field h applied along the x-direction is such that it couples the spin-singlet C_0^l and spin-triplet C_x^l Cooperons, as discussed for conventional metals [126]. Ising SOC behaves similarly to an effective Zeeman field in z-direction, but acts differently from the true Zeeman field as it does not break the time-reversal symmetry, and therefore does not affect the spin- and valley-singlet C_0^0, which is protected by this symmetry. It couples the Cooperons $C_x^{0(z)}$ with $C_y^{z(0)}$, and $C_0^{x(y)}$ with $C_z^{y(x)}$, as discussed in Ref. [23]. The equations for all the coupled Cooperon modes can be compactly written in a matrix form

$$\begin{pmatrix} \mathcal{P}_0^{x(y)} & \mp 2\Delta_{so} & -2ih \\ \pm 2\Delta_{so} & \mathcal{P}_z^{y(x)} & 0 \\ -2ih & 0 & \mathcal{P}_x^{x(y)} \end{pmatrix} \begin{pmatrix} C_{00}^{xx(yy)} & C_{0z}^{xy(yx)} & C_{0x}^{xx(yy)} \\ C_{z0}^{yx(xy)} & C_{zz}^{yy(xx)} & C_{zx}^{yx(xy)} \\ C_{x0}^{xx(yy)} & C_{xz}^{xy(yx)} & C_{xx}^{xx(yy)} \end{pmatrix} = \frac{1}{2\pi\nu_{0K}\tau_0^2},$$

$$\begin{pmatrix} \mathcal{P}_x^{0(z)} & -2\Delta_{so} & -2ih \\ 2\Delta_{so} & \mathcal{P}_y^{z(0)} & 0 \\ -2ih & 0 & \mathcal{P}_0^{0(z)} \end{pmatrix} \begin{pmatrix} C_{xx}^{00(zz)} & C_{xy}^{0z(z0)} & C_{x0}^{00(zz)} \\ C_{yx}^{z0(0z)} & C_{yy}^{zz(00)} & C_{y0}^{z0(0z)} \\ C_{0x}^{00(zz)} & C_{0y}^{0z(z0)} & C_{00}^{00(zz)} \end{pmatrix} = \frac{1}{2\pi\nu_{0K}\tau_0^2}, \tag{7.19}$$

(see Appendix D.4 for derivation). Eq. (7.19) summarizes 4 matrix equations, each involving 3 coupled modes. Since the Green's functions are diagonal in valley space, the equations for intra- and intervalley Cooperons are decoupled. This can be seen in Eq. (7.19), where the left-hand (right-hand) side describes matrix equations for intravalley (intervalley) Cooperon modes.

Relaxation gaps for C^0 and C^z	Relaxation gaps for C^x and C^y at $\Xi = -1$
$\Gamma^0_0 = 0$	$\Gamma^x_x = \Gamma^x_y = \Gamma^y_x = \Gamma^y_y = \tau_*^{-1} + 2\tau_{z,e}^{-1} + \tau_{z,o}^{-1} + \tau_{zv,o}^{-1} + \tau_{BR}^{-1}$
$\Gamma^0_x = \Gamma^0_y = 2\tau_{z,e}^{-1} + \tau_{z,o}^{-1} + 2\tau_{zv,e}^{-1} + \tau_{zv,o}^{-1} + 2\tau_{iv,e}^{-1} + \tau_{iv,o}^{-1} + \tau_{BR}^{-1} = \tau_s^{-1}$	$\Gamma^x_0 = \Gamma^y_0 = \tau_*^{-1} + 2\tau_{zv,e}^{-1} + 2\tau_{zv,o}^{-1}$
$\Gamma^0_z = 2\tau_{z,o}^{-1} + 2\tau_{zv,o}^{-1} + 2\tau_{iv,o}^{-1} + 2\tau_{BR}^{-1} = 2\tau_{asy}^{-1}$	$\Gamma^x_z = \Gamma^y_z = \tau_*^{-1} + 2\tau_{z,o}^{-1} + 2\tau_{zv,e}{}^{-1} + 2\tau_{BR}^{-1}$
$\Gamma^z_0 = 2\tau_{iv}^{-1} + 2\tau_{iv,e}^{-1} + 2\tau_{iv,o}^{-1}$	Relaxation gaps for C^x and C^y at $\Xi = 1$
$\Gamma^z_x = \Gamma^z_y = 2\tau_{iv}^{-1} + 2\tau_{z,e}^{-1} + \tau_{z,o}^{-1} + 2\tau_{zv,e}^{-1} + \tau_{zv,o}^{-1} + \tau_{iv,o}^{-1} + \tau_{BR}^{-1}$	$\Gamma^x_x = \Gamma^x_y = \Gamma^y_x = \Gamma^y_y = \tau_{**}^{-1} + \tau_{z,o2}^{-1} + \tau_{zv,o}^{-1} + \tau_{BR}^{-1}$
$\Gamma^z_z = 2\tau_{iv}^{-1} + 2\tau_{z,o}^{-1} + 2\tau_{zv,o}^{-1} + 2\tau_{iv,e}^{-1} + 2\tau_{BR}^{-1}$	$\Gamma^x_0 = \Gamma^y_0 = \tau_{**}^{-1} + 2\tau_{z,e2}^{-1} + 2\tau_{z,o2}^{-1} + 2\tau_{zv,e}^{-1} + 2\tau_{zv,o}^{-1}$
	$\Gamma^x_z = \Gamma^y_z = \tau_{**}^{-1} + 2\tau_{z,e2}^{-1} + 2\tau_{zv,e}^{-1} + 2\tau_{BR}^{-1}$
$\tau_*^{-1} = \tau_{iv}^{-1} + 2\tau_z^{-1} + \tau_{iv,e}^{-1} + \tau_{iv,o}^{-1} + \tau_W^{-1} + \frac{2}{\tau_0}\frac{E_g^2}{\mu^2}$	
$\tau_{**}^{-1} = \tau_{iv}^{-1} + \tau_{z1}^{-1} + \tau_{z,e1}^{-1} + \tau_{z,o1}^{-1} + \tau_{iv,e}^{-1} + \tau_{iv,o}^{-1} + \tau_W^{-1} + \frac{1}{16\tau_0}\frac{v^4 q_F^4}{\mu^4}$	

Table 7.1: Left: Relaxation gaps Γ^l_s for intervalley Cooperons, where indices s and l denote spin and valley, respectively. There are 8 intervalley Cooperons. The time-reversal symmetry sets the gap Γ^0_0 to zero, while the $x - y$ symmetry imposes equality of all x and y spin-triplet gaps. As a result, there are only 5 independent gaps. The scattering rates τ_{asy}^{-1} and $\tau_s^{-1} = \tau_{sym}^{-1} + \tau_{asy}^{-1}$, related to the valley-singlet gaps Γ^0_i $(i = x, y, z)$, are introduced in Eqs. (7.26) and (7.27). Right: Relaxation rates for intravalley Cooperons, which depend on the chemical potential, captured by the coefficient Ξ. In each regime, there are 8 intravalley Cooperons. $x - y$ symmetry imposes equality of all x and y triplet gaps, in both spin and valley space. As a result, there are only 3 independent gaps. Since at $\Xi = 0$ intravalley Cooperons do not contribute to the quantum correction, the related gaps are not included in the table. For a definition of the different scattering rates, see Table 3.1.

7.3 Interference-induced magnetoconductance

After inverting the matrices in Eq. (7.19), we obtain all Cooperon modes. Combining them with Eq. (7.16), and introducing the conductance quantum $\sigma_0 = e^2/(2\pi^2\hbar)$, we arrive at the expression for the interference correction

$$\begin{aligned}\delta\sigma = \; 2\pi\sigma_0 D\int\frac{d^2\mathbf{Q}}{(2\pi)^2}\Bigg[-\Xi\Bigg(\frac{1}{\mathcal{P}^x_y}+\frac{1}{\mathcal{P}^y_y}+\mathcal{A}\left(\begin{smallmatrix} y & x & x\\ z, & x, & 0\end{smallmatrix}\right)+\mathcal{A}\left(\begin{smallmatrix} x & y & y\\ z, & x, & 0\end{smallmatrix}\right)\Bigg)\\ -\frac{1}{\mathcal{P}^0_z}+\frac{1}{\mathcal{P}^z_z}+\mathcal{A}\left(\begin{smallmatrix} z & 0 & 0\\ y, & 0, & x\end{smallmatrix}\right)-\mathcal{A}\left(\begin{smallmatrix} 0 & z & z\\ y, & 0, & x\end{smallmatrix}\right)\Bigg],\end{aligned} \tag{7.20}$$

where

$$\mathcal{A}\left(\begin{smallmatrix} l_1 & l_2 & l_3\\ s_1, & s_2, & s_3\end{smallmatrix}\right) = 2\pi\nu_{0K}\tau_0^2(C^{l_1}_{s_1}+C^{l_2}_{s_2}-C^{l_3}_{s_3}) = \frac{-\mathcal{P}^{l_1}_{s_1}\mathcal{P}^{l_2}_{s_2}+\mathcal{P}^{l_3}_{s_3}\mathcal{P}^{l_1}_{s_1}+4h^2+\mathcal{P}^{l_2}_{s_2}\mathcal{P}^{l_3}_{s_3}+4\Delta^2_{so}}{\mathcal{P}^{l_1}_{s_1}\mathcal{P}^{l_2}_{s_2}\mathcal{P}^{l_3}_{s_3}+4h^2\mathcal{P}^{l_1}_{s_1}+4\Delta^2_{so}\mathcal{P}^{l_2}_{s_2}}. \tag{7.21}$$

Here, each $\mathcal{A}$ accounts for one set of coupled Cooperons, that is, one matrix equation from Eq. (7.19).

The above equation is the main result of this Chapter. It is readily evaluated analytically in the absence of the in-plane Zeeman field. The divergent integral over momenta in Eq. (7.20) can be handled by introducing an upper cutoff associated with the inverse mean free path $l^{-1} = \sqrt{D\tau_0}$, which is the smallest length scale in our system. At $h = 0$, we then obtain

$$\begin{aligned}\frac{\delta\sigma}{\sigma_0} = -2\Xi\ln\left(\frac{\tau^{-1}}{\tau_\phi^{-1}+\Gamma^x_x}\right)-\frac{1}{2}\ln\left(\frac{\tau^{-1}}{\tau_\phi^{-1}+\Gamma^0_z}\right)+\frac{1}{2}\ln\left(\frac{\tau^{-1}}{\tau_\phi^{-1}}\right)-\frac{1}{2}\ln\left(\frac{\tau^{-1}}{\tau_\phi^{-1}+\Gamma^z_0}\right)\\ +\frac{1}{2}\ln\left(\frac{\tau^{-1}}{\tau_\phi^{-1}+\Gamma^z_z}\right)+\gamma_{iv}\sum_{\pm}\pm\ln\left(\frac{\tau^{-1}}{\tau_\phi^{-1}+\Gamma^+_{iv}\pm\frac{\Gamma^-_{iv}}{\gamma_{iv}}}\right)+\Xi\gamma_s\sum_{\pm}\pm\ln\left(\frac{\tau^{-1}}{\tau_\phi^{-1}+\Gamma^+_s\pm\frac{\Gamma^-_s}{\gamma_s}}\right).\end{aligned} \tag{7.22}$$

Here, we have introduced $\Gamma^\pm_{iv} = (\Gamma^z_x \pm \Gamma^0_x)/2$ and $\Gamma^\pm_s = (\Gamma^x_0 \pm \Gamma^x_z)/2$, as well as

$$\gamma_{iv,s} = \frac{1}{\sqrt{1-\left(\frac{2\Delta_{so}}{\Gamma^-_{iv,s}}\right)^2}}. \tag{7.23}$$

The coefficients γ_{iv} and γ_s capture the effect of the spin splitting. They are real if $1 \geq 4\Delta^2_{so}/\Gamma^2_{iv,s}$, and imaginary otherwise. Although the rates $\Gamma^-_{iv,s}$ can be negative and the coefficients $\gamma_{iv,s}$ can be imaginary, their combination entering Eq. (7.22) is such that the imaginary parts cancel out, so that the conductance is always real (as it should be).

Quantum interference is very sensitive to a magnetic field $B_\perp$ perpendicular to the monolayer, as it breaks the coherence of time-reversed paths of electrons, responsible for WL and WAL. This is used as a probe of W(A)L in experiments, which measure the magnetoconductance as a function of $B_\perp$. The perpendicular field couples to the momentum of the electrons, unlike the parallel field $B_\|$, which only couples to spin via the Zeeman effect. It leads to a quantization of momenta, $|\mathbf{Q}| \to Q_n = (n+1/2)/l_B^2$, where $n = 0, 1, 2...$ denotes the Landau levels and $l_B = \sqrt{\hbar/4eB_\perp}$ is the magnetic length. We assume $l_B \gg l$, such that the diffusive limit is not violated, which imposes a constraint on the maximum field $B_\perp \ll \hbar/(4eD\tau_0)$. We then evaluate the magnetoconductance $\Delta\sigma = \delta\sigma(B_\perp) - \delta\sigma(0)$ as

$$\begin{aligned}\frac{\Delta\sigma}{\sigma_0} = 2\Xi F\left(\frac{B_\perp}{B_\phi + B_x^x}\right) + \frac{1}{2}F\left(\frac{B_\perp}{B_\phi + B_z^0}\right) - \frac{1}{2}F\left(\frac{B_\perp}{B_\phi}\right) + \frac{1}{2}F\left(\frac{B_\perp}{B_\phi + B_0^z}\right) \\ - \frac{1}{2}F\left(\frac{B_\perp}{B_\phi + B_z^z}\right) - \gamma_{iv}\sum_\pm \pm F\left(\frac{B_\perp}{B_\phi + B_{iv}^+ \pm \frac{B_{iv}^-}{\gamma_{iv}}}\right) - \Xi\gamma_s \sum_\pm \pm F\left(\frac{B_\perp}{B_\phi + B_s^+ \pm \frac{B_s^-}{\gamma_s}}\right).\end{aligned} \tag{7.24}$$

Here, we have introduced

$$F(z) = \ln(z) + \psi\left(\frac{1}{2} + \frac{1}{z}\right) \approx \begin{cases} \frac{z^2}{24}, & z \ll 1, \\ \ln z, & z \gg 1, \end{cases} \tag{7.25}$$

where $\psi(z)$ is the digamma function, and $B_i^j = \hbar\Gamma_i^j/(4eD)$ are effective magnetic fields associated with the scattering rates.

Eq. (7.24) acquires a simple form if the decoherence rate τ_ϕ^{-1} is either the dominant or the smallest scattering rate. For very long τ_ϕ, such that $\tau_\phi^{-1} \ll \Gamma_s^l$, all the gapped Cooperons can be neglected, and only the third term in Eq. (7.24) remains. Then, we have $\Delta\sigma/\sigma_0 = -(1/2)F(B_\perp/B_\phi)$, as in conventional metal with strong spin-dependent disorder. For short decoherence times, $\tau_\phi^{-1} \gg \Gamma_s^l$, all the Cooperon gaps can be neglected. Different contributions to Eq. (7.24) then cancel pairwise, and we obtain $\Delta\sigma/\sigma_0 = 2\Xi F(B_\perp/B_\phi)$. This exhibits WL, WAL or a vanishing quantum correction for $\Xi = 1, -1, 0$ respectively, similarly to a Dirac material in a smooth disorder potential. This limiting case contributes to the interference correction with a four times larger prefactor compared to the previous one - a consequence of spin and valley degeneracy.

The magnetoconductance formula Eq. (7.24) captures the rich weak localization behavior of TMDs and graphene/TMD. Due to the large number of parameters it is difficult to apply it directly to experiments. In the next section, we will present and discuss several realistic regimes in which this result significantly simplifies, and compare them to the existing theories. Furthermore, we will discuss the effect of a finite in-plane Zeeman field.

7.3.1 Regime of strong short-range disorder

The regime where intervalley scattering dominates over all spin-dependent scattering rates, $\tau_{iv}^{-1} \gg \tau_{i,j}^{-1}$, with $i = z, zv, iv$ and $j = z, o$, is the most commonly used regime when interpreting the measurements of the quantum correction. Such a large magnitude of intervalley scattering is expected in samples with an abundance of atomic defects, or in small samples, where the edges can contribute to this kind of scattering. In that case, the effect of spin-dependent disorder can be captured with only two scattering rates,

$$\begin{aligned}\tau_{sym}^{-1} &= 2(\tau_{z,e}^{-1} + \tau_{zv,e}^{-1} + \tau_{iv,e}^{-1}), \\ \tau_{asy}^{-1} &= \tau_{z,o}^{-1} + \tau_{zv,o}^{-1} + \tau_{iv,o}^{-1} + \tau_{BR}^{-1}.\end{aligned} \tag{7.26}$$

Here τ_{sym}^{-1} contains all the spin-dependent scattering processes that satisfy mirror ($z \to -z$) symmetry and, thus, preserve the electron spin. On the other hand, τ_{asy}^{-1} contains spin-flip processes that break this symmetry. In the presence of potential disorder only, we can use the estimates provided in Table 3.1 to identify the dominant contributions to these rates. In that case, we find that the symmetric rate is dominated by $\tau_{z,e}^{-1}$, which describes the Elliott-Yafet spin-relaxation mechanism induced by Kane-Mele SOC, while the asymmetric rate is dominated by τ_{BR}^{-1}, which describes the Dyakonov-Perel spin relaxation mechanism induced by Rashba SOC. If additional spin-orbit impurities are present in the system, the symmetric and asymmetric rates are not limited by the band structure SOC parameters.

In this regime, $\Gamma_{iv}^{-} \approx \Gamma_{iv}^{+} \approx \tau_{iv}^{-1}$, and $\gamma_{iv} \approx 1/\sqrt{1-4\Delta_{so}^2\tau_{iv}^2}$. Furthermore, we will assume that the effect of trigonal warping captured in τ_*^{-1} and τ_{**}^{-1} for intravalley Cooperons (see the bottom of Table 7.1) is small compared to intervalley scattering. Then, we have $\tau_*^{-1} \approx \tau_{**}^{-1} \approx \tau_{iv}^{-1}$, and the magnetoconductance (7.24) becomes

$$\begin{aligned}\frac{\Delta\sigma}{\sigma_0} =& 2\Xi F\left(\frac{B_\perp}{B_\phi + B_{iv}}\right) + \frac{1}{2}F\left(\frac{B_\perp}{B_\phi + 2B_{asy}}\right) - \frac{1}{2}F\left(\frac{B_\perp}{B_\phi}\right) \\ &- \gamma_{iv}\left[F\left(\frac{B_\perp}{B_\phi + B_{iv}(1+\frac{1}{\gamma_{iv}})}\right) - F\left(\frac{B_\perp}{B_\phi + B_{iv}(1-\frac{1}{\gamma_{iv}}) + B_s}\right)\right]. \end{aligned} \tag{7.27}$$

Here $\tau_s^{-1} = \tau_{sym}^{-1} + \tau_{asy}^{-1}$, and $B_i = \hbar/(4eD\tau_i)$. We see that the magnetoconductance is determined by a combination of valley and spin physics, described by the intervalley scattering rate τ_{iv}^{-1}, and spin scattering rates τ_{sym}^{-1} and τ_{asy}^{-1}. The interplay between intervalley scattering and Ising SOC is captured by the coefficient γ_{iv}. We will proceed by analyzing this interplay in two limits: $\tau_{iv}^{-1} \gg \Delta_{so}$ and $\Delta_{so} \gg \tau_{iv}^{-1}$.

Within these two limits, we can readily address 3 regimes of the decoherence rate: $(i)\,\tau_\phi^{-1} \ll \tau_s^{-1}$, $(ii)\,\tau_s^{-1} \ll \tau_\phi^{-1} \ll \tau_{iv}^{-1}$, and $(iii)\,\tau_{iv}^{-1} \ll \tau_\phi^{-1}$, where the quantum correction acquires a simple form. The cases (i) and (iii), where the decoherence rate is the dominant or the smallest one, respectively, were previously discussed in the general context of Eq. (7.24). The intermediate regime (ii) is not universal. In the limit $\tau_{iv}^{-1} \gg \Delta_{so}$, it yields $\Delta\sigma/\sigma_0 = F(B/B_\phi)$. This is analogous to a conventional metal without SO impurities, and represents a sum of three spin-triplets C_i^0 ($i = x, y, z$), which contribute as $(3/2)F(B_\perp/B_\phi)$, and a spin-singlet C_0^0, which contributes as $-(1/2)F(B_\perp/B_\phi)$. For $\Delta_{so} \gg \tau_{iv}^{-1}$, the two triplets C_x^0 and C_y^0 are suppressed by the SOC, and the quantum correction vanishes.

We obtain more complex behavior in the crossover regimes $\tau_\phi^{-1} \sim \tau_s^{-1}$ [which includes (i) and (ii)] and $\tau_\phi^{-1} \sim \tau_{iv}^{-1}$ [which includes (ii) and (iii)]. Strong intervalley scattering completely suppresses the valley structure in the first regime, so that the magnetoconductance is determined by the spin physics only. On the other hand, the valley physics dominates in the second regime, as the effect of spin-scattering is washed out by electron decoherence.

a. Limit $\tau_{iv}^{-1} \gg \Delta_{so}$: Here, Eq. (7.27) simplifies, as $\gamma_{iv} \approx 1$. In the crossover regime $\tau_\phi^{-1} \sim \tau_s^{-1}$, the first and the fourth term of Eq. (7.27) are suppressed by the large intervalley scattering, and we obtain

$$\frac{\Delta\sigma}{\sigma_0} = \frac{1}{2}F\left(\frac{B_\perp}{B_\phi + 2B_{asy}}\right) - \frac{1}{2}F\left(\frac{B_\perp}{B_\phi}\right) + F\left(\frac{B_\perp}{B_\phi + \tilde{B}_s}\right). \tag{7.28}$$

Here, we have introduced

$$\tilde{\tau}_s^{-1} = \tau_{iv}^{-1}\left(1 - \frac{1}{\gamma_{iv}}\right) + \tau_s^{-1} \approx 2\Delta_{so}^2\tau_{iv} + \tau_s^{-1}, \tag{7.29}$$

and $\tilde{B}_s = \hbar/(4eD\tilde{\tau}_s)$. As valley structure and spin-splitting are suppressed in this regime, the system behaves similarly to a diffusive metal with spin-orbit impurities, and Eq. (7.28) is equivalent to the conventional Hikami-Larkin-Nagaoka (HLN) formula (see also Sec. 1.2.1). This remains true even when intervalley scattering becomes comparable to intervalley scattering, for $\tau_{iv}^{-1} \sim \tau_0^{-1}$. Equation (7.28) still holds in that case, although with a modified diffusion constant (see Appendix D.5).

The effect of Ising SOC is captured by an additional contribution to the symmetric rate, $\tau_{sym}^{-1} \to \tau_{sym}^{-1} + 2\Delta_{so}^2\tau_{iv}$[1], which stems from the coupling of the Cooperon modes $C_x^{0(z)}$ with $C_y^{z(0)}$ by this SOC. This effect was already discussed in Refs. [83,127,128], and used to estimate Δ_{so} from the experimental data in graphene/TMD heterostructures. However, the estimated SOC is of the same order of magnitude as τ_{iv}^{-1}, which is outside of the region of validity of this formula ($\tau_{iv}^{-1} \gg \Delta_{so}$). Instead, the full formula provided by Eq. (7.27) should be used in order to get a more reliable estimate of the Ising SOC.

If $\tilde{\tau}_s^{-1} \sim \tau_\phi^{-1} \sim \tau_{asy}^{-1}$, Eq. (7.28) exhibits WAL-WL crossover as the magnitude of the perpendicular field is increased. We next consider the regime $\tilde{\tau}_s \gg \tau_\phi^{-1} \sim \tau_{asy}^{-1}$. Here, the last term of Eq. (7.28) is suppressed due to the combined effect of all mirror-symmetric SOC in the system, as $\tau_{sym}^{-1} + 2\Delta_{so}^2\tau_{iv} \gg \tau_\phi^{-1}$. We thus have

$$\frac{\Delta\sigma}{\sigma_0} = \frac{1}{2}F\left(\frac{B_\perp}{B_\phi + 2B_{asy}}\right) - \frac{1}{2}F\left(\frac{B_\perp}{B_\phi}\right). \tag{7.30}$$

This corresponds to pure WAL behavior as a function of $B_\perp$, that saturates on the scale of B_{asy}. This kind of saturation was noticed in several recent experiments that show flat WAL curves, such as Refs. [78,82,83]. The interference correction vanishes for $\tilde{\tau}_s^{-1} \gg \tau_\phi^{-1} \gg \tau_{asy}^{-1}$, and shows pure WL behavior if $\tilde{\tau}_s^{-1} \sim \tau_\phi^{-1} \gg \tau_{asy}^{-1}$, given as

$$\frac{\Delta\sigma}{\sigma_0} = F\left(\frac{B_\perp}{B_\phi + \tilde{B}_s}\right). \tag{7.31}$$

Next, we address the crossover regime $\tau_\phi^{-1} \sim \tau_{iv}^{-1}$. Here, the spin scattering rates can be neglected, and the second and third term of Eq. (7.27) cancel out, which yields

$$\frac{\Delta\sigma}{\sigma_0} = 2\Xi F\left(\frac{B_\perp}{B_\phi + B_{iv}}\right) + F\left(\frac{B_\perp}{B_\phi}\right) - F\left(\frac{B_\perp}{B_\phi + 2B_{iv}}\right). \tag{7.32}$$

---

[1] We remind that this effective rate was also found in our study of Ising superconductivity in Sec. 5.3 in the same parameter regime.

This result at $\Xi = -1$ is equivalent to Ref. [70], which describes graphene without spin-dependent impurities. As a function of a perpendicular field, it exhibits pure WL for $\Xi = 1$ and $\Xi = 0$, and a WL-WAL crossover for $\Xi = -1$.

Fig. 7.3 (a) gives a schematic representation of the different regimes in the limit $\tau_{iv}^{-1} \gg \Delta_{so}$.

b. Limit $\Delta_{so} \gg \tau_{iv}^{-1}$: Since $\gamma_{iv} \approx 0$, here only the first three terms of Eq. (7.27) contribute to the magnetoconductance. In the crossover regime $\tau_\phi^{-1} \sim \tau_s^{-1}$,we again obtain Eq. (7.30). Similarly to the previously considered case analyzed below Eq. (7.30), saturated WAL in this regime can be understood as a consequence of strong mirror-symmetric SOC which suppresses Cooperons that would lead to WL. However, this suppression is now predominantly caused by spin-splitting due to Δ_{so}, irrespective of the magnitude of τ_{sym}^{-1}. This regime, therefore, presents an alternative to the standard HLN theory to interpret the experiments showing saturated WAL signals.

Finally, we analyze the crossover regime $\tau_\phi^{-1} \sim \tau_{iv}^{-1}$. We find

$$\frac{\Delta\sigma}{\sigma_0} = 2\Xi F\left(\frac{B_\perp}{B_\phi + B_{iv}}\right), \tag{7.33}$$

which exhibits pure WAL, pure WL, or vanishes for $\Xi = 1$, $\Xi = -1$ and $\Xi = 0$, respectively.

Fig. 7.3 (b) gives a schematic representation of the different regimes in the limit $\Delta_{so} \gg \tau_{iv}^{-1}$.

Fig. 7.4 illustrates the behavior of the magnetoconductance beyond the two extreme limits $\tau_{iv}^{-1} \gg \Delta_{so}$ and $\Delta_{so} \gg \tau_{iv}^{-1}$, analyzed above. In particular, Fig. 7.4 (a) addresses the crossover from the regime described by Eq. (7.28) to Eq. (7.30) as the magnitude of Ising SOC is increased. Similary Fig. 7.4 (b) shows a crossover from Eq. (7.32) to Eq. (7.33).

7.3.2 Regime of weak short-range disorder

In this section, we analyze the regime where intervalley scattering rate is much weaker than the spin-scattering rates, $\tau_{sym}^{-1}, \tau_{asy}^{-1} \gg \tau_{iv}^{-1}$, which is appropriate for large samples without atomic defects. The intervalley spin-scattering rates are assumed to be even weaker, $\tau_{iv,e/o}^{-1} \ll \tau_{iv}^{-1}$, and thus neglected. The magnetoconductance formula is then given as

$$\frac{\Delta\sigma}{\sigma_0} = 2\Xi F\left(\frac{B_\perp}{B_\phi + B_x^x}\right) - \frac{1}{2}F\left(\frac{B_\perp}{B_\phi}\right) + \frac{1}{2}F\left(\frac{B_\perp}{B_\phi + 2B_{iv}}\right) - \Xi\gamma_s \sum_{\pm} \pm F\left(\frac{B_\perp}{B_\phi + B_s^+ \pm \frac{B_s^-}{\gamma_s}}\right). \tag{7.34}$$

In this regime, the quantum correction is governed by the interplay between Δ_{so} and a combination of the spin-scattering rates Γ_s^-, described by the coefficient γ_s. Unlike the case of strong short-range disorder, the Cooperons containing γ_{iv} cancel out in this regime, so the ratio of intervalley scattering and Ising SOC does not affect $\Delta\sigma$. The three intravalley Cooperon gaps Γ_i^x ($i = 0, x, y, z$) that enter Eq. (7.34) have a similar structure. To simplify further analysis, we will assume that they are of the same order of magnitude.

(a) $\tau_{iv}^{-1} \gg \Delta_{so}$:

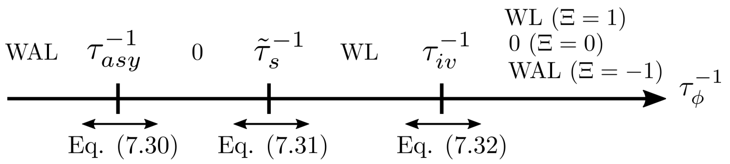

(b) $\Delta_{so} \gg \tau_{iv}^{-1}$:

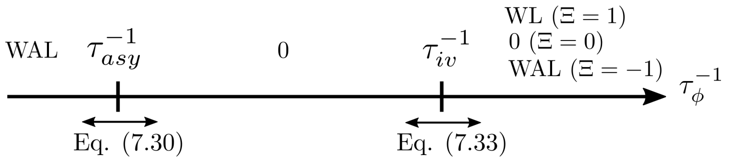

Figure 7.3: Schematic representation of the WL behavior in the regime of strong short-range disorder, $\tau_{iv}^{-1} \gg \tau_s^{-1}$. In the crossover regions described by Eqs. (7.28)-(7.33), the magnetoconductance at low (high) perpendicular field behaves the same as in the left (right) adjacent region on the τ_ϕ^{-1} arrow. In panel (a), the regime of vanishing interference correction between τ_{asy}^{-1} and $\tilde{\tau}_s^{-1}$ disappears if $\tau_{asy}^{-1} \sim \tilde{\tau}_{sym}^{-1}$. Starting from the regime $\tau_{iv}^{-1} \gg \Delta_{so}$, upon increasing Δ_{so}, the region of WL between $\tilde{\tau}_s^{-1}$ and τ_{iv}^{-1} in panel (a) "shrinks", until it disappears for $\Delta_{so} \sim \tau_{iv}^{-1}$. As Δ_{so} is further increased to $\Delta_{so} \gg \tau_{iv}^{-1}$, the behavior in the regime $\tau_\phi^{-1} \sim \tau_{iv}^{-1}$ reduces to Eq. (7.33), and we finally reach the situation depicted in the panel (b).

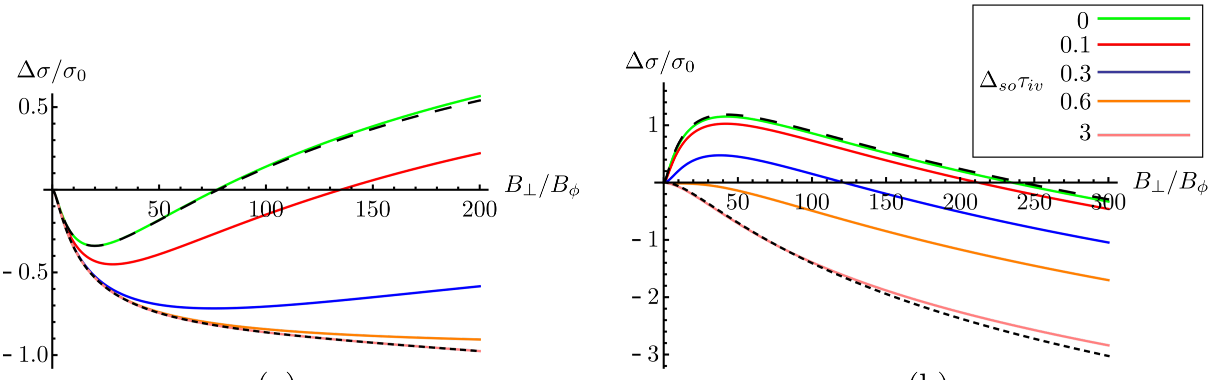

(a) (b)

Figure 7.4: Interference-induced magnetoconductance as a function of a weak perpendicular magnetic field under the influence of increasing Ising SOC. We take the chemical potential to be deep in the conduction band, such that $\Xi = -1$. The fields B_{sym} and B_{asy} are determined by the Elliott-Yaffet contribution from the Kane-Mele SOC, and the Dyakonov-Perel contribution due to the Rashba SOC, respectively, as well as other sources of spin-orbit scattering [see Table 3.1 and Eq. (7.26)]. The effect of the valley-Zeeman SOC is captured by the parameter $\Delta_{so}\tau_{iv}$. (a) All curves are plotted for the parameters $B_{iv} = 200B_\phi, B_{sym} = B_{asy} = 3B_\phi$. The dashed black line corresponds to Eq. (7.28), while the dotted line corresponds to Eq. (7.30) (b) All curves are plotted for the parameters $B_{iv} = 10B_\phi, B_{sym} = B_{asy} = 0.02B_\phi$. The dashed black line corresponds to Eq. (7.32), while the dotted line corresponds to Eq. (7.33).

We proceed similarly to the previous section, and analyze the three extreme limits with respect to the decoherence rate. If it is the smallest, $\tau_\phi^{-1} \ll \tau_{iv}^{-1}$, or the largest, $\Gamma_i^x \ll \tau_\phi^{-1}$, scattering rate, the general arguments presented after Eq. (7.24) apply. In the intermediate limit $\tau_{iv}^{-1} \ll \tau_\phi^{-1} \ll \Gamma_i^x$, the quantum correction vanishes.

We next examine the crossover regimes. For $\tau_\phi^{-1} \sim \tau_{iv}^{-1}$, we have

$$\frac{\Delta\sigma}{\sigma_0} = -\frac{1}{2}F\left(\frac{B_\perp}{B_\phi}\right) + \frac{1}{2}F\left(\frac{B_\perp}{B_\phi + 2B_{iv}}\right). \tag{7.35}$$

This formula is determined by intervalley scattering only, and exhibits WAL behavior which saturates on the scale of B_{iv}. Finally, in the crossover regime $\tau_\phi^{-1} \sim \Gamma_i^x$ we have

$$\frac{\Delta\sigma}{\sigma_0} = 2\Xi F\left(\frac{B_\perp}{B_\phi + B_x^x}\right) - \Xi\gamma_s \sum_\pm \pm F\left(\frac{B_\perp}{B_\phi + B_s^+ \pm \frac{B_s^-}{\gamma_s}}\right). \tag{7.36}$$

In the limit $\Gamma_s^- \gg \Delta_{so}$, one should consider all three terms in Eq. (7.36) since $\gamma_s \approx 1$. As Δ_{so} increases, the second line of Eq. (7.36) becomes suppressed, until it vanishes for $\Delta_{so} \gg \Gamma_s^-$, where $\gamma_s \approx 0$. We see that the qualitative behavior of the magnetoconductance remains the same for any γ_s, and thus, any Δ_{so}. It only depends on the doping coefficient Ξ, and exhibits WL, WAL, or neither for $\Xi = 1, -1$, and 0, respectively. These conclusions are schematically represented in Fig. 7.5.

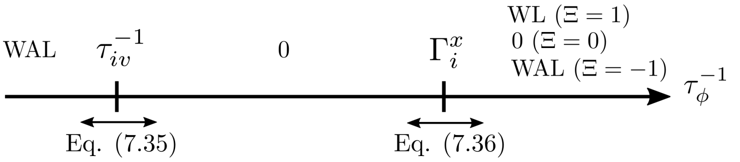

Figure 7.5: Schematic representation of the WL behavior in the regime of weak short-range disorder, $\tau_{sym}^{-1}, \tau_{asy}^{-1} \gg \tau_{iv}^{-1} \gg \tau_{iv,e/o}^{-1}$. The behavior in the crossover regions is represented in the same way as in Fig. 7.3.

7.4 Effect of an in-plane Zeeman field

At sufficiently high in-plane Zeeman field, all spin-singlet C_0^l and spin-triplet C_x^l Cooperons are suppressed, and we arrive at the asymptotic formula for the magnetoconductace,

$$\frac{\Delta\sigma}{\sigma_0} = \sum_{i=x,z}\left[\Xi F\left(\frac{B_\perp}{B_\phi + B_i^x}\right) + \frac{1}{2}F\left(\frac{B_\perp}{B_\phi + B_i^0}\right) - \frac{1}{2}F\left(\frac{B_\perp}{B_\phi + B_i^z}\right)\right]. \tag{7.37}$$

The magnitude of the in-plane Zeeman field required to reach the high-field formula (7.37) differs depending on the parameter regime, as will be discussed in the following. Note that it will always be reached if $h \gg \Delta_{so}, \tau_i^{-1}$, where τ_i^{-1} are all scattering rates except the diagonal one, τ_0^{-1}.

First, we analyze the regime where the short-range disorder rate is much larger than all spin-dependent disorder rates, $\tau_{iv}^{-1} \gg \tau_s^{-1}$. In this case the asymptotic formula acquires the form

$$\frac{\Delta\sigma}{\sigma_0} = 2\Xi F\left(\frac{B_\perp}{B_\phi + B_{iv}}\right) + \frac{1}{2}F\left(\frac{B_\perp}{B_\phi + 2B_{asy}}\right) + \frac{1}{2}F\left(\frac{B_\perp}{B_\phi + B_s}\right) - F\left(\frac{B_\perp}{B_\phi + 2B_{iv}}\right). \tag{7.38}$$

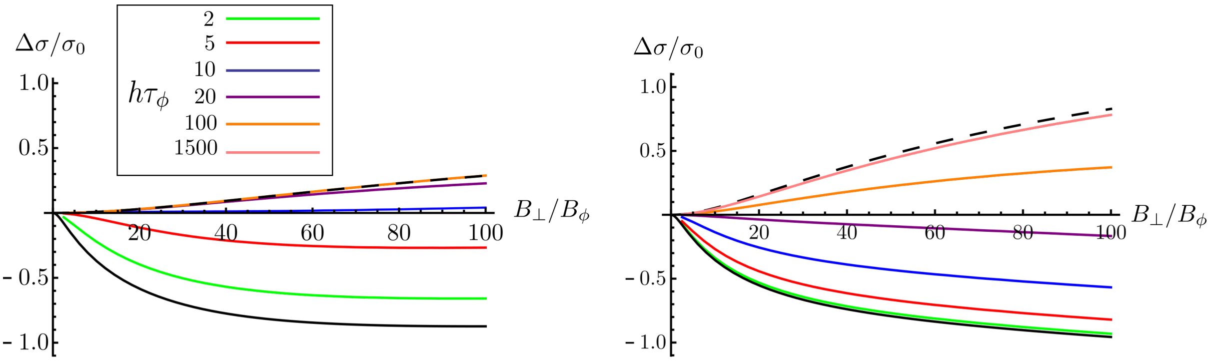

(a) (b)

Figure 7.6: Influence of the in-plane Zeeman field on the magnetoconductance curves. The solid black line represents the curve at zero in-plane Zeeman field, while the dashed line represents the saturation curve given by Eq. (7.38) at high fields. (a) The parameters for the plot are $B_{iv} = 100B_\phi$, $B_{sym} = B_{asy} = 10B_\phi, B_{so} = 0$, and $\Xi = -1$. The crossover to WL happens at $B_\perp \approx 10B_\phi$. (b) The parameters for the plot are $B_{iv} = 100B_\phi$, $B_{sym} = B_{asy} = 3.5B_\phi, B_{so} = 120B_\phi$, and $\Xi = -1$. The crossover to WL happens at $B_\perp \approx 30B_\phi$.

Starting from the general expression (7.20), we will next check the magnitude of h needed to reach this formula in the limits $\tau_{iv}^{-1} \gg \Delta_{so}$ and $\Delta_{so} \gg \tau_{iv}^{-1}$.

Let us consider $\tau_{iv}^{-1} \gg \Delta_{so}$. If the decoherence rate τ_ϕ^{-1} is larger than all spin-scattering rates, the spin structure is suppressed, and the in-plane Zeeman field has no effect. In this case, the formula (7.38) is valid for any h and is equivalent to Eq. (7.32). On the other hand, if τ_ϕ^{-1} is of the order of the spin-scattering rates, all the valley-singlet Cooperons, C_s^0, contribute to the magnetoconductance at $h = 0$ [Eq. (7.28)], and a finite h acts by suppressing the spin-singlet Cooperon C_0^0 and the spin-triplet Cooperon C_x^0. For fields of the order $\tilde{\tau}_s^{-1} \ll h \ll \tau_{iv}^{-1}$, Eq. (7.38) holds, but with B_s replaced with $\tilde{B}_s$. Therefore, unless $\tau_s^{-1} \gg \Delta_{so}^2 \tau_{iv}$, the Ising SOC still has an effect at such fields, through the contribution $2\Delta_{so}^2 \tau_{iv}$ to the effective rate $\tilde{\tau}_s^{-1}$. In that case, the high-field asymptotic formula is reached only at very high fields of the order of intervalley scattering, namely $h \gg \tau_{iv}^{-1}$.

Next, we consider the limit $\Delta_{so} \gg \tau_{iv}^{-1}$. In this regime, the Cooperons C_i^j and C_j^i, where $i = x, y$ and $j = 0, z$, are suppressed by the strong Δ_{so} at $h = 0$. In order to reach the asymptotic formula Eq. (7.38), a large field $h \gg \Delta_{so}$ is needed. It negates the effect of the Ising SOC and restores C_y^j and C_z^i Cooperons, while suppressing all C_0^l and C_x^l Cooperons.

Finally, we address the limit of weak short-range disorder, $\tau_{sym}^{-1}, \tau_{asy}^{-1} \gg \tau_{iv}^{-1} \gg \tau_{iv,e/o}^{-1}$, described by Eq. (7.34) at $h = 0$. Similarly to the previously considered case, strong h negates the effect of Δ_{so} and suppresses all spin-singlet and x-triplet Cooperons. Here, the asymptotic formula takes the form

$$\frac{\Delta\sigma}{\sigma_0} = \Xi \sum_{i=x,z} F\left(\frac{B_\perp}{B_\phi + B_i^x}\right), \tag{7.39}$$

and is reached if the in-plane Zeeman field is the largest energy scale, $h \gg \Gamma_i^x, \Delta_{so}, \tau_\phi^{-1}$ $(i = 0, x, y, z)$. The prefactor Ξ indicates that it can exhibit WAL, WL, or neither depending on the doping, similarly to Eq. (7.36).

To illustrate a situation where applying the in-plane field can help in the interpretation of the quantum correction, we plot two magnetoconductance curves with a similar shape, but with significantly different parameters in Fig. 7.6 (black line). The first curve [Fig. 7.6 (a)] has strong spin-scattering and no Ising SOC, while the second one has weaker spin-scattering and strong SOC [Fig. 7.6 (b)]. The high-field saturation curve (dashed line) has a similar shape in both cases, and is described by Eq. (7.38). The amplitude of WL at high fields is somewhat larger in the case of strong SOC, as the spin-orbit scattering is weaker, which means that the second line of Eq. (7.38) gives a larger contribution compared to the other case. More importantly, this case is more resistant to the effect of the applied field, and the crossover to WL happens at a much higher field amplitude. This is consistent with the above analysis, as the expected crossover field is $h \sim \tau_s^{-1}$ for Fig. 7.6 (a) and $h \sim \Delta_{so}$ for Fig. 7.6 (b). Thus, applying an in-plane field helps distinguish the contributions of Ising SOC and spin-dependent scattering to the quantum correction.

7.5 Comparison with experiments

A significant number of W(A)L magnetoconductance measurements were recently performed in TMDs [76–78] and graphene/TMD heterostructures [17, 79–83]. They generally observe strong WAL signals at low perpendicular fields, that either saturate as the field is increased [78, 82, 83] [as illustrated in Figs. 7.7(a) and (c)], or cross over to WL [17, 77, 79–81] [as illustrated in Fig. 7.7 (b)]. An exception is Ref. [76], which observed WL at low fields and WAL at high fields.

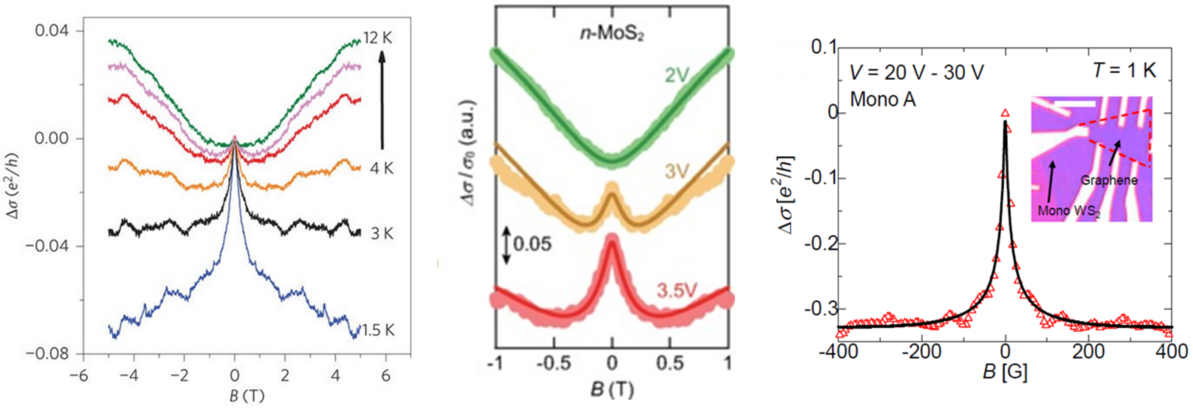

(a) (b) (c)

Figure 7.7: Measurements of the interference-induced magnetoconductance as a function of applied perpendicular field in some TMDs and graphene/TMD heterostructures. (a) and (b): measurement results for ionic-liquid gated MoS_2 samples, from Refs. [78] and [77], respectively. Differently colored curves in (a) and (b) correspond to various temperatures and gate voltages, respectively. (c): measurements for a graphene/WS_2 heterostructure, from Ref. [82].

Most of these experiments were interpreted using the conventional HLN formula, given by Eq. (7.28). As we discuss in Sec. 7.3.1, this formula only holds if intervalley scattering is very large ($\tau_{iv}^{-1} \gg \Delta_{so}$). However, it is not clear if this regime is justified, especially taking into account that both TMDs [8] and graphene/TMD heterostructures [16, 17] are expected to host substantial valley-Zeeman SOC. Our theory, for instance Eq. (7.27), holds for any ratio of Δ_{so} and τ_{iv}^{-1}, and might provide an alternative explanation of the experiments.

The case where saturated WAL behavior is observed in graphene/TMD heterostructures [82, 83] is of particular interest. Namely, such scenario can be taken as a proof that strong, mirror symmetric SOC is induced in the graphene sheet by the TMD. As discussed in Sec. 7.3.1, the magnetoconductance in this case is described by Eq. (7.30). However, the question remains if the dominant contribution to the symmetric rate $\tilde{\tau}_{sym}^{-1}$ comes from the Kane-Mele SOC [$\tilde{\tau}_{sym}^{-1} \propto \frac{1}{\tau_0}(\frac{\Delta_{KM}}{\mu})^2$], or from the valley-Zeeman SOC ($\tilde{\tau}_{sym}^{-1} \propto \Delta_{VZ}^2 \tau_{iv}$). Applying a perpendicular magnetic field could be helpful in distinguishing them. Namely, as shown in Sec. 7.4, the WAL signal from valley-Zeeman SOC is significantly more resistant to the in-plane fields. These two kinds of SOC lead to different spin-dependent phenomena in graphene (as discussed in Sec. 2.4), and only the Kane-Mele SOC is linked to the quantum spin Hall effect.

An in-plane Zeeman field was applied in one experiment in graphene/TMD heterostructures [83]. However, in contrast to our and other theories that account for such fields [72, 126], the experiment measured vanishing magnetoconductance at high fields. This is explained as a consequence of ripples, which increasingly contribute to the dephasing rate τ_ϕ^{-1} as the field is increased [129]. Therefore, the effect of the in-plane fields can only be studied in samples which are sufficiently flat, or, alternatively, if a theoretical model for $\tau_\phi^{-1}(h)$ for a rippled sample is known. Such a model was developed for graphene in Ref. [129].

7.6 Summary

In this Chapter, we have developed a theory of weak localization magnetoconductance for TMD monolayers and their heterostructures with graphene, using the standard diagrammatic technique for disordered systems. The interplay between spin and valley physics in these materials yields a rich behavior of the quantum correction to the conductivity, which we discuss in several regimes of interest for the interpretation of recent experimental data. We generalize the HLN and MF theories and propose a formula that can be used to extract the magnitude of Ising SOC and disorder from the experiments in all regimes. In some cases, interpreting the experiments is not straightforward, as different parameter combinations may explain the data equally well. An in-plane Zeeman field can be used as an additional tuning parameter to help distinguish between the contributions of different processes.

Chapter 8

Universal conductance fluctuations

In Chapter 7, we studied one manifestation of electronic interference in conducting TMDs and graphene/TMD heterostructures – the weak (anti)localization. In this Chapter, we expand upon this by studying another interference phenomenon – universal conductance fluctuations (UCF), for the same systems. We use the same model as in Chapter 7, which accounts for physics of the K-band, under the same assumptions of dominant diagonal disorder $\tau_0^{-1} \approx \tau^{-1}$, and taking the diffusive limit $|\mu| - E_g \gg \tau_0^{-1} \gg \Delta_{so}, \lambda, \kappa q_F^2$. Note that, unlike in Chapter 7, we do not consider the effect of an in-plane Zeeman field here.

Similarly to WL, we show that the amplitude of UCF is determined by a combination of several processes: spin-splitting due to SOC, valley- and spin-dependent scattering, and the Berry phase due the Dirac-like band structure. Measuring the amplitude of UCF in experiments can be used to gain insight about these processes, which is particularly useful if combined with information extracted from W(A)L experiments.

To start, we calculate the diffusons in Sec. 8.1, which are the basic building blocks needed to formulate the theory of UCF. We only briefly discuss this calculation, as it shares many similarities with the calculation of Cooperons in Sec. 7.2. We proceed by calculating the general expression for the UCF in Sec. 8.2. Finally, we discuss our results in a regime which corresponds to a likely experimental situation, where Ising SOC and intervalley scattering are much stronger than spin-dependent scattering.

8.1 Diffusons

Diffusons $D^{ab,a'b'}_{\alpha\beta,\alpha'\beta'}$ are disorder averages of two Green's functions, which correspond to ladder diagrams in diagrammatic perturbation theory (different from Cooperons, which correspond to maximally-crossed diagrams, see also Sec. 7.1). The diffusons satisfy the system of coupled Bethe-Salpeter equations (shown in diagrammatic form in Fig. 8.1)

$$\begin{aligned} D^{ab,a'b'}_{\alpha\beta,\alpha'\beta'}(\theta,\theta';\mathbf{q}) = {}& \tilde{W}^{ab,a'b'}_{\alpha\beta,\alpha'\beta'}(\theta,\theta') \\ &+ \int_0^{2\pi} \frac{d\theta''}{2\pi} \tilde{W}^{aa_1,bb_1}_{\alpha\alpha_1,\beta\beta_1}(\theta,\theta'')\tilde{\Pi}^{a_1b_1,a_2b_2}_{\alpha_1\beta_1,\alpha_2\beta_2}(\theta'';\mathbf{q}) D^{a_2b_2,a'b'}_{\alpha_2\beta_2,\alpha'\beta'}(\theta'',\theta';\mathbf{q}). \quad (8.1) \end{aligned}$$

We use the same notation conventions as in Sec. 7.2, where the Greek indices in the subscript (Latin indices in the superscript) correspond to spin (valley) degrees of freedom

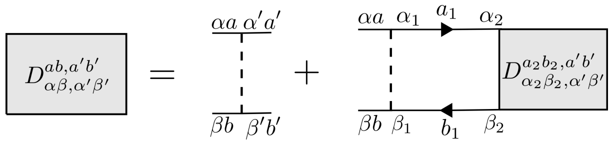

Figure 8.1: Diagrammatic form of the Bethe-Salpeter equation for the diffusons. Greek indices in the subscript describe spin, while Latin indices in the superscript describe valley degree of freedom.

and take values ±1. Summation over repeated indices is assumed. We have introduced the disorder correlator $\tilde{W}$ and the polarization operator $\tilde{\Pi}$ as

$$\begin{aligned} \tilde{W}^{ab,a'b'}_{\alpha\beta,\alpha'\beta'}(\theta,\theta') &= \langle [\mathcal{H}^D_{\mathbf{q}\mathbf{q}'}]^{aa'}_{\alpha\alpha'} [\mathcal{H}^D_{\mathbf{q}'\mathbf{q}}]^{b'b}_{\beta'\beta} \rangle \qquad \text{and} \\ \tilde{\Pi}^{ab}_{\alpha\beta,\alpha'\beta'}(\theta;\mathbf{q}) &= \nu_{0K} \int d\xi_{\mathbf{p}} [G^R_{\mathbf{p}\epsilon+\omega}]^a_{\alpha\alpha'} [G^A_{\mathbf{p}+\mathbf{q}\omega}]^b_{\beta'\beta}. \end{aligned} \tag{8.2}$$

Note that they are different from the related quantities introduced for Cooperons in Eq. (7.5), as they have different configurations of momenta and indices related to the advanced Green's functions (lower branch of the diagrams in Fig. 8.1).

As done in Sec. 7.2.1 for Cooperons, we first resolve the angular structure of diffusons by calculating them in the presence of diagonal disorder only. We distinguish intravalley diffusons $D^{aa,aa}$, which are related to the Drude conductivity, and intervalley ones $D^{a\bar{a},a\bar{a}}$, which do not enter the conductivity but appear in the expression for UCF. We expand in harmonics

$$\begin{aligned} D^{ab,a'b'}(\theta,\theta';\mathbf{q}) &= \sum_{n,m=-\infty}^{\infty} D^{ab,a'b'}_{nm}(\mathbf{q}) e^{-i(n\theta - m\theta')}, \\ \tilde{W}^{ab,a'b'}(\theta,\theta') &= \sum_{n=-\infty}^{\infty} \tilde{W}^{ab,a'b'}_n e^{-in(\theta-\theta')}, \end{aligned} \tag{8.3}$$

and by solving Eq. (8.1), we find for intravalley diffusons[1]

$$D^{aa,aa}(\theta,\theta') = \frac{1}{2\pi\nu_{0K}\tau_0^2} \frac{1}{D|\mathbf{q}|^2 - i\omega + \tau_\phi^{-1}}, \tag{8.4}$$

while the intervalley diffusons are

$$\begin{aligned} D^{a\bar{a},a\bar{a}}(\theta,\theta';\mathbf{q}) &= D^{a\bar{a},a\bar{a}}_{00}(\mathbf{q}) + D^{a\bar{a},a\bar{a}}_{aa}(\mathbf{q}) e^{-ia(\theta-\theta')} \\ \text{with} \quad D^{aa,aa}_{ii}(\mathbf{q}) &= \frac{1}{2\pi\nu_{0K}\tau_0^2} \frac{1}{D_i|\mathbf{q}|^2 - i\omega + \tau_\phi^{-1} + \Gamma_i}. \end{aligned} \tag{8.5}$$

Here, D_i and Γ_i are diffusion constants and gaps introduced below Eq. (7.8). Therefore, same as intravalley Cooperons, intervalley diffusons are suppressed by a large gap $\Gamma_i \propto$

---

[1] The appearance of the dephasing rate τ_ϕ^{-1} in diffusons might seem surprising at first. Namely, diffusons are most commonly associated with Goldstone modes that correspond to the conservation of the number of particles [28], and dephasing is therefore forbidden. However, diffusons that enter conductance fluctuations are different. Here, the paired electron trajectories correspond to two *separate* copies of the sample. These trajectories explore different configurations of external degrees of freedom, and as a consequence, the resulting diffusons are sensitive to dephasing [28, 85].

τ_0^{-1}, except close to the band bottom ($\mu/E_g - 1 \lesssim 2\sqrt{\tau_0/\tau_\phi}$) where D_{00} is not suppressed, and deep in the conduction band ($\mu/E_g \gtrsim 2\sqrt{\tau_0/\tau_\phi}$), where D_{aa} is not suppressed. We can write

$$D^{a\bar{a},a\bar{a}}(\theta,\theta') = \frac{1}{2\pi\nu_{0K}\tau_0^2}\left[\frac{\delta_{\Xi,1}}{D|\mathbf{q}|^2 - i\omega + \tau_\phi^{-1} + \Gamma_1} + \frac{\delta_{\Xi,-1}}{D|\mathbf{q}|^2 - i\omega + \tau_\phi^{-1} + \Gamma_{-1}} e^{-ia(\theta-\theta')}\right], \tag{8.6}$$

where the coefficient Ξ and gaps $\Gamma_{\pm 1}$ are introduced in Eq. (7.9).

We proceed by finding diffusons in the presence of all disorder terms in the same manner as in Sec. 7.2.2. We can write the angularly-independent form for all diffusons

$$\begin{aligned} D^{ab,a'b'}(\Xi;\mathbf{q}) &= D_{00}^{aa,a'a'}(\mathbf{q})\delta_{ab}\delta_{a'b'} + [D_{00}^{a\bar{a},a\bar{a}}(\mathbf{q})\delta_{\Xi,1} + D_{aa}^{a\bar{a},a\bar{a}}(\mathbf{q})\delta_{\Xi,-1}]\delta_{aa'}\delta_{bb'}\delta_{a\bar{b}}, \\ \tilde{W}^{ab,a'b'}(\Xi) &= \tilde{W}_0^{aa,a'a'}\delta_{ab}\delta_{a'b'}, + [\tilde{W}_0^{a\bar{a},a\bar{a}}\delta_{\Xi,1} + \tilde{W}_{aa}^{a\bar{a},a\bar{a}}\delta_{\Xi,-1}]\delta_{aa'}\delta_{bb'}\delta_{a\bar{b}}. \end{aligned} \tag{8.7}$$

Then, the angularly-independent form of the Bethe-Salpeter equation (8.1) reads

$$D^{ab,a'b'}_{\alpha\beta,\alpha'\beta'}(\Xi;\mathbf{q}) = \tilde{W}^{ab,a'b'}_{\alpha\beta,\alpha'\beta'}(\Xi) + \tilde{W}^{aa_1,bb_1}_{\alpha\alpha_1,\beta\beta_1}(\Xi)\tilde{\Pi}^{a_1b_1}_{\alpha_1\beta_1,\alpha_2\beta_2}(\mathbf{q})D^{a_1b_1,a'b'}_{\alpha_2\beta_2,\alpha'\beta'}(\Xi;\mathbf{q}). \tag{8.8}$$

Next, we employ the transformation to the singlet-triplet basis [28]

$$\tilde{M}^{ll'}_{ss'} = \frac{1}{4}[s_s]_{\alpha\beta}[\eta_l]^{ab}M^{ab,a'b'}_{\alpha\beta,\alpha'\beta'}[s_{s'}]_{\beta'\alpha'}[\eta_{l'}]^{b'a'} \tag{8.9}$$

to Eqs. (8.7) and (8.8). It differs from the transformation for Cooperons given in Eq. (7.14), as it does not involve the matrix $s_y\eta_x$, related to time-reversal of the advanced Green's function in Cooperons. Finally, in the absence of the Zeeman field, we find that $D^{ll'}_{ss'}(\Xi,\mathbf{q})$ satisfy the same equations as $C^{ll'}_{ss'}(\Xi,\mathbf{Q})$, namely Eqs. (7.17) and (7.19), with the same gaps, summarized in Table. 7.1. The fact that diffusons and Cooperons are dephased in the same way by the spin-orbit and valley-dependent scattering, was reported previously in Refs. [88] and [89, 90], respectively.

8.2 General expression for the UCF

Let us consider a rectangular sample, with a length L along the x-direction and the width W along the y-direction. We take that the sample is connected to leads along the x-direction, as shown in Fig. 8.2.

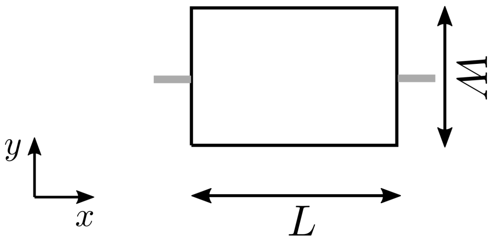

Figure 8.2: Rectangular sample geometry, where L and W are the length and width of the sample, respectively. The gray lines represent leads to which the sample is connected.

Within the linear response theory, conductance along the x-direction, before disorder averaging, is given as $\sigma \propto \sum_{\mathbf{p_1p_2}} \mathcal{J}_{x\mathbf{p_1}} G^R_{\mathbf{p_1p_2}} \mathcal{J}_{x\mathbf{p_2}} G^A_{\mathbf{p_2p_1}}$. Here, $\mathcal{J}_{x\mathbf{p}}$ is the current operator, introduced above Eq. (7.2). Fluctuations of this conductance can be expressed as

$$\overline{\delta G^2} = \langle\sigma\sigma\rangle - \langle\sigma\rangle\langle\sigma\rangle \propto \sum_{\mathbf{p_1p_2p_3p_4}} \langle \mathcal{J}_{x\mathbf{p_1}} G^R_{\mathbf{p_1p_2}} \mathcal{J}_{x\mathbf{p_2}} G^A_{\mathbf{p_2p_1}} \mathcal{J}_{x\mathbf{p_3}} G^R_{\mathbf{p_3p_4}} \mathcal{J}_{x\mathbf{p_4}} G^A_{\mathbf{p_4p_3}} \rangle_c, \tag{8.10}$$

where the subscript c means that factorizable contributions are subtracted, i.e., $\langle AB\rangle_c = \langle AB\rangle - \langle A\rangle\langle B\rangle$. There are two processes that contribute to $\overline{\delta G^2}$ [28]: fluctuations of the density of states and of the diffusion constant, represented diagrammaticaly in Figs. 8.3(a) and (b), respectively. The diagrams for UCF, in general, involve products of two diffusons, or two Cooperons. In the following, we assume the regime of strong perpendicular magnetic fields, such that all Cooperons are suppressed. Then, only the diffusons (which remain unaffected by the field, see Sec. 4.2.1) contribute to the UCF. This high-field regime is suitable for experimental investigation of the UCF, as one can tune the magnetic field to observe the fluctuations, whose amplitude remains constant as a function of the field. At the same time, the field-dependent W(A)L effects are suppressed and do not influence the measurements.

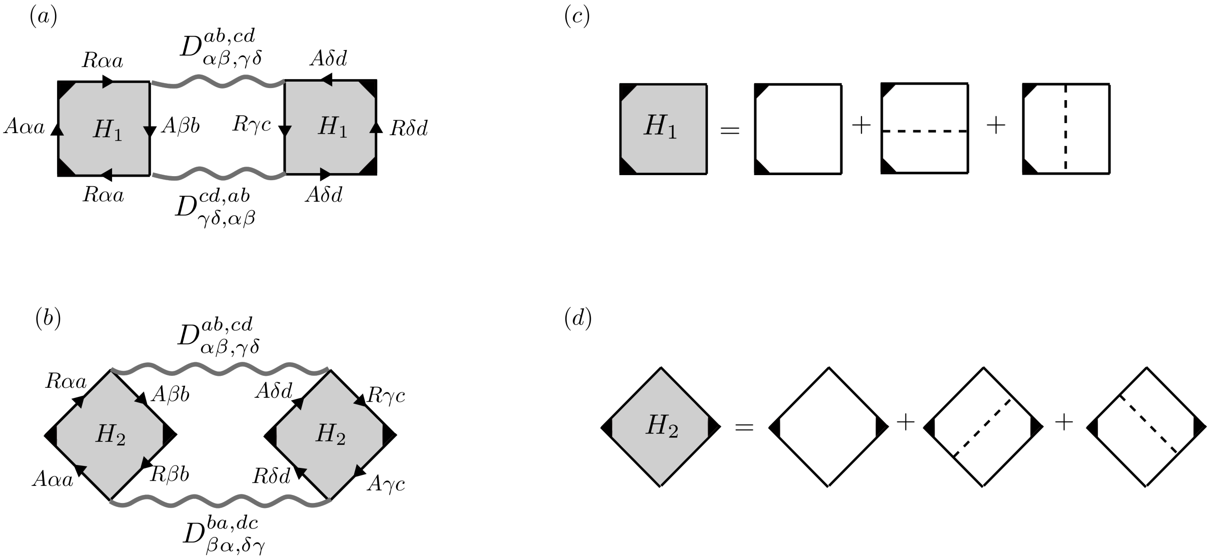

Figure 8.3: (a) and (b): Diagrammatic form of the two contributions to the UCF – fluctuations of the density of states (a) and fluctuations of the diffusion constant (b). Gray wavy lines represent diffusons. Diagrams where the retarded (R) and advanced (A) Green's functions exchange places need to be considered as well. (c) and (d): Dressed Hikami boxes.

Fluctuations of the density of states [Fig. 8.3 (a)] are given as

$$\overline{\delta G_1^2} = 2\left(\frac{e^2}{2\pi L^2}\right)^2 H_1^2 \int \frac{d^2\mathbf{q}}{(2\pi)^2} D^{ab,cd}_{\alpha\beta,\gamma\delta}(\mathbf{q}) D^{cd,ab}_{\gamma\delta,\alpha\beta}(\mathbf{q}) [\delta_{ab}\delta_{cd} + \Xi^2 \delta_{a\bar{b}}\delta_{c\bar{d}}], \tag{8.11}$$

while the fluctuations of the diffusion constant [Fig. 8.3 (b)] are

$$\overline{\delta G_2^2} = \left(\frac{e^2}{2\pi L^2}\right)^2 H_2^2 \int \frac{d^2\mathbf{q}}{(2\pi)^2} D^{ab,cd}_{\alpha\beta,\gamma\delta}(\mathbf{q}) D^{ba,dc}_{\beta\alpha,\delta\gamma}(\mathbf{q}) [\delta_{ab}\delta_{cd} + \Xi^2 \delta_{a\bar{b}}\delta_{c\bar{d}}]. \tag{8.12}$$

Here, H_1 and H_2 are dressed Hikami boxes, shown in diagrammatic form in Fig. 8.3 (c) and (d). They evaluate to

$$H_1 = \pi\nu_{0K}\tau_0^3\left(\frac{\tau_{tr}}{\tau_0}\right)v_F^2, \qquad H_2 = 2H_1. \tag{8.13}$$

Next, after the transformation to the singlet-triplet basis, we have

$$\begin{aligned}
\overline{\delta G_1^2} &= 2\left(\frac{e^2 D\nu_{0K}\tau_0^2}{L^2}\right)^2 \sum_{ss'}\int\frac{d^2\mathbf{q}}{(2\pi)^2}\left[\sum_{ll'=0,z} D^{ll'}_{ss'}(\mathbf{q})D^{l'l}_{s's}(\mathbf{q}) + \Xi^2\sum_{ll'=x,y} D^{ll'}_{ss'}(\mathbf{q})D^{l'l}_{s's}(\mathbf{q})\right],\\
\overline{\delta G_2^2} &= \left(\frac{e^2 D\nu_{0K}\tau_0^2}{L^2}\right)^2 \sum_{ss'}\int\frac{d^2\mathbf{q}}{(2\pi)^2}\left[\sum_{ll'=0,z} [D^{ll'}_{ss'}(\mathbf{q})]^2 + \Xi^2\sum_{ll'=x,y} [D^{ll'}_{ss'}(\mathbf{q})]^2\right].
\end{aligned} \tag{8.14}$$

We can split the diffusons to ones diagonal in singlet-triplet space ($D^{ll}_{ss} = D^l_s$) and the non-diagonal ones. As seen from Eq. (7.19), the off-diagonal diffusons vanish in the absence of Ising SOC, and only a number of them are non-zero when Ising SOC is present: D^{kl}_{ij} and D^{ij}_{kl}, where $(i,j) = (x,y),(y,x)$ and $(k,l) = (0,z),(z,0)$. Let us introduce functions $M_{1,2}(\mathbf{q})$, that collect all non-diagonal diffusons

$$\begin{aligned}
M_1(\mathbf{q}) &= D^{0z}_{xy}(\mathbf{q})D^{z0}_{yx}(\mathbf{q}) + D^{z0}_{xy}(\mathbf{q})D^{0z}_{yx}(\mathbf{q}) = -\frac{1}{2}\sum_{(i,j)}\sum_{(k,l)}[D^{kl}_{ij}(\mathbf{q})]^2,\\
M_2(\mathbf{q}) &= D^{xy}_{0z}(\mathbf{q})D^{yx}_{z0}(\mathbf{q}) + D^{yx}_{0z}(\mathbf{q})D^{xy}_{z0}(\mathbf{q}) = -\frac{1}{2}\sum_{(i,j)}\sum_{(k,l)}[D^{ij}_{kl}(\mathbf{q})]^2.
\end{aligned} \tag{8.15}$$

The total UCF, $\overline{\delta G^2} = \overline{\delta G_1^2} + \overline{\delta G_2^2}$, are then

$$\begin{aligned}
\overline{\delta G^2} = 4\left(\frac{e^2 D\nu_{0K}\tau_0^2}{L^2}\right)^2 \int\frac{d^2\mathbf{q}}{(2\pi)^2}\Bigg[6\sum_{l=0,z;s}\left[D^l_s(\mathbf{q})\right]^2 + 6\Xi^2\sum_{l=x,y;s}\left[D^l_s(\mathbf{q})\right]^2\\
- 4M_1(\mathbf{q}) - 4\Xi^2 M_2(\mathbf{q})\Bigg].
\end{aligned} \tag{8.16}$$

After expressing the diffusons with Eqs. (7.17) and (7.19), the expression for the UCF becomes

$$\begin{aligned}
\overline{\delta G^2} = \left(\frac{e^2 D}{hL^2}\right)^2\int\frac{d^2\mathbf{q}}{(2\pi)^2}\Bigg[\sum_{s,l=0,z}\frac{6}{(\mathcal{P}^l_s)^2} + \sum_{\pm}\frac{4(1+2\gamma_{iv}^2)}{(\mathcal{P}^+_{iv} \pm \frac{\Gamma^-_{iv}}{\gamma_{iv}})^2} + \frac{24\Xi^2}{(\mathcal{P}^x_x)^2} + \sum_{\pm}\frac{4\Xi^2(1+2\gamma_s^2)}{(\mathcal{P}^+_s \pm \frac{\Gamma^-_s}{\gamma_s})^2}\\
+ \frac{16(1-\gamma_{iv}^2)}{(\mathcal{P}^+_{iv})^2 - (\frac{\Gamma^-_{iv}}{\gamma_{iv}})^2} + \frac{16\Xi^2(1-\gamma_s^2)}{(\mathcal{P}^+_s)^2 - (\frac{\Gamma^-_s}{\gamma_s})^2}\Bigg].
\end{aligned} \tag{8.17}$$

The quantities $\mathcal{P}^l_s$ were defined below Eq. (7.17), and $\Gamma^{\pm}_{iv,s}$ and $\gamma_{iv,s}$ were defined in Eq. (7.23). Furthermore, we have introduced $\mathcal{P}^+_{iv,s} = D|\mathbf{q}|^2 - i\omega + \tau_\phi^{-1} + \Gamma^+_{iv,s}$.

The integral over momenta can be evaluated by introducing the quantization $q_x = n\pi/L, (n = 1,2,3...)$ and $q_y = n\pi/W (m = 0,1,2...)$. As the sample is connected to leads in the x-direction, as illustrated in Fig. 8.2, the zero mode ($m = 0$) appears only for the y-direction. UCF are then

$$\overline{\delta G^2} = \left(\frac{e^2}{h}\right)^2 \sum_{m,n} \Bigg[\sum_{s,l=0,z} \frac{6}{[\alpha_{nm} + (\frac{L}{L_s^l})^2]^2} + \sum_{\pm} \frac{4(1+2\gamma_{iv}^2)}{[\alpha_{nm} + (\frac{L}{L_{iv}^+})^2 \pm \frac{1}{\gamma_{iv}}(\frac{L}{L_{iv}^-})^2]^2} \\ + \frac{24\Xi^2}{[\alpha_{nm} + (\frac{L}{L_x^x})^2]^2} + \sum_{\pm} \frac{4\Xi^2(1+2\gamma_s^2)}{[\alpha_{nm} + (\frac{L}{L_s^+})^2 \pm \frac{1}{\gamma_s}(\frac{L}{L_s^-})^2]^2} \\ + \frac{16(1-\gamma_{iv}^2)}{[\alpha_{nm} + (\frac{L}{L_{iv}^+})^2]^2 - [\frac{1}{\gamma_{iv}}(\frac{L}{L_{iv}^-})^2]^2} + \frac{16\Xi^2(1-\gamma_s^2)}{[\alpha_{nm} + (\frac{L}{L_s^+})^2]^2 - [\frac{1}{\gamma_s}(\frac{L}{L_s^-})^2]^2} \Bigg]. \tag{8.18}$$

Here, $\alpha_{nm} = \pi^2 n^2 + (L/W)^2 \pi^2 m^2 + (L/L_\phi)^2$, and we have introduced length scales associated with the diffuson gaps, $L_s^l = \sqrt{D/\Gamma_s^l}$, and $L_\phi = \sqrt{D\tau_\phi}$.

8.3 Regimes of UCF

Eq. (8.18) is the main result of this Chapter, which describes the behavior of UCF in TMDs and their heterostructures with graphene. In the following, we analyze this result in various regimes and compare it with previous theories. We will take the length of the sample $L \lesssim L_\phi$, which is a necessary condition for UCF to appear, as otherwise all coherence effects are suppressed.

We will assume a realistic regime where intervalley scattering and Ising SOC dominate over spin-dependent scattering: $\Delta_{so}, \tau_{iv}^{-1} \gg \tau_s^{-1}$. As discussed in Sec. 7.3.1, the effect of spin-dependent scattering in this regime is captured by only two rates, τ_{sym}^{-1} and τ_{asy}^{-1}, defined in Eq. (7.26). Furthermore, $\gamma_{iv} = 1/\sqrt{1 - 4\Delta_{so}^2 \tau_{iv}}$ and $\gamma_s \approx 0$. We will assume that the effect of trigonal warping, captured by the rates τ_*^{-1} and τ_{**}^{-1} is negligible compared to intervalley scattering, such that $\tau_*^{-1}, \tau_{**}^{-1} \approx \tau_{iv}^{-1}$. In that case, Eq. (8.18) becomes

$$\overline{\delta G^2} = \left(\frac{e^2}{h}\right)^2 \sum_{mn} \Bigg[\frac{6}{\alpha_{nm}^2} + \frac{6}{(\alpha_{nm} + 2\frac{L^2}{L_{asy}^2})^2} + \frac{12}{(\alpha_{nm} + 2\frac{L^2}{L_{iv}^2})^2} + \frac{4(1+2\gamma_{iv}^2)}{[\alpha_{nm} + \frac{L^2}{L_{iv}^2}(1 + \frac{1}{\gamma_{iv}})]^2} \\ + \frac{4(1+2\gamma_{iv}^2)}{[\alpha_{nm} + \frac{L^2}{L_{iv}^2}(1 - \frac{1}{\gamma}) + \frac{L^2}{L_s^2}]^2} + \frac{24\Xi^2}{(\alpha_{nm} + \frac{L^2}{L_{iv}^2})^2} + \sum_{\pm} \frac{4\Xi^2}{[\alpha_{nm} + \frac{L^2}{L_{iv}^2} \pm 2i\frac{L^2}{L_{so}^2}]^2} \\ + \frac{16(1-\gamma_{iv}^2)}{[\alpha_{nm}^2 + \frac{L^2}{L_{iv}^2}(1 - \frac{1}{\gamma_{iv}}) + \frac{L^2}{L_s^2}][\alpha_{nm} + \frac{L^2}{L_{iv}^2}(1 + \frac{1}{\gamma_{iv}})]} + \frac{16\Xi^2}{(\alpha_{nm} + \frac{L^2}{L_{iv}^2})^2 - (2i\frac{L^2}{L_{so}^2})^2} \Bigg]. \tag{8.19}$$

Here, we introduced $L_{asy} = \sqrt{D\tau_{asy}}$, $L_s = \sqrt{D\tau_s}$ and $L_{so} = \sqrt{D/\Delta_{so}}$. The following separation between relevant length scales holds under our assumptions: L_{iv}, $L_{so} \ll L_s < L_{asy}$.

We can represent the conductance fluctuations as

$$\langle \delta G^2 \rangle = A\mathcal{R}_0, \qquad \mathcal{R}_0 = 24\left(\frac{e^2}{h}\right)^2 \sum_{mn} \alpha_{nm}^{-2}, \tag{8.20}$$

where $\mathcal{R}_0$ is the amplitude of UCF in a conventional metal. It depends on the geometry of the sample, e.g. taking a long and narrow sample (nanowire) with $L_\phi \gg L \gg W$ yields $\mathcal{R}_0 = 24\sum_n(\pi^4n^4)^{-1}(e^2/h^2)^2 = 4/15(e^2/h)^2$ [28].

The value of A depends on the details of non-diagonal disorder, as well as on spin-orbit coupling. If L is the largest length scale in the system, $L \gg L_{asy}$, we obtain $A = 1/4$. This is the same result as in conventional metals with strong spin-dependent impurities [87,88]. On the other hand, if L is the shortest length scale, $L \ll L_{iv}, L_{so}$, we obtain $A = 2(1+\Xi^2)$, which corresponds to a case of a Dirac material in a smooth (diagonal) disorder potential. For the case $\Xi = -1$, which holds in graphene, we reproduce the result $A = 4$ found for pristine graphene [89, 90]. The same result holds in Dirac materials with high mass E_g ($\Xi = 1$). The four-fold increase in the amplitude of UCF, compared to conventional metals, is a consequence of the valley degeneracy.

Outside of these two extreme cases, $A \in [\frac{1}{4}, 2(1+\Xi^2)]$. Spin- and valley-dependent disorder, as well as Ising SOC, all act by suppressing the value of A compared to the maximal one. We analyze this value in the two cases, for $\tau_{iv}^{-1} \gg \Delta_{so}$ and for $\Delta_{so} \gg \tau_{iv}^{-1}$, and summarize our results in Table 8.1. In the regime $\tau_{iv}^{-1} \gg \Delta_{so}$, as in Sec. 7.3.1, it is useful to introduce an effective scattering rate $\tilde{\tau}_s^{-1} = \tau_s^{-1} + 2\Delta_{so}^2\tau_{iv}$, and the associated length scale $\tilde{L}_s = \sqrt{D\tilde{\tau}_s}$.

(a) $\tau_{iv}^{-1} \gg \Delta_{so}$

$L \gg L_{asy}$	$L_{asy} \gg L \gg \tilde{L}_s$	$\tilde{L}_s \gg L \gg L_{iv}$	$L_{iv} \gg L$
1/4	1/2	1	$2(1+\Xi^2)$

(b) $\Delta_{so} \gg \tau_{iv}^{-1}$

$L \gg L_{asy}$	$L_{asy} \gg L \gg L_{iv}$	$L_{iv} \gg L \gg L_{so}$	$L_{so} \gg L$
1/4	1/2	$1+\Xi^2$	$2(1+\Xi^2)$

Table 8.1: Value of the coefficient A, related to the amplitude of universal conductance fluctuations, in the regimes (a) $\tau_{iv}^{-1} \gg \Delta_{so}$, and (b) $\Delta_{so} \gg \tau_{iv}^{-1}$

The amplitude of UCF can be measured in experiment, and serve as an useful probe of various microscopic processes that influence the quantum interference. The system behaves as a conventional metal ($A = 1$) in the regime $\tau_{iv}^{-1} \gg \Delta_{so}$ with $\tilde{L}_s \gg L \gg L_{iv}$. Here, both valley and spin physics are suppressed, by intervalley scattering and electron decoherence, respectively. Value of $A < 1$, indicates that the physics of the sample is dominated by spin-dependent phenomena, either due to spin-orbit scattering or due to Ising SOC. Value of $A > 1$ shows that the valley physics dominates (due to intervalley scattering and Ising SOC), while spin-dependent scattering plays a lesser role. Finally, the value $A > 2$ could serve as an indication that the Fermi level of the system is either close to the band bottom ($\Xi = 1$), or deep in the band ($\Xi = -1$).

UCF can be studied in the same experimental setup as WL magnetoconductance, but preferably at higher perpendicular magnetic fields, where field-sensitive Cooperons are suppressed and do not contribute. As discussed in Chapter 7, it is difficult to reliably interpret the WL magnetoconductance measurements in TMDs and graphene/TMD heterostructures, due to a large number of processes that can influence it. Measuring UCF could provide useful complementary information.

So far, no dedicated, high-field, experimental studies of the UCF in TMDs or graphene/ TMD heterostructures have been performed. Let us mention that in Ref. [17] (see its supplemental material), which measured W(A)L magnetoconductance in graphene / WS_2, the UCF signal was extracted in the low-field regime. This was done by subtracting the W(A)L contribution, obtained by fitting the data to the HLN formula, from the magnetoconductance. The amplitude of UCF was then used to estimate the coherence rate τ_ϕ^{-1}, which was found to be in agreement with the HLN fits.

8.4 Summary

In this Chapter, we have studied UCF in TMDs and graphene/TMD heterostructures using the standard diagrammatic technique for disordered systems. We generalize previous theories that concern simple metals with spin-orbit impurities and graphene. We account for the complex behavior of UCF in these materials, resulting from the interplay of spin, valley, and Berry phase physics, and provide a formula that can be used to interpret experiments in all parameter regimes.

Chapter 9

Conclusions and perspectives

In this thesis, we investigated how the unique interplay of intrinsic, Ising, spin-orbit coupling and disorder influences the quantum coherent phenomena in transition metal dichalcogenide monolayers (TMD). In Part I, we addressed the unusual Ising superconductivity in TMDs, while in Part II, we studied the quantum interference corrections to the conductance in the normal state of TMDs and their heterostructures with graphene. The results are directly applicable to a significant number of recent experiments. To obtain them, we used analytical techniques for disordered systems, including the quasiclassical Eilenberger Green's functions for superconductivity, and diagrammatic methods. Below we summarize our main findings:

- Measurements of the upper critical field in the n-doped ($\mathrm{MoS_2}$, $\mathrm{WS_2}$) and p-doped ($\mathrm{NbSe_2}$, $\mathrm{TaS_2}$) TMD superconductors show a large enhancement of the upper critical field (H_{c2}), well beyond the Pauli limit, which has been attributed to the intrinsic Ising SOC. The simple theory for clean Ising superconductors, however, fails to describe these experiments, as it overestimates H_{c2}. In order to study how disorder affects this picture, we formulated the quasiclassical theory of disordered TMDs, and calculated H_{c2} and the density of states in the superconducting state, in both n- and p-doped regimes. We found that *intravalley* scattering, which can be caused by any kind of disorder, does not modify the superconducting properties, similarly to the Anderson theorem for conventional superconductors.
    - We first studied n-doped Ising superconductors in Chapter 5, where only the K-bands are present at the Fermi level. We showed that *intervalley* scattering, which is caused by short-range disorder, has a significant effect on the superconducting properties, as it acts as an effective spin-flip mechanism. Thus, it limits H_{c2} and introduces smearing of the density of states. We found that weak intervalley scattering of the order of the superconducting gap is enough to explain the experimental measurements of H_{c2}.
    - In Chapter 6, we studied p-doped TMDs, which are multiband superconductors. Here, aside from the K-band, the Γ-band contributes to the superconductivity as well. We assumed that superconductivity develops primarily in the K-band, and that it is induced by proximity effect in the Γ-band. The two bands are coupled by *interband disorder*, in-line with recent experiments [57]. We found that weak interband disorder, of the order of the superconducting

gap, can account for both the amplitude of the upper critical field and the shape of the density of states measured in experiment.

- Having established that disorder plays a crucial role in explaining the superconducting properties of TMDs, we turned to studying the quantum interference corrections to their conductance in the normal state, as an additional, independent probe of disorder and SOC. Our results also extend to graphene/TMD heterostructures, which are described by a similar model as TMDs. We studied weak (anti-) localization in Chapter 7 and universal conductance fluctuations in Chapter 8. Both of these phenomena are governed by a complex interplay of several ingredients that infuence quantum interference: spin-splitting due to Ising SOC, valley structure and intervalley scattering, and the Berry phase due to the Dirac-like band structure. Our results generalize previous theories for graphene and simple metals with spin-orbit impurities, and describe novel behavior beyond them. We discussed our results in various regimes of interest for the interpretation of recent experiments.

Many questions still remain open for future work, in particular in relation to superconductivity in TMDs. In this thesis, we considered only the simplest, uniform, s-wave phase. A number of theoretical studies have considered more exotic scenarios with triplet pairing and topological properties [51, 52], but only in the clean case. An extension of the quasiclassical formalism presented in this thesis could be used to study the effect of disorder. In order to explore the viability of these exotic phases in realistic experimental situations, and to examine the robustness of edge states, it is important to know the effect of disorder, particularly because unconventional superconductivity is usually very sensitive to it.

Hybrid systems of TMDs and other materials, such as ferromagnets, topological materials, or other superconductors, are still largely unexplored. Such systems could host novel physical phenomena, including topological superconductivity, as recently predicted for a junction of an Ising superconductor and a half-metal wire [53]. Furthermore, additional information about TMDs can be obtained from their non-equilibrium properties. For instance, the inverse Edelstein effect [130] is a phenomenon where a non-equilibrium spin accumulation drives electric currents. Studying it in TMDs in a juction with a ferromagnet under ferromagnetic resonance condition could provide additional information about spin-relaxation. Some experiments in such setups have already been performed [131]. The hybrid systems mentioned above can also be studied using the quasiclassical formalism.

Conclusion (Français)

Au cours de cette thèse, nous avons étudié comment les effets mutuels du couplage spin-orbite (SOC) d'Ising intrinsèque et du désordre influencent les phénomènes de cohérence quantique dans les monocouches de dichalcogénures de métaux de transition (TMD). Dans la première partie, nous avons étudié la supraconductivité exotique, dite d'Ising, dans les TMD ; dans la deuxième partie, nous avons étudié les corrections à la conductance dans l'état normal qui sont induites par les interférences quantiques dans les TMD et les hétérostructures graphène /TMD. Les résultats sont directement applicables à un nombre considérable d'expériences récentes. Nous les avons obtenus par des méthodes analytiques adaptées à l'étude des systèmes désordonnés, telles que les fonctions de Green quasiclassiques pour la supraconductivité, et les méthodes diagrammatiques pour les interférences quantiques. Nous résumons ci-dessous nos principaux résultats :

- Les mesures du champ critique dans les supraconducteurs TMD dopés n (MoS_2, WS_2) et dopés p ($NbSe_2$, TaS_2) montrent une nette augmentation du champ critique (H_{c2}) - bien au-delà de la limite de Pauli - qui a été attribuée au SOC d'Ising. Cependant, la théorie simple des supraconducteurs d'Ising sans désordre ne parvient pas à décrire ces expériences, car elle surestime H_{c2}. Afin d'étudier comment le désordre affecte cette image, nous avons formulé la théorie quasiclassique des TMD désordonnés, puis nous avons calculé H_{c2} et la densité des états dans l'état supraconducteur dans les régimes dopés n et p. Nous avons constaté que la diffusion intra-vallée, qui peut être causée par tout type de désordre, ne modifie pas les propriétés supraconductrices, de façon analogue au "théorème d'Anderson" pour les supraconducteurs conventionnels.

  - Dans le Chapitre 5, nous avons d'abord étudié les supraconducteurs d'Ising dopés n, dans lesquels seules les bandes K sont présentes au niveau Fermi. Nous avons montré que la diffusion inter-vallées, qui est causée par un désordre à courte portée, a un effet significatif sur les propriétés supraconductrices, car elle agit comme un mécanisme efficace de spin-flip. Ainsi, ce type de désordre limite H_{c2} et induit un élargissement de la densité d'états. Nous avons constaté qu'une faible diffusion inter-vallée caractérisée par un taux de transition de l'ordre du gap supraconducteur suffit à expliquer les mesures expérimentales de H_{c2}.
  - Dans le Chapitre 6, nous avons étudié les TMD dopés p qui sont des supraconducteurs multibandes. En plus des bandes K, la bande Γ contribue également à la supraconductivité. Nous avons supposé que la supraconductivité se développe principalement dans les bandes K et qu'elle est induite par effet de proximité

dans la bande Γ. Les deux bandes sont couplées par le désordre inter-bande, en accord avec des expériences récentes [57]. Nous avons constaté qu'un faible désordre inter-bande, caractérisé par un taux de transition de l'ordre de gap supraconducteur, peut expliquer à la fois l'amplitude du champ critique et la forme de la densité d'états mesurée expérimentalement.

- Ayant établi que le désordre a un rôle crucial dans l'explication des propriétés supraconductrices des TMD, nous nous sommes tournés vers l'étude des corrections à la conductance dues aux interférences quantiques dans l'état normal. Ces études fournissent une sonde supplémentaire et indépendante du désordre et du SOC. Nos résultats s'étendent également aux hétérostructures graphène/TMD, qui sont décrites par un modèle similaire aux TMD. Nous avons étudié la localisation et l'antilocalisation faibles au Chapitre 7 et les fluctuations universelles de la conductance au Chapitre 8. Ces deux phénomènes sont régis par une interaction complexe de plusieurs ingrédients qui modifient les interférences quantiques : le spin-splitting dû au couplage spin-orbite d'Ising, la structure des vallées, la diffusion inter-vallée et la phase Berry due à la structure de bande de type Dirac. Nos résultats généralisent les théories antérieures pour le graphène et les métaux simples contenant des impuretés spin-orbite. Nous avons discuté nos résultats dans divers régimes pertinents pour l'interprétation d'expériences récentes.

De nombreuses questions restent ouvertes pour les travaux futurs, en particulier en ce qui concerne la supraconductivité dans les TMD. Dans cette thèse, nous n'avons considéré que le cas le plus simple d'une supraconductivité de type s. Un certain nombre d'études théoriques ont examiné des scénarios plus exotiques conduisant à des appariements triplets et exhibant des propriétés topologiques [51, 52], mais seulement dans le cas sans désordre. Une extension du formalisme quasi classique présenté ici pourrait être utilisée pour étudier l'effet du désordre. Afin d'explorer la viabilité de ces phases exotiques dans des situations expérimentales réalistes et d'examiner la robustesse des états de bord, il est important de connaître l'effet du désordre, notamment parce que la supraconductivité non-conventionnelle y est généralement très sensible.

Les systèmes hybrides de TMD et d'autres matériaux, tels que les composés ferromagnétiques, les matériaux topologiques ou d'autres supraconducteurs, sont encore peu explorés. De tels systèmes pourraient présenter de nouveaux phénomènes physiques, y compris la supraconductivité topologique, comme il a été récemment prédit dans une jonction entre un supraconducteur d'Ising et un fil demi-métallique [53]. En outre, des informations supplémentaires sur les TMD peuvent être obtenues à partir de leurs propriétés hors-équilibre. Par exemple, l'effet Edelstein inverse [130] est un phénomène où une accumulation de spin hors-équilibre induit des courants électriques. Etudier ces effets dans une jonction entre un TMD et un métal ou un isolant ferromagnétique placé dans les conditions de la résonance ferromagnétique pourrait fournir des informations supplémentaires sur la relaxation du spin. Des expériences ont déjà été réalisées dans de telles configurations [131]. Les systèmes hybrides mentionnés ci-dessus peuvent également être étudiés en utilisant le formalisme quasi-classique.

Abbreviations

2D	Two-dimensional
2DEG	Two-dimensional electron gas
AG	Abrikosov-Gor'kov
BCS	Bardeen-Cooper-Schrieffer
BdG	Bogoliubov-de Gennes
DFT	Density functional theory
DoS	Density of states
FFLO	Fulde-Ferrell-Larkin-Ovchinnikov
HLN	Hikami-Larkin-Nagaoka
MF	McCann-Fal'ko
SOC	Spin-orbit coupling
TMD	Transition metal dichalcogenide monolayer
UCF	Universal conductance fluctuations
W(A)L	Weak (anti-) localization

Appendix A

Some useful definitions

In this Appendix, we define a number of functions related with anisotropy of the disorder potential in the projected basis. They will be extensively used in Appendices B and D, where they appear in impurity lines in diagrammatic calculations, as well as in disorder-induced self-energy in the quasiclassical formalism. We define

$$\begin{aligned} F^i_{\theta,\theta'} &= [f^i_{\theta,\theta'}]_\eta [f^i_{\bar\theta,\bar\theta'}]_{\bar\eta} = [f^i_{\theta,\theta'}]_\eta [f^i_{\theta',\theta}]_\eta, & \tilde F^i_{\eta\theta,\theta'} &= [f^i_{\theta,\theta'}]_\eta [f^i_{\bar\theta,\bar\theta'}]_\eta = [f^i_{\theta,\theta'}]_\eta [f^i_{\theta,'\theta}]_{\bar\eta}, \\ G^j_{\theta,\theta'} &= [g^j_{\theta,\theta'}]_\eta [g^j_{\bar\theta,\bar\theta'}]_{\bar\eta} = [g^j_{\theta,\theta'}]_\eta [g^j_{\theta',\theta}]_{\bar\eta}, & G^y_{\theta,\theta'} &= [g^y_{\theta,\theta'}]_\eta [g^y_{\bar\theta,\bar\theta'}]_{\bar\eta} = -[g^y_{\theta,\theta'}]_\eta [g^y_{\theta',\theta}]_{\bar\eta}. \end{aligned} \tag{A.1}$$

Where $i = 0, x, y, z$ and $j = +, -, x$. Functions f and g are defined in Eq. (3.9). Functions F are related to intravalley disorder, and are given as

$$\begin{aligned} F^0_{\theta,\theta'} &= \cos^2\left(\frac{\theta-\theta'}{2}\right) + \frac{E_g^2}{\mu^2}\sin^2\left(\frac{\theta-\theta'}{2}\right), & F^z_{\theta,\theta'} &= \frac{E_g^2}{\mu^2}\cos^2\left(\frac{\theta-\theta'}{2}\right) + \sin^2\left(\frac{\theta-\theta'}{2}\right), \\ F^x_{\theta,\theta'} &= \frac{v^2 q_F^2}{\mu^2}\cos^2\left(\frac{\theta+\theta'}{2}\right), & F^y_{\theta,\theta'} &= \frac{v^2 q_F^2}{\mu^2}\sin^2\left(\frac{\theta+\theta'}{2}\right), \end{aligned} \tag{A.2}$$

and

$$\begin{aligned} \tilde F^0_{\eta\theta,\theta'} &= e^{-i\eta(\theta-\theta')}\left[\cos^2\left(\frac{\theta-\theta'}{2}\right) - \frac{E_g^2}{\mu^2}\sin^2\left(\frac{\theta-\theta'}{2}\right) + i\eta\frac{E_g}{\mu}\sin(\theta-\theta')\right], \\ \tilde F^z_{\eta\theta,\theta'} &= e^{-i\eta(\theta-\theta')}\left[\frac{E_g^2}{\mu^2}\cos^2\left(\frac{\theta-\theta'}{2}\right) - \sin^2\left(\frac{\theta-\theta'}{2}\right) + i\eta\frac{E_g}{\mu}\sin(\theta-\theta')\right], \\ \tilde F^x_{\eta\theta,\theta'} &= -e^{-i\eta(\theta-\theta')}\frac{v^2 q_F^2}{\mu^2}\cos^2\left(\frac{\theta+\theta'}{2}\right), \qquad \tilde F^x_{\eta\theta,\theta'} = -e^{-i\eta(\theta-\theta')}\frac{v^2 q_F^2}{\mu^2}\sin^2\left(\frac{\theta+\theta'}{2}\right). \end{aligned} \tag{A.3}$$

Functions G are related with intervalley disorder, and are given as

$$\begin{aligned} G^+_{\theta,\theta'} &= \left(1 \pm \frac{E_g}{\mu}\right)^2, & G^-_{\theta,\theta'} &= \left(1 \mp \frac{E_g}{\mu}\right)^2, \\ G^x_{\theta,\theta'} &= \frac{v^2 q_F^2}{\mu^2}\sin^2\left(\frac{\theta-\theta'}{2}\right), & G^y_{\theta,\theta'} &= -\frac{v^2 q_F^2}{\mu^2}\cos^2\left(\frac{\theta-\theta'}{2}\right). \end{aligned} \tag{A.4}$$

The upper and lower sign in Eq. (A.4) hold in conduction and valence band, respectivelly.

Appendix B

Ising superconductivity

In this Appendix, we provide technical details and derivations related to Chapter 5. We derive the Eilenberger equation (5.4) in Sec. B.1. In Sec. B.2, we write the full quasiclassical Green's function in the absence of intervalley disorder, and present derivations of Eqs. (5.21) and (5.27). We present the results of a numerical analysis of h_{c2} in a broad range of intervalley disorder in Sec. B.3. Finally, in Sec. B.4 we show the derivation of Eq. (5.11) using the diagrammatic technique, alternative to the quasiclassical approach used in the main text.

B.1 Derivation of the Eilenberger equation

Starting from the BdG Hamiltonian for single-band Ising superconductors (5.2), we find that the disorder-averaged Gor'kov Green's function $\mathcal{G}_{\eta\mathbf{q}}$ is determined by the equation

$$(i\omega_n - \xi_{\mathbf{q}}\tau_z - \eta\Delta_{so}s_z\tau_z - \Delta\tau_x - hs_x - \Sigma_{\eta\mathbf{q}})\langle\mathcal{G}_{\eta\mathbf{q}}\rangle = 1. \tag{B.1}$$

Here, $\Sigma_{\eta\mathbf{q}}$ is the self-energy associated with the potential disorder (3.6), calculated using the self-consistent Born approximation. It is defined as

$$\Sigma_{\eta\mathbf{q}} = \int \frac{d^2\,\mathbf{q}'}{(2\pi)^2}\left[U_0^2 F^0_{\theta,\theta'}\tau_z\langle\mathcal{G}_{\eta\mathbf{q}'}\rangle\tau_z + \sum_{i=\pm,x}\sum_{j=x,y} V_{ij}^2 G^i_{\theta,\theta'}\tau_z\langle\mathcal{G}_{\bar{\eta}\mathbf{q}'}\rangle\tau_z\right]. \tag{B.2}$$

Next, we define the quasiclassical Green's function as

$$g_{\eta\theta} = \frac{i}{\pi}\int d\xi_{\mathbf{q}}\,\langle\mathcal{G}_{\eta\mathbf{q}}\rangle. \tag{B.3}$$

Note that it depends on the angle θ, due to the anisotropy of the projected disorder potential. After integrating Eq. (B.1) over energies $\xi_{\mathbf{q}}$ and using the definition (B.3), we obtain the Eilenberger equation

$$[(\omega_n + ihs_x + i\Delta\tau_x)\tau_z + i\eta\Delta_{so}s_z + \sigma_{\eta\theta}, g_{\eta\theta}] = 0, \tag{B.4}$$

where we have introduced the reduced self-energy

$$\sigma_{\eta\theta} = \pi\nu_{0K}\int\frac{d\theta'}{2\pi}U_0^2 F^0_{\theta,\theta'}g_{\eta\theta'} + \pi\nu_{0K}\int\frac{d\theta'}{2\pi}\sum_{i=\pm,x}\sum_{j=x,y}V_{ij}^2 G^i_{\theta,\theta'}g_{\bar{\eta}\theta'}. \tag{B.5}$$

Functions F^0 and G^i are defined in Appendix A. The quasiclassical Green's function must satisfy the normalization condition

$$g_{\eta\theta}^2 = 1. \tag{B.6}$$

In order to resolve the angular structure of $g_{\eta\theta}$, we expand it into first harmonics in angle θ

$$g_{\eta\theta} \approx g_{\eta 0} + g_{\eta 1}\cos\theta + g_{\eta 2}\sin\theta. \tag{B.7}$$

Then, we substitute this expansion in Eq. (B.4) to obtain a system of coupled equations for the harmonics $g_{\eta i}$. We find its solution yields $g_{\eta 0} \neq 0$ and $g_{\eta 1}, g_{\eta 2} = 0$. Therefore, the quasiclassical Green's function can be taken to be independent on angles. Thus, the reduced self-energy (B.5) simplifies to

$$\sigma_\eta = \frac{1}{2\tau_0} g_\eta + \frac{1}{2\tau_{iv}} g_{\bar{\eta}}, \tag{B.8}$$

and Eq. (B.4) reduces to the Elenberger equation (5.4) from the main text.

B.2 Derivations of some results from Chapter 5

Full quasiclassical Green's function in the absence of intervalley scattering. Solving the system of equations (5.10) in the absence of intervalley scattering ($\tau_{iv}^{-1} = 0$) yields

$$\begin{aligned} c_0 = \frac{\Delta}{\sqrt{2}} &\Big[[\omega_n^2 + \Delta_{so}^2 + (\Delta - h)^2][\omega_n^2 + \Delta_{so}^2 + (\Delta + h)^2][(\omega_n^2 + \Delta^2)\Delta_{so}^2 + \omega_n^2 h^2)] \Big]^{-1/2} \\ &\times \Big[\Delta_{so}^2(\omega_n^2 + \Delta^2 + \Delta_{so}^2)^2 + [(\omega_n^2 + \Delta_{so}^2)^2 + \Delta^2(\omega_n^2 - \Delta_{so}^2)]h^2 - \omega_n^2 h^4 \\ &+ [\Delta_{so}^2(\omega_n^2 + \Delta^2 + \Delta_{so}^2) + \omega_n^2 h^2]\sqrt{(\omega_n^2 + \Delta^2 + \Delta_{so}^2 + h^2)^2 - 4\Delta^2 h^2} \Big]^{1/2}. \end{aligned} \tag{B.9}$$

Other components can then be expressed as

$$d_0 = \frac{\omega_n}{2\Delta(\omega_n^2 + \Delta_{so}^2)} \left[\omega_n^2 + \Delta_{so}^2 + h^2 - \Delta^2 + \sqrt{(\omega_n^2 + \Delta_{so}^2 + h^2 - \Delta^2)^2 + 4\Delta^2(\omega_n^2 + \Delta_{so}^2)} \right], \tag{B.10}$$

and

$$d_x = -i\frac{c_0(\omega_n c_0 - \Delta d_0)}{h d_0}, \qquad b_y = \frac{\Delta_{so}(\omega_n c_0 - \Delta d_0)}{\omega_n h}. \tag{B.11}$$

Derivation of Eq. (5.21) The system of equations (5.10), after some algebraic manipulations, can be rewritten as

$$h^2 c_0 d_0 + (\omega_n c_0 - \Delta d_0)(\omega_n d_0 + \Delta c_0) + \frac{\Delta_{so}^2 \tau_{iv}(\omega_n c_0 - \Delta d_0)}{\frac{\omega_n \tau_{iv}}{d_0} + 1 + \frac{d_x^2}{c_0^2}} = 0, \tag{B.12}$$

with

$$d_x = -i\frac{c_0(\omega_n c_0 - \Delta d_0)}{h d_0}, \qquad b_y = i\Delta_{so}\frac{d_x d_0}{c_0}\left[\omega_n + \frac{1}{\tau_{iv}} d_0 \left(1 + \frac{d_x^2}{c_0^2} \right) \right]^{-1}. \tag{B.13}$$

If we assume $\Delta_{so}^2\tau_{iv} \gg \Delta_0$, we can take $d_x/c_0 \ll 1$, which will be justified *a posteriori.* Then, Eq. (B.12) becomes

$$\omega_n c_0 - \Delta d_0 = -\frac{h^2}{\Delta_{so}^2\tau_{iv}} c_0 d_0 \left(1 + \frac{\omega_n \tau_{iv}}{d_0}\right), \tag{B.14}$$

which leads to

$$\frac{d_x}{c_0} = -\frac{ih}{\Delta_{so}^2\tau_{iv}} c_0 \left(1 + \frac{\omega_n \tau_{iv}}{d_0}\right), \qquad b_y = -\frac{h}{\Delta_{so}} c_0. \tag{B.15}$$

Starting from the expression for d_x in Eq. (B.15), we immediately see that the assumption $d_x/c_0 \ll 1$ is justified for $h_{c2} \ll \Delta_{so}^2\tau_{iv}$. However, this assumption holds even at higher fields $h \sim \Delta_{so}^2\tau_{iv}$, as in that case Eq. (B.14) gives $c_0 \sim \Delta\Delta_{so}^2\tau_{iv}/h^2 \ll 1$, which yields $d_x/c_0 \ll 1$ when combined with Eq. (B.15).

The normalization condition (5.9) now simplifies to

$$c_0^2 \frac{\Delta_{so}^2}{\rho^2} + d_0^2 = 1. \tag{B.16}$$

After performing the analytical continuation $i\omega_n \to \epsilon + i0^+$, and defining the effective order parameter $\Delta(\epsilon) = -i\epsilon c_0(\epsilon)/d_0(\epsilon)$, Eqs. (B.14) and (B.16) straightforwardly lead to Eq. (5.21) in the main text.

Derivation of Eq. (5.27) In the limit $\tau_{iv}^{-1} \gg \Delta_0$, we obtain from Eq. (B.12)

$$b_y = \frac{i\Delta_{so}\tau_{iv}\frac{d_x}{c_0}}{1 + \frac{d_x^2}{c_0^2}} \ll 1. \tag{B.17}$$

Then, the normalization condition (5.9) becomes

$$(c_0^2 + d_0^2)\left(1 + \frac{d_x^2}{c_0^2}\right) = 1, \tag{B.18}$$

and the system of equations (5.10) simplifies to

$$\begin{aligned} &-\omega_n c_0 - ihc_x + \Delta d_0 = 0, \\ &-\omega_n c_x - ihc_0 + \Delta d_x + \Delta_{so}^2\tau_{iv}(c_0 d_x - d_0 c_x) = 0. \end{aligned} \tag{B.19}$$

Next, we introduce $c_\pm = \frac{1}{2}(c_0 \pm c_x)$ and $d_\pm = \frac{1}{2}(d_0 \pm d_x)$. The normalization condition (B.19) becomes

$$c_\pm^2 + d_\pm^2 = 1, \tag{B.20}$$

and Eq. (B.19) can be rewritten as

$$-(\omega_n \pm ih)c_\pm - \Delta d_\pm \pm \Delta_{so}^2\tau_{iv}(c_- d_+ - d_- c_+) = 0. \tag{B.21}$$

Then, after performing the analytical continuation $i\omega_n \to \epsilon + i0^+$, and defining the effective order parameters $\Delta_\pm(\epsilon) = -i\epsilon c_\pm(\epsilon)/[d_\pm(\epsilon)]$, Eqs. (B.20) and (B.21) lead to Eq. (5.27) in the main text.

B.3 Numerical analysis of h_{c2} in the limits $T \to 0$ and $T \to T_c$

In this section, we numerically evaluate h_{c2} for single band Ising superconductors in the limits $T \to 0$ and $T \to T_c$ in a broad range of intervalley disorder. We compare these results with analytical estimates made in Sec. 5.3.

The value of upper critical field at zero temperature $h_{c2}(0)$ can be obtained from the following equation

$$\ln \frac{2h_{c2}(0)}{\Delta_0} = \int_0^\infty d\omega \left[\frac{\Delta_{so}^2 + \omega_n(\omega_n + \tau_{iv}^{-1})}{h_{c2}^2(\omega_n + \tau_{iv}^{-1}) + \omega_n[\Delta_{so}^2 + \omega_n(\omega_n + \tau_{iv}^{-1})]} - \frac{\omega}{\omega^2 + h_{c2}^2} \right]. \tag{B.22}$$

We plot $h_{c2}(0)$ obtained this way in Fig. B.1 (a) as a function of $1/\tau_{iv}$. We verify that Eq. (5.19) is in good agreement with these results in the relevant parameter regime and that $h_{c2}(0)$ reaches $\Delta_0/2$ for strong disorder.

Close to T_c, the critical field h_{c2} is small, and the assumptions $\Delta_{so} \gg h_{c2}$ and $\ln \frac{T_c}{T} \approx \frac{T_c - T}{T_c}$ hold. Expanding Eq. (5.11) in the main text in this regime yields a square-root behavior

$$h_{c2} \simeq \sqrt{\frac{T_c(T_c - T)}{C}}, \tag{B.23}$$

with

$$C = 2\pi T_c^3 \sum_{\omega_n > 0} \frac{\omega_n + \frac{1}{\tau_{iv}}}{\omega_n^2[\omega_n(\omega_n + \frac{1}{\tau_{iv}}) + \Delta_{so}^2]} \tag{B.24}$$

and $\omega_n = (2n+1)\pi T_c$ (n integer). We plot $1/\sqrt{C}$ obtained this way in Fig. B.1 (b). We verify that Eq. (5.16) is in good agreement with these results in the relevant parameter regime, and that $h_{c2} \approx 2.16 T_c \sqrt{1 - T/T_c}$ for strong disorder.

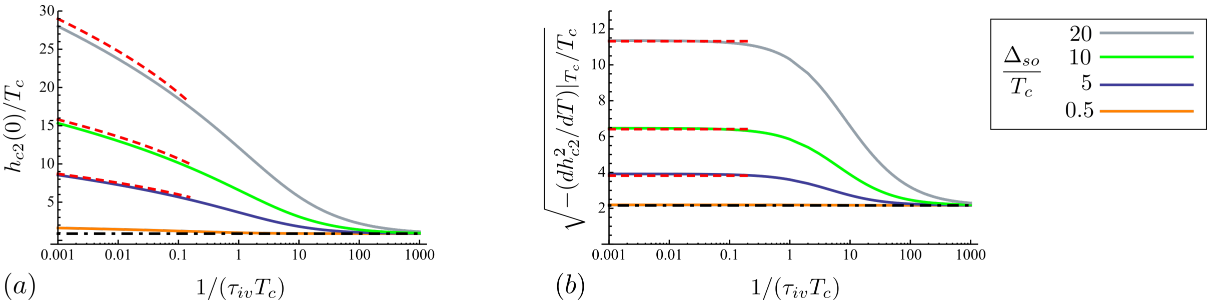

Figure B.1: Behavior of the critical field $h_{c2}(T)$ close to 0 and T_c as a function of disorder strength for various values of the Ising SOC. We show numerical (solid lines) and approximate (dashed lines) results. (a) The critical fields $h_{c2}(0)$ at $T = 0$, obtained from Eq. (B.22) and from Eq. (5.19), calculated up to the second order in the logarithmic approximation. The black dash-dotted line corresponds to the result in the absence of SOC, $h_{c2} = \Delta_0/2$. (b) Behavior of h_{c2} close to T_c: we plot $1/\sqrt{C} = [-(dh_{c2}^2(T)/dT)|_{T_c}/T_c]^{1/2}$, obtained from Eq. (B.24) and from Eq. (5.16). The black dash-dotted line corresponds to $1/\sqrt{C} = 2\pi/\sqrt{7\zeta(3)} \approx 2.16$ in the absence of SOC.

B.4 Diagrammatic calculation of h_{c2} [Eq. (5.11)]

In the vicinity of the second-order phase transition, in the absence of disorder, Δ solves the linearized self-consistent gap equation

$$\Delta = \frac{\lambda T}{4} \sum_{\eta,\mathbf{q},|\omega_n|<\Omega_D} \mathrm{Tr}[is_y \mathcal{G}^{+}_{\bar{\eta}\bar{\mathbf{q}}\omega_n} \Delta i s_y \mathcal{G}^{-}_{\eta\mathbf{q}\omega_n}], \tag{B.25}$$

where λ is the BCS pairing amplitude and Ω_D is a cut-off frequency. Here, we have introduced particle and hole Green's functions, defined as

$$\mathcal{G}^{-}_{\eta\mathbf{q}\omega_n} = (i\omega_n - \mathcal{H}_{\eta\mathbf{q}})^{-1}, \qquad \text{and} \qquad \mathcal{G}^{+}_{\eta\mathbf{q}\omega_n} = (-i\omega_n - \mathcal{H}^{T}_{\eta\mathbf{q}})^{-1}, \tag{B.26}$$

respectively.

In the presence of impurities, the disorder-averaged Green's function can be calculated from the Dyson equation represented diagrammatically in Fig. 4.3. That is, $\langle \mathcal{G}^{\pm}_{\eta\mathbf{q}\omega_n}\rangle = ({\mathcal{G}^{\pm}_{\eta\mathbf{q}\omega_n}}^{-1} - \Sigma^{\pm}_{\eta})^{-1}$, where the self-energy $\Sigma^{\pm}_{\eta}$ is obtained using the self-consistent Born approximation. As a result, we find $\Sigma^{\pm}_{\eta} = \mp i[1/(2\tau_0) + 1/(2\tau_{iv})]\mathrm{sgn}(\omega_n)$.

In Fig. B.2, we define Feynman rules for the diagrammatic perturbative theory. The upper and lower branch in all these diagrams represent the Green's functions $\mathcal{G}^{+}$ and $\mathcal{G}^{-}$, respectively, and all internal momenta (in-between scattering events) are integrated over. In Fig. B.3 (a) we show the diagrammatic representation of the linearized gap equation in the presence of disorder. It involves the vertex functions Π, which are found from a system of coupled Bethe-Salpeter equations, shown in diagrammatic form in Fig. B.3 (b). Here, the first diagram represents the bare vertex, while the second one is a ladder diagram. There are eight distinct vertex functions $\Pi^{ss'}_{\eta}$ (4 combinations of spin indices and 2 values of the valley index).

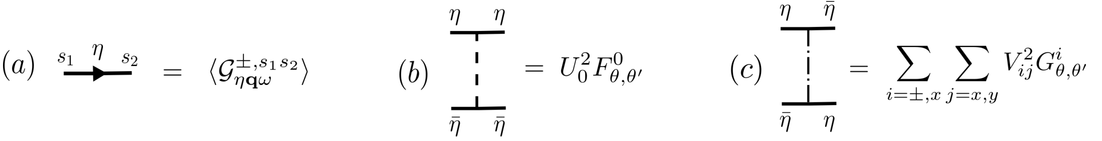

Figure B.2: Feynman rules. (*a*) Disorder-averaged Green's function. (b) Impurity line for intravalley scattering. (c) Impurity line for intervalley scattering. θ and θ' are polar angles associated with the momenta before and after the scattering event. Functions F^0 and G^i are defined in Appendix A.

The diagrams for the disorder-averaged self-consistent gap equation, Fig. B.3 (a), translate to

$$1 = \frac{\lambda}{4} T \int \frac{d^2\,\mathbf{q}}{(2\pi)^2} \sum_{\eta\omega_n s s' s''} s\langle \mathcal{G}^{+,ss'}_{\eta\mathbf{q}\omega_n}\rangle \langle \mathcal{G}^{-,\bar{s}s''}_{\bar\eta\bar{\mathbf{q}}\omega_n}\rangle \left[s'\delta_{\bar{s}'s''} + \Pi^{s's''}_{\eta}(\theta)\right]. \tag{B.27}$$

Here, $s, s', s'' = \pm 1$ denote spin indices. We evaluate the integrals over the momenta using the residue theorem with the substitution $\int \frac{d^2\mathbf{q}}{(2\pi)^2} \approx \frac{\nu_{0K}}{2\pi}\int d\xi_{\mathbf{q}} \int d\theta$, valid in the regime of

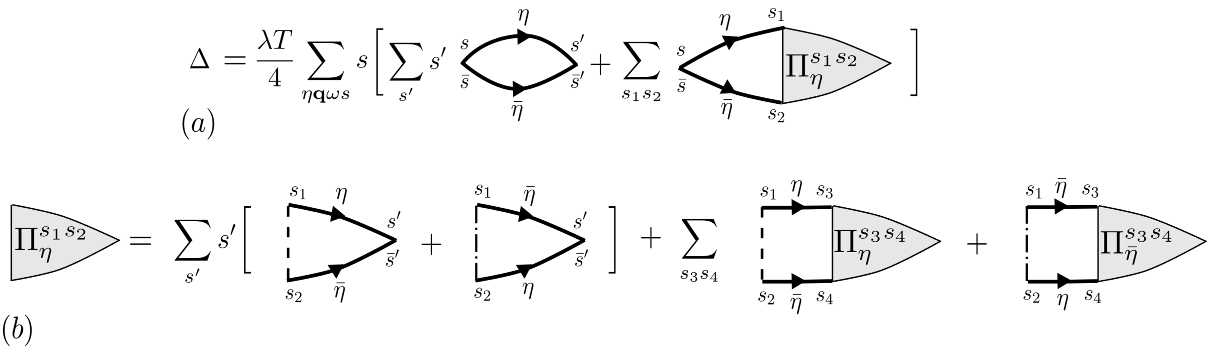

Figure B.3: (a) Diagrammatic representation of the disorder-averaged self-consistency condition given by Eq. (B.25). (b) Bethe-Salpeter equation for the renormalized vertex functions $\Pi_\eta^{ss'}$. For the definition of diagram elements, see Fig. B.2. We use the abbreviation $\bar{s} = -s$.

chemical potentials specified in the main text. In particular, we obtain

$$\begin{aligned}\nu_{0K} \int d\,\xi_{\mathbf{q}} \langle \mathcal{G}^{+,s_1 s_2}_{\eta \mathbf{q} \omega_n} \rangle \langle \mathcal{G}^{-,s_3 s_4}_{\bar{\eta} \bar{\mathbf{q}} \omega_n} \rangle = & \frac{\pi \nu_{0K} \operatorname{sgn}(\omega_n)}{2\tilde{\omega}_n (\tilde{\omega}_n^2 + h^2 + \Delta_{so}^2)} \\ & \times \Big[h^2 (1-\delta_{s_1 s_2})(1-\delta_{s_3 s_4}) + h(i\tilde{\omega}_n - s_3 \eta \Delta_{so})(1-\delta_{s_1 s_2})\delta_{s_4 s_4} \\ - h(i\tilde{\omega}_n - s_1 \eta \Delta_{so})\delta_{s_1 s_2}(1-\delta_{s_3 s_4}) & + (2\tilde{\omega}_n^2 + h^2 + \Delta_{so}^2 \delta_{s_1 \bar{s}_3} + s_1 2 i \tilde{\omega}_n \eta \Delta_{so} \delta_{s_1 s_3}) \delta_{s_1 s_2} \delta_{s_3 s_4} \Big], \end{aligned} \tag{B.28}$$

where we used the notation $\tilde{\omega}_n = \omega_n + 1/(2\tau_0) + 1/(2\tau_{iv})$.

We note that, in general, the renormalized vertex function Π_η is dependent on the polar angle θ, due to the anisotropy of the projected disorder potential, Eq. (3.9). The Π_η are determined by a system of Bethe-Salpeter equations [corresponding to diagrams in Fig. B.3 (b)]:

$$\begin{aligned}\Pi_\eta^{s_1 s_2}(\theta) = \int \frac{d^2\,\mathbf{q}'}{(2\pi)^2} \sum_{ss'} \Big[& U_0^2 F^0_{\theta,\theta'} \langle \mathcal{G}^{+,s_1 s}_{\eta \mathbf{q}' \omega_n} \rangle \langle \mathcal{G}^{-,s_2 s'}_{\bar{\eta} \bar{\mathbf{q}}' \omega_n} \rangle [s \delta_{\bar{s} s'} + \Pi_\eta^{ss'}(\theta)] \\ & + \sum_{i=\pm,x} \sum_{j=x,y} V_{ij}^2 G^i_{\theta,\theta'} \langle \mathcal{G}^{+,s_1 s}_{\bar{\eta} \bar{\mathbf{q}}' \omega_n} \rangle \langle \mathcal{G}^{-,s_2 s'}_{\eta \mathbf{q}' \omega_n} \rangle [s \delta_{\bar{s} s'} + \Pi_{\bar{\eta}}^{ss'}(\theta)] \Big]. \end{aligned} \tag{B.29}$$

We readily check that $\Pi_\eta(\theta)$ is fully determined by its first harmonics in θ:

$$\Pi_\eta^{s_1 s_2}(\theta) = \Pi_{\eta 0}^{s_1 s_2} + \Pi_{\eta 1}^{s_1 s_2} \cos\theta + \Pi_{\eta 2}^{s_1 s_2} \sin\theta. \tag{B.30}$$

Namely, by combining Eqs. (B.29) and (B.30), after integration over θ', we verify that no higher harmonics are generated. Furthermore, the equation for the constant part of the vertex functions $\Pi_{\eta 0}$ is decoupled from the angle-dependent parts $\Pi_{\eta 1}$ and $\Pi_{\eta 2}$. Replacing the $\Pi_\eta(\theta)$ in Eq. (B.27), we see that the angle-dependent contributions vanish after the integration over momenta. Therefore, it is sufficient to compute only $\Pi_{\eta 0}$.

The eight different $\Pi_{\eta 0}$ are determined from the linear system of equations obtained after integrating (B.29) over angles:

$$\Pi_{\eta 0}^{s_1 s_2} = \int \frac{d\,\xi_{\mathbf{q}'}}{2\pi} \sum_{ss'} \left[\frac{1}{\tau_0} \langle \mathcal{G}^{+,s_1 s}_{\eta \mathbf{q}' \omega_n} \rangle \langle \mathcal{G}^{-,s_2 s'}_{\bar{\eta} \bar{\mathbf{q}}' \omega_n} \rangle [s \delta_{\bar{s} s'} + \Pi^{ss'}_{\eta 0}] + \frac{1}{\tau_{iv}} \langle \mathcal{G}^{+,s_1 s}_{\bar{\eta} \bar{\mathbf{q}}' \omega_n} \rangle \langle \mathcal{G}^{-,s_2 s'}_{\eta \mathbf{q}' \omega_n} \rangle [s \delta_{\bar{s} s'} + \Pi^{ss'}_{\bar{\eta} 0}] \right]. \tag{B.31}$$

Inserting the vertex functions that solve Eq. (B.31) into Eq. (B.27) yields Eq. (5.11) in the main text.

Appendix C

Multiband superconductivity

In this Appendix, we provide technical details and derivations related to Chapter 6. In Sec. C.1, we derive Eq. (6.2) from the main text, and justify the use of the rate $\tau_{\Gamma,so}^{-1}$ to describe SOC in the Γ-band. In Sec. C.2, we derive the expression for the DoS given in Eq. (6.15) from the main text. Finally, in Sec. C.3, we derive h_{c2} estimates given in Eqs. (6.19) and (6.20).

C.1 Spin-orbit coupling and the diffusive limit in the Γ-band

The Eilenberger equations for the K- and Γ-band are

$$[(\omega_n + ihs_x)\tau_z + i\eta\Delta_{so}s_z + \Delta\tau_y + \Gamma_{K\Gamma}\langle g_\theta^\Gamma\rangle_\theta + \frac{1}{2\tau_{iv}}g_{\bar\eta}^K, g_\eta^K] = 0, \tag{C.1}$$

and

$$[(\omega_n + ihs_x)\tau_z + i\Delta_{so}^\Gamma s_z\cos(3\theta) + \frac{1}{2\tau_\Gamma}\langle g_\theta^\Gamma\rangle_\theta + \frac{\Gamma_{\Gamma K}}{2}(g_\eta^K + g_{\bar\eta}^K), g_\theta^\Gamma] = 0, \tag{C.2}$$

respectively. Here, $\langle ...\rangle_\theta$ denotes averaging over the Fermi surface in the Γ-band. We proceed by assuming that disorder is the dominant energy scale in the Γ-band (diffusive limit), such that $\tau_\Gamma^{-1} \gg \Delta, h, \Delta_{so}^\Gamma, \Gamma_{K\Gamma}, \Gamma_{\Gamma,K}$. In that case, the quasiclassical Green's function g_θ^Γ is nearly isotropic. We can expand it into harmonics as $g_\theta^\Gamma = g_0^\Gamma + g_1^\Gamma\cos 3\theta$, such that $g_0^\Gamma \gg g_1^\Gamma$. From the normalization condition $(g_\theta^\Gamma)^2 = 1$, we obtain $(g_0^\Gamma)^2 \approx 1$ and $\{g_0^\Gamma, g_1^\Gamma\} = 0$.

The Eilenberger equation (C.2) then yields

$$\begin{gathered}[\mathcal{M} + \frac{1}{2\tau_\Gamma}g_0^\Gamma + i\Delta_{so}^\Gamma s_z\cos 3\theta, g_0^\Gamma + g_1^\Gamma\cos 3\theta] = 0 \implies \\ [\mathcal{M}, g_0^\Gamma] + \frac{i\Delta_{so}^\Gamma}{2}[s_z, g_1^\Gamma] + \cos 3\theta\left(\frac{1}{2\tau_\Gamma}[g_0^\Gamma, g_1^\Gamma] + i\Delta_{so}[s_z, g_0^\Gamma]\right) = 0,\end{gathered} \tag{C.3}$$

where we introduced $\mathcal{M} = (\omega_n + ihs_x)\tau_z + \frac{\Gamma_{\Gamma K}}{2}(g_\eta^K + g_{\bar\eta}^K)$. From the angularly-dependent part of this equation, we have

$$g_1^\Gamma = -i\Delta_{so}^\Gamma\tau_\Gamma(s_z - g_0 s_z g_0). \tag{C.4}$$

Finally, this allows us to write for the angluarly-independent part as

$$[\mathcal{M} + \frac{1}{2}(\Delta_{so}^\Gamma)^2 \tau_\Gamma s_z g_0^\Gamma s_z, g_0^\Gamma] = 0, \tag{C.5}$$

which, finally, reduces to Eq. (6.2).

C.2 Derivation of Eq. (6.15)

Substituting Eq. (6.4) into the Eilenberger equation (6.1), we obtain the system of equations for the components of g_η^K:

$$\begin{aligned}
-\omega_n c_0^K - ihc_x^K + \Delta d_0^K + \Gamma_{K\Gamma}(c_0^\Gamma d_0^K + c_x^\Gamma d_x^K - d_0^\Gamma c_0^K - d_x^\Gamma c_x^K) &= 0,\\
-\omega_n c_x^K - ihc_0^K - i\Delta_{so} b_y^K + \Delta d_x^K + \Gamma_{K\Gamma}(c_0^\Gamma d_x^K + c_x^\Gamma d_0^K - d_0^\Gamma c_x^K - d_x^\Gamma c_0^K) &= 0,\\
-iha_z^K + i\Delta_{so} d_x^K - \Delta b_y^K - \frac{1}{\tau_{iv}}\left(1 + \frac{(d_x^K)^2}{(c_0^K)^2}\right) c_0^K - \Gamma_{K\Gamma}(c_0^\Gamma b_y^K + d_x^\Gamma a_z^K) &= 0,\\
\omega_n b_y^K + i\Delta_{so} c_x^K + \frac{1}{\tau_{iv}} b_y^K \left(1 + \frac{(d_x^K)^2}{(c_0^K)^2}\right) d_0^K - \Gamma_{K\Gamma}(c_x^\Gamma a_z^K - d_0^\Gamma b_y^K) &= 0,
\end{aligned} \tag{C.6}$$

which needs to be supplemented with the normalization condition (6.3), yielding

$$a_z^K = \frac{b_y d_x}{c_0}, \qquad c_x^K = -\frac{d_x^K d_0^K}{c_0^K}, \qquad [(c_0^K)^2 + (d_0^K)^2 + (b_y^K)^2]\left(1 + \frac{(d_x^K)^2}{(c_0^K)^2}\right) = 1. \tag{C.7}$$

Similarly, for the Γ-band, upon substituting Eq. (6.5) into the Eilenberger equation (6.2), we obtain the system of equations for the components of g^Γ:

$$\begin{aligned}
-\omega_n c_0^\Gamma - ihc_x^\Gamma + \Gamma_{\Gamma K}(c_0^K d_0^\Gamma + c_x^K d_x^\Gamma - d_0^K c_0^\Gamma - d_x^K c_x^\Gamma) &= 0,\\
-\omega_n c_x^\Gamma - ihc_0^\Gamma + \frac{1}{\tau_{\Gamma,so}}(c_0^\Gamma d_x^\Gamma - d_0^\Gamma c_x^\Gamma) + \Gamma_{\Gamma K}(d_x^\Gamma c_0^K + d_0^\Gamma c_x^K - c_x^\Gamma d_0^K - c_0^\Gamma d_x^K) &= 0,
\end{aligned} \tag{C.8}$$

and the normalization condition yields

$$c_x^\Gamma = -\frac{d_x^\Gamma d_0^\Gamma}{c_0^\Gamma}, \qquad [(c_0^\Gamma)^2 + (d_0^\Gamma)^2]\left(1 + \frac{(d_x^\Gamma)^2}{(c_0^\Gamma)^2}\right) = 1. \tag{C.9}$$

In the limit assumed in the main text, $\Delta_{so} \gg T_c, \tau_{iv}^{-1}, \tau_{\Gamma,so}^{-1}, \Gamma_{K\Gamma}, \Gamma_{\Gamma K}$, we can take $d_x^K / c_0^K \ll 1$ (similarly to Sec. B.2). Then, the second line of Eq. (C.6) yields

$$b_y^K \approx -\frac{h}{\Delta_{so}} c_0^K. \tag{C.10}$$

Using this, from the fourth line of Eq. (C.6), we get

$$d_x^K \approx -\frac{ih}{\Delta_{so}^2} \frac{(c_0^K)^2}{d_0^K} \left[\omega_n + \frac{1}{\tau_{iv}} d_0^K + \Gamma_{K\Gamma} d_0^\Gamma\right]. \tag{C.11}$$

Then, substituting Eqs. (C.10) and (C.11) into the first or third line of Eq. (C.6), we obtain

$$\omega_n \frac{\rho^2}{\Delta_{so}^2} c_0^K + \frac{1}{\tau_{iv}} \frac{h^2}{\Delta_{so}^2} c_0^K d_0^K = \Delta d_0^K + \Gamma_{K\Gamma}[c_0^\Gamma d_0^K - \frac{\rho^2}{\Delta_{so}^2} d_0^\Gamma c_0^K]. \tag{C.12}$$

Finally, the normalization condition (C.9) now simplifies to

$$(c_0^K)^2 \frac{\Delta_{so}^2}{\rho^2} + (d_0^K)^2 = 1. \tag{C.13}$$

In the Γ-band, we can define $c_\pm^\Gamma = \frac{1}{2}(c_0^\Gamma \pm c_x^\Gamma)$ and $d_\pm^\Gamma = \frac{1}{2}(d_0^\Gamma \pm d_x^\Gamma)$. Then, Eq. (C.8) can be rewritten as

$$-(\omega_n \pm ih)c_\pm^\Gamma \pm \frac{1}{\tau_{\Gamma,so}}(c_-^\Gamma d_+^\Gamma - d_-^\Gamma c_+^\Gamma) + \Gamma_{\Gamma K}(c_0^K d_\pm^\Gamma - d_0^K c_\pm^\Gamma) = 0, \tag{C.14}$$

and the normalization condition (C.9) becomes

$$(c_\pm^\Gamma)^2 + (d_\pm^\Gamma)^2 = 1. \tag{C.15}$$

Finally, we perform the analytical continuation $i\omega_n \to \epsilon + i0^+$, and define effective order parameters $\Delta_K(\epsilon) = -i\epsilon c_0^K(\epsilon)/d_0^K(\epsilon)$ and $\Delta_\Gamma^\pm(\epsilon) = -i\epsilon c_\pm^\Gamma(\epsilon)/d_\pm^\Gamma(\epsilon)$. Then, the first line of Eq. (6.15) readily follows from Eqs. (C.12) and (C.13), whereas the second line of Eq. (6.15) follows from Eqs. (C.14) and (C.15).

C.3 Derivation of Eqs. (6.19) and (6.20)

The sum over Matsubara frequencies in the linearized gap equation (6.18) can be evaluated analytically to yield

$$\ln\frac{T}{T_c^*} = \Re\sum_\pm \frac{\gamma_i}{\chi^2}\left[\psi\left(\frac{1}{2} + \frac{\beta_i}{2\pi T}\right) - \psi\left(\frac{1}{2}\right)\right]. \tag{C.16}$$

Here, we have introduced

$$\begin{aligned}
\chi &= \left(4\Gamma_{K\Gamma}\Gamma_{\Gamma K} + [\Gamma_{K\Gamma} - \Gamma_{\Gamma K} + \alpha^K(h_{c2}) - \alpha^\Gamma(h_{c2})]^2\right)^{1/2}, \\
\gamma_\pm &= \frac{1}{2}\left(- \chi^2 \pm \chi[\Gamma_{K\Gamma} - \Gamma_{\Gamma K} + \alpha^K(h_{c2}) - \alpha^\Gamma(h_{c2})]\right), \\
\beta_\pm &= \frac{1}{2}\left(\Gamma_{K\Gamma} + \Gamma_{\Gamma K} + \alpha^K(h_{c2}) + \alpha^\Gamma(h_{c2}) \mp \chi\right),
\end{aligned} \tag{C.17}$$

where h_{c2} is the upper critical field.

For temperatures close to $T = 0$, using the asymptotic behavior $\psi(z) \approx \ln z$ when $|z| \gg 1$, Eq. (C.16) gives

$$-\ln\frac{\Delta_0^*}{2} = \frac{\gamma_+}{\chi^2}\ln\beta_+ + \frac{\gamma_-}{\chi^2}\ln\beta_-. \tag{C.18}$$

Then, assuming that $\Delta_{so}^2\tau_{iv} \gg \tau_{\Gamma,so}^{-1}$, such that $\alpha_\Gamma(h_{c2}) \gg T_c$, Eq. (C.18) becomes $\ln(\Delta_0^*/2) = \ln[\Gamma_{K\Gamma} + \alpha_K(h_{c2})]$, which evaluates to Eq. (6.20) in the main text.

For temperatures close to $T = T_c$, the critical field is small $h_{c2} \ll \Delta_{so}^2 \tau_{iv}, \tau_{\Gamma,so}^{-1}$, and we may approximate $\ln \frac{T}{T_c} \approx \frac{T_c - T}{T_c}$. Then, expanding Eq. (6.18) in this regime gives

$$h \approx \sqrt{T_c - T} \sqrt{\frac{F_0(\Gamma_{K\Gamma}, \Gamma_{\Gamma K})}{F_1(\Gamma_{K\Gamma}, \Gamma_{\Gamma K})/[\Delta_{so}^2 \tau_{iv}] + F_2(\Gamma_{K\Gamma}, \Gamma_{\Gamma K}) \tau_{\Gamma,so}}}. \tag{C.19}$$

Here, we introduced the functions

$$\begin{aligned} F_0(\Gamma_1, \Gamma_2) &= 1 - \frac{\Gamma_{K\Gamma}}{2\pi T_c} \psi^{(1)}\left(\frac{1}{2} + \frac{\Gamma_{K\Gamma} + \Gamma_{\Gamma K}}{2\pi T_c}\right), \\ F_1(\Gamma_{K\Gamma}, \Gamma_{\Gamma K}) &= 2\pi T_c^2 \sum_{\omega_n} \frac{1}{[\omega_n + \Gamma_{K\Gamma} - \Gamma_{K\Gamma}\Gamma_{\Gamma K}/(\omega_n + \Gamma_{\Gamma K})]^2}, \\ F_2(\Gamma_{K\Gamma}, \Gamma_{\Gamma K}) &= 2\pi T_c^2 \sum_{\omega_n} \frac{\Gamma_{K\Gamma}\Gamma_{\Gamma K}/(\omega_n + \Gamma_{\Gamma K})^2}{[\omega_n + \Gamma_{K\Gamma} - \Gamma_{K\Gamma}\Gamma_{\Gamma K}/(\omega_n + \Gamma_{\Gamma K})]^2}. \end{aligned} \tag{C.20}$$

Here $\psi^{(1)}(z)$ is the first derivative of the digamma function $\psi(z)$. Finally, after assuming $\Delta_{so}^2 \tau_{iv} \gg \tau_{\Gamma,so}^{-1}$, we obtain Eq. (6.19) from the main text, where

$$C = \sqrt{\frac{F_0(\Gamma_{K\Gamma}, \Gamma_{\Gamma K})}{F_2(\Gamma_{K\Gamma}, \Gamma_{\Gamma K})}}. \tag{C.21}$$

Appendix D

Weak localization

In this Appendix, we provide technical details and derivations related to Chapter 7. In Sec. D.1, we derive the renormalized current vertex (7.2) and the Drude conductivity (7.3). In Sec. D.2, we provide details on the angular structure of Cooperons. First, in Secs. D.2.1 and D.2.2, we show the derivation of Eqs. (7.8) and (7.10) from the main text, describing intra- and invervalley Cooperons in the presence of diagonal disorder only. Then, in Sec. D.2.3, we explicitly write the components of the disorder correlator from Eq. (7.11), which will be used in later calculations. In Sec. D.3, we provide details on the transformation to the singlet-triplet basis. In Sec. D.4, we solve the Cooperon equations, and derive Eqs. (7.17) and (7.19) from the main text. Lastly, in Sec. D.5, we generalize the expression for the Diffusion constant (7.2) in the regime $\tau_{iv}^{-1} \sim \tau_0^{-1}$.

D.1 Derivation of the Drude conductivity

As shown in diagrammatic form in Fig. 7.1 (a) of the main text, the renormalized vertex $\tilde{\mathcal{J}}_{x\theta}$ satisfies the following equation

$$\tilde{\mathcal{J}}_{x\theta} = \mathcal{J}_{x\theta} + (2\pi\nu_{0K}\tau_0)U_0^2 \int_0^{2\pi} \frac{d\theta'}{2\pi} \mathcal{J}_{x\theta'} F^0_{\theta\theta'}. \tag{D.1}$$

Here, the factor $(2\pi\nu_{0K}\tau_0)$ comes from the energy integral of two Green's functions. If we assume that the renormalized vertex has a form $\tilde{\mathcal{J}}_{x\theta} = A\cos\theta$, we readily obtain

$$\tilde{\mathcal{J}}_{x\theta} = v_F \frac{2(\mu^2 + E_g^2)}{\mu^2 + 3E_g^2} \cos\theta = v_F \frac{\tau_{tr}}{\tau_0} \cos\theta, \tag{D.2}$$

which is Eq. (7.2) from the main text.

Next, as shown on Fig. 7.1 (b) of the main text, Drude conductivity is

$$\sigma = \frac{4e^2}{2\pi}(2\pi\nu_{0K}\tau_0) \int \frac{d\theta}{2\pi} \tilde{\mathcal{J}}_{x\theta} \mathcal{J}_{x\theta} = 4e^2\nu_{0K}\frac{1}{2}v_F^2\tau_{tr} = 4e^2\nu_{0K}D, \tag{D.3}$$

which is Eq. (7.3) from the main text. Here, the factor 4 comes from spin and valley degeneracy.

D.2 Angular structure of Cooperons

D.2.1 Intravalley Cooperons

Let us consider the intravalley Cooperon $C^{aa,aa}(\theta,\theta';\mathbf{Q})$. In the presence of diagonal disorder only, it satisfies the following Bethe-Salpeter equation

$$\begin{aligned}&C^{aa,aa}(\theta,\theta',\mathbf{Q}) = U_0^2\tilde{F}^0_{a\theta\theta'}+\\ &U_0^2(2\pi\nu_{0K}\tau_0)\int_0^{2\pi}\frac{d\theta''}{2\pi}\tilde{F}^0_{a\theta\theta''}[1+i\omega\tau_0-\tau_\phi^{-1}\tau_0-i\mathbf{Q}\cdot\mathbf{e}_{\theta''}v_F\tau_0-(\mathbf{Q}\cdot\mathbf{e}_{\theta''})^2v_F^2\tau_0^2]C^{aa,aa}(\theta'',\theta';\mathbf{Q}),\end{aligned} \tag{D.4}$$

where $\mathbf{e}_{\theta''}=(\cos\theta'',\sin\theta'')$, and we expand up to second order in small momentum $\mathbf{Q}$. The function $\tilde{F}^0$ is defined in Appendix A. The impurity line can be rewritten as

$$U_0^2\tilde{F}^0_{a\theta\theta'} = \frac{1}{2\pi\nu_{0K}\tau_0}\left[z_0+z_1e^{-ia(\theta-\theta')}+z_2e^{-2ia(\theta-\theta')}\right], \tag{D.5}$$

where

$$z_0=\frac{(1+E_g/\mu)^2}{2(1+E_g^2/\mu^2)},\qquad z_1=\frac{1-E_g^2/\mu^2}{(1+E_g^2/\mu^2)},\qquad z_2=\frac{(1-E_g/\mu)^2}{2(1+E_g^2/\mu^2)}. \tag{D.6}$$

We expand in harmonics

$$U_0^2\tilde{F}^0_{a\theta\theta'}=\sum_{n,m=0,1,2}z_{nm}e^{i(n\theta-m\theta')},\qquad C^{aa,aa}(\theta,\theta';\mathbf{Q})=\sum_{n,m=0,1,2}Z_{nm}(\mathbf{Q})e^{i(n\theta-m\theta')}, \tag{D.7}$$

and we define

$$\Phi_{nm}=\int_0^{2\pi}\frac{d\theta''}{2\pi}e^{i(n-m)\theta''}[1+i\omega\tau_0-\tau_\phi^{-1}\tau_0-i\mathbf{Q}\cdot\mathbf{e}_{\theta''}v_F\tau_0-(\mathbf{Q}\cdot\mathbf{e}_{\theta''})^2v_F^2\tau_0^2],\qquad n,m=0,1,2. \tag{D.8}$$

The expansion coefficients then satisfy $Z=(1-z\Phi)^{-1}z$, with

$$z=\begin{pmatrix}z_0&0&0\\0&z_1&0\\0&0&z_2\end{pmatrix},$$

$$\Phi=\begin{pmatrix}1-\Pi_0\tau_0-\frac{1}{2}Q^2v_F^2\tau_0^2 & -\frac{iQ_+}{2}v_F\tau_0 & -\frac{Q_+^2}{4}v_F^2\tau_0^2\\ -\frac{iQ_-}{2}v_F\tau_0 & 1-\Pi_0\tau_0-\frac{1}{2}Q^2v_F^2\tau_0^2 & -\frac{iQ_+}{2}v_F\tau_0\\ -\frac{Q_+^2}{4}v_F^2\tau_0^2 & -\frac{iQ_-}{2}v_F\tau_0 & 1-\Pi_0\tau_0-\frac{1}{2}Q^2v_F^2\tau_0^2\end{pmatrix}, \tag{D.9}$$

where $Q_\pm=Q_x\pm iQ_y$, and $\Pi_0=-i\omega+\tau_\phi^{-1}$. The diagonal elements Z_{ii} are the leading order terms in the diffusive limit. Z_{22} will always have a non-vanishing Cooperon gap of the order τ_0^{-1}, so we only need to consider Z_{00} and Z_{11}. They are given by

$$\begin{aligned}Z_{00}&=\frac{1}{2\pi\nu_{0K}\tau_0^2}\frac{1}{\frac{g_0}{2\tau_0}+\frac{1}{2}\left(\frac{1}{g_1}+1\right)Q^2v_F^2\tau_0+\Pi_0},\\ Z_{11}&=\frac{1}{2\pi\nu_{0K}\tau_0^2}\frac{1}{\frac{g_1}{2\tau_0}+\frac{1}{2}\left(\frac{1}{g_0}+\frac{1}{g_2}+1\right)Q^2v_F^2\tau_0+\Pi_0},\end{aligned} \tag{D.10}$$

where $g_i = 2(1 - z_i)/z_i$. Finally, after introducing $C_0^{aa,aa}(\mathbf{Q}) = Z_{00}$ and $C_a^{aa,aa}(\mathbf{Q}) = Z_{11}$, as well as $\Gamma_0 = \frac{g_0}{2\tau_0} = \frac{1}{\tau_0}\frac{(\mu-E_g)^2}{(\mu+E_g)^2}$, $\Gamma_a = \frac{g_1}{2\tau_0} = \frac{1}{\tau_0}\frac{2E_g^2}{\mu^2-E_g^2}$, $D_0 = \frac{1}{2}\big(\frac{1}{g_1}+1\big)v_F^2\tau_0 = \frac{1}{8}v_F^2\tau_0(3+\frac{E_g^2}{\mu^2})$ and $D_a = \frac{1}{2}\big(\frac{1}{g_0}+\frac{1}{g_2}+1\big)v_F^2\tau_0 = v_F^2\tau_0\frac{(E_g^2+\mu^2)^2}{(\mu^2-E_g^2)^2}$, we obtain Eq. (7.8) from the main text

$$C^{aa,aa}(\theta,\theta';\mathbf{Q}) = C_0^{aa,aa}(\mathbf{Q}) + C_a^{aa,aa}(\mathbf{Q})e^{-ia(\theta-\theta')}. \tag{D.11}$$

D.2.2 Intervalley Cooperons

To find the intervalley Cooperons $C^{a\bar{a},a\bar{a}}(\theta,\theta';\mathbf{Q})$ in the presence of diagonal disorder only, we repeat the same procedure as in Sec. D.2.1. They are determined by the Bethe-Salpeter equation

$$\begin{aligned}C^{a\bar{a},a\bar{a}}(\theta,\theta',\mathbf{Q}) &= U_0^2F_{\theta\theta'}^0\\ &+U_0^2(2\pi\nu_{0K}\tau_0)\int_0^{2\pi}\frac{d\theta''}{2\pi}F_{\theta\theta'}^0[1+i\omega\tau_0-\tau_\phi^{-1}\tau_0-i\mathbf{Q}\cdot\mathbf{e}_{\theta''}v_F\tau_0-(\mathbf{Q}\cdot\mathbf{e}_{\theta''})^2v_F^2\tau_0^2]C^{a\bar{a},a\bar{a}}(\theta'',\theta';\mathbf{Q}),\end{aligned} \tag{D.12}$$

where the function F^0 is defined in Appendix A. The impurity line can be rewritten as

$$U_0^2F_{\theta\theta'}^0 = \frac{1}{2\pi\nu_{0K}\tau_0}\left[z_{\bar{1}}'e^{-i(\theta-\theta')} + z_0' + z_1'e^{i(\theta-\theta')}\right], \tag{D.13}$$

where

$$z_{\bar{1}}' = z_1' = \frac{1-E_g^2/\mu^2}{2(1+E_g^2/\mu^2)}, \qquad z_0' = 1. \tag{D.14}$$

Then, as in Sec. D.2.1, we expand in harmonics

$$U_0^2F_{\theta\theta'}^0 = \sum_{n,m=-1,0,1} z_{nm}'e^{i(n\theta-m\theta')}, \qquad C^{a\bar{a},a\bar{a}}(\theta,\theta',\mathbf{Q}) = \sum_{n,m=-1,0,1} Z_{nm}'(\mathbf{Q})e^{i(n\theta-m\theta')}, \tag{D.15}$$

and find that the expansion coefficients satisfy $Z' = (1 - z'\Phi)^{-1}z'$.

The diagonal elements Z_{ii}' are the leading order terms in the diffusive limit. Z_{11}' and $Z_{\bar{1}\bar{1}}'$ will always has a non-vanishing Cooperon gap of the order τ_0^{-1}, so we only need to consider Z_{00}', which is given as

$$Z_{00}'(\mathbf{Q}) = \frac{1}{2\pi\nu_{0K}\tau_0^2}\frac{1}{\frac{g_0'}{2\tau_0}+\frac{1}{2}\left(1+\frac{1}{g_{\bar{1}}'}+\frac{1}{g_1'}\right)Q^2v_F^2\tau_0+\Pi_0}, \tag{D.16}$$

where $g_i' = 2(1 - z_i')/z_i'$. Finally, after introducing $C_0^{a\bar{a},a\bar{a}} = Z_{00}'$ we obtain Eq. (7.10) of the main text

$$C^{a\bar{a},a\bar{a}}(\theta,\theta';\mathbf{Q}) = C_0^{a\bar{a},a\bar{a}}. \tag{D.17}$$

D.2.3 Angularly independent form of the disorder correlator

The explicit expression for the disorder correlator defined in Eq. (7.5) is

$$\begin{aligned} W^{ab,a'b'}_{\alpha\beta,\alpha'\beta'}(\theta,\theta') &= \delta_{aa'}\delta_{bb'} \sum_{i=0,x,y,z} \left[\delta_{a\bar{b}} F^i_{\theta\theta'} + \delta_{ab}\tilde{F}^i_{a\theta\theta'}\right] \\ &\quad \times \left[U_i^2 \delta_{\alpha\alpha'}\delta_{\beta\beta'} + (A_{ix}^2 + A_{iy}^2) ab\delta_{\alpha\bar{\beta}}\delta_{\alpha\bar{\alpha}'}\delta_{\beta\bar{\beta}'} + A_{iz}^2 ab\alpha\beta\delta_{\alpha\alpha'}\delta_{\beta\beta'}\right] \\ &+\delta_{a\bar{a}'}\delta_{b\bar{b}'}\delta_{a\bar{b}}\left[\sum_{i=\pm,x}\sum_{j=x,y} G^i_{\theta\theta'}V_{ij}^2 + G^y_{\theta\theta'}\sum_{i,j=x,y} M_{i,j}^2\delta_{\alpha\bar{\alpha}'}\delta_{\beta\bar{\beta}'}\delta_{\alpha\bar{\beta}} + G^y_{\theta\theta'}(M_{zx}^2 + M_{zy}^2)\alpha\beta\delta_{\alpha\alpha'}\delta_{\beta\beta'}\right]. \end{aligned} \tag{D.18}$$

The functions $F^i, \tilde{F}^i$ and G^i are defined in Appendix A. From here, we find the components of $W(\theta,\theta')$ that appear in Eq. (7.11) of the main text as

$$\begin{aligned} W_0^{aa,aa}(\Xi=1) = \frac{1}{2\pi\nu_{0K}} \Big[&(\tau_0^{-1} + \tau_{z2}^{-1})\delta_{\alpha\alpha'}\delta_{\beta\beta'} + (\tau_{zv,e}^{-1} + \tau_{z,e2}^{-1})\alpha\beta\delta_{\alpha\alpha'}\delta_{\beta\beta'} \\ &+ (\tau_{zv,o}^{-1} + \tau_{z,o2}^{-1})\delta_{\alpha\bar{\alpha}'}\delta_{\beta\bar{\beta}'}\delta_{\alpha\bar{\beta}} \Big], \end{aligned} \tag{D.19}$$

$$\begin{aligned} W_a^{aa,aa}(\Xi=-1) = \frac{1}{2\pi\nu_{0K}} \Big[&(\tau_0^{-1} - \tau_z^{-1})\delta_{\alpha\alpha'}\delta_{\beta\beta'} + (\tau_{zv,e}^{-1} - \tau_{z,e}^{-1})\alpha\beta\delta_{\alpha\alpha'}\delta_{\beta\beta'} \\ &+ (\tau_{zv,o}^{-1} - \tau_{z,o}^{-1})\delta_{\alpha\bar{\alpha}'}\delta_{\beta\bar{\beta}'}\delta_{\alpha\bar{\beta}} \Big], \end{aligned} \tag{D.20}$$

$$\begin{aligned} W_0^{a\bar{a},b\bar{b}} = &\frac{\delta_{ab}}{2\pi\nu_{0K}} \Big[(\tau_0^{-1} + \tau_z^{-1})\delta_{\alpha\alpha'}\delta_{\beta\beta'} + (\tau_{zv,e}^{-1} + \tau_{z,e}^{-1})\alpha\beta\delta_{\alpha\alpha'}\delta_{\beta\beta'} + (\tau_{zv,o}^{-1} + \tau_{z,o}^{-1})\delta_{\alpha\bar{\alpha}'}\delta_{\beta\bar{\beta}'}\delta_{\alpha\bar{\beta}} \Big] \\ &+ \frac{\delta_{a\bar{b}}}{2\pi\nu_{0K}} \Big[\tau_{iv}^{-1}\delta_{\alpha\alpha'}\delta_{\beta\beta'} - \tau_{iv,e}^{-1}\alpha\beta\delta_{\alpha\alpha'}\delta_{\beta\beta'} - \tau_{iv,o}^{-1}\delta_{\alpha\bar{\alpha}'}\delta_{\beta\bar{\beta}'}\delta_{\alpha\bar{\beta}} \Big]. \end{aligned} \tag{D.21}$$

D.3 Transformation to the singlet-triplet basis

In this section, we will provide details about the transformation of the interference correction $\delta\sigma$, Bethe-Salpeter equation, disorder correlator Π and polarization operator W to the singlet-triplet basis. This transformation is given as

$$A^{ll'}_{ss'} = \frac{1}{4}[s_y s_s]_{\alpha\beta}[\eta_x\eta_l]^{ab} A^{ab,a'b'}_{\alpha\beta,\alpha'\beta'}[s_{s'}s_y]_{\beta'\alpha'}[\eta_{l'}\eta_x]^{b'a'}. \tag{D.22}$$

The inverse transformation is

$$A^{ab,a'b'}_{\alpha\beta,\alpha'\beta'} = \frac{1}{4}\sum_{ss'll'}[s_s s_y]_{\beta\alpha}[\eta_l\eta_x]^{ba} A^{ll'}_{ss'}[s_y s_{s'}]_{\alpha'\beta'}[\eta_x\eta_{l'}]^{a'b'}. \tag{D.23}$$

Instead of four indices in spin and valley space, the transformed quantities are simpler with only two spin (s, s') and two valley indices (l, l').

Transforming the interference correction $\delta\sigma$. For the upcoming calculation, it is convenient to introduce the quantity

$$\tilde{C}^{ab,a'b'}_{\alpha\beta,\alpha'\beta'}(\Xi,\mathbf{Q}) \equiv C^{ab,a'b'}_{\alpha\beta,\alpha'\beta'}(\Xi;\mathbf{Q})[\Xi\delta_{ab}\delta_{a'b'} + \delta_{a\bar{b}}\delta_{a'\bar{b}'}], \tag{D.24}$$

so that the interference correction Eq. (7.13) may be rewritten as

$$\delta\sigma = -\frac{e^2 D}{\pi}(2\pi\nu_{0K}\tau_0^2)\int \frac{d^2\mathbf{Q}}{(2\pi)^2}\tilde{C}^{ab,ba}_{\alpha\beta,\beta\alpha}(\Xi,\mathbf{Q}), \tag{D.25}$$

where summation over repeated indices is assumed. Then, transforming $\tilde{C}^{ab,a'b'}_{\alpha\beta,\alpha'\beta'}(\Xi,\mathbf{Q})$ to the singlet-triplet basis yields

$$\begin{aligned}\tilde{C}^{ab,ba}_{\alpha\beta,\beta\alpha}(\Xi,\mathbf{Q}) &= \frac{1}{4}\sum_{ss'll'}[s_s s_y]_{\beta\alpha}[\eta_l\eta_x]^{ba}\tilde{C}^{ll'}_{ss'}(\Xi,\mathbf{Q})[s_y s_{s'}]_{\beta\alpha}[\eta_x\eta_{l'}]^{ba}\\ &= \frac{1}{4}\sum_{ss'll'}Tr[s_s s_y s_{s'}^T s_y^T]Tr[\eta_l\eta_x\eta_{l'}^T\eta_x^T]\tilde{C}^{ll'}_{ss'}(\Xi,\mathbf{Q})\\ &= \sum_{ss'll'}\delta_{ss'}\delta_{ll'}(-\delta_{s0}+\delta_{sx}+\delta_{sy}+\delta_{sz})(\delta_{l0}+\delta_{lx}+\delta_{ly}-\delta_{lz})\tilde{C}^{ll'}_{ss'}(\Xi,\mathbf{Q}).\end{aligned} \tag{D.26}$$

Here, $\tilde{C}^{ll'}_{ss'}(\mathbf{Q})$ is obtained by transforming Eq. (D.24) to singlet-triplet basis as

$$\tilde{C}^{ll'}_{ss'}(\Xi,\mathbf{Q}) = C^{ll'}_{ss'}(\Xi,\mathbf{Q})[\Xi(\delta_{lx}+\delta_{ly})(\delta_{l'x}+\delta_{l'y}) + (\delta_{l0}+\delta_{lz})(\delta_{l'0}+\delta_{l'z})]. \tag{D.27}$$

Finally, combining Eqs. (D.26) and (D.27) leads to Eq. (7.16) of the main text.

Transforming the Bethe-Salpeter equation. We start from the Bethe-Salpeter equation in the original basis, Eq. (7.12), and express all relevant quantities in the singlet-triplet basis using Eq. (D.23). Then, using the completeness relation of Pauli matrices

$$\frac{1}{4}\sum_{sl}[s_s s_y]_{\beta\alpha}[\eta_l\eta_x]^{ba}[s_y s_s]_{\alpha'\beta'}[\eta_x\eta_l]^{a'b'} = \delta_{aa'}\delta_{bb'}\delta_{\alpha\alpha'}\delta_{\beta\beta'}, \tag{D.28}$$

we readily obtain the Bethe-Salpeter equation in the singlet-triplet basis, Eq. (7.15).

Transforming the disorder correlator W. Starting from the expressions for the disorder correlator in the original basis, Eqs. (D.19)-(D.21), and applying the transformation (D.22), we obtain

$$W^{ll'}_{ss'}(\Xi) = \frac{1}{2\pi\nu_{0K}\tau_0}\delta_{ss'}\delta_{ll'} + \frac{1}{2\pi\nu_{0K}}\Omega^l_s(\Xi)\delta_{ss'}\delta_{ll'}. \tag{D.29}$$

Here, for $l \in \{x,y\}$, we have

$$\Omega^l_s(\Xi=1) = \frac{1}{2\pi\nu_{0K}}\left[\tau_{z,2}^{-1} + (\tau_{zv,e}^{-1}+\tau_{z,e2}^{-1})(\delta_{sx}+\delta_{sy}-\delta_{s0}-\delta_{sz}) + (\tau_{zv,o}^{-1}+\tau_{z,o2}^{-1})(-\delta_{s0}+\delta_{sz})\right], \tag{D.30}$$

$$\Omega_s^l(\Xi=-1)=\frac{1}{2\pi\nu_{0K}}\left[-\tau_z^{-1}+(\tau_{zv,e}^{-1}-\tau_{z,e}^{-1})(\delta_{sx}+\delta_{sy}-\delta_{s0}-\delta_{sz})+(\tau_{zv,o}^{-1}-\tau_{z,o}^{-1})(-\delta_{s0}+\delta_{sz})\right], \tag{D.31}$$

while for $l,l'\in\{0,z\}$ we have

$$\begin{aligned}\Omega_s^l(\Xi)=&\ \frac{1}{2\pi\nu_{0K}}\left[\tau_z^{-1}+(\tau_{zv,e}^{-1}+\tau_{z,e}^{-1})(\delta_{sx}+\delta_{sy}-\delta_{s0}-\delta_{sz})+(\tau_{zv,o}^{-1}+\tau_{z,o}^{-1})(-\delta_{s0}+\delta_{sz})\right]\\&+\frac{1}{2\pi\nu_{0K}}(\delta_{l0}-\delta_{lz})\left[\tau_{iv}^{-1}-\tau_{iv,e}^{-1}(\delta_{sx}+\delta_{sy}-\delta_{s0}-\delta_{sz})-\tau_{iv,o}^{-1}(\delta_{s0}+\delta_{sz})\right].\end{aligned} \tag{D.32}$$

Transforming the polarization operator Π**.** The polarization operator, defined in Eq. (7.5), has the following form in the singlet-triplet basis

$$\begin{aligned}\Pi_{ss'}^{ll'}(\theta;\mathbf{Q})&=\frac{\nu_{0K}}{4}\int d\xi_{\mathbf{q}}[s_ys_s]_{\alpha\beta}[\eta_x\eta_l]^{ab}[G^R_{\mathbf{q}\epsilon+\omega}]^{aa'}_{\alpha\alpha'}[G^A_{\bar{\mathbf{q}}+\mathbf{Q}\epsilon}]^{bb'}_{\beta\beta'}[s_{s'}s_y]_{\beta'\alpha'}[\eta_{l'}\eta_x]^{b'a'}\\&=\frac{\nu_{0K}}{4}\int d\xi_{\mathbf{q}}Tr[s_ys_s\eta_x\eta_lG^A_{\bar{\mathbf{q}}+\mathbf{Q}\omega}s_{s'}s_y\eta_{l'}\eta_x[G^R_{\mathbf{q}\epsilon+\omega}]^T].\end{aligned} \tag{D.33}$$

After solving the energy integrals of Green's functions, we get

$$\Pi_{ss'}^{ll'}(\mathbf{Q})=\delta_{ss'}\delta_{ll'}2\pi\nu_{0K}\tau_0\left(1-\tau_0\Pi-\tau_0\tau_i^{-1}\right)+\mathcal{N}_{ss'}^{ll'}+\mathcal{M}_s^l\delta_{ss'}\delta_{ll'}, \tag{D.34}$$

where $\Pi=D|\mathbf{Q}|^2+\tau_\phi^{-1}-i\omega$, and τ_i^{-1} is the sum of all scattering rates except the dominant one, τ_0^{-1}:

$$\tau_i^{-1}=\tau_z^{-1}+\tau_{iv}^{-1}+\sum_{k=z,iv,zv}\sum_{l=e,o}\tau_{k,l}^{-1}. \tag{D.35}$$

The polarization operator (D.34) consists of three parts. The first term is diagonal, while the second and third term have a more complicated structure. The second term, $\mathcal{N}$, is responsible for the coupling of different Cooperon modes via Ising SOC and the in-plane Zeeman field. The third term, $\mathcal{M}$, introduces Dyakonov-Perel-like scattering rates to the Cooperon gaps. We have

$$\begin{aligned}&\mathcal{N}_{ss'}^{ll'}(\mathbf{Q})=-4\pi\nu_{0K}\tau_0^2\Delta_{so}[(\delta_{s0}\delta_{s'z}+\delta_{s'0}\delta_{sz})\epsilon_{l'lz}(\delta_{l0}-1)(\delta_{l'0}-1)]|\\&-4\pi\nu_{0K}\tau_0^2\Delta_{so}[(\delta_{l0}\delta_{l'z}+\delta_{l'0}\delta_{lz})\epsilon_{s'sz}(\delta_{s0}-1)(\delta_{s'0}-1)]+4\pi\nu_{0K}\tau_0^2ih\delta_{ll'}(\delta_{s0}\delta_{s'x}+\delta_{s'0}\delta_{sx}),\end{aligned}$$

where ϵ_{ijk} is the Levi-Civita symbol, and

$$\mathcal{M}_s^l=-2\pi\nu_{0K}\tau_0^2\left[\tau_{BR}^{-1}(\delta_{sx}+\delta_{sy}+2\delta_{sz})+\tau_W^{-1}(\delta_{lx}+\delta_{ly})]\right]. \tag{D.36}$$

Here, τ_{BR}^{-1} and τ_W^{-1} are the scattering rates introduced in Eq. (7.18) of the main text.

D.4 Solving the Cooperon equations

Having transformed all the relevant quantities to the singlet-triplet space in Sec. (D.3), we proceed to solve the Bethe-Salpeter equations. Using the expressions from Sec. (D.3), we obtain from Eq. (7.15)

$$\begin{aligned} C^{ll'}_{ss'}(\Xi;\mathbf{Q}) = \frac{1}{2\pi\nu_{0K}\tau_0}\delta_{ss'}\delta_{ll'} + \Big(1+\Omega^l_s(\Xi)\tau_0\Big)\Big(1-\Pi\tau_0-\tau_0\tau_i^{-1}+\frac{\mathcal{M}^l_s}{2\pi\nu_{0K}\tau_0}\Big)C^{ll'}_{ss'}(\Xi;\mathbf{Q}) \\ + \frac{1}{2\pi\nu_{0K}\tau_0}\sum_{l_1s_1}\mathcal{N}^{ss_1}_{ll_1}C^{l_1l'}_{s_1s'}(\Xi,\mathbf{Q}), \end{aligned} \tag{D.37}$$

which becomes

$$\frac{1}{2\pi\nu_{0K}\tau_0^2}\delta_{ll'}\delta_{ss'} = \Big(\Pi+\tau_i^{-1}-\Omega^l_s-\frac{\mathcal{M}^l_s}{2\pi\nu_{0K}\tau_0^2}\Big)C^{ll'}_{ss'} - \frac{1}{2\pi\nu_{0K}\tau_0^2}\sum_{l_1s_1}\mathcal{N}^{ss_1}_{ll_1}C^{l_1l'}_{s_1s'}(\mathbf{Q}). \tag{D.38}$$

Next, we introduce the Cooperon relaxation gaps as

$$\Gamma^l_s(\Xi) = \tau_i^{-1}-\Omega^l_s(\Xi)-\frac{\mathcal{M}^l_s}{2\pi\nu_{0K}\tau_0^2}, \tag{D.39}$$

which are calculated and summarized in Table. 7.1 of the main text. Finally, we have

$$\frac{1}{2\pi\nu_{0K}\tau_0^2}\delta_{ll'}\delta_{ss'} = \Big(\Pi+\Gamma^l_s(\Xi)\Big)C^{ll'}_{ss'}(\Xi,\mathbf{Q}) - \frac{1}{2\pi\nu_{0K}\tau_0^2}\sum_{l_1s_1}\mathcal{N}^{ss_1}_{ll_1}C^{l_1l'}_{s_1s'}(\Xi,\mathbf{Q}), \tag{D.40}$$

which can be compactly rewritten as 4 scalar equations for uncoupled Cooperon modes - Eq. (7.17) of the main text, and 4 matrix equations for Cooperon modes coupled by Δ_{so} and h - Eq. (7.19) of the main text.

D.5 Diffusion constant in the regime $\tau_{iv}^{-1} \sim \tau_0^{-1}$

We generalize the calculation of the transport time and the diffusion constant presented in Eq. (7.2), to account for intra- and intervalley terms of the potential disorder $H^{D0}_{\mathbf{qq}'}$ on an equal footing. This yields

$$\tau_{tr}^{-1} = \tau_0^{-1}\frac{\mu^2+3E_g^2}{2(\mu^2+E_g^2)} + \tau_{iv,+}^{-1} + \tau_{iv,-}^{-1} + \frac{3}{2}\tau_{iv,x}^{-1}. \tag{D.41}$$

Here,

$$\tau_{iv,\pm}^{-1} = 2\pi\nu_{0K}\sum_{i=x,y}V_{\pm i}^2\Big(1\pm(\mp)\frac{E_g}{\mu}\Big)^2 \tag{D.42}$$

describes on-site intervalley disorder, while

$$\tau_{iv,x}^{-1} = \pi\nu_{0K}\sum_{i=x,y}V_{xi}^2\frac{v^2q_F^2}{\mu^2} \tag{D.43}$$

describes hopping intervalley disorder.

The signs outside and inside the parentheses concern n- and p-doped samples, respectively. At $\mu \approx E_g$, the intervalley contribution to the transport time comes predominantly from one site ("+" for n-doped, "-" for p-doped samples), and the diffusion constant is $D = \frac{1}{2} v_F (\tau_0^{-1} + \tau_{iv,+}^{-1})^{-1}$. At $\mu \gg E_g$, both sites contribute equally, together with hopping disorder, and the diffusion constant is $D = \frac{1}{2} v_F (\frac{\tau_0^{-1}}{2} + \tau_{iv,+}^{-1} + \tau_{iv,-}^{-1} + \frac{3}{2} \tau_{iv,x}^{-1})^{-1}$.

Bibliography

[1] K. S. Novoselov, A. K. Geim, S. V. Morozov, D. Jiang, Y. Zhang, S. V. Dubonos, I. V. Grigorieva, and A. A. Firsov, “Electric field effect in atomically thin carbon films,” *Science*, vol. 306, no. 5696, pp. 666–669, 2004.

[2] K. Novoselov, A. Mishchenko, A. Carvalho, and A. C. Neto, “2D materials and van der Waals heterostructures,” *Science*, vol. 353, no. 6298, p. aac9439, 2016.

[3] K. F. Mak, C. Lee, J. Hone, J. Shan, and T. F. Heinz, “Atomically thin MoS_2: a new direct-gap semiconductor,” *Physical Review Letters*, vol. 105, no. 13, p. 136805, 2010.

[4] Q. H. Wang, K. Kalantar-Zadeh, A. Kis, J. N. Coleman, and M. S. Strano, “Electronics and optoelectronics of two-dimensional transition metal dichalcogenides,” *Nature Nanotechnology*, vol. 7, no. 11, pp. 699–712, 2012.

[5] B. Radisavljevic, A. Radenovic, J. Brivio, I. V. Giacometti, and A. Kis, “Single-layer MoS_2 transistors,” *Nature Nanotechnology*, vol. 6, no. 3, pp. 147–150, 2011.

[6] E. Navarro-Moratalla and P. Jarillo-Herrero, “Two-dimensional superconductivity: The Ising on the monolayer,” *Nature Physics*, vol. 12, no. 2, p. 112, 2016.

[7] Z. Zhu, Y. Cheng, and U. Schwingenschlögl, “Giant spin-orbit-induced spin splitting in two-dimensional transition-metal dichalcogenide semiconductors,” *Physical Review B*, vol. 84, no. 15, p. 153402, 2011.

[8] A. Kormányos, G. Burkard, M. Gmitra, J. Fabian, V. Zólyomi, N. D. Drummond, and V. Fal’ko, “k· p theory for two-dimensional transition metal dichalcogenide semiconductors,” *2D Materials*, vol. 2, no. 2, p. 022001, 2015.

[9] D. Xiao, G.-B. Liu, W. Feng, X. Xu, and W. Yao, “Coupled spin and valley physics in monolayers of MoS_2 and other group-VI dichalcogenides,” *Physical Review Letters*, vol. 108, no. 19, p. 196802, 2012.

[10] K. F. Mak, K. He, J. Shan, and T. F. Heinz, “Control of valley polarization in monolayer MoS_2 by optical helicity,” *Nature Nanotechnology*, vol. 7, no. 8, pp. 494–498, 2012.

[11] H. Zeng, J. Dai, W. Yao, D. Xiao, and X. Cui, “Valley polarization in MoS_2 monolayers by optical pumping,” *Nature Nanotechnology*, vol. 7, no. 8, pp. 490–493, 2012.

[12] Y. Saito, Y. Nakamura, M. S. Bahramy, Y. Kohama, J. Ye, Y. Kasahara, Y. Nakagawa, M. Onga, M. Tokunaga, T. Nojima, *et al.*, "Superconductivity protected by spin-valley locking in ion-gated MoS_2," *Nature Physics*, vol. 12, no. 2, pp. 144–149, 2016.

[13] J. Lu, O. Zheliuk, I. Leermakers, N. F. Yuan, U. Zeitler, K. T. Law, and J. Ye, "Evidence for two-dimensional Ising superconductivity in gated MoS_2," *Science*, vol. 350, no. 6266, pp. 1353–1357, 2015.

[14] X. Xi, Z. Wang, W. Zhao, J.-H. Park, K. T. Law, H. Berger, L. Forró, J. Shan, and K. F. Mak, "Ising pairing in superconducting NbSe_2 atomic layers," *Nature Physics*, vol. 12, pp. 139–143, 2016.

[15] C. Sergio, M. R. Sinko, D. P. Gopalan, N. Sivadas, K. L. Seyler, K. Watanabe, T. Taniguchi, A. W. Tsen, X. Xu, D. Xiao, *et al.*, "Tuning Ising superconductivity with layer and spin–orbit coupling in two-dimensional transition-metal dichalcogenides," *Nature Communications*, vol. 9, no. 1, p. 1427, 2018.

[16] M. Gmitra, D. Kochan, P. Högl, and J. Fabian, "Trivial and inverted Dirac bands and the emergence of quantum spin Hall states in graphene on transition-metal dichalcogenides," *Physical Review B*, vol. 93, no. 15, p. 155104, 2016.

[17] B. Yang, M.-F. Tu, J. Kim, Y. Wu, H. Wang, J. Alicea, R. Wu, M. Bockrath, and J. Shi, "Tunable spin–orbit coupling and symmetry-protected edge states in graphene/WS_2," *2D Materials*, vol. 3, no. 3, p. 031012, 2016.

[18] A. Avsar, J. Y. Tan, T. Taychatanapat, J. Balakrishnan, G. Koon, Y. Yeo, J. Lahiri, A. Carvalho, A. Rodin, E. O'Farrell, *et al.*, "Spin–orbit proximity effect in graphene," *Nature Communications*, vol. 5, p. 4875, 2014.

[19] J. H. Garcia, A. W. Cummings, and S. Roche, "Spin Hall effect and weak antilocalization in graphene/transition metal dichalcogenide heterostructures," *Nano Letters*, vol. 17, no. 8, pp. 5078–5083, 2017.

[20] M. Milletarì, M. Offidani, A. Ferreira, and R. Raimondi, "Covariant conservation laws and the spin Hall effect in Dirac-Rashba systems," *Physical Review Letters*, vol. 119, no. 24, p. 246801, 2017.

[21] K. Kaasbjerg, J. H. Martiny, T. Low, and A.-P. Jauho, "Symmetry-forbidden intervalley scattering by atomic defects in monolayer transition-metal dichalcogenides," *Physical Review B*, vol. 96, no. 24, p. 241411, 2017.

[22] D. Möckli and M. Khodas, "Robust parity-mixed superconductivity in disordered monolayer transition metal dichalcogenides," *Physical Review B*, vol. 98, no. 14, p. 144518, 2018.

[23] H. Ochoa, F. Finocchiaro, F. Guinea, and V. I. Fal'ko, "Spin-valley relaxation and quantum transport regimes in two-dimensional transition-metal dichalcogenides," *Physical Review B*, vol. 90, no. 23, p. 235429, 2014.

[24] S. Ilic, J. S. Meyer, and M. Houzet, “Enhancement of the upper critical field in disordered transition metal dichalcogenide monolayers,” *Physical Review Letters*, vol. 119, no. 11, p. 117001, 2017.

[25] S. Ilić, J. S. Meyer, and M. Houzet, “Weak localization in transition metal dichalcogenide monolayers and their heterostructures with graphene,” *Physical Reviev B*, vol. 99, no. 20, p. 205407, 2019.

[26] E. Sosenko, J. Zhang, and V. Aji, “Unconventional superconductivity and anomalous response in hole-doped transition metal dichalcogenides,” *Physical Review B*, vol. 95, no. 14, p. 144508, 2017.

[27] M. Tinkham, *Introduction to superconductivity.* Courier Corporation, 2004.

[28] E. Akkermans and G. Montambaux, *Mesoscopic physics of electrons and photons.* Cambridge University Press, 2007.

[29] M. Smidman, M. Salamon, H. Yuan, and D. Agterberg, “Superconductivity and spin–orbit coupling in non-centrosymmetric materials: A review,” *Reports on Progress in Physics*, vol. 80, no. 3, p. 036501, 2017.

[30] E. Bauer and M. Sigrist, *Non-centrosymmetric superconductors: introduction and overview*, vol. 847. Springer Science & Business Media, 2012.

[31] H. Kamerlingh Onnes, “The resistance of pure mercury at helium temperatures,” *Commun. Phys. Lab. Univ. Leiden, b*, vol. 120, 1911.

[32] W. Meissner and R. Ochsenfeld, “Ein neuer effekt bei eintritt der supraleitfähigkeit,” *Naturwissenschaften*, vol. 21, no. 44, pp. 787–788, 1933.

[33] J. Bardeen, L. N. Cooper, and J. R. Schrieffer, “Theory of superconductivity,” *Physical Review*, vol. 108, no. 5, p. 1175, 1957.

[34] M. Houzet, “Applications of symmetries in superconductivity,” in *EPJ Web of Conferences*, vol. 22, p. 00014, EDP Sciences, 2012.

[35] V. P. Mineev and K. Samokhin, *Introduction to unconventional superconductivity.* CRC Press, 1999.

[36] B. D. Josephson, “Possible new effects in superconductive tunnelling,” *Physics Letters*, vol. 1, no. 7, pp. 251–253, 1962.

[37] E. Dagotto, “Correlated electrons in high-temperature superconductors,” *Reviews of Modern Physics*, vol. 66, no. 3, p. 763, 1994.

[38] S. G. Stewart, “Heavy-fermion systems,” *Reviews of Modern Physics*, vol. 56, no. 4, p. 755, 1984.

[39] J. Linder and J. W. Robinson, “Superconducting spintronics,” *Nature Physics*, vol. 11, no. 4, p. 307, 2015.

[40] M. Sato and Y. Ando, "Topological superconductors: a review," *Reports on Progress in Physics*, vol. 80, no. 7, p. 076501, 2017.

[41] G. Dresselhaus, "Spin-orbit coupling effects in zinc blende structures," *Physical Review*, vol. 100, no. 2, p. 580, 1955.

[42] Y. A. Bychkov and E. I. Rashba, "Oscillatory effects and the magnetic susceptibility of carriers in inversion layers," *Journal of Physics C: Solid State Physics*, vol. 17, no. 33, p. 6039, 1984.

[43] L. P. Gor'kov and E. I. Rashba, "Superconducting 2D system with lifted spin degeneracy: mixed singlet-triplet state," *Physical Review Letters*, vol. 87, no. 3, p. 037004, 2001.

[44] P. Fulde and R. A. Ferrell, "Superconductivity in a strong spin-exchange field," *Physical Review*, vol. 135, no. 3A, p. A550, 1964.

[45] A. Larkin and I. Ovchinnikov, "Inhomogeneous state of superconductors," *Soviet Physics-JETP*, vol. 20, pp. 762–769, 1965.

[46] V. Edel'shtein, "Characteristics of the Cooper pairing in two-dimensional noncentrosymmetric electron systems," *Soviet Physics-JETP*, vol. 68, no. 6, pp. 1244–1249, 1989.

[47] W.-Y. He and K. Law, "Novel Magnetoelectric Effects in Gyrotropic Superconductors and the Case Study of Transition Metal Dichalcogenides," *arXiv preprint arXiv:1902.02514*, 2019.

[48] A. Y. Kitaev, "Unpaired Majorana fermions in quantum wires," *Physics-Uspekhi*, vol. 44, no. 10S, p. 131, 2001.

[49] C. Nayak, S. H. Simon, A. Stern, M. Freedman, and S. D. Sarma, "Non-Abelian anyons and topological quantum computation," *Reviews of Modern Physics*, vol. 80, no. 3, p. 1083, 2008.

[50] J. Alicea, "New directions in the pursuit of Majorana fermions in solid state systems," *Reports on Progress in Physics*, vol. 75, no. 7, p. 076501, 2012.

[51] Y.-T. Hsu, A. Vaezi, M. H. Fischer, and E.-A. Kim, "Topological superconductivity in monolayer transition metal dichalcogenides," *Nature Communications*, vol. 8, p. 14985, 2017.

[52] W.-Y. He, B. T. Zhou, J. J. He, N. F. Yuan, T. Zhang, and K. Law, "Magnetic field driven nodal topological superconductivity in monolayer transition metal dichalcogenides," *Communications Physics*, vol. 1, no. 1, p. 40, 2018.

[53] B. T. Zhou, N. F. Yuan, H.-L. Jiang, and K. T. Law, "Ising superconductivity and Majorana fermions in transition-metal dichalcogenides," *Physical Review B*, vol. 93, no. 18, p. 180501, 2016.

[54] P. W. Anderson, "Theory of dirty superconductors," *Journal of Physics and Chemistry of Solids*, vol. 11, no. 1-2, pp. 26–30, 1959.

[55] J. Lu, O. Zheliuk, Q. Chen, I. Leermakers, N. E. Hussey, U. Zeitler, and J. Ye, "Full superconducting dome of strong Ising protection in gated monolayer WS_2," *Proceedings of the National Academy of Sciences*, vol. 115, no. 14, pp. 3551–3556, 2018.

[56] P. Frigeri, D. Agterberg, and M. Sigrist, "Spin susceptibility in superconductors without inversion symmetry," *New Journal of Physics*, vol. 6, no. 1, p. 115, 2004.

[57] T. Dvir, F. Massee, L. Attias, M. Khodas, M. Aprili, C. H. Quay, and H. Steinberg, "Spectroscopy of bulk and few-layer superconducting $NbSe_2$ with van der Waals tunnel junctions," *Nature Communications*, vol. 9, no. 1, p. 598, 2018.

[58] E. Sohn, X. Xi, W.-Y. He, S. Jiang, Z. Wang, K. Kang, J.-H. Park, H. Berger, L. Forró, K. T. Law, *et al.*, "An unusual continuous paramagnetic-limited superconducting phase transition in 2D $NbSe_2$," *Nature Materials*, vol. 17, pp. 504–508, 2018.

[59] N. Schopohl and K. Scharnberg, "Tunneling density of states for the two-band model of superconductivity," *Solid State Communications*, vol. 22, no. 6, pp. 371–374, 1977.

[60] W. McMillan, "Tunneling model of the superconducting proximity effect," *Physical Review*, vol. 175, no. 2, p. 537, 1968.

[61] H. Schmidt, J. Zasadzinski, K. Gray, and D. Hinks, "Evidence for two-band superconductivity from break-junction tunneling on MgB_2," *Physical Review Letters*, vol. 88, no. 12, p. 127002, 2002.

[62] Y. Noat, J. Silva-Guillén, T. Cren, V. Cherkez, C. Brun, S. Pons, F. Debontridder, D. Roditchev, W. Sacks, L. Cario, *et al.*, "Quasiparticle spectra of 2 H-$NbSe_2$: Two-band superconductivity and the role of tunneling selectivity," *Physical Review B*, vol. 92, no. 13, p. 134510, 2015.

[63] P. W. Anderson, "Absence of diffusion in certain random lattices," *Physical Review*, vol. 109, no. 5, p. 1492, 1958.

[64] J. Rammer, *Quantum transport theory.* CRC Press, 2018.

[65] H.-Z. Lu and S.-Q. Shen, "Weak localization and weak anti-localization in topological insulators," in *Spintronics VII*, vol. 9167, p. 91672E, International Society for Optics and Photonics, 2014.

[66] L. Gor'kov, A. I. Larkin, and D. Khmel'nitskiĭ, "Particle conductivity in a two-dimensional random potential," in *30 Years Of The Landau Institute—Selected Papers*, pp. 157–161, World Scientific, 1996.

[67] S. Hikami, A. I. Larkin, and Y. Nagaoka, “Spin-orbit interaction and magnetoresistance in the two dimensional random system,” *Progress of Theoretical Physsics*, vol. 63, no. 2, pp. 707–710, 1980.

[68] H. Suzuura and T. Ando, “Crossover from symplectic to orthogonal class in a two-dimensional honeycomb lattice,” *Physical Review Letters*, vol. 89, no. 26, p. 266603, 2002.

[69] H.-Z. Lu, J. Shi, and S.-Q. Shen, “Competition between weak localization and antilocalization in topological surface states,” *Physical Review Letters*, vol. 107, no. 7, p. 076801, 2011.

[70] E. McCann, K. Kechedzhi, V. I. Fal’ko, H. Suzuura, T. Ando, and B. Altshuler, “Weak-localization magnetoresistance and valley symmetry in graphene,” *Physical Review Letters*, vol. 97, no. 14, p. 146805, 2006.

[71] K. Imura, Y. Kuramoto, and K. Nomura, “Anti-localization of graphene under the substrate electric field,” *Europhysics Letters*, vol. 89, no. 1, p. 17009, 2010.

[72] E. McCann and V. I. Fal’ko, “z→- z symmetry of spin-orbit coupling and weak localization in graphene,” *Physical Review Letters*, vol. 108, no. 16, p. 166606, 2012.

[73] I. Garate and L. Glazman, “Weak localization and antilocalization in topological insulator thin films with coherent bulk-surface coupling,” *Physical Review B*, vol. 86, no. 3, p. 035422, 2012.

[74] H. Steinberg, J.-B. Laloë, V. Fatemi, J. S. Moodera, and P. Jarillo-Herrero, “Electrically tunable surface-to-bulk coherent coupling in topological insulator thin films,” *Physical Review B*, vol. 84, no. 23, p. 233101, 2011.

[75] J. Chen, X. He, K. Wu, Z. Ji, L. Lu, J. Shi, J. Smet, and Y. Li, “Tunable surface conductivity in Bi_2Se_3 revealed in diffusive electron transport,” *Physical Review B*, vol. 83, no. 24, p. 241304, 2011.

[76] H. Schmidt, I. Yudhistira, L. Chu, A. C. Neto, B. Özyilmaz, S. Adam, and G. Eda, “Quantum Transport and Observation of Dyakonov-Perel Spin-Orbit Scattering in Monolayer MoS_2,” *Physical Review Letters*, vol. 116, no. 4, p. 046803, 2016.

[77] Y. Zhang, W. Shi, J. Ye, R. Suzuki, and Y. Iwasa, “Robustly protected carrier spin relaxation in electrostatically doped transition-metal dichalcogenides,” *Physical Review B*, vol. 95, no. 20, p. 205302, 2017.

[78] D. Costanzo, S. Jo, H. Berger, and A. F. Morpurgo, “Gate-induced superconductivity in atomically thin MoS_2 crystals,” *Nature Nanotechnology*, vol. 11, no. 4, p. 339, 2016.

[79] Z. Wang, D.-K. Ki, J. Y. Khoo, D. Mauro, H. Berger, L. S. Levitov, and A. F. Morpurgo, “Origin and magnitude of “designer” spin-orbit interaction in graphene on semiconducting transition metal dichalcogenides,” *Physical Review X*, vol. 6, no. 4, p. 041020, 2016.

[80] B. Yang, M. Lohmann, D. Barroso, I. Liao, Z. Lin, Y. Liu, L. Bartels, K. Watanabe, T. Taniguchi, and J. Shi, "Strong electron-hole symmetric Rashba spin-orbit coupling in graphene/monolayer transition metal dichalcogenide heterostructures," *Physical Review B*, vol. 96, no. 4, p. 041409, 2017.

[81] T. Völkl, T. Rockinger, M. Drienovsky, K. Watanabe, T. Taniguchi, D. Weiss, and J. Eroms, "Magnetotransport in heterostructures of transition metal dichalcogenides and graphene," *Physical Review B*, vol. 96, no. 12, p. 125405, 2017.

[82] T. Wakamura, F. Reale, P. Palczynski, S. Guéron, C. Mattevi, and H. Bouchiat, "Strong anisotropic spin-orbit interaction induced in graphene by monolayer WS_2," *Physical Review Letters*, vol. 120, no. 10, p. 106802, 2018.

[83] S. Zihlmann, A. W. Cummings, J. H. Garcia, M. Kedves, K. Watanabe, T. Taniguchi, C. Schönenberger, and P. Makk, "Large spin relaxation anisotropy and valley-Zeeman spin-orbit coupling in WSe_2/graphene/h-BN heterostructures," *Physical Review B*, vol. 97, no. 7, p. 075434, 2018.

[84] B. Altshuler, "Fluctuations in the extrinsic conductivity of disordered conductors," *JETP Letters*, vol. 41, no. 12, pp. 648–651, 1985.

[85] P. A. Lee and A. D. Stone, "Universal conductance fluctuations in metals," *Physical Review Letters*, vol. 55, no. 15, p. 1622, 1985.

[86] B. Altshuler and B. Shklovskii, "Repulsion of energy levels and conductivity of small metal samples," *Soviet Physics-JETP*, vol. 64, no. 1, pp. 127–135, 1986.

[87] S. Feng, "Mesoscopic conductance fluctuations in the presence of spin-orbit coupling and Zeeman splitting," *Physical Review B*, vol. 39, no. 12, p. 8722, 1989.

[88] V. Chandrasekhar, P. Santhanam, and D. Prober, "Effect of spin-orbit and spin-flip scattering on conductance fluctuations," *Physical Review B*, vol. 42, no. 10, p. 6823, 1990.

[89] M. Y. Kharitonov and K. B. Efetov, "Universal conductance fluctuations in graphene," *Physical Review B*, vol. 78, no. 3, p. 033404, 2008.

[90] K. Kechedzhi, O. Kashuba, and V. I. Fal'ko, "Quantum kinetic equation and universal conductance fluctuations in graphene," *Physical Review B*, vol. 77, no. 19, p. 193403, 2008.

[91] S. Washburn and R. A. Webb, "Aharonov-Bohm effect in normal metal quantum coherence and transport," *Advances in Physics*, vol. 35, no. 4, pp. 375–422, 1986.

[92] A. A. Soluyanov, D. Gresch, Z. Wang, Q. Wu, M. Troyer, X. Dai, and B. A. Bernevig, "Type-II Weyl semimetals," *Nature*, vol. 527, no. 7579, p. 495, 2015.

[93] K. Deng, G. Wan, P. Deng, K. Zhang, S. Ding, E. Wang, M. Yan, H. Huang, H. Zhang, Z. Xu, *et al.*, "Experimental observation of topological Fermi arcs in type-II Weyl semimetal $MoTe_2$," *Nature Physics*, vol. 12, no. 12, p. 1105, 2016.

[94] Y. Sun, S.-C. Wu, M. N. Ali, C. Felser, and B. Yan, “Prediction of Weyl semimetal in orthorhombic $MoTe_2$,” *Physical Review B*, vol. 92, no. 16, p. 161107, 2015.

[95] Y. Qi, P. G. Naumov, M. N. Ali, C. R. Rajamathi, W. Schnelle, O. Barkalov, M. Hanfland, S.-C. Wu, C. Shekhar, Y. Sun, *et al.*, “Superconductivity in Weyl semimetal candidate $MoTe_2$,” *Nature Communications*, vol. 7, p. 11038, 2016.

[96] E. Sajadi, T. Palomaki, Z. Fei, W. Zhao, P. Bement, C. Olsen, S. Luescher, X. Xu, J. A. Folk, and D. H. Cobden, “Gate-induced superconductivity in a monolayer topological insulator,” *Science*, vol. 362, no. 6417, pp. 922–925, 2018.

[97] Y.-T. Hsu, W. S. Cole, R.-X. Zhang, and J. D. Sau, “Inversion-protected topological crystalline superconductivity in monolayer WTe_2,” *arXiv preprint arXiv:1904.06361*, 2019.

[98] S. Wu, V. Fatemi, Q. D. Gibson, K. Watanabe, T. Taniguchi, R. J. Cava, and P. Jarillo-Herrero, “Observation of the quantum spin Hall effect up to 100 kelvin in a monolayer crystal,” *Science*, vol. 359, no. 6371, pp. 76–79, 2018.

[99] Y. Shi, J. Kahn, B. Niu, Z. Fei, B. Sun, X. Cai, B. A. Francisco, D. Wu, Z.-X. Shen, X. Xu, *et al.*, “Imaging quantum spin Hall edges in monolayer WTe_2,” *Science Advances*, vol. 5, no. 2, p. eaat8799, 2019.

[100] “Transition metal dichalcogenide monolayers.” `https://en.wikipedia.org/wiki/Transition_metal_dichalcogenide_monolayers`. Accessed: 21/05/2019.

[101] R. Frindt, “Superconductivity in Ultrathin $NbSe_2$ Layers,” *Physical Review Letters*, vol. 28, no. 5, p. 299, 1972.

[102] A. Goldman, “Electrostatic gating of ultrathin films,” *Annual Review of Materials Research*, vol. 44, pp. 45–63, 2014.

[103] N. Huy, A. Gasparini, D. De Nijs, Y. Huang, J. Klaasse, T. Gortenmulder, A. de Visser, A. Hamann, T. Görlach, and H. v. Löhneysen, “Superconductivity on the border of weak itinerant ferromagnetism in UCoGe,” *Physical Review Letters*, vol. 99, no. 6, p. 067006, 2007.

[104] P. Samuely, P. Szabó, J. Kačmarčık, A. Jansen, A. Lafond, A. Meerschaut, and A. Briggs, “Two-dimensional behavior of the naturally layered superconductor $(LaSe)_{1.14}$ $(NbSe_2)$,” *Physica C: Superconductivity*, vol. 369, no. 1-4, pp. 61–67, 2002.

[105] R. C. Morris and R. V. Coleman, “Anisotropic superconductivity in layer compounds,” *Physical Review B*, vol. 7, no. 3, p. 991, 1973.

[106] T. Sekihara, R. Masutomi, and T. Okamoto, “Two-dimensional superconducting state of monolayer Pb films grown on GaAs (110) in a strong parallel magnetic field,” *Physical Review Letters*, vol. 111, no. 5, p. 057005, 2013.

[107] E. Khestanova, J. Birkbeck, M. Zhu, Y. Cao, G. Yu, D. Ghazaryan, J. Yin, H. Berger, L. Forro, T. Taniguchi, *et al.*, "Unusual suppression of the superconducting energy gap and critical temperature in atomically thin $\mathrm{NbSe_2}$," *Nano Letters*, vol. 18, no. 4, pp. 2623–2629, 2018.

[108] T. Ando, T. Nakanishi, and R. Saito, "Berry's phase and absence of back scattering in carbon nanotubes," *Journal of the Physical Society of Japan*, vol. 67, no. 8, pp. 2857–2862, 1998.

[109] Y. Zhang, Y.-W. Tan, H. L. Stormer, and P. Kim, "Experimental observation of the quantum Hall effect and Berry's phase in graphene," *Nature*, vol. 438, no. 7065, p. 201, 2005.

[110] C. L. Kane and E. J. Mele, "Quantum spin Hall effect in graphene," *Physical Review Letters*, vol. 95, no. 22, p. 226801, 2005.

[111] A. Altland and B. D. Simons, *Condensed matter field theory.* Cambridge University Press, 2010.

[112] H. Bruus and K. Flensberg, *Many-body quantum theory in condensed matter physics: an introduction.* Oxford University Press, 2004.

[113] M. V. Sadovskii, *Diagrammatics: lectures on selected problems in condensed matter theory.* World Scientific, 2006.

[114] N. Kopnin, *Theory of nonequilibrium superconductivity*, vol. 110. Oxford University Press, 2001.

[115] P. Frigeri, D. Agterberg, A. Koga, and M. Sigrist, "Superconductivity without Inversion Symmetry: MnSi versus $\mathrm{CePt_3S}$ i," *Physical Review Letters*, vol. 92, no. 9, p. 097001, 2004.

[116] A. A. Abrikosov and L. P. Gor'kov, "Contribution to the theory of superconducting alloys with paramagnetic impurities," *Zhur. Eksptl'. i Teoret. Fiz.*, vol. 39, 1960.

[117] K. Maki, "Gapless superconductivity," in *Superconductivity*, pp. 1035–1105, Routledge, 2018.

[118] K. Maki and T. Tsuneto, "Pauli paramagnetism and superconducting state," *Progress of Theoretical Physics*, vol. 31, no. 6, pp. 945–956, 1964.

[119] L. Aslamazov, "Influence of impurities on the existence of an inhomogeneous state in a ferromagnetic superconductor," *Soviet Physics-JETP*, vol. 28, no. 4, pp. 773–775, 1969.

[120] A. Kaiser and M. Zuckermann, "McMillan model of the superconducting proximity effect for dilute magnetic alloys," *Physical Review B*, vol. 1, no. 1, p. 229, 1970.

[121] B. A. Bernevig and T. L. Hughes, *Topological insulators and topological superconductors.* Princeton University Press, 2013.

[122] W.-Y. Shan, H.-Z. Lu, and S.-Q. Shen, "Spin-orbit scattering in quantum diffusion of massive Dirac fermions," *Physical Review B*, vol. 86, no. 12, p. 125303, 2012.

[123] R. . J. Elliott, "Theory of the effect of spin-orbit coupling on magnetic resonance in some semiconductors," *Physical Review*, vol. 96, no. 2, p. 266, 1954.

[124] Y. Yafet, "g Factors and spin-lattice relaxation of conduction electrons," in *Solid State Physics*, vol. 14, pp. 1–98, Elsevier, 1963.

[125] M. D'yakonov and V. Perel, "Spin orientation of electrons associated with the interband absorption of light in semiconductors," *Soviet Physics-JETP*, vol. 33, p. 1053, 1971.

[126] S. Maekawa and H. Fukuyama, "Magnetoresistance in two-dimensional disordered systems: effects of Zeeman splitting and spin-orbit scattering," *Journal of the Physical Society of Japan*, vol. 50, no. 8, pp. 2516–2524, 1981.

[127] A. W. Cummings, J. H. García, J. Fabian, and S. Roche, "Giant Spin Lifetime Anisotropy in Graphene Induced by Proximity Effects," *Physical Review Letters*, vol. 119, p. 206601, 2017.

[128] J. H. Garcia, M. Vila, A. W. Cummings, and S. Roche, "Spin transport in graphene/transition metal dichalcogenide heterostructures," *Chemical Society Reviews*, vol. 47, no. 9, pp. 3359–3379, 2018.

[129] M. B. Lundeberg and J. A. Folk, "Rippled graphene in an in-plane magnetic field: effects of a random vector potential," *Physical Review Letters*, vol. 105, no. 14, p. 146804, 2010.

[130] V. M. Edelstein, "Spin polarization of conduction electrons induced by electric current in two-dimensional asymmetric electron systems," *Solid State Communications*, vol. 73, no. 3, pp. 233–235, 1990.

[131] Q. Shao, G. Yu, Y.-W. Lan, Y. Shi, M.-Y. Li, C. Zheng, X. Zhu, L.-J. Li, P. K. Amiri, and K. L. Wang, "Strong Rashba-Edelstein effect-induced spin–orbit torques in monolayer transition metal dichalcogenide/ferromagnet bilayers," *Nano Letters*, vol. 16, no. 12, pp. 7514–7520, 2016.

Publications of the author in refereed journals

1. S. Ilić, J. S. Meyer, M. Houzet, “Enhancement of the upper critical field in disordered transition metal dichalcogenide monolayers,” *Physical Review Letters*, vol. 119, no. 11, p. 117001, 2017.
2. S. Ilić, J. S. Meyer, M. Houzet, “Weak localization in transition metal dichalcogenide monolayers and their heterostructures with graphene,” *Physical Review B*, vol. 99, no. 20, p. 205407, 2019.